

# **Synthesis and Characterization of the TiO<sub>2</sub>(B) phase**

Yothin Chimupala

Submitted in accordance with the requirements for the degree of  
Doctor of Philosophy

The University of Leeds  
School of Chemical and Process Engineering (SCAPE)  
Institute for Materials Research

August, 2015

The candidate confirms that the work submitted is his own, except where work which has formed part of jointly authored publications has been included. The contribution of the candidate and the other authors to this work has been explicitly indicated below. The candidate confirms that appropriate credit has been given within the thesis where reference has been made to the work of others.

Y. Chimupala, G. Hyett, R. Simpson and R. Brydson, *J. Phys. Conf. Ser.*, 2014, 522, 012074.

- The work in this paper contributes to Chapter 5 of my thesis
- My contribution to work in the paper was all experimental processes including characterizations & discussions and wrote the first draft of the paper.

Y. Chimupala, G. Hyett, R. Simpson, R. Mitchell, R. Douthwaite, S. J. Milne and R. D. Brydson, *RSC Adv.*, 2014, 4, 48507.

- The work in this paper contributes to Chapter 5 of my thesis
- My contribution to work in the paper was all experimental processes including characterizations & discussions and wrote the first draft of the paper

Y. Chimupala, P. Junploy, T. Hardcastle, A. Westwood and R. Brydson, *J. Mater. Chem. A*, 2015 (under review)

- The work in this paper contributes to Chapter 6 of my thesis
- My contribution to work in the paper was all experimental processes including characterizations & discussions and wrote the first draft of the paper.

This copy has been supplied on the understanding that it is copyright material and that no quotation from the thesis may be published without proper acknowledgement.

© 2015 The University of Leeds and Yothin Chimupala

## Acknowledgement

I would like to express my deep and sincere thanks to my supervisor, Prof. Dr. Rik Brydson, for his kindness, useful advice and constant guidance throughout this work.

I would like to thank Dr. Steven Milne, my co-supervisor, for his counseling and recommendation especially on a hydrothermal synthesis for TiO<sub>2</sub> nanomaterials.

I would like to thank Dr. Geoffrey Hyett, for his valuable suggestions in a LPCVD technique and every equipment for setting up the LPCVD rig. I also wish to sincerely thank Mr. Robert Simpson who is a technical supporter in my experimental process especially setting up the LPCVD rig.

I would like to special thank my project consultant and co-workers:

- Mr. Robert Mitchell and Dr. Richard Dounthwaite from the University of York, for their generous guidance, unfailing support and valuable catalyst samples;
- Dr. Aidan Westwood, SCAPE, University of Leeds who always provide the valuable guidance;
- A part of this research has been carried out by a team which has includes Mrs. Marzoqa Mabrok-H-Alnairi and Mr. Navadacho Chankhunthod who are an intelligent master student under my supervision and Miss Patcharanan Junploy (an exchange research student from Thailand). They was very active and diligent;

I reveal my gratitude to Institute of Materials Research (IMR), School of Chemical and Materials Engineering (SCAPE), University of Leeds for every technical instrument support including cooperative people, Dr. Mike Ward, Mr. John Harrington, Mr. Stuart Micklethwaite and Dr. Tim Comyn.

My profound thanks give to all the other members of IMR especially Dr. Brindusa Mironov, Mr. Antonio Salituro, Mr. Tarun Kakkar, Mr. Faith Bamiduro, Mr. Thiago Simoes, Mr. Omar Matar, Miss Helen Freeman and Mr. Jayakrishnan Chandrappan including my Thai friends: Mr. Siwarote Siriluck, Mr. Thana Sutthibutpong and Miss Thanisorn Mahatnirunkul for the numerous assistance, sincere guidance, admirable cooperation and inspiration.

Thankfulness is given to everyone who has a part in this project research and my life, although their names are not listed here.

Finally, I would like to give all acknowledgements to Ministry of Science and Technology, The Royal Thai Government, Thailand for a financial support throughout my Ph.D life in UK.

Yothin Chimupala

## Abstract

TiO<sub>2</sub>(B) or “bronze” is a TiO<sub>2</sub> polymorph which is difficult to synthesise in a pure form and does not commonly exist in minerals. TiO<sub>2</sub>(B) potentially plays an important role in applications both as a photocatalytic component alongside anatase for degradation reactions and as an anode material in lithium ion batteries due to its distinctive crystal structure which exhibits large channels and voids. In this research, TiO<sub>2</sub>(B) has been successfully synthesised by both a hydrothermal route and a Low Pressure Chemical Vapour Deposition (LPCVD) process. Samples were characterised using powder-XRD, Raman spectroscopy, TEM, SEM and UV-Vis spectroscopy. Phase formation mechanisms for both the hydrothermal route and LPCVD process have been proposed.

Initially, in order to investigate the TiO<sub>2</sub>(B) phase formation mechanism via a sodium titanate phase transformation, hydrothermal synthesis was employed to produce TiO<sub>2</sub>(B) nanorods including an investigation of the products at each stage of the reaction. The results were used to propose an integrated reaction mechanism which corresponds well with literature. This involved the structural transformation of a sodium titanate intermediate phase which is of interest in relation to the other TiO<sub>2</sub>(B) fabrication methods where Na<sup>+</sup> ions are present in the system such as CVD on glass substrates. As a result, the synthesis of mixed phase TiO<sub>2</sub>(B) and anatase thin films on a soda lime glass substrate has been achieved, for the first time, by LPCVD synthesis. Titanium isopropoxide (TTIP) and N<sub>2</sub> gas were used as the precursor and carrier gas respectively. The optimal LPCVD condition for preparing a mixed phase of TiO<sub>2</sub> containing TiO<sub>2</sub>(B) was 550°C (actual temperature) with a 1 mL/s N<sub>2</sub> flow rate. A possible thin-film formation mechanism during the LPCVD process has been proposed.

Subsequently a pre-treatment method involving spraying a Na<sup>+</sup>-containing solution, such as sodium ethoxide, onto a number of different substrates including silicon wafer, fused quartz, highly ordered pyrolytic graphite (HOPG) and pressed graphite flake (grafoil) was applied in conjunction with the LPCVD method in order to promote the TiO<sub>2</sub>(B) phase in the thin film products formed on any substrate.

Finally, the effects of different alkali metal ions (Li<sup>+</sup>, Na<sup>+</sup> and K<sup>+</sup> from alkali metal hydroxide solutions) during the pre-treatment step were investigated in relation to the phase formation in the thin films produced during the LPCVD process. Only Na<sup>+</sup> ions were found to encourage the phase formation of TiO<sub>2</sub>(B), K<sup>+</sup> ions produced only a minority of the TiO<sub>2</sub>(B) phase, whereas Li<sup>+</sup> ions did not produce TiO<sub>2</sub>(B).

Phase formation mechanisms have been proposed based on alkali metal migration from the pre-treatment layer into the deposited nascent titania film and the formation of intermediate titanate phases.

## Table of Contents

|   |                |
|---|----------------|
| <b>Acknowledgement</b> .....  | <b>- iii -</b> |
| <b>Abstract</b> .....   | <b>- v -</b>   |
| <b>Table of Contents</b> .....  | <b>- vii -</b> |
| <b>List of Tables</b> .....   | <b>- xi -</b>  |
| <b>List of Figures</b> .....  | <b>- xii -</b> |
| <b>Chapter 1 Introduction</b> .....   | <b>- 1 -</b>   |
| 1.1 Background and Rationale.....   | - 1 -          |
| 1.2 Aims and Objectives.....  | - 4 -          |
| 1.3 Layout of the thesis .....  | - 5 -          |
| 1.4 List of publications and presentations .....  | - 6 -          |
| 1.5 References .....  | - 7 -          |
| <b>Chapter 2 Titanium Dioxide: Structure, Processing &amp; Properties</b> .....                     | <b>- 8 -</b>   |
| 2.1 Structures of 11 TiO <sub>2</sub> Crystalline Phases.....                                       | - 8 -          |
| 2.2 General applications of Titanium dioxide (TiO <sub>2</sub> ).....                               | - 15 -         |
| 2.3 Applications of TiO <sub>2</sub> (B).....   | - 16 -         |
| 2.3.1 TiO <sub>2</sub> (B) for Lithium ion anode batteries.....                                     | - 16 -         |
| 2.3.2 TiO <sub>2</sub> (B) for photocatalytic applications .....                                    | - 19 -         |
| 2.4 Fabrication method of TiO <sub>2</sub> (B) phase .....  | - 24 -         |
| 2.4.1 Solid State Synthesis .....   | - 25 -         |
| 2.4.2 Hydrothermal Synthesis .....  | - 25 -         |
| 2.5 References .....  | - 32 -         |
| <b>Chapter 3 Sample Preparations and Characterization methods</b> .....                             | <b>- 40 -</b>  |
| 3.1 Fabrication Methods .....   | - 40 -         |
| 3.1.1 Hydrothermal Synthesis .....  | - 40 -         |
| 3.1.1.1 Background and theory of hydrothermal synthesis   | - 40 -         |
| 3.1.1.2 Experimental Procedure for Hydrothermal synthesis<br>of the TiO <sub>2</sub> (B) phase..... | - 42 -         |
| 3.1.2 Chemical Vapour Deposition (CVD) .....  | - 43 -         |
| 3.1.2.1 Background and Theory of CVD method.....  | - 43 -         |
| 3.1.2.2 CVD for TiO <sub>2</sub> synthesis .....  | - 46 -         |
| 3.1.2.3 Experimental Procedure on LPCVD method for<br>TiO <sub>2</sub> (B) phase preparation.....   | - 52 -         |
| 3.2 Characterisation methods .....  | - 56 -         |

|  |               |
|--|---------------|
| 3.2.1 Powder X-Ray Diffraction (PXRD) .....  | - 56 -        |
| 3.2.1.1 XRD methodology .....  | - 56 -        |
| 3.2.1.2 XRD experimental details .....   | - 60 -        |
| 3.2.2 Electron Microscopy .....  | - 61 -        |
| 3.2.2.1 Scanning Electron Microscopy (SEM).....  | - 61 -        |
| 3.2.2.2 Transmission Electron Microscopy (TEM).....  | - 64 -        |
| 3.2.3 Energy Dispersive X-ray Spectroscopy (EDX) .....   | - 67 -        |
| 3.2.4 Raman Spectroscopy .....   | - 68 -        |
| 3.2.5 UV-Visible Diffuse Reflectance Spectroscopy .....  | - 68 -        |
| 3.3 Reference .....  | - 69 -        |
| <b>Chapter 4 Hydrothermal Synthesis of TiO<sub>2</sub>(B) Nanorods via Alkali Metal Titanate Phase Transformation.....</b>   | <b>- 73 -</b> |
| 4.1 Experimental Procedure .....   | - 73 -        |
| 4.1.1 Hydrothermal synthesis method .....  | - 73 -        |
| 4.1.2 Materials Characterization.....  | - 73 -        |
| 4.2 Results .....  | - 74 -        |
| 4.2.1 X-ray Diffraction.....   | - 74 -        |
| 4.2.2 Raman Spectroscopy .....   | - 78 -        |
| 4.2.3 Scanning electron microscopy (SEM).....  | - 79 -        |
| 4.2.4 Transmission electron microscopy (TEM).....  | - 80 -        |
| 4.3 Discussion .....   | - 84 -        |
| 4.4 Conclusion .....   | - 88 -        |
| 4.5 References.....  | - 88 -        |
| <b>Chapter 5 Synthesis and characterization of mixed phase anatase TiO<sub>2</sub> and sodium-doped TiO<sub>2</sub>(B) thin films by low pressure chemical vapour deposition (LPCVD) .....</b> | <b>- 90 -</b> |
| 5.1 Experimental Procedure .....   | - 90 -        |
| 5.1.1 Thin Film Preparation .....  | - 90 -        |
| 5.1.2 Materials Characterization.....  | - 90 -        |
| 5.2 Results .....  | - 91 -        |
| 5.2.1 X-ray Diffraction.....   | - 91 -        |
| 5.2.2 Raman Spectroscopy .....   | - 93 -        |
| 5.2.3 UV-Visible Spectroscopy .....  | - 93 -        |
| 5.2.4 Scanning Electron Microscopy .....   | - 94 -        |
| 5.2.5 Transmission Electron Microscopy .....   | - 98 -        |
| 5.3 Discussion .....   | - 102 -       |

|   |   |         |
|---|---|---------|
| 5.4   | Conclusions .....   | - 104 - |
| 5.5   | References .....  | - 105 - |
| <b>Chapter 6 Universal synthesis method for mixed phase TiO<sub>2</sub>(B) and anatase TiO<sub>2</sub> thin films on substrates via a modified low pressure chemical vapour deposition (LPCVD) route.....</b> |   |         |
| 6.1   | Experimental Procedure .....  | - 108 - |
| 6.1.1   | Substrate Pre-treatment .....   | - 108 - |
| 6.1.2   | TiO <sub>2</sub> Thin Film Deposition .....   | - 108 - |
| 6.1.3   | Materials Characterization.....   | - 109 - |
| 6.2   | Results and Discussion.....   | - 109 - |
| 6.2.1   | X-ray Diffraction.....  | - 109 - |
| 6.2.2   | Raman Spectroscopy .....  | - 109 - |
| 6.2.3   | Scanning Electron Microscopy .....  | - 110 - |
| 6.2.4   | Transmission Electron Microscopy .....  | - 113 - |
| 6.2.5   | Effect of Na content in the Substrate Pre-treatment .....   | - 119 - |
| 6.3   | Discussion .....  | - 120 - |
| 6.4   | Conclusions .....   | - 124 - |
| 6.5   | References .....  | - 124 - |
| <b>Chapter 7 The modified LPCVD method using an alkali metal ion pretreatment of substrate surfaces .....</b>   |   |         |
| 7.1   | Experiment procedure .....  | - 127 - |
| 7.1.1   | Pre-treatment of the Si wafer substrate.....  | - 127 - |
| 7.1.2   | Deposition of TiO <sub>2</sub> thin films on pre-treatment substrates by LPCVD method .....                     | - 127 - |
| 7.1.3   | Materials characterization .....  | - 127 - |
| 7.2   | Results .....   | - 128 - |
| 7.2.1   | Effect of type of alkali metal ion on titania or titanate thin films composition prepared by LPCVD method ..... | - 128 - |
| 7.2.2   | Influence of alkali metal hydroxide concentration used in pre-treatment process on phase formation .....        | - 132 - |
| 7.2.2.1   | Pre-treatment with LiOH solution .....  | - 132 - |
| 7.2.2.2   | Pre-treatment with NaOH solution .....  | - 133 - |
| 7.2.2.3   | Pre-treatment with KOH solution .....   | - 134 - |
| 7.2.3   | Influence of the different type of alkali metal ion on the physical appearance of the films .....               | - 136 - |
| 7.3   | Discussion .....  | - 139 - |

|   |                |
|---|----------------|
| 7.3.1 The influence of Na <sup>+</sup> ions on titania/titanate phase formation during LPCVD method ..... | - 140 -        |
| 7.3.2 The influence of K <sup>+</sup> ions on titania/titanate phase formation during LPCVD.....          | - 143 -        |
| 7.3.3 The influence of Li <sup>+</sup> on titania/titanate phase formation during LPCVD method .....      | - 146 -        |
| 7.4 Conclusions .....   | - 149 -        |
| 7.5 References .....  | - 150 -        |
| <b>Chapter 8 Conclusions and Future work .....</b>  | <b>- 152 -</b> |
| 8.1 Research Summary .....  | - 152 -        |
| 8.2 Main Findings from the Research.....  | - 154 -        |
| 8.3 Future Work .....   | - 155 -        |
| <b>Appendix I Standard operating percedure.....</b>   | <b>- 157 -</b> |
| <b>Appendix II Supporting imformation .....</b>   | <b>- 162 -</b> |

## List of Tables

|  |         |
|--|---------|
| <b>Table 2-1</b> Structural data of 11 TiO <sub>2</sub> crystalline polymorphs.....  | - 10 -  |
| <b>Table 2-2</b> General physical, chemical and optical properties of TiO <sub>2</sub> structures-   | 16 -    |
| <b>Table 2-3</b> Literature articles which have synthesized TiO <sub>2</sub> (B) for application as an electrode in Li ion batteries .....   | - 18 -  |
| <b>Table 2-4</b> Literature articles which have synthesized TiO <sub>2</sub> (B) for application as a photocatalyst. ....  | - 23 -  |
| <b>Table 2-5</b> Literature articles which have used the hydrothermal process to synthesise TiO <sub>2</sub> (B) materials. This table shows the phase/s and morphology of the TiO <sub>2</sub> product, synthesis routes and synthesis parameters: .....                    | - 27 -  |
| <b>Table 3-1</b> Literature articles which have used the CVD method to synthesise TiO <sub>2</sub> materials. This table shows the synthesis parameters and physical appearance of TiO <sub>2</sub> final product.....   | - 47 -  |
| <b>Table 4-1</b> List of synthesised samples with results of SEM/EDX quantitative elemental analysis, XRD crystallite size and primary particle size derived from SEM .....  | - 76 -  |
| <b>Table 6-1</b> List of synthesised samples with results of SEM/EDX quantitative elemental analysis, XRD crystallite size and primary particle size and film thickness derived from SEM.....  | - 112 - |
| <b>Table 7-1</b> List of synthesized samples with the details of alkaline hydroxide concentration used in pre-treatment of substrates by spraying .....  | - 128 - |
| <b>Table 7-2</b> The conclusions of titania/titanate phases of thin film products synthesized by modified LPCVD with pre-treatment of Si wafer substrates by spraying three different alkaline hydroxide solution in varied concentration. ....                              | - 131 - |
| <b>Table 7-3</b> List of synthesised samples following LiOH pre-treatment with results of SEM/EDX quantitative elemental analysis, XRD crystallite size and measured aggregate particle size and film thickness derived from SEM images. Note Li not detectable by EDX. .... | - 138 - |
| <b>Table 7-4</b> List of synthesised samples following NaOH pre-treatment with results of SEM/EDX quantitative elemental analysis, XRD crystallite size and measured aggregate particle size and film thickness derived from SEM images. ....                                | - 138 - |
| <b>Table 7-5</b> List of synthesised samples following KOH pre-treatment with results of SEM/EDX quantitative elemental analysis, XRD crystallite size and measured aggregate particle size and film thickness derived from SEM images. ....                                 | - 138 - |

## List of Figures

- Figure 1-1** Graphical representation of the number of research publications which are relevant to the study of TiO<sub>2</sub> for the water splitting reaction. .... - 2 -
- Figure 1-2** Graphical representation of the number of research publications which are relevant to the use of TiO<sub>2</sub> as an electrode in Li-ions batteries. .. - 3 -
- Figure 1-3** Graphical representation of the number of research publications which are relevant to the TiO<sub>2</sub>(B) phase..... - 4 -
- Figure 2-1** Pressure-temperature phase diagram for TiO<sub>2</sub> system ..... - 10 -
- Figure 2-2** Schematic representation of a TiO<sub>6</sub> octahedra unit and edge-sharing and corner-sharing configuration ..... - 11 -
- Figure 2-3** Crystal structures of Titanium dioxide:(a) anatase; (b) rutile; (c) brookite and TiO<sub>2</sub>(B). Ball-and-stick models are located on the left hand side comparing with the polyhedron models as shown on the right hand side. .... - 12 -
- Figure 2-4** Crystal structures of anatase, rutile, brookite and TiO<sub>2</sub>(B) viewed along a ([100]), b ([010]) and c ([001]) axes. .... - 13 -
- Figure 2-5** The crystal voids structures of anatase, rutile, brookite and TiO<sub>2</sub>(B) with percentages of crystal voids calculated from Crystal Explorer with isovalue of 0.008\* e.au<sup>-3</sup>. .... - 14 -
- Figure 2-6** Diagram illustrating the lithium ion capacity of conventional electrode materials and their electrochemical reduction potentials ..... - 17 -
- Figure 2-7** Schematic of TiO<sub>2</sub> semiconductor photocatalysis and charge separating reaction..... - 19 -
- Figure 2-8** Schematic description of the different proposed charge transfer processes and energy band structures of the mixed phases ..... - 20 -
- Figure 2-9** Summarized diagrams showing applications of TiO<sub>2</sub>(B) involving both pure TiO<sub>2</sub>(B) and a mixed phase of TiO<sub>2</sub>(B) with other TiO<sub>2</sub> phases.- 24 -
- Figure 3-1** (a) Diagram showing the components of a large capacity acid digestion vessel (b) an image of the large capacity acid digestion vessel employed in the hydrothermal synthesis for TiO<sub>2</sub>(B). .... - 41 -
- Figure 3-2** The basic principles of the main steps occurring in the CVD process ..... - 44 -
- Figure 3-3** Particle formation in the furnace via Homogeneous Reaction Route - 45 -
- Figure 3-4** Low Pressure Chemical Vapour Deposition (LPCVD) rig at SCAPE, the University of Leeds ..... - 54 -
- Figure 3-5** (a) Schematic representation showing the LPCVD system for preparing TiO<sub>2</sub> (b) temperature profile in the tube furnace for a nominal reaction temperature of 600°C ..... - 55 -
- Figure 3-6** Schematic of pre-treatment process by spraying alkali metal solution onto a Si-wafer substrate..... - 56 -

|   |        |
|---|--------|
| <b>Figure 3-7</b> X-ray diffraction from parallel planes of atoms in a crystalline material.....  | - 57 - |
| <b>Figure 3-8</b> The orientation of observed crystal plane depend on scanning mode: (a) Out-of-Plane scanning; (b) In-Plane scanning. ....   | - 58 - |
| <b>Figure 3-9</b> The In-plane and Out-of-plane XRD patterns of mixed phase TiO <sub>2</sub> (B) and anatase thin films on soda-lime glass substrate with a preferred [001] orientation of TiO <sub>2</sub> (B) parallel to the substrate. ....                                   | - 59 - |
| <b>Figure 3-10</b> Schematic showing the internal polygrains and/or polycrystals of TiO <sub>2</sub> thinfilms deposited on a glass substrate with their X-ray diffraction of lattice planes in individual single crystals.....   | - 59 - |
| <b>Figure 3-11</b> The XRD machines operated in this research .....   | - 60 - |
| <b>Figure 3-12</b> Secondary signals generated by high-energy electrons interaction with the specimen materials.....  | - 62 - |
| <b>Figure 3-13</b> Schematic representation of the basic operation of a scanning electron microscope.....   | - 63 - |
| <b>Figure 3-14</b> Two ray diagrams showing two main operating modes of the TEM: (a) The imaging mode and (b) the diffraction mode. ....  | - 65 - |
| <b>Figure 3-15</b> Example TEM images of: (a) BF image of TiO <sub>2</sub> nanoparticles ;(b) DF image of TiO <sub>2</sub> nanoparticles at the same area as Figure 3-15(a) and ;(c) HRTEM of nanoparticles mixed phase anatase and Rutile TiO <sub>2</sub> .....                 | - 66 - |
| <b>Figure 3-16</b> The possible electron transitions in the electron energy levels of Tungsten atom. ....   | - 67 - |
| <b>Figure 3-17</b> TEM-EDX spectrum of a group of TiO <sub>2</sub> (B) needle particles on the holey carbon film supported on a Cu TEM grid .....   | - 67 - |
| <b>Figure 3-18</b> (a) Raman spectrum of mixed phase TiO <sub>2</sub> (B) and anatase thin films on soda-lime glass substrate (b) The Renishaw's inVia Raman microscope machine proceeding at SCAPE, Faculty of Engineering, University of Leeds. ....                            | - 68 - |
| <b>Figure 3-19</b> (a) two types of reflections, a smooth surface usually provides specular reflection whereas a rough surface prefers to generate diffuse reflection (b) basic optical layout for a double beam 150 mm integrating sphere of Perkin Elmer UV-Vis Lambda 900..... | - 69 - |
| <b>Figure 4-1</b> XRD pattern of A <sub>1</sub> ; the first intermediate product from the hydrothermal procedure. ....  | - 74 - |
| <b>Figure 4-2</b> XRD patterns of A <sub>2</sub> , R <sub>2</sub> , T <sub>2</sub> and P <sub>2</sub> ; the second intermediate products after the ion-exchange process. ....   | - 75 - |
| <b>Figure 4-3</b> XRD patterns of A@400, R@400, T@400 and P@400; the final products after calcination of the second intermediate phase at 400°C for 5 hr.....   | - 76 - |
| <b>Figure 4-4</b> In-situ hot-stage XRD characterization of A <sub>2</sub> , heating rate: 5 °C min <sup>-1</sup> .....   | - 78 - |
| <b>Figure 4-5</b> Raman spectra of A@400 and P@400 .....  | - 79 - |

|  |        |
|--|--------|
| <b>Figure 4-6</b> SEM secondary electron images of TiO <sub>2</sub> (B) final products from the four different Ti precursors: (a) P25, P@400 (b) TTIP, T@400 (c) Rutile, R@400 and (d) Anatase, A@400. ....  | - 80 - |
| <b>Figure 4-7</b> (a) A HRTEM image taken from P@400 (b) a ring diffraction pattern taken from a group of particles shown in the image inset, (c) a spot diffraction pattern of a single particle shown in the image inset.-   | 81 -   |
| <b>Figure 4-8</b> (a) A HRTEM image taken from T@400 (b) a ring diffraction pattern taken from a group of particles shown in the image inset, (c) a spot diffraction pattern of a single particle shown in the image inset.-   | 82 -   |
| <b>Figure 4-9</b> (a) A HRTEM image taken from R@400 (b) a ring diffraction pattern taken from a group of particles shown in the image inset, (c) a spot diffraction pattern of a single particle shown in the image inset.-   | 83 -   |
| <b>Figure 4-10</b> (a) A HRTEM image taken from A@400 (b) a ring diffraction pattern taken from a group of particles shown in the image inset, (c) a spot diffraction pattern of a single particle shown in the image inset.-  | 84 -   |
| <b>Figure 4-11</b> Schematic view of a TiO <sub>2</sub> (B) nanorod (P@400) with an orientation corresponding to the evidence from XRD, HRTEM and SADP.....  | - 85 - |
| <b>Figure 4-12</b> Schematic diagram depicting the hydrothermal phase transformation mechanism for preparing the TiO <sub>2</sub> (B) phase. ....  | - 87 - |
| <b>Figure 5-1</b> Out of plane XRD patterns of TiO <sub>2</sub> thin film deposited onto soda-lime glass substrates and a quartz substrate at position Plate 4 prepared by LPCVD at 600°C.....   | - 92 - |
| <b>Figure 5-2</b> In plane and out of plane XRD patterns of Plate 4 .....  | - 93 - |
| <b>Figure 5-3</b> Raman spectra of Plate 4 and Quartz-plate 4 .....  | - 94 - |
| <b>Figure 5-4</b> (a) UV-Vis diffuse reflectance spectra of the samples prepared at optimum LPCVD condition (b) Estimation of the band gap energy by plotting the corresponding graph of photon energy (eV) versus transformed Kubelka-Munk function. ....   | - 95 - |
| <b>Figure 5-5</b> (a) SEM secondary electron image of TiO <sub>2</sub> thin film from the top surface of Plate 4; (b) SEM secondary electron image of TiO <sub>2</sub> thin film from the top surface of Quartz-plate 4.....   | - 96 - |
| <b>Figure 5-6</b> SEM cross-sectional images of thin film fracture surfaces of Plate 4 on: (a) soda lime glass and (b) fused quartz substrates; (c) Plot of the film thickness relative to the gas entry point (d) The decreasing of TiO <sub>2</sub> film thickness on Soda lime glass substrate relative to the gas entry point..... | - 97 - |
| <b>Figure 5-7</b> (a) A TEM image taken from Plate 4, showing both anatase polygonal plates and TiO <sub>2</sub> (B) needle-shaped particles; (b) HRTEM and diffraction pattern of a TiO <sub>2</sub> (B) needle; (c) HRTEM image of an anatase polygonal plate.....   | - 98 - |

|  |         |
|--|---------|
| <b>Figure 5-8</b> TEM-EDS spectrum of: (a) a group of needles particles investigated in the same area of Figure 5-7(b); (b) a polygonal plate particle correlated with Figure 5-7(b) .....   | - 99 -  |
| <b>Figure 5-9</b> (a) A TEM image of FIB cross section of Plate 4;(b) A HRTEM image taken from FIB-section at a square area labelled as 5-9(b) on the Figure 5-9(a); (c) A HRTEM image taken from different square area of the Figure 5-9(a), labelled as 5-9(c) of TiO <sub>2</sub> (B) needle-shaped particles | - 100 - |
| <b>Figure 5-10</b> STEM-EDS elemental maps of FIB cross section of Plate 4 .....   | - 101 - |
| <b>Figure 5-11</b> STEM-EDS line scanning of FIB cross section of Plate 4.....   | - 102 - |
| <b>Figure 5-12</b> Proposed mechanism for synthesis of mixed phase TiO <sub>2</sub> thin films by LPCVD method.....  | - 104 - |
| <b>Figure 6-1</b> XRD patterns of TiO <sub>2</sub> thin films deposited onto four different substrates: Si wafer, fused quartz, HOPG and Grafoil.....  | - 110 - |
| <b>Figure 6-2</b> Raman spectra of TiO <sub>2</sub> thin films deposited onto four different substrates: Si wafer, fused quartz, HOPG and Grafoil.....   | - 111 - |
| <b>Figure 6-3</b> SEM secondary electron images of TiO <sub>2</sub> particles from the top surface of thin films deposited on: (a) Si wafer (b) fused quartz (c) HOPG and (d) Grafoil substrates respectively. ....  | - 111 - |
| <b>Figure 6-4</b> SEM cross-sectional images of TiO <sub>2</sub> thin films deposited on: (a) Si wafer (b) fused- quartz (c) HOPG and (d) Grafoil substrates .....   | - 112 - |
| <b>Figure 6-5</b> (a) A bright field TEM image taken from 0.5%_Si; (b) a HRTEM image of a TiO <sub>2</sub> (B) particle and (c) a HRTEM image of anatase particles, both with the corresponding fast Fourier transforms of the image inset..   | - 113 - |
| <b>Figure 6-6</b> (a) A bright field TEM image taken from 0.5%_Fused quartz; (b) a HRTEM image of TiO <sub>2</sub> (B) with corresponding fast Fourier transform of the image inset;(c) a diffraction pattern of a group of particles shown in the image inset. ....   | - 114 - |
| <b>Figure 6-7</b> (a) A typical TEM image taken from 0.5%_HOPG; (b) a HRTEM image of a TiO <sub>2</sub> (B) particle with associated electron diffraction pattern; (c) diffraction pattern taken from a group of particles shown in the image inset. ....  | - 115 - |
| <b>Figure 6-8</b> (a) A bright field TEM image taken from 0.5%_Grafoil; (b) a HRTEM image of a group of TiO <sub>2</sub> (B) with corresponding fast Fourier transform of the image inset;(c) a diffraction pattern of a group of particles shown in the image inset. ....                                       | - 116 - |
| <b>Figure 6-9</b> (a) A TEM image of a FIB cross-section of 0.5%_Si; (b) corresponding HRTEM image at the TiO <sub>2</sub> /Si wafer interface labeled as 10B in (a); (c) HRTEM image taken from the TiO <sub>2</sub> /protective Pt layer interface labeled as 10C in (a).....                                  | - 117 - |
| <b>Figure 6-10</b> STEM-EDX elemental maps from the FIB cross-sectional sample of 0.5%_Si, showing the elemental distribution in the thin film and the TiO <sub>2</sub> /Si wafer and TiO <sub>2</sub> /protective Pt layer interfacial areas. ....  | - 118 - |

|   |         |
|---|---------|
| <b>Figure 6-11</b> XRD patterns of TiO <sub>2</sub> thin films deposited onto Si wafer substrates pre-coated with a very thin sodium-containing layer by spraying different concentrations of sodium ethoxide/ethanol solution. .   | - 119 - |
| <b>Figure 6-12</b> Off axis XRD patterns of TiO <sub>2</sub> thin film samples showing the peaks due to the TiO <sub>2</sub> phases without interference from the silicon wafer substrate. ....   | - 120 - |
| <b>Figure 6-13</b> Proposed mechanism for the synthesis of mixed phase TiO <sub>2</sub> (B) and anatase thin films by LPCVD method onto substrate pre-treated with a very thin layer of Na-containing compound .....  | - 121 - |
| <b>Figure 6-14</b> Schematic drawing of the monoclinic sodium titanates showing the tunnel structure of Na <sub>2</sub> Ti <sub>3</sub> O <sub>7</sub> and Na <sub>2</sub> Ti <sub>6</sub> O <sub>13</sub> . ....   | - 123 - |
| <b>Figure 7-1</b> XRD patterns of thin film samples deposited by LPCVD on the Si wafer substrates which were pre-treated by spraying LiOH, NaOH and KOH solution in the same mole amount of alkali metal ions .....   | - 130 - |
| <b>Figure 7-2</b> Raman spectrum of thin film sample deposited on a pre-treatment Si wafer substrate by spraying 1.69% W/V of KOH solution. Inset is a light microscope image of thin film in plan view. ....   | - 131 - |
| <b>Figure 7-3</b> XRD patterns of titania/titanate thin film samples deposited onto a Si wafer substrate which was pre-treated by spraying LiOH solution in four different concentrations. ....   | - 132 - |
| <b>Figure 7-4</b> XRD patterns of TiO <sub>2</sub> thin film samples deposited onto a Si wafer substrate which was pre-treated by spraying NaOH solution in three different concentrations. ....  | - 134 - |
| <b>Figure 7-5</b> XRD patterns of titania/titanate thin film samples deposited on a Si wafer substrate which was pre-treated by spraying KOH solution in four different concentrations. ....  | - 135 - |
| <b>Figure 7-6</b> SEM plan-view images of titania/titanate thin film samples deposited by LPCVD onto a pre-treated Si wafer substrate by spraying: (a) 0.3% <sup>w/v</sup> of LiOH; (b) 0.1% <sup>w/v</sup> of NaOH; (c) 1.69% <sup>w/v</sup> of KOH and SEM cross-sectional images of the thin films deposited on pre-treated Si wafer substrates: (d) 0.3% <sup>w/v</sup> of LiOH; (e) 0.1% <sup>w/v</sup> of NaOH; (f) 1.69% <sup>w/v</sup> of KOH ..... | - 136 - |
| <b>Figure 7-7</b> Schematic diagram summarizing the hierarchical phase formation of titania/titanate thin films fabricated by modified LPCVD process using alkali metal ions (Li <sup>+</sup> , Na <sup>+</sup> , K <sup>+</sup> ) pre-treatment of the substrate surface. ..   | - 141 - |
| <b>Figure 7-8</b> The phase diagram of the Na <sub>2</sub> O-TiO <sub>2</sub> system .....  | - 142 - |
| <b>Figure 7-9</b> Schematic diagram representation of a phase transformation from an intermediate phase (Na <sub>2</sub> Ti <sub>6</sub> O <sub>13</sub> and/or Na <sub>x</sub> Ti <sub>y</sub> O <sub>z</sub> ) with the step-like layered structure to a porous structure of TiO <sub>2</sub> (B) phase. ....   | - 143 - |
| <b>Figure 7-10</b> Schematic diagram of the phase transformation from an intermediate phase (K <sub>2</sub> Ti <sub>6</sub> O <sub>13</sub> and/or K <sub>x</sub> Ti <sub>y</sub> O <sub>z</sub> ) with the step-like layered structure to a porous structure of TiO <sub>2</sub> (B) phase.....  | - 144 - |
| <b>Figure 7-11</b> The phase diagram of the K <sub>2</sub> O-TiO <sub>2</sub> system.....   | - 145 - |

**Figure 7-12** Proposed steps of structural transformation during the process of an elimination of  $\text{Li}^+$  at  $600^\circ\text{C}$  ..... - 147 -

**Figure 7-13** Schematic diagram of a cubic crystal structure of  $\text{Li}_4\text{Ti}_5\text{O}_{12}$  and a monoclinic crystal structure of  $\text{Li}_2\text{TiO}_3$  showing a net-like framework and a plane layered structure respectively..... - 148 -

**Figure 7-14** The binary phase diagram of the  $\text{Li}_2\text{O}$ - $\text{TiO}_2$  system. .... - 149 -

## Chapter 1 Introduction

### 1.1 Background and Rationale

Despite an unceasingly rising demand for an improved quality of life, the consciousness of increasing environmental issues have drawn global society to investigate environmentally-benign lifestyles and technologies. One of the largest concerns is an insufficiency in global energy production for supporting the development of technologies. There is a challenge to develop alternative energy resources which permit the use of renewable energy instead of fossil fuels including an improvement in the security and efficiency of the energy storage system.

Utilization of solar energy has become increasingly attractive to many researchers. In recent years, the use of semiconductor photocatalysts has been one of the interesting methods to change photon energy into fuel.  $\text{TiO}_2$  semiconductor polymorphs (and in some cases polymorph mixtures) are amongst the most widely used materials owing to their cost-effective, highly stable and environmentally-friendly nature combined with their well-known electronic and optical properties [1]. The use of  $\text{TiO}_2$  as a semiconductor photocatalyst for the water splitting reaction into  $\text{H}_2$  and  $\text{O}_2$  was first discovered by Fujishima and Honda [2]. Subsequently,  $\text{TiO}_2$  has been the focus of an efficient means of renewable energy production by many researchers as shown by the rapid increase in the number of article publications in the last decade illustrated graphically in Figure 1-1. This involves not only the application of  $\text{TiO}_2$  as a photocatalyst for the water splitting reaction (to produce hydrogen and oxygen), but in addition  $\text{TiO}_2$  is also employed as a photocatalyst in a number of degradation reactions of chemical pollutants. A major factor in the practical application of  $\text{TiO}_2$  photocatalysts, is their ability to be reused whilst retaining high photocatalytic efficiency. In this respect immobilized  $\text{TiO}_2$  thin films on rigid substrates are a key form if these photocatalysts are to be employed in the various chemical industries and in construction materials.

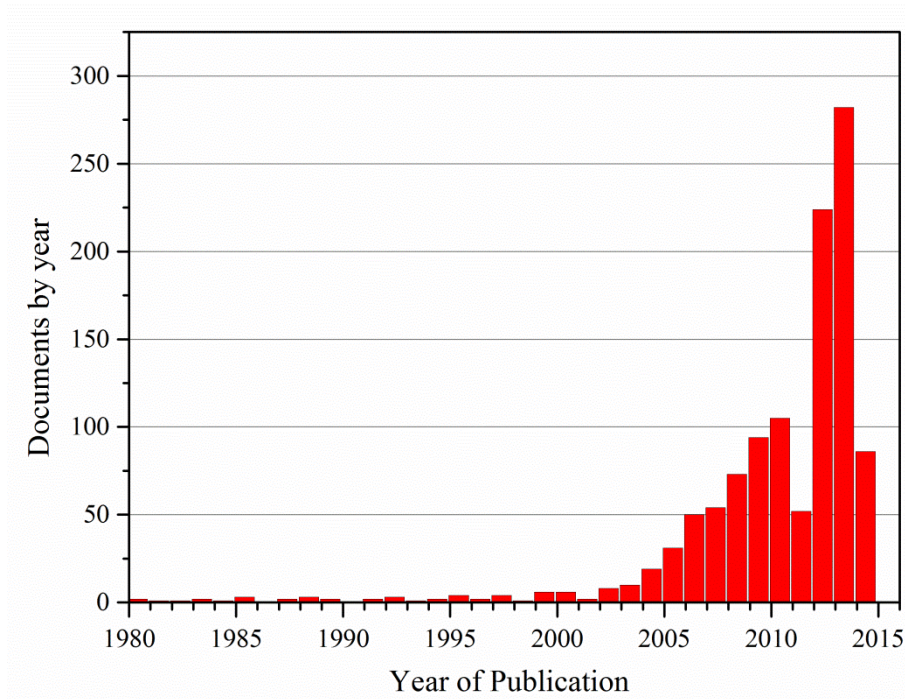


**Figure 1-1** Graphical representation of the number of research publications which are relevant to the study of  $\text{TiO}_2$  for the water splitting reaction searched from the Scopus database during 1980-2015 by using a search text of  $\text{TiO}_2$  and water splitting in the search field of the title, abstract and keywords.

Thin films based on the crystalline anatase phase of  $\text{TiO}_2$  have been shown to possess a higher photocatalytic activity than rutile. Current improvement strategies focus on the use of ultrafine nanoparticles in the thin films, the modification of charge transfer processes to prevent the recombination reaction between the photogenerated electron and hole pair, and the controlled production of phase mixtures in the thin films such as anatase/rutile [3] or anatase/ $\text{TiO}_2(\text{B})$  [4] which may potentially provide higher photocatalytic activities than pure anatase.

Additionally,  $\text{TiO}_2$  has recently been proposed as an electrode material for lithiation in lithium-ion batteries and the growth in reported research in this area is shown in Figure 1-2. Amongst the titania polymorphs, the  $\text{TiO}_2(\text{B})$  or “bronze” phase has attracted considerable interest due to its distinctive monoclinic crystal structure which, because of its low-density crystal framework, exhibits larger channels and voids [5] as compared with the other titania polymorphs (anatase, rutile and brookite). In addition  $\text{TiO}_2(\text{B})$  also shows a higher specific Li storage capacity as compared to the tetragonal structures of anatase and rutile [6], [7].

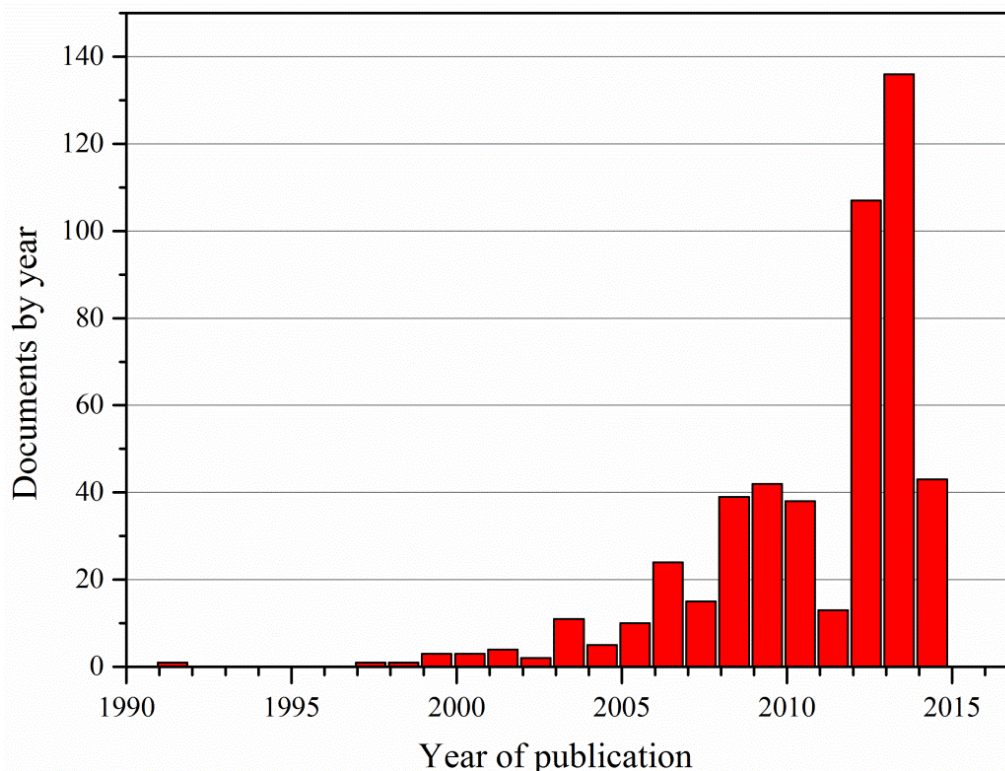


**Figure 1-2** Graphical representation of the number of research publications which are relevant to the use of  $\text{TiO}_2$  as an electrode in Li-ions batteries derived from the Scopus database during 1990-2015 by using a search text of  $\text{TiO}_2$  and Li-ion batteries in the search field of the title, abstract and keywords.

Thus overall  $\text{TiO}_2(\text{B})$  potentially plays an important role in applications both as a photocatalyst and as an anode in lithium ions batteries.  $\text{TiO}_2(\text{B})$  was first synthesised in 1982 by René Marchand [8] via hydrolysis of  $\text{K}_2\text{Ti}_4\text{O}_9$  followed by calcination at  $500^\circ\text{C}$ . Subsequently, a number of studies have investigated the preparation methods and the applications of this material. In particular, the number of research articles on  $\text{TiO}_2(\text{B})$  published in this decade has dramatically increased as shown in Figure 1-3. This highlights the interest in studying improvements in the synthesis methods and the further applications of  $\text{TiO}_2(\text{B})$ .

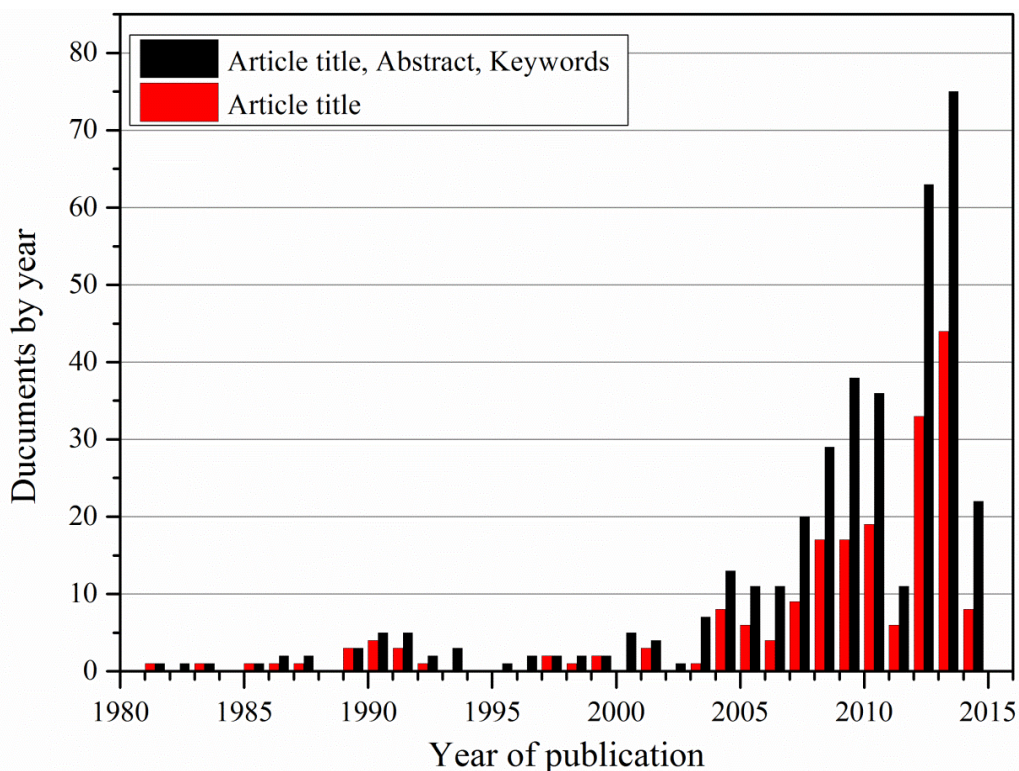


**Figure 1-3** Graphical representation of the number of research publications which are relevant to the  $\text{TiO}_2(\text{B})$  phase searched from the Scopus database during 1980-2015 by using a search text of  $\text{TiO}_2\text{-B}$  and  $\text{TiO}_2(\text{B})$  in the search field of only the research title (red bar) comparing with the search field of the mixing of title, abstract and keywords (black bar)

## 1.2 Aims and Objectives

Commonly, alkali metal titanates have been used as precursors for  $\text{TiO}_2(\text{B})$  preparation in many synthetic methods such as sol-gel [9],[10], hydrothermal [11] and solid-state reaction [8]. In this research project we principally chose to use a method specialised for thin film production – namely chemical vapour deposition (CVD). The overall aims of my research project were therefore: a) to understand initially the nature of  $\text{TiO}_2(\text{B})$  phase formation via the alkali metal titanate phase transformation process relevant to hydrothermal synthesis; b) to employ a Low Pressure Chemical Vapour Deposition (LPCVD) method to synthesise thin films of  $\text{TiO}_2(\text{B})$  phase on a substrate (for the first time); c) to study the phase formation mechanism of titania thin films during the LPCVD synthesis process.

Specific objectives which developed during the course of the project were as follows:

- As an initial reference point, synthesise  $\text{TiO}_2(\text{B})$  phase nanoparticles using a hydrothermal route to study  $\text{TiO}_2(\text{B})$  phase formation during the hydrothermal process via the phase transformation process from alkali metal titanate.
- Synthesise the  $\text{TiO}_2(\text{B})$  phase or a mixed phase of anatase  $\text{TiO}_2$  and  $\text{TiO}_2(\text{B})$  thin films on a general glass substrate by LPCVD method;
- Synthesise the  $\text{TiO}_2(\text{B})$  phase or a mixed phase of anatase  $\text{TiO}_2$  and  $\text{TiO}_2(\text{B})$  thin films on a number of different substrates such as silicon wafer, fused quartz, etc. by a modified LPCVD method;
- Investigate the mechanism for  $\text{TiO}_2(\text{B})$  phase formation and growth of thin films during the LPCVD process;
- Investigate the effects of the soda-lime glass substrate on the  $\text{TiO}_2(\text{B})$  phase formation during the LPCVD process including the effect of  $\text{Na}^+$  ion diffusion from the glass substrate into the deposited titania thin films;
- Investigate the effects of migration of alkali metal ions such as  $\text{Li}^+$ ,  $\text{Na}^+$  and  $\text{K}^+$  on titania/titanate phase formation in the thin films during the LPCVD process;

### 1.3 Layout of the thesis

The thesis comprises eight chapters which may be summarised as follows:

- Chapter 1 contains the background and rationale to the research, an outline of research objectives and the layout of the whole thesis;
- Chapter 2 will review the structure, processing and properties of titanium dioxide ( $\text{TiO}_2$ );
- Chapter 3 will describe and review the methods employed to synthesise the  $\text{TiO}_2(\text{B})$  phase including the principles and practice of the characterization techniques employed during the research;
- Chapter 4 will present the synthesis of pure phase  $\text{TiO}_2(\text{B})$  nanorods by a hydrothermal synthesis route including the study of  $\text{TiO}_2(\text{B})$  phase formation via the phase transformation of an alkali metal titanate;
- Chapter 5 will present the successful synthesis method and the formation mechanism of mixed phase anatase  $\text{TiO}_2$  and  $\text{TiO}_2(\text{B})$  thin films on soda-lime glass substrates by the LPCVD synthesis method;
- Chapter 6 will describe the modified LPCVD method by spraying a  $\text{Na}^+$  containing solution onto a number of substrates prior to thin film deposition by CVD. This demonstrates a universal synthesis method for mixed phase  $\text{TiO}_2(\text{B})$  and anatase  $\text{TiO}_2$  thin films on any substrate. A phase formation

mechanism related to Na<sup>+</sup> migration from the pre-treated substrate into the deposited TiO<sub>2</sub> thin films is proposed;

- Chapter 7 will describe the effect of different alkali metal ions (Li<sup>+</sup>, Na<sup>+</sup> and K<sup>+</sup>) during the pre-treatment of a Si-wafer substrate on titania/titanate phase formation during the LPCVD process;
- Chapter 8 will summarize and conclude the research. Finally, potential future study will be suggested and recommended.

## 1.4 List of publications and presentations

This work has been published in the following papers and presented at the following conferences.

### Papers

- Y. Chimupala, G. Hyett, R. Simpson and R. Brydson, *J. Phys. Conf. Ser.*, 2014, 522, 012074.
- Y. Chimupala, G. Hyett, R. Simpson, R. Mitchell, R. Douthwaite, S. J. Milne and R. D. Brydson, *RSC Adv.*, 2014, 4, 48507.
- Y. Chimupala, P. Junploy, A. Westwood and R. D. Brydson, *J. Mater. Chem. A*, 2015 (under review)

### Conferences

- Poster Presentation at European Microscopy Congress 2012 (EMC 2012) in Manchester, UK.
- Poster Presentation at Electron Microscopy and Analysis Group Conference 2013 (EMAC 2013) in York, UK
- Poster Presentation at Pure and Applied Chemistry International Conference 2014 (PACCON 2014) in Khon Kaen, Thailand (obtained a prize for my poster presentation at PACCON 2014)
- Poster Presentation at Microscience Microscopy Congress 2014 (MMC 2014) in Manchester, UK.
- Oral Presentation at 249<sup>th</sup> American Chemical Society National Meeting & Exposition 2015 (249<sup>th</sup> ACS meeting 2015) in Denver, CO, US

## 1.5 References

- [1] M.R. Hoffmann, S.T. Martin, W. Choi, and D.W. Bahnemann, "Environmental applications of semiconductor photocatalysis," *Chem. Rev.*, vol. 95, pp. 69–96, 1995.
- [2] A. Fujishima and K. Honda, "Electrochemical photolysis of water at a semiconductor electrode," *Nature*, vol. 238, pp. 37–38, 1972.
- [3] A.J. Cross, C.W. Dunnill, and I.P. Parkin, "Production of predominantly anatase thin films on various grades of steel and other metallic substrates from  $\text{TiCl}_4$  and ethyl Acetate by atmospheric pressure CVD" *Chem. Vap. Depos.*, vol. 18, no. 4–6, pp. 133–139, 2012.
- [4] M.M. Mohamed, B.H.M. Asghar, and H.A. Muathen, "Facile synthesis of mesoporous bicrystallized  $\text{TiO}_2(\text{B})$ /anatase (rutile) phases as active photocatalysts for nitrate reduction," *Catal. Commun.*, vol. 28, pp. 58–63, 2012.
- [5] B. Laskova, M. Zikalava, A. Zikal, M. Bousa, "Capacitive contribution to Li-storage in  $\text{TiO}_2(\text{B})$  and  $\text{TiO}_2(\text{anatase})$ ," *J. Power Sources*, vol. 246, pp. 103–109, 2014.
- [6] T.P. Feist and P.K. Davies, "The soft chemical synthesis of  $\text{TiO}_2(\text{B})$  from layered titanates," *J. Solid State Chem.*, vol. 101, pp. 275–295, 1992.
- [7] A.G. Dylla, P. Xiao, G. Henkelman, and K.J. Stevenson, "Morphological dependence of lithium insertion in nanocrystalline  $\text{TiO}_2(\text{B})$  nanoparticles and nanosheets," *J. Phys. Chem. Lett.*, vol. 3, no. 15, pp. 2015–2019, 2012.
- [8] M. René, B. Luc, and T. Michel, " $\text{TiO}_2(\text{B})$  a new form of titanium dioxide and the Potassium octatitanate  $\text{K}_2\text{Ti}_8\text{O}_{17}$ ," *Mater. Res. Bull.*, vol. 15, pp. 1129–1133, 1980.
- [9] R. Giannuzzi, M. Manca, L.D. Marco, M.R. Belviso, A. Cannavale, T. Sibillano, C. Giannini, P.D. Cozzoli, and G. Gigli, "Ultrathin  $\text{TiO}_2(\text{B})$  nanorods with superior lithium-ion storage performance," *ACS Appl. Mater. Interfaces*, vol. 6, no. 3, pp. 1933–1943, 2014.
- [10] T. Beuvier, M. Richard-plouet, and L. Brohan, "Accurate methods for quantifying the relative ratio of anatase and  $\text{TiO}_2(\text{B})$  nanoparticles," *J. Phys. Chem. C*, vol. 113, no. 31, pp. 13703–13706, 2009.
- [11] A.R. Armstrong, G. Armstrong, J. Canales, R. García, and P.G. Bruce, "Lithium-ion intercalation into  $\text{TiO}_2\text{-B}$  nanowires," *Adv. Mater.*, vol. 17, no. 7, pp. 862–865, 2005.

## Chapter 2 Titanium Dioxide: Structure, Processing & Properties

This chapter provides information about the crystal structures, the properties and the applications of titanium dioxide phases particularly the  $\text{TiO}_2(\text{B})$  phase. In addition, a literature review of  $\text{TiO}_2(\text{B})$  for an application for both electrodes in Li ion batteries and photocatalysts will be briefly described.

### 2.1 Structures of 11 $\text{TiO}_2$ Crystalline Phases

There are many chemical compositions of titanium oxides such as  $\text{TiO}_2$ ,  $\text{Ti}_2\text{O}_3$ ,  $\text{Ti}_3\text{O}_5$ ,  $\text{Ti}_4\text{O}_7$ ,  $\text{Ti}_5\text{O}_9$ ,  $\text{Ti}_6\text{O}_{11}$ ,  $\text{Ti}_7\text{O}_{13}$ ,  $\text{Ti}_8\text{O}_{15}$  and  $\text{Ti}_9\text{O}_{17}$  [1]. Each form exhibits different crystal structures providing several applications.  $\text{TiO}_2$  polymorphs (and in some cases polymorph mixtures) are amongst the most widely used materials owing to their cost effective, highly stable and environmentally-friendly nature combined with their well-known electronic and optical properties [2]. There are at least 11 polymorphs of Titanium dioxide ( $\text{TiO}_2$ ) that have been reported in both bulk phases and/or nanocrystalline phases. The formal names of these  $\text{TiO}_2$  polymorphs are: 1.) Rutile  $\text{TiO}_2$ ; 2.) Anatase  $\text{TiO}_2$ ; 3.) Brookite  $\text{TiO}_2$ ; 4.) the bronze-like phase,  $\text{TiO}_2(\text{B})$ ; 5.) the hollandite-like phase,  $\text{TiO}_2(\text{H})$ ; 6.) the ramsdellite ( $\text{VO}_2$ )-like phase,  $\text{TiO}_2(\text{R})$ ; 7.) the columbite ( $\alpha\text{-PbO}_2$ )-like phase  $\text{TiO}_2(\text{II})$ , 8.) the baddeleyite ( $\text{ZrO}_2$ )-like phase, baddeleyite  $\text{TiO}_2$ ; 9.) the  $\text{ZrO}_2$  brookite-like phase, OI phase  $\text{TiO}_2$ ; 10.) the cotunnite ( $\text{PbCl}_2$ )-like phase, OII phase  $\text{TiO}_2$  and 11.) the fluorite ( $\text{CaF}_2$ )-like phase, cubic  $\text{TiO}_2$  [3]–[8].

The structural characteristics of the  $\text{TiO}_2$  crystalline phases are summarised in Table 2-1. Only the first 6 polymorphs in the table list, especially rutile, anatase, brookite and  $\text{TiO}_2(\text{B})$ , are stable at ambient or low-pressure [8]. Typically, three of the the  $\text{TiO}_2$  polymorphs: rutile, anatase and brookite, are recognized to occur naturally, whereas there are only a few reports of the presence of the  $\text{TiO}_2(\text{B})$  phase in natural samples [9], [10]. Whereas, another five  $\text{TiO}_2$  phases:  $\text{TiO}_2\text{II}$  or srilankite; OI; OII or Cotunnite; Cubic or Fluorite and Baddeleyite have been reported to occur at high-pressure conditions [11].

A pressure-temperature phase diagram for  $\text{TiO}_2$  systems is shown in Figure 2-1, indicating the stability of anatase phase at atmospheric pressure and room temperature, whereas the rutile phase is more stable at high temperature. Interestingly, both rutile and anatase phases at high pressures can structurally transform to the  $\text{TiO}_2(\text{II})$  phase.

**Table 2-1** Structural data of 11 TiO<sub>2</sub> crystalline polymorphs [adapted from [8]]

| Phases   | Rutile                    | Anatase                   | Brookite      | TiO <sub>2</sub> (B) | TiO <sub>2</sub> (H) | TiO <sub>2</sub> (R) | TiO <sub>2</sub> (II) | OI                                   | OII                            | Baddeleyite                | Cubic                          |
|--|---------------------------|---------------------------|---------------|----------------------|----------------------|----------------------|-----------------------|--------------------------------------|--------------------------------|----------------------------|--------------------------------|
| Crystal system                                       | tetragonal                | tetragonal                | ortho-rhombic | monoclinic           | tetragonal           | ortho-rhombic        | ortho-rhombic         | ortho-rhombic                        | ortho-rhombic                  | monoclinic                 | cubic                          |
| Space group  | <i>P4<sub>2</sub>/mmm</i> | <i>I4<sub>1</sub>/amd</i> | <i>Pbca</i>   | <i>C2/m</i>          | <i>I4/m</i>          | <i>Pbnm</i>          | <i>Pbcn</i>           | <i>Pbca</i>                          | <i>Pnma</i>                    | <i>P2<sub>1</sub>/c</i>    | <i>Fm<math>\bar{3}</math>m</i> |
| Group  | 136                       | 141                       | 61            | 12                   | 87                   | 62                   | 60                    | 61                                   | 62                             | 14                         | 225                            |
| <i>a</i> (Å)   | 4.5941                    | 3.7842                    | 9.184         | 12.1787              | 10.161               | 4.9022               | 4.515                 | 9.052                                | 5.163                          | 4.589                      | 4.516                          |
| <i>b</i> (Å)   | 4.5941                    | 3.7842                    | 5.447         | 3.7412               | 10.161               | 9.4590               | 5.497                 | 4.836                                | 2.989                          | 4.849                      | 4.516                          |
| <i>c</i> (Å)   | 2.9589                    | 9.5146                    | 5.145         | 6.5249               | 2.970                | 2.9585               | 4.939                 | 4.617                                | 5.966                          | 4.736                      | 4.516                          |
| $\alpha$ (°)   | 90                        | 90                        | 90            | 90                   | 90                   | 90                   | 90                    | 90                                   | 90                             | 90                         | 90                             |
| $\beta$ (°)  | 90                        | 90                        | 90            | 107.054              | 90                   | 90                   | 90                    | 90                                   | 90                             | 98.6                       | 90                             |
| $\gamma$ (°)   | 90                        | 90                        | 90            | 90                   | 90                   | 90                   | 90                    | 90                                   | 90                             | 90                         | 90                             |
| Density (g/cm <sup>3</sup> )                         | 4.248                     | 3.895                     | 4.123         | 3.734                | 3.461                | 3.868                | 4.329                 | 5.251                                | 5.763                          | 5.092                      | 5.761                          |
| Polyhedron type                                      | Octa-hedron               | Octa-hedron               | Octa-hedron   | Octa-hedron          | Octa-hedron          | Octa-hedron          | Octa-hedron           | Distorted augmented triangular prism | Triaug-mented triangular prism | Augmented triangular prism | Cube                           |
| Polyhedron per unit cell volume (1/Å <sup>3</sup> )* | 0.03203                   | 0.02936                   | 0.03108       | 0.02815              | 0.02609              | 0.02916              | 0.03263               | 0.03839                              | 0.03958                        | 0.04345                    | 0.04343                        |
| Coordination number (Ti)                             | 6                         | 6                         | 6             | 6                    | 6                    | 6                    | 6                     | 7                                    | 9                              | 7                          | 8                              |
| Lattice energy (kJ/mol)**                            | 0                         | 24.75                     | 18.53         | 49.16                | 73.05                | 68.49                | 8.86                  | 141.07                               | 141.97                         | 155.55                     | 147.78                         |
| Reference  | ICSD 9161                 | COD 9008213               | ICSD 15409    | ICSD 41056           | COD 1008514          | ICSD 75179           | ICSD 15328            | ICSD 173960                          | ICSD 27736                     | COD 9015355                | ICSD 44937                     |

\* Calculated using the program GULP \*\*Relative to that of rutile; calculated at 0 K and 0 GPa

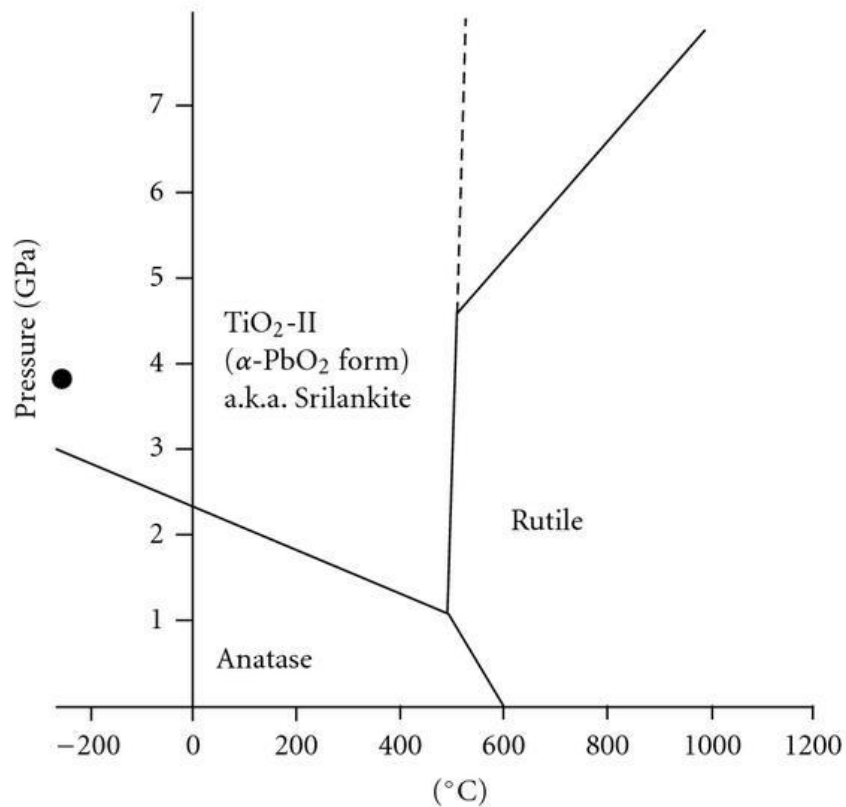


**Figure 2-1** Pressure-temperature phase diagram for TiO<sub>2</sub> system [12]

However, these four polymorphic forms: anatase, rutile, brookite and TiO<sub>2</sub>(B) have been extensively studied and synthesised in the last two decades due to their stability and their ability to be widely utilized in many fields such as treatment of both water and air pollution [13], antibacterial surfaces, antifogging materials, self-cleaning materials [14], [15], sunscreen [16] and white pigment [17].

Based on lattice energy, generally rutile is the most abundant and the most stable phase of the TiO<sub>2</sub> polymorphs, however it is usually reported to occur at high temperatures >700°C [18], [19]. The relative stabilities of each phase (in terms of packing density) can be investigated by the calculated number of polyhedra per unit cell volume of each phase as shown in Table 2-1 which suggests rutile>brookite>anatase>TiO<sub>2</sub>(B). Anatase, brookite and TiO<sub>2</sub>(B) are considered to be metastable phases which can be transformed to the more stable rutile phase via an external thermal driving force. Crystal densities, range from 4.248 g.cm<sup>-3</sup> for rutile to 3.734 g.cm<sup>-3</sup> for TiO<sub>2</sub>(B) and decrease in the order rutile>brookite>anatase>TiO<sub>2</sub>(B).

TiO<sub>2</sub> crystalline structures consist of TiO<sub>6</sub> octahedral units (building blocks) in which six O<sup>2-</sup> ions are bound to Ti<sup>4+</sup> forming an octahedral building block presented as a blue polyhedral unit in Figure 2-2. These TiO<sub>6</sub> octahedral units assemble by either edge- or corner- sharing of oxygen atoms [20] as shown in Figure 2-2. In the different

polymorphs, the octahedron shares their edges, corners and/or faces in different combinations. These depend on many factors during the phase-formation process e.g. temperature, pressure and chemical conditions. The details of each polymorph crystalline structure are generally described in terms of their octahedral connections as follows:

- Rutile - 2 edge sharing (2 out of 12 edges per octahedron);
- Brookite - 3 edge sharing (3 out of 12 edges per octahedron);
- Anatase - 4 edge sharing (4 out of 12 edges per octahedron);
- TiO<sub>2</sub>(B) - 4 edge sharing (4 out of 12 edges per octahedron).

The anatase framework consists of edge-sharing TiO<sub>6</sub> octahedra, whereas the rutile, brookite and TiO<sub>2</sub>(B) structures exhibits both edge- and corner- sharing of a TiO<sub>6</sub> octahedra. The crystal structure of TiO<sub>2</sub>(B) shows the same number of edge-sharing octadra as anatase but with a different arrangement in 3D to form a layered structure.

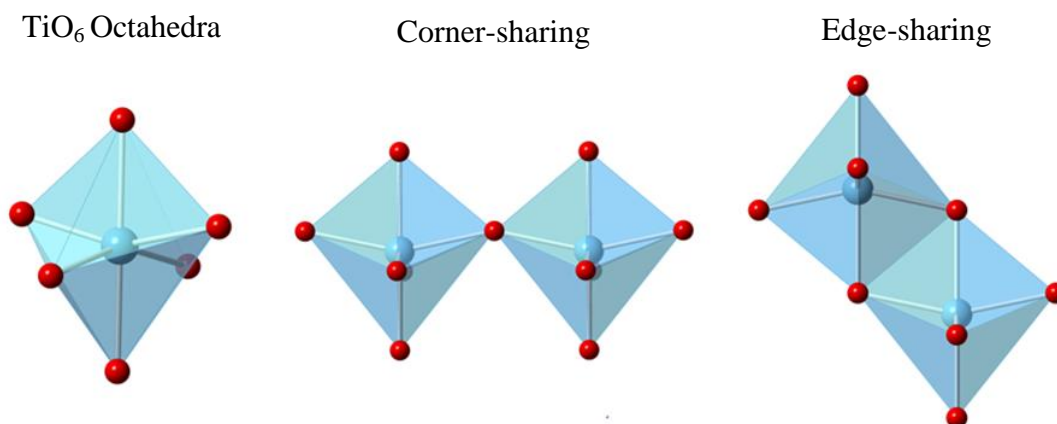


**Figure 2-2** Schematic representation of a TiO<sub>6</sub> octahedra unit and edge-sharing and corner-sharing configuration

The crystal structures of these four phases are presented in Figure 2-3 in both ball-and-stick and polyhedron models. To compare these polymorphs, the views along the *a*, *b* and *c* axes in each crystal structure is shown in Figure 2-4. In fact, common structural slabs are easily observed in anatase and TiO<sub>2</sub>(B). The outstanding presentation of structural slabs is shown in Figure 2-3(d) and Figure 2-4 viewing along *c* axis [001] of TiO<sub>2</sub>(B) crystal structure.

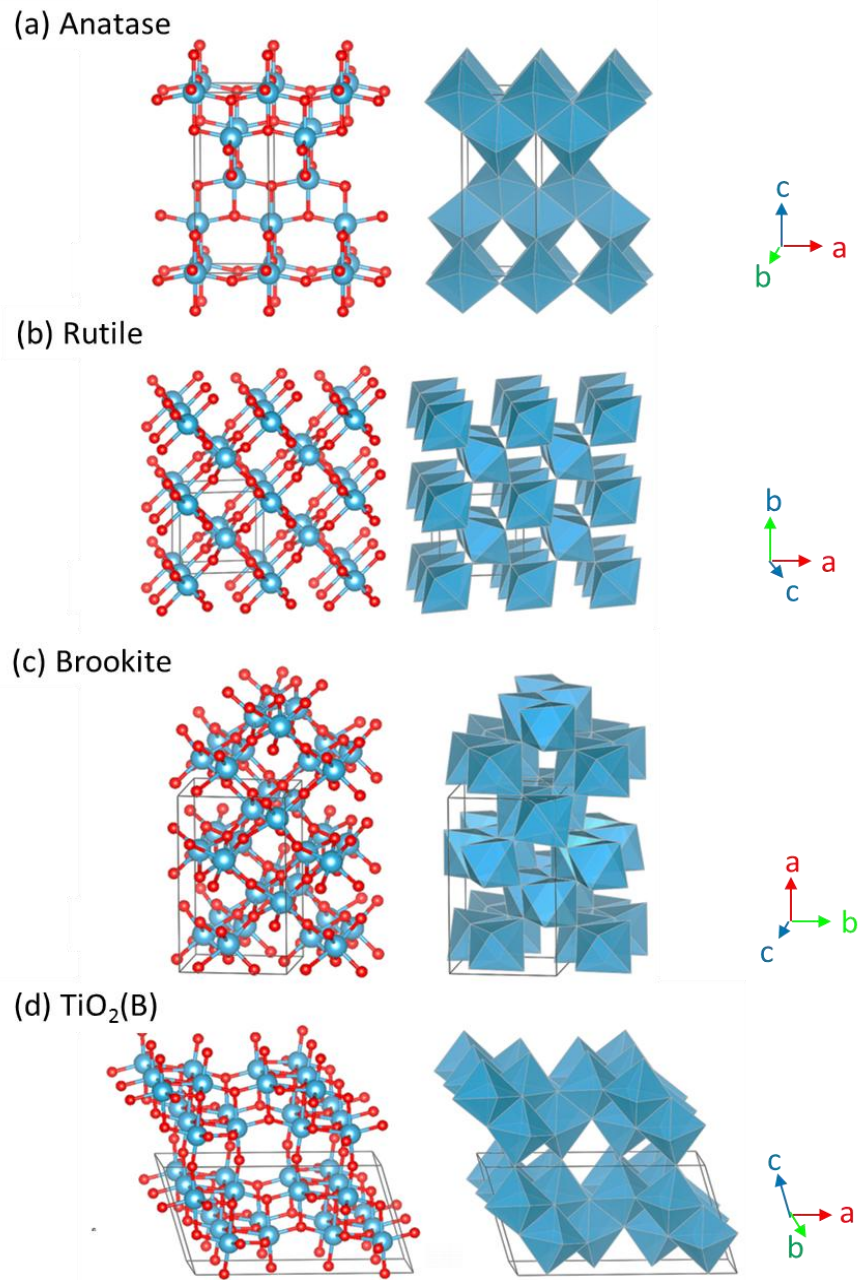


**Figure 2-3** Crystal structures of Titanium dioxide:(a) anatase; (b) rutile; (c) brookite and  $\text{TiO}_2(\text{B})$ . Ball-and-stick models are located on the left hand side comparing with the polyhedron models as shown on the right hand side. Red balls and blue balls are representatives of oxygen atoms and titanium atoms respectively whereas the bright-blue polyhedron units present an octahedral building unit constructed from a  $\text{Ti}^{4+}$  ion and six of  $\text{O}^{2-}$  ions.

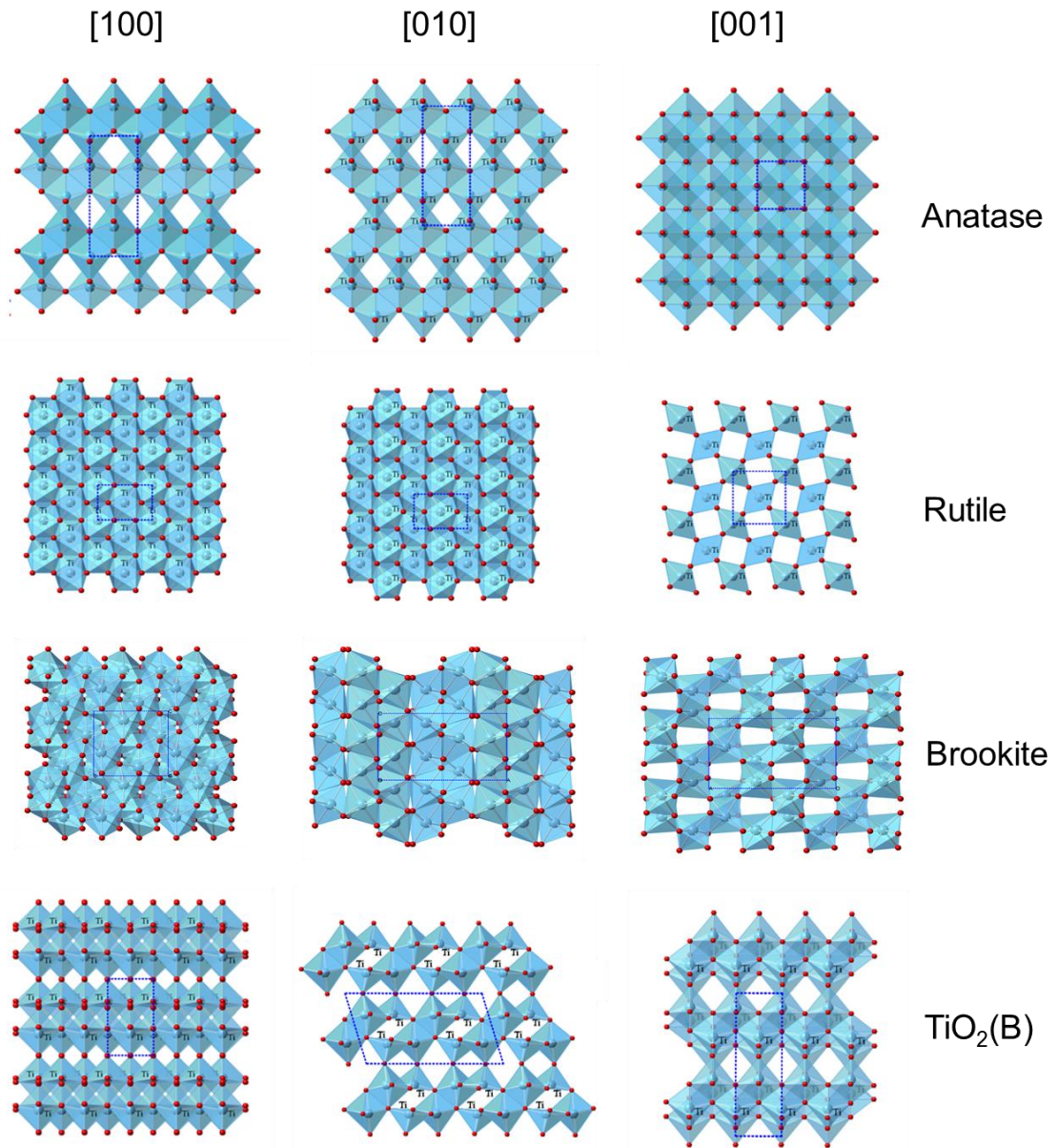


**Figure 2-4** Crystal structures of anatase, rutile, brookite and  $\text{TiO}_2(\text{B})$  viewed along a ([100]), b ([010]) and c ([001]) axes. All of the structures was drawn at the same scale. Unit cells are outlined using blue-thin dash lines.

Besides the anatase, rutile and brookite phases, the  $\text{TiO}_2(\text{B})$  or bronze phase has attracted significant interest for many researchers over the last decade due to the distinctive monoclinic crystal structure which, because of its low-density crystal framework, exhibits larger channels and voids and also a higher specific Li storage capacity as compared to the tetragonal structures of anatase and rutile [21]–[23] as shown in Figure 2-5. As calculated by Crystal Explorer software (Version 3.1, 2012), with a standard pore size for occupying small cations such as  $\text{Li}^+$ ,  $\text{TiO}_2(\text{B})$  shows the highest %voids per structural volume of 12.45% whereas anatase, rutile and brookite are considerably lower than  $\text{TiO}_2(\text{B})$  with calculated %voids/volume of around 4.63%, 0.63% and 0.87% respectively.

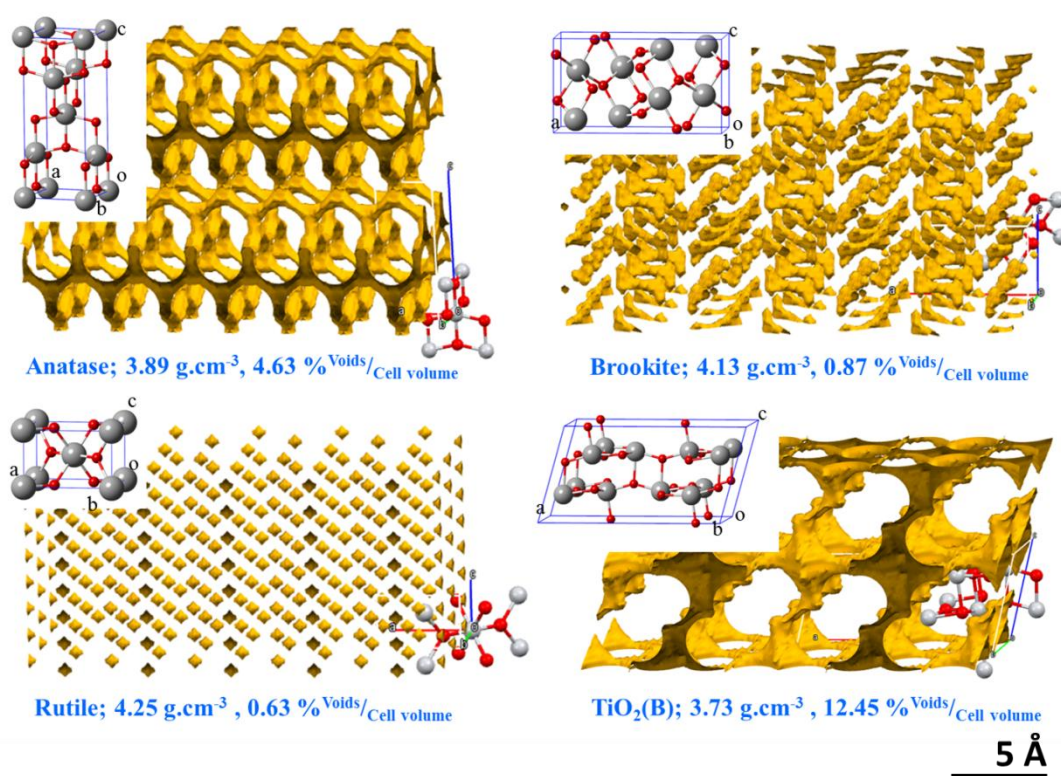


**Figure 2-5** The crystal voids structures of anatase, rutile, brookite and  $\text{TiO}_2(\text{B})$  with percentages of crystal voids calculated from Crystal Explorer with isovalue of  $0.008^*$  e.au<sup>-3</sup> (e.au<sup>-3</sup> = electron per cubic atomic units of length: the atomic units of length is equal to the Bohr radius). Red and grey balls represent oxygen and titanium atoms respectively. The yellow structures display void volumes (Shading = isolated pores or connected pore structures). \*standard pore size for Li insertion.

## 2.2 General applications of Titanium dioxide (TiO<sub>2</sub>)

Titanium dioxide (TiO<sub>2</sub>) is a very versatile material which has been utilised in many fields of application over the past few decades. There are four types of TiO<sub>2</sub> polymorphs: anatase; rutile; brookite and TiO<sub>2</sub>(B). The individual applications of each phase depend on their physical and chemical properties arising as a result of the crystal structures.

The pigment industry is currently the largest consumer of TiO<sub>2</sub>. The rutile phase is more desired in white pigment applications over other phases due to an appropriate brightness of its white colour, higher phase stability and its very high reflective index of 2.72 as shown in Table 2-2. As well as whiteness, the powder form of rutile (and other TiO<sub>2</sub> phases) is also a very effective opacifier. This means TiO<sub>2</sub> can be employed as a pigment to provide whiteness and opacity at the same time for many applications such as paints, coatings, plastics, rubber, glass, papers, inks, cosmetics as well as a colouring component in toothpastes.

Titanium dioxide is one of the well-known semiconductors. The band gap energies of TiO<sub>2</sub> polymorphs are within the range 3.0-3.4 eV as illustrated in Table 2-2, which directly relate to the individual band structure of each of the phases. Based on the band gap energies, TiO<sub>2</sub> phases can utilize photon energies in the ultraviolet and near-ultraviolet visible region of the electromagnetic spectrum for desired applications.

TiO<sub>2</sub> semiconductors especially the anatase phase (and in some cases polymorph mixtures) are amongst the most widely used materials owing to their electronic and their optical properties combined with their cost effective, highly stable and environmentally-friendly nature [2], [13], [24]. TiO<sub>2</sub> can be applied in several different photo-applications, for example being an ingredient in cosmetics (an ultraviolet (UV) blocking agent) [16], an optically reflective coating material, an additive in porcelains and ceramics [25], [26], a component in dye sensitised solar cells (DSSC) [27]–[29], an excellent anti-fogging material and self-cleaning surface [14], [30], and as an anode in the photo-electrochemical splitting of water [31]. A further interesting property of titania is the ability to catalyse chemical reactions under *uv*-visible light irradiation e.g. for use as a purifier for water and air pollution (photocatalysts for chemical degradation) [32]–[34]. Recently, the trend of TiO<sub>2</sub> utilization has been altered from normally focusing on only the anatase and rutile phases to the TiO<sub>2</sub>(B) phase instead. Potential applications of the TiO<sub>2</sub>(B) phase have been highlighted by many researchers owing to its crystal structure and its specific properties as described in the following section.

**Table 2-2** General physical, chemical and optical properties of TiO<sub>2</sub> structures

| Properties  | Rutile                    | Anatase                    | Brookite     | TiO <sub>2</sub> (B)                  |
|---|---------------------------|----------------------------|--------------|---------------------------------------|
| Crystal system                                    | tetragonal                | tetragonal                 | orthorhombic | monoclinic                            |
| Space group                                       | <i>P4<sub>2</sub>/mnm</i> | <i>I4<sub>1</sub>/amd</i>  | <i>Pbca</i>  | <i>C2/m</i>                           |
| Melting/boiling point                             | ← 1,843 °C/ 2,972 °C →    |                            |              |                                       |
| Molar mass  | ← 79.866 g/mol →          |                            |              |                                       |
| Solubility in water                               | ← insoluble →             |                            |              |                                       |
| Density (g/cm <sup>3</sup> )                      | 4.248                     | 3.895                      | 4.123        | 3.734                                 |
| Volume of cell (10 <sup>6</sup> pm <sup>3</sup> ) | 136.31                    | 62.42                      | 257.63       | 284.22                                |
| % Voids per unit cell volume*                     | 0.63%                     | 4.63%                      | 0.87%        | 12.45%                                |
| Refractive index **                               | 2.72-2.73                 | 2.52-2.55                  | 2.63         | n/a                                   |
| Band gap energy (eV)                              | 3.02 # [35]               | 3.21# [35]<br>/3.2 ## [36] | 3.27 # [35]  | 3.0-3.22 # [37], [38]<br>/3.2 ## [36] |

\* crystal voids calculated from Crystal Explorer with isovalue of 0.008 e au<sup>-3</sup>

\*\* Polymers, Light and the Science of TiO<sub>2</sub>, DuPont and [17]

# derived from experimental data, ## calculated from CASTEP and DMol<sup>3</sup>

## 2.3 Applications of TiO<sub>2</sub>(B)

### 2.3.1 TiO<sub>2</sub>(B) for Lithium ion anode batteries

An additional application of titanium dioxide is as an electrode in Lithium ion batteries. TiO<sub>2</sub> has been increasingly investigated as an electrode material for lithiation owing to its cost effectiveness, environmental friendliness and structural stability over multiple charge/discharge cycles [39], [40]. Many polymorphs of TiO<sub>2</sub> such as anatase and TiO<sub>2</sub>(B) phases as well as metal titanates such as Li<sub>4</sub>Ti<sub>5</sub>O<sub>12</sub> have been reported as effective anode materials for Li ion batteries. Amongst the titania polymorphs, the TiO<sub>2</sub>(B) or bronze phase attracts considerable interest due to its larger channels and pores as compared with the other titania polymorphs as shown in Figure 2-5. Bulk TiO<sub>2</sub>(B) is able to accommodate 0.85 Li<sup>+</sup> per Ti atom whereas the capacities of anatase, rutile and brookite are 0.5, 0.1 and 0.1 respectively [41]. This number can be increased by decreasing the particle size and hence surface area, for example it becomes 1.0 Li<sup>+</sup> per Ti atom for TiO<sub>2</sub>(B) in nanotubular and/or nanoparticulate forms [41]. The open pores allow intercalation of Li into the structure and result in TiO<sub>2</sub>(B) having an optimum theoretical charge capacity of around 335 mAh/g (milliampere hours per gram) which is higher than for titanates such as Li<sub>4</sub>Ti<sub>5</sub>O<sub>12</sub> (175 mAh/g) and

would be satisfactory for Li-ion battery applications when compared with a typical commercial graphite electrode (372 mAh/g). In addition, TiO<sub>2</sub>(B) anode materials provide benefits over graphite electrodes owing to a minor volume expansion during Li intercalation (there is ~10% of volume expansion in graphite electrode), providing low levels of generated heat [39]. Moreover, graphite is very sensitive towards electrolytes and can easily be exfoliated, limiting its lifetime and utilization [42]–[45].

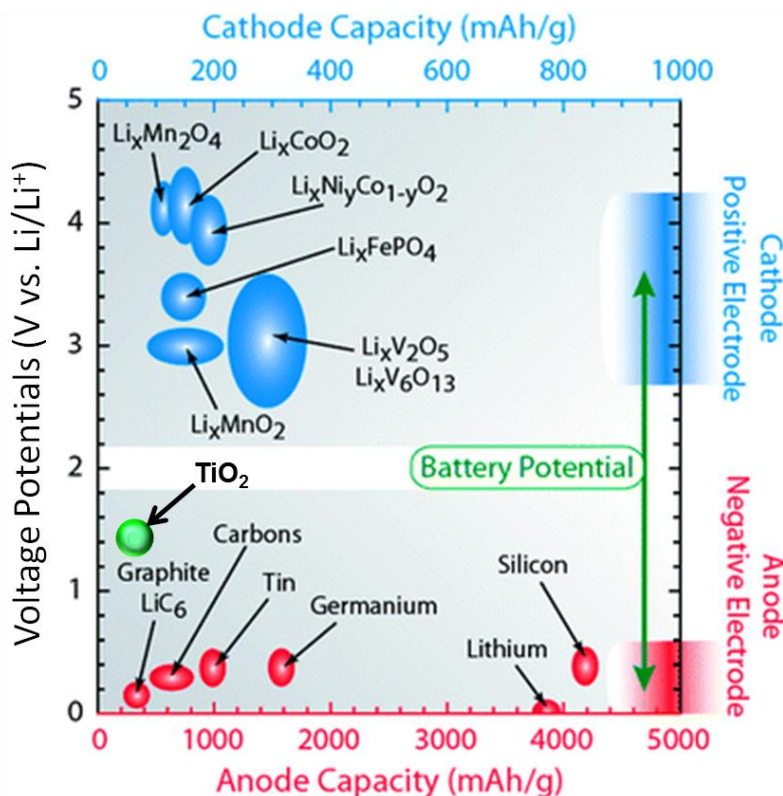


**Figure 2-6** Diagram illustrating the lithium ion capacity of conventional electrode materials and their electrochemical reduction potentials with respect to lithium metal for anode (red) materials including TiO<sub>2</sub>(B) (green) and cathode materials (blue). [adapted from [46], [47]]

The battery potential is another factor to be considered in Li-ion battery applications; this is the difference in electrode potential between the anode and cathode shown in Figure 2-6. However, in comparison with other Li-ion battery anode materials, the electrochemical reduction potential of TiO<sub>2</sub>(B) is around 1.5 V relative to Li/Li<sup>+</sup> which is relatively high. This means that, for a given cathode, the battery-cell potential from a TiO<sub>2</sub>(B) anode is lower than for other conventional anode materials and this might limit its use.

Recently, the amount of research which has studied TiO<sub>2</sub>(B) preparation methods and its application in Li-ion anode batteries, has dramatically increased. A list of publications related to TiO<sub>2</sub>(B) for Li-ion anode batteries is summarized in Table 2-3.

**Table 2-3** Literature articles which have synthesized TiO<sub>2</sub>(B) for application as an electrode in Li ion batteries

| Ref/Year                     | Phases/Morphologies  | Synthesized method                              | Properties/Li+ storage capacities   |
|------------------------------|--|---|---|
| Giannuzzi et al./ 2014 [48]  | TiO <sub>2</sub> (B) nanorods  | An surfactant-assisted nonaqueous sol-gel route | 222 mAh g <sup>-1</sup> at 0.5 C  |
| Fehse et al./ 2013 [49]      | Mixed TiO <sub>2</sub> (B) and anatase phase in different ratio                      | Hydrothermal                                    | Capacities exceeding 220 mAh g <sup>-1</sup> with good capacity retention at low cycling rate   |
| Liu et al./ 2012 [50]        | Porous TiO <sub>2</sub> (B) constructed by nanosheet                                 | Hydrothermal                                    | Specific capacity and high-rate capability with 213 mAh g <sup>-1</sup> at 10 C   |
| Li et al./ 2011 [51]         | TiO <sub>2</sub> (B) nanowires   | Hydrothermal                                    | Discharge capacity 220 mAh g <sup>-1</sup> at a rate of 50 mA g <sup>-1</sup>   |
| Qu et al./ 2014 [52]         | TiO <sub>2</sub> (B) nanoparticles/ double-walled nanotubes                          | Hydrothermal                                    | 163 mAh g <sup>-1</sup> at the rate of 2000 mA g <sup>-1</sup>  |
| Xia et al./ 2014 [53]        | Hierarchical TiO <sub>2</sub> (B) nanowire@ $\alpha$ -Fe <sub>2</sub> O <sub>3</sub> | Hydrothermal                                    | TiO <sub>2</sub> (good structural stabilities) and Fe <sub>2</sub> O <sub>3</sub> (large specific capacity) Large reversible capacity up to 800 mAh g <sup>-1</sup> |
| Ren et al./ 2012 [54]        | TiO <sub>2</sub> (B) nanoparticles   | Hydrothermal                                    | The first discharge and charge capacities 322 mAh g <sup>-1</sup> and 247 mAh g <sup>-1</sup>   |
| Etacheri et al./ 2013 [55]   | Nanosheet-assembled TiO <sub>2</sub> (B) microflowers                                | Hydrothermal                                    | A high discharge capacity of 270 mAh g <sup>-1</sup> at 1 C   |
| Guo et al./ 2013 [56]        | TiO <sub>2</sub> (B) nanofiber bundles   | Hydrothermal                                    | A reversible capacity of 206 mAh g <sup>-1</sup> at the current density of 10 mA g <sup>-1</sup> (0.05 C)   |
| Armstrong et al./ 2005 [57], | TiO <sub>2</sub> (B) nanowires   | Hydrothermal                                    | Specific capacity of 200 mAh g <sup>-1</sup> at rate of 200 mA g <sup>-1</sup>  |
| Armstrong et al./ 2005 [58]  | TiO <sub>2</sub> (B) nanotubes   | Hydrothermal                                    | 325 mAh g <sup>-1</sup> corresponding to Li <sub>0.98</sub> TiO <sub>2</sub> (B)  |
| Su et al./ 2014 [59]         | TiO <sub>2</sub> (B) nanowires   | Hydrothermal                                    | Discharge capacity of 226.8 mAh g <sup>-1</sup><br>After 20 <sup>th</sup> cycle at 50 mA g <sup>-1</sup> , it remains at 129.0 mAh g <sup>-1</sup>                  |

### 2.3.2 TiO<sub>2</sub>(B) for photocatalytic applications

Titanium dioxide (TiO<sub>2</sub>) has been introduced in many chemical reactions as an effective photocatalyst under UV-visible light irradiation. Here an electron (e<sup>-</sup>) in the valence band (VB) of TiO<sub>2</sub> is excited to the conducting band (CB) by absorption of an external photon which possesses an energy equal or higher than the band gap of the TiO<sub>2</sub>. In the meantime, this generates a positive hole (h<sup>+</sup>) in the VB as shown in Figure 2-7. The photo-generated electron and hole in the CB and the VB respectively, can both migrate to the surface and then directly react with active species to perform a reduction reaction and an oxidation reaction respectively. During the charge transfer process, a photo-generated electron in the CB can release its energy by coming back to the VB. This is called a recombination reaction which is a drawback because it is a competitive reaction with the photocatalytic reaction.

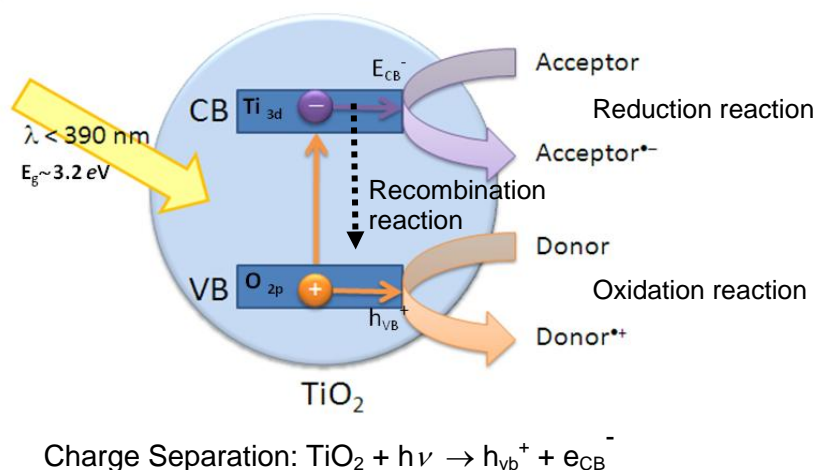


**Figure 2-7** Schematic of TiO<sub>2</sub> semiconductor photocatalysis and charge separating reaction

In principle, the direct band gap energy of TiO<sub>2</sub>(B) is in the range 3.0-3.2 eV, slightly smaller than for anatase (3.2-3.3 eV): which is reported to be the most effective photocatalyst of the TiO<sub>2</sub> polymorphs. Therefore, one might expect similar photo-catalytic activities of TiO<sub>2</sub>(B) under UV irradiation and/or visible light as conventional anatase, which has been widely developed for many applications such as photocatalyst and water-splitting devices. Furthermore, TiO<sub>2</sub>(B) is a potential material for applications in anti-fogging, anti-fouling, anti-bacterial materials including self-cleaning devices, even though only a small amount of research has been focused on these applications [22].

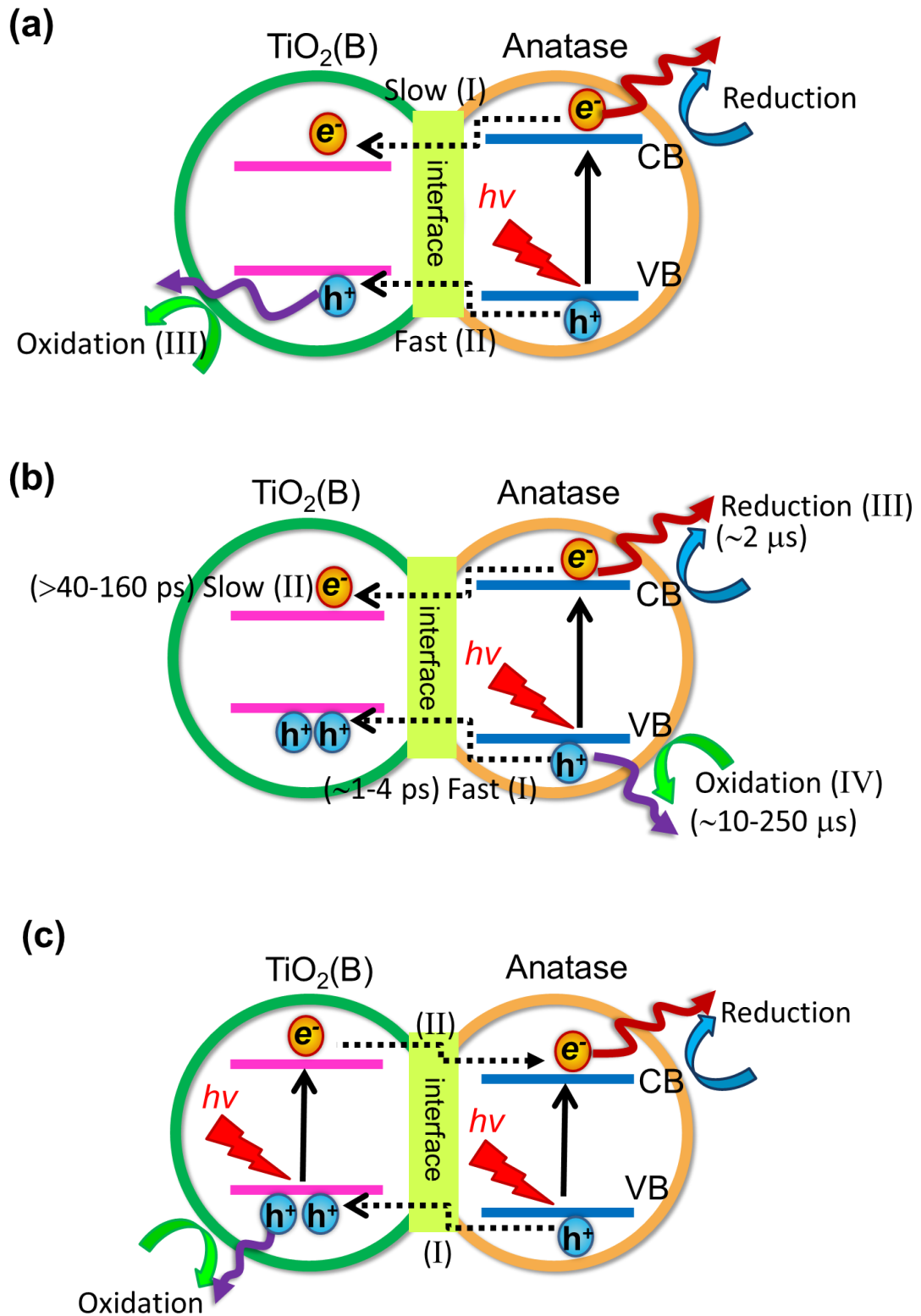


**Figure 2-8** Schematic description of the different proposed charge transfer processes and energy band structures of the mixed phases  $\text{TiO}_2(\text{B})$  and anatase: (a) by Zhanfeng et al, 2010; (b), by Dongjiang et al, 2009; and (c) by Yang et al, 2009.

Many researchers have reported that the anatase phase is considered to have a higher photocatalytic activity than  $\text{TiO}_2(\text{B})$  [60]. However mixing different phases of  $\text{TiO}_2$  [33], [34] such as anatase/rutile or anatase/ $\text{TiO}_2(\text{B})$  has been found to result in better photocatalytic efficiency than solely pure anatase. The mixed phases directly affect the charge transfer process between the different phases possibly reducing recombination of photo-generated electrons and so enhancing the photocatalytic activity [60], [62]. This directly improves the efficiency of oxidative stripping of organic molecules from water or air. The phenomenon in the mixed band structures has been proposed for the industry standard  $\text{TiO}_2$  Degussa P25 which is a mixed phase of anatase and rutile nano-crystalline powder in a mass ratio of 80:20 anatase:rutile [36], [63]. The experimental band gaps of anatase and  $\text{TiO}_2(\text{B})$  phases were determined by Dongjiang et al, 2009 to be 3.19 eV and 3.05 eV respectively. It can be implied that there is a difference between the valence band (VB) and/or conduction band (CB) edge potentials of the two phases when in contact. Most studies describe that the VB edge potential of anatase is generally lower than that of  $\text{TiO}_2(\text{B})$  which means, electrons in the VB of anatase can absorb a photon energy easier than in  $\text{TiO}_2(\text{B})$ . However, the relative levels of the CB edge between the two phases are still ambiguous. There are three slightly different proposed mechanisms for the charge-transfer process between mixed phase anatase and  $\text{TiO}_2(\text{B})$ , described by Zhanfeng et al, 2010; Dongjiang et al, 2009; and Yang et al, 2009 as shown in Figure 2-8.

In Figure 2-8 (a), Zheng et al. proposed a possible three step irreversible interfacial charge transfer process in mixed phase  $\text{TiO}_2$  nanofibers with interfaces between  $\text{TiO}_2(\text{B})$  and anatase, based on Electron Paramagnetic Resonance (EPR) observation: (I) an electron in the valence band (VB) of anatase absorbs an external photon and jumps up to the conduction band (CB) leaving a hole in the VB, this interfacial electron then migrates from the CB of anatase to the CB of  $\text{TiO}_2(\text{B})$ . However, this  $e^-$  transfer process is very slow therefore most of excited electrons usually take part in the reduction reaction in the CB of anatase; (II) The remaining holes in the anatase VB interfacially transfer to the VB of  $\text{TiO}_2(\text{B})$  very quickly; (III) this VB hole continuously moves to the surface of  $\text{TiO}_2(\text{B})$  to drive an oxidation reaction. Zheng et al concluded that the photo-generated holes can transfer faster to the neighbouring  $\text{TiO}_2(\text{B})$  particles than the photo-generated electrons because the effective mass of a hole is smaller than that of electrons.

Another possible electron-hole separation mechanism published by Dongjiang et al, 2009, described a slightly different mechanism with the same relative energy band structure as proposed by Zheng, as schematically shown in Figure 2-8 (b). This mechanism was detected by EPR of  $\text{TiO}_2(\text{B})$  nanofibers with a shell of nano-crystalline anatase. Dongjiang proposed 4 processes of electron-hole separation: (I) an

electron in the external anatase phase shell is excited by light irradiation leaving a hole in the VB of anatase and generating an excited electron in the CB. Due to fast diffusivity of the hole, it can rapidly migrate to the adjacent VB in  $\text{TiO}_2(\text{B})$  or the surface of the anatase shell; (II) a photo-generated electron in the CB of anatase requires 40 times ( $>40\text{-}160$  ps) longer to transfer from anatase to  $\text{TiO}_2(\text{B})$  than this hole migration. Therefore it can be assumed that only photo-generated holes can migrate from anatase through an interface region to  $\text{TiO}_2(\text{B})$  in a one-way process; (III) the remaining photo-induced electrons in the CB of anatase can easily migrate to the shell surface and directly react with adsorbed chemical molecules; even though this process takes a longer time of  $\sim 2$   $\mu\text{s}$  than the interface charge transfer processes (I)&(II), this might help to decrease the electron-hole recombination reaction probability; (IV) similarly, the holes in the VB can migrate to the shell surface of anatase and slowly react ( $\sim 10\text{-}250$   $\mu\text{s}$ ) with surface chemical molecules. Only the holes in the VB of anatase can produce a reduction reaction of chemical molecules since the specific morphology is  $\text{TiO}_2(\text{B})$  nanofibers with a shell of nano-crystallite anatase. As a result, more photo-generated electrons than holes are left in the anatase phase and excess holes can then diffuse into the  $\text{TiO}_2(\text{B})$  phase to maintain the charge balance in the anatase. It should be noted that all processes (I)-(III) are similar to the proposed mechanism of Zheng et al, only process (IV) is different due to the core-shell structure of the nanomaterials.

The last possible charge transfer process and energy band structure has been presented by Yang et al, 2009 as shown in Figure 2-8 (c). The proposed band structure is different in two key respects: (1) the CB edge potential of  $\text{TiO}_2(\text{B})$  is higher than that of anatase and (2) the band gap of  $\text{TiO}_2(\text{B})$  is  $3.2$  eV instead of  $\sim 3.0$  eV. However, a proposed mechanism was presented by Yang et al without any experimental evidence. They reported that excited electrons and holes are generated in the anatase phase by absorption of photon energy and the holes prefer to migrate to  $\text{TiO}_2(\text{B})$  owing to the higher VB edge potential than in the anatase, subsequently this hole migrates to the surface and oxidizes adsorbed species. In addition, photo-generated electrons and holes can also occur in  $\text{TiO}_2(\text{B})$  phase, followed by oxidation between surface holes and surface chemical molecules. Photo-induced electrons in the CB of  $\text{TiO}_2(\text{B})$  usually transfer to anatase due to the lower CB edge potential of anatase. Both transferred electrons from  $\text{TiO}_2(\text{B})$  and electrons directly excited to the anatase CB can react with surface oxidants (reduction reaction).

**Table 2-4** Literature articles which have synthesized TiO<sub>2</sub>(B) for application as a photocatalyst.

| Ref./Year                 | Phases/Morphologies  | Synthesized method                                 | Photo catalytic Reaction                                    |
|---------------------------|--|--|---|
| Bai et al. /2009 [61]     | Mesoporous Pt-(anatase/TiO <sub>2</sub> (B)) nanoarchitecture                  | A simple soft-chemistry and template-free approach | CHCl <sub>3</sub> degradation and H <sub>2</sub> evolution  |
| Zhu et al. /2005 [65]     | Bicrystalline phase containing anatase and TiO <sub>2</sub> (B)                | Sol-gel process                                    | The degradation of an active organic dye, active yellow XRG |
| Parayil et al. /2013 [66] | Mixed phase anatase-TiO <sub>2</sub> (B)                                       | Sol-gel process                                    | H <sub>2</sub> evolution                                    |
| Huang et al. /2012 [67]   | TiO <sub>2</sub> (B)/anatase bicrystal phase TiO <sub>2</sub> nanotube         | Hydrothermal                                       | Methyl orange degradation                                   |
| Mohamed et al. /2012 [34] | Mesoporous bicrystallized TiO <sub>2</sub> (B)/anatase (rutile) phase          | Hydrothermal                                       | Nitrate reduction   |
| Xiang et al. /2010 [68]   | TiO <sub>2</sub> (B) nanosheet   | Hydrothermal                                       | Methyl orange degradation                                   |
| Wang et al. /2010 [69]    | TiO <sub>2</sub> (B) crystallines/nanopores structure                          | Hydrothermal                                       | Methyl orange degradation                                   |
| Hongo et al. /2010 [70]   | Mesoporous titania (a wormhole-like structure) containing TiO <sub>2</sub> (B) | The evaporation-induced self-assembly method       | Acetic acid decomposition                                   |
| Liu et al. /2011 [71]     | TiO <sub>2</sub> (B) core and anatase shell-core heterojunction nanowires      | Hydrothermal                                       | Methyl orange degradation                                   |
| Zheng et al. /2009 [62]   | Titania nanofibers with mixed anatase and TiO <sub>2</sub> (B) phases          | Hydrothermal                                       | Sulforhodamine (SRB) degradation                            |
| Wang et al. /2014 [72]    | Antase/TiO <sub>2</sub> (B) heterojunction                                     | Hydrothermal                                       | Acetaldehyde decomposition                                  |

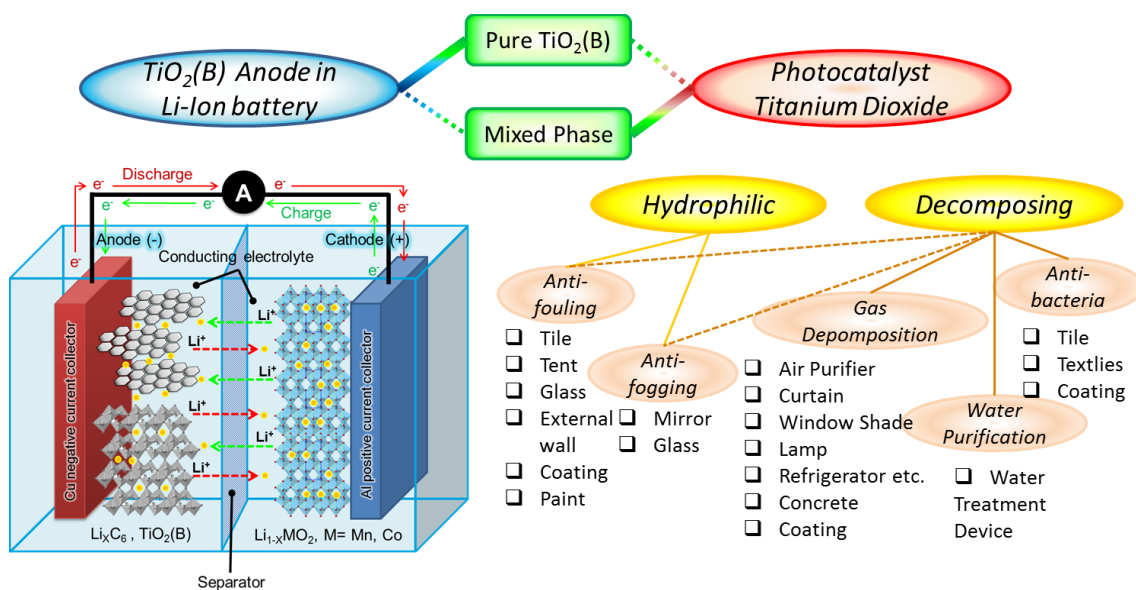


**Figure 2-9** Summarized diagrams showing applications of  $\text{TiO}_2(\text{B})$  involving both pure  $\text{TiO}_2(\text{B})$  and a mixed phase of  $\text{TiO}_2(\text{B})$  with other  $\text{TiO}_2$  phases.

Recent research in the field of  $\text{TiO}_2(\text{B})$  for photocatalytic applications is listed in Table 2.4. These report that mixed phases containing  $\text{TiO}_2(\text{B})$  exhibit higher photocatalytic efficiency than either pure  $\text{TiO}_2(\text{B})$  or pure anatase in every catalysed chemical reaction. The number of publications concerning mixed phase  $\text{TiO}_2(\text{B})$  & anatase as photocatalysts has extensively grown over the last decade. This implies mixed phase anatase &  $\text{TiO}_2(\text{B})$  is a potentially promising material for improvement of photocatalytic technology and could be of benefit for the production of water-splitting photocatalytic devices.

To conclude several applications of  $\text{TiO}_2(\text{B})$ , are presented in Figure 2-9. Generally, the pure  $\text{TiO}_2(\text{B})$  phase usually applies in Li-ion battery anode materials whereas the mixed phase between  $\text{TiO}_2(\text{B})$  and anatase applies in photocatalytic applications. Both of these applications practically require a high surface area and a high stability of materials. The high surface area provides: a large amount of reactive sites for photo-catalytic reaction and an improvement in the rate of electron-transfer during a charge/discharge process for Li-ion batteries [64], whereas, the higher stability of materials for both applications encourages an enhancement of its cycle-life time providing a greater utilization.

## 2.4 Fabrication method of $\text{TiO}_2(\text{B})$ phase

There are two main preparation methods for  $\text{TiO}_2(\text{B})$  that have been proposed since 1980. Solid state synthesis and wet chemical process (sol-gel and hydrothermal methods) have all been reported to prepare  $\text{TiO}_2(\text{B})$  phase. Most of the prior  $\text{TiO}_2(\text{B})$  synthetic routes require three basic strategies of: (i) a formation of alkaline metal

titanates; (ii) a subsequent cation exchange between the alkali metal cation and external protons to form hydrogen titanate structures and (iii) finally, the thermal treatment of hydrogen titanate to reconstruct the structure to form TiO<sub>2</sub>(B) framework.

#### 2.4.1 Solid State Synthesis

The TiO<sub>2</sub>(B) phase was first published by Marchand *et al.* in 1980 [22]. The first preparation method of a new form of titanium dioxide as called TiO<sub>2</sub>(B) consisted of: a synthesis of starting materials K<sub>2</sub>Ti<sub>4</sub>O<sub>9</sub> by solid state reaction between KNO<sub>3</sub> and TiO<sub>2</sub> in the molar ratio 1:2 at 1000°C for 48 hr; the subsequent hydrolysis (cation exchange) of K<sub>2</sub>Ti<sub>4</sub>O<sub>9</sub> in a diluted HNO<sub>3</sub> solution (N<0.5) for 3 days followed by filtration and vacuum drying at room temperature to form a structure of K<sub>2-x</sub>H<sub>x</sub>Ti<sub>4</sub>O<sub>9</sub>.nH<sub>2</sub>O; and the thermal treatment at moderate temperature (500°C). In 1986, the same group as mentioned above [5] proposed a new idea to complete potassium removal from intermediate titanate by increasing the concentration HNO<sub>3</sub> to be excess 3.0 M including structurally comparing of TiO<sub>2</sub>(B) and K<sub>2</sub>Ti<sub>4</sub>O<sub>9</sub> with the other similar forms of layer alkali metal titanate structures e.g. Na<sub>2</sub>Ti<sub>3</sub>O<sub>7</sub>, Na<sub>2</sub>Ti<sub>6</sub>O<sub>13</sub>, and K<sub>2</sub>Ti<sub>8</sub>O<sub>17</sub>.

Not only the K<sub>2</sub>Ti<sub>4</sub>O<sub>9</sub> obtained from a solid stage reaction can be employed as starting materials for TiO<sub>2</sub>(B) preparation but this can be achieved by using the other layered titanates with the formula A<sub>2</sub>Ti<sub>n</sub>O<sub>2n+1</sub> (A= Na, K, Cs; 3≤n≤6) as was suggested by Feist and Davies in 1992 [21]. These A<sub>2</sub>Ti<sub>n</sub>O<sub>2n+1</sub> starting materials were produced by conventional solid state reaction at 850°C of either Na<sub>2</sub>CO<sub>3</sub>, K<sub>2</sub>CO<sub>3</sub> or CsNO<sub>3</sub> and TiO<sub>2</sub>(anatase). The proton exchange of a variety of layered titanates A<sub>2</sub>Ti<sub>n</sub>O<sub>2n+1</sub> (A=Na, K, Cs) by stirring in acid solution and subsequent dehydration including thermal treatment were required to yield TiO<sub>2</sub>(B) phase.

The solid state synthetic technique was claimed to be the first synthesis method for preparing TiO<sub>2</sub>(B) phase and it is still employed since the compound products can be prepared in large amount, however, it provides many disadvantages of the final product such as an aggregation of particles with a rather than the large grain size, poor chemical homogeneity and lack of control of the product form [73]. This leads to development of a variety of material synthesis methods for preparation of TiO<sub>2</sub>(B).

#### 2.4.2 Hydrothermal Synthesis

An achievement for synthesis of nanocrystalline TiO<sub>2</sub>(B) by using a variety of wet chemical processes such as sol-gel method followed by calcination at moderate temperature (around 400-500°C) has been suggested [23],[48],[66],[74]-[76]. However, the sol-gel method required many starting materials and using multistep synthesis followed by calcination. Therefore, it is highly desirable to synthesis nanocrystalline TiO<sub>2</sub>(B) by a simplified technique. The number of preparation steps

and starting materials can be reduced by using a hydrothermal process. However, the products after hydrothermal treatment need to be crystallized by a heat treatment process at moderate temperatures of 400°C. The hydrothermal synthesis method is another suitable technique to synthesise TiO<sub>2</sub>(B) phase materials as powders, with control of particle size, particle morphology and phase formation. This method has been extensively employed to synthesise TiO<sub>2</sub>(B) nanoparticles, nanorods, nanotubes or even thin films by many research groups in the last decade [61]-[72].

In last decade (2004-2014), many researchers have reported the successful preparation of pure phase TiO<sub>2</sub>(B) and/or mixed phase TiO<sub>2</sub>(B) with anatase *via* hydrothermal synthesis. This research is summarized in Table 2-5. From the literature, it can be separated into 2 groups based on the category of solvent employed in the hydrothermal system. The first group is the majority and uses the same basic concept for the preparation of the TiO<sub>2</sub>(B) phase via an alkali metal titanate (A<sub>2</sub>Ti<sub>n</sub>O<sub>2n+1</sub>; A=Na,K) intermediate [77]-[79]. Most of them require a proton exchange process and finish by calcination to form the TiO<sub>2</sub>(B) structure. A titanium source e.g. anatase TiO<sub>2</sub>, P25, TTIP or Ti foils have been used as the precursor together with a high concentration of alkali metal hydroxide solution (≥10 M NaOH or KOH). The hydrothermal reaction temperature and time is in the range of 150-200°C for 1-3 days. The primary hydrothermal intermediate products have monoclinic crystal structures with the empirical formula of A<sub>2</sub>Ti<sub>n</sub>O<sub>2n+1</sub> (A=Na,K) depending on what kind of alkali metal solution is used. These intermediate products are immersed in dilute acid solution, generally 0.1-1M HCl for the purpose of alkali metal ion-proton exchange at the pore sites of A<sub>2</sub>Ti<sub>n</sub>O<sub>2n+1</sub> to form the secondary intermediate product of H<sub>2</sub>Ti<sub>n</sub>O<sub>2n+1</sub>. The final step is the calcination of H<sub>2</sub>Ti<sub>n</sub>O<sub>2n+1</sub> at a temperature around 350-450°C for 2-5 hr. One-dimensional nanopowders such as nanotubes, nanowires or nanoribbons of TiO<sub>2</sub>(B) are often the final product of these preparation procedures. However, some of them might occur as mixed phase anatase and TiO<sub>2</sub>(B) depending on the final calcination temperature.

**Table 2-5** Literature articles which have used the hydrothermal process to synthesise TiO<sub>2</sub>(B) materials. This table shows the phase/s and morphology of the TiO<sub>2</sub> product, synthesis routes and synthesis parameters: A and B refer to the assignment of the anatase and TiO<sub>2</sub>(B) respectively.

| Ref /year    | Phases of Product  | Morphology of Product  | Synthesis Route   | Hydrothermal Conditions           | Post Treatment                     | Precursor  |
|--------------|--|--|---|-----------------------------------|------------------------------------|--|
| [80]<br>2004 | B  | Nanotubes  | 3 steps synthesis:<br>Hydrothermal →<br>Ion Exchange 0.05 M HCl→<br>Calcination | 150°C for 72 hr                   | Calcination<br>@ 400°C<br>for 4 hr | Anatase TiO <sub>2</sub> ,<br>10 M NaOH,<br>0.05 M HCl                       |
|              | B  | Nanowires  |   | 170°C for 72 hr                   |                                    | Anatase TiO <sub>2</sub> ,<br>15 M NaOH,<br>0.05 M HCl                       |
| [58]<br>2005 | B  | Nanotubes  | 3 steps synthesis:<br>Hydrothermal →<br>Ion Exchange 0.05 M HCl→<br>Calcination | 150°C for 72 hr,<br>70% filling   | Calcination<br>@ 400°C<br>for 5 hr | Anatase TiO <sub>2</sub> ,<br>15 M NaOH,<br>0.05 M HCl                       |
|              |  | Nanowires  |   | 170°C for 72 hr,<br>82.5% filling |                                    |  |
| [57]<br>2005 | B  | Nanowires  | 3 steps synthesis:<br>Hydrothermal →<br>Ion Exchange 0.05 M HCl→<br>Calcination | 170°C for 72 hr                   | Calcination<br>@400°C<br>for 4 hr  | Anatase TiO <sub>2</sub> ,<br>15 M NaOH,<br>0.05 M HCl                       |
| [78]<br>2007 | A <sub>2</sub> Ti <sub>n</sub> O <sub>2n+1</sub><br>(A= Li, Na* & K*)<br>*reported as<br>template structure of<br>TiO <sub>2</sub> (B) | Snowflakes<br>(Li <sub>2</sub> TiO <sub>3</sub> )<br>nanorods<br>(Na <sub>2</sub> Ti <sub>3</sub> O <sub>7</sub> &<br>K <sub>2</sub> Ti <sub>8</sub> O <sub>17</sub> ) | 1 step hydrothermal synthesis   | 180°C for 48 hr                   | -                                  | TiCl <sub>4</sub> , 1.5 M<br>HCL, DI water,<br>25 M of<br>LiOH/NaOH /<br>KOH |

| Ref /year    | Phases of Product  | Morphology of Product                                 | Synthesis Route   | Hydrothermal Conditions   | Post Treatment  | Precursor   |
|--------------|--|---|---|---|---|---|
| [83]<br>2010 | $K_2Ti_6O_{13}^* \rightarrow (NH_4)_2Ti_6O_{13}^* \rightarrow TiO_2(\text{anatase})$<br>*both of them have been reported as template structure of $TiO_2(B)$ | Nanotubes →<br>Nanotubes →<br>Octahedral nanocrystals | 3 steps synthesis:<br>Hydrothermal →<br>Ion Exchange<br>$0.1M NH_4NO_3 \rightarrow$<br>Hydrothermal | Step 1, 200°C for 24 hr<br>Step 3, 200°C for 24 hr              | -   | P25 $TiO_2$ ,<br>10 M KOH,<br>$0.1M NH_4NO_3$ ,<br>DI water |
| [69]<br>2010 | B  | Nanopores structure                                   | 1 step hydrothermal synthesis   | 180°C for 8 hr  | -   | TTIP, Ethylene glycol (EG),<br>DI water                     |
| [68]<br>2010 | B  | Nanosheets  | 1 step hydrothermal synthesis   | 140-180°C for 4 hr  | -   | $TiCl_3$ , Ethylene glycol (EG),<br>DI water                |
| [62]<br>2010 | B, A+B, A  | Nanofibers  | 3 steps synthesis:<br>Hydrothermal →<br>Ion Exchange 0.1 M HCl →<br>Calcination                     | 180°C for 48 hr   | Calcination @ 300-700°C for 4 hr<br>(phase of products directly depends on calcination Temp.) | Anatase $TiO_2$ ,<br>10 M NaOH                              |
| [51]<br>2011 | B<br>(via K-titanate intermediate)   | Nanowires   | 3 steps synthesis:<br>Hydrothermal →<br>Ion Exchange<br>$0.1 M HNO_3 \rightarrow$<br>Hydrothermal   | Step 1, 200°C for 24 hr<br>Step 3, 120, 150 and 180°C for 24 hr | -   | P25 $TiO_2$ ,<br>10M KOH,<br>$0.1M HNO_3$                   |
|              | B<br>(via Na-titanate intermediate)  | Nanowires   | 3 steps synthesis:<br>Hydrothermal →<br>Ion Exchange<br>$0.01 M HNO_3 \rightarrow$<br>Calcination   | 200°C for 24 hr   | Calcination @ 450°C for 3 hr  | P25 $TiO_2$ ,<br>10 M NaOH,<br>$0.01 M HNO_3$               |

| Ref /year    | Phases of Product | Morphology of Product   | Synthesis Route   | Hydrothermal Conditions   | Post Treatment   | Precursor  |
|--------------|-------------------|---|---|---|--|--|
| [82]<br>2011 | B, A+B, A         | Nanotubes   | 3 steps synthesis:<br>Hydrothermal →<br>Ion Exchange<br>0.1 M HCl→<br>Calcination                               | 150°C for 72 hr<br>(nanotube)   | Calcination<br>@200-800°C for 2<br>hr (phase of<br>products directly<br>depends on<br>calcination Temp.) | P25 TiO <sub>2</sub> ,<br>10 M NaOH,<br>0.1 M HCl          |
|              |                   | Nano-ribbons  |   | 200°C for 24 hr<br>(nanoribbon)<br>Hydrothermal method  |  |  |
| [71]<br>2011 | B/A core-shell    | Nanowires   | 4 steps synthesis:<br>Hydrothermal →<br>Ion Exchange 0.6 M HCl→<br>Hydrothermal in acid<br>solution→Calcination | 220°C for 48 hr   | Calcination<br>@500°C<br>for 2 hr  | Ti foil,<br>1 M NaOH,<br>0.6 M HCl                         |
| [67]<br>2012 | Bicrystal B+A     | Nanotubes   | 3 steps synthesis:<br>Hydrothermal →<br>Ion Exchange 0.1 M HCl→<br>Calcination                                  | 150°C for 60 hr   | Calcination<br>@ 300°C<br>for 1 hr   | Anatase TiO <sub>2</sub> , 10<br>M NaOH,<br>0.1M HCl       |
| [34]<br>2012 | B+A               | Polyhedral<br>and<br>wormhole-<br>like meso-<br>porous<br>nanoparticles | 2 steps synthesis:<br>Hydrothermal →<br>Calcination   | 100°C for 48 hr<br>(the mixture was<br>adjusted pH to 0.7 by<br>HNO <sub>3</sub> before<br>hydrothermal reaction) | Calcination<br>@ 350°C<br>for 4 hr   | TTIP,<br>PELE/PVA/PAA,<br>DI water,<br>EtOH                |
| [50]<br>2012 | B                 | Porous<br>nanosheets  | 2 steps synthesis:<br>Hydrothermal →<br>Calcination   | 150°C for 24 hr   | Calcination<br>@ 350°C<br>for 2 hr   | TiCl <sub>4</sub> , Ethylene<br>glycol, NH <sub>4</sub> OH |

| Ref /year    | Phases of Product  | Morphology of Product     | Synthesis Route   | Hydrothermal Conditions                          | Post Treatment  | Precursor  |
|--------------|--|---------------------------|---|--|---|--|
| [83]<br>2013 | B  | Nanotubes                 | 3 steps synthesis:<br>Hydrothermal →<br>Ion Exchange 0.1 M HCl→<br>Calcination  | 150°C for 48 hr                                  | Calcination<br>@ 300°C<br>for 2 hr  | Anatase TiO <sub>2</sub> ,<br>10 M NaOH,<br>0.1 M HCl<br>.                       |
| [84]<br>2013 | Na <sub>2</sub> Ti <sub>6</sub> O <sub>13</sub> *  | Nano-ribbons              | 2 steps synthesis:<br>Hydrothermal → Calcination  | 200°C for 40 hr                                  | Calcination<br>@800°C<br>for 2 hr   | P25 TiO <sub>2</sub> ,<br>10 M NaOH,<br>0.1M HCl                                 |
|              | H <sub>2</sub> Ti <sub>3</sub> O <sub>7</sub> *→A<br>*both of them have<br>been reported as<br>template structure of<br>TiO <sub>2</sub> (B) | Nano-ribbons/<br>Nanorods | 3 steps synthesis:<br>Hydrothermal →<br>Ion Exchange 0.1 M HCl→<br>Calcination  | 200°C for 24 hr                                  | Calcination<br>@800°C<br>for 2 hr   |  |
| [85]<br>2014 | Biphase B and A  | Nanofibers                | 4 steps synthesis:<br>Hydrothermal →<br>Ion Exchange 0.1 M HCl→<br>Solvothermal in 0.05M HNO <sub>3</sub><br>→Calcination | Step 1,180°C for 72 hr<br>Step 3,110°C for 20 hr | Calcination<br>@ 400°C<br>for 4 hr  | Anatase TiO <sub>2</sub> ,<br>15 M NaOH,<br>0.1 M HCl,<br>0.05M HNO <sub>3</sub> |
|              | B  | Nanofibers                | 3 steps synthesis:<br>Hydrothermal →<br>Ion Exchange 0.1 M HCl→<br>Calcination  | 180°C for 72 hr                                  | Calcination<br>@ 400°C<br>for 4 hr  |  |
| [72]<br>2014 | B, A+B, A  | Nano-ribbons              | 2 steps synthesis:<br>Hydrothermal →<br>Calcination   | 180°C for 12 hr                                  | Calcination for 2 hr<br>@ 400°C for B,<br>@ 550°C for A+B,<br>@ 750°C for A | TTIP, Acetic acid  |

| Ref /year    | Phases of Product | Morphology of Product | Synthesis Route  | Hydrothermal Conditions | Post Treatment  | Precursor   |
|--------------|-------------------|-----------------------|--|-------------------------|---|---|
| [86]<br>2014 | B                 | Nanosheets            | 1 step hydrothermal synthesis  | 180°C for 12 hr         | -   | TiCl <sub>3</sub> , Ethylene glycol (EG)              |
| [59]<br>2014 | B                 | Nanowires             | 3 steps synthesis:<br>Hydrothermal →<br>Ion Exchange 0.1 M HCl→<br>Calcination | 180°C for 48 hr         | Calcination<br>@ 300°C and 400°C<br>for 2 hr<br>(@400°C, as-<br>prepared TiO <sub>2</sub> (B)<br>shows higher<br>crystallinity) | Anatase TiO <sub>2</sub> ,<br>10 M NaOH,<br>0.1 M HCl |

Where:

- TTIP is Titanium Isopropoxide
- PVA is Polyvinyl Alcohol
- PAA is Polyacrylamide
- PELE is Polyethylene Terephthalate
- EG is Ethylene Glycol
- A is anatase TiO<sub>2</sub>
- B is TiO<sub>2</sub>(B)

The general concept in the second group of literature reports is totally dissimilar to the first one. These employed other solvents beside alkali hydroxide solutions such as ethylene glycol (EG), acetic acid and even polymer solutions (PVA, PELE & PAA) and normally have only one hydrothermal synthesis step or two steps with a calcination process to complete the  $\text{TiO}_2(\text{B})$  preparation. These preparation procedures mostly used a liquid Ti source e.g. TTIP,  $\text{TiCl}_3$  and  $\text{TiCl}_4$  as the precursor. The hydrothermal temperature was in the range of 150-180°C for a reaction time less than 24 hr, except when the hydrothermal solvent was a polymer solution, when they reported a reaction temperature of only 100°C for a longer reaction time of 48 hr. However, all of the second group of research reports showed that the crystallinity of  $\text{TiO}_2(\text{B})$  was lower than the  $\text{TiO}_2(\text{B})$  products from the first group. The physical morphology of their  $\text{TiO}_2$  final product was mainly nanosheets with a porous structure

Due to many synthetic steps for preparing nanocrystalline  $\text{TiO}_2(\text{B})$  by the solid-state synthesis route and the hydrothermal method, a new synthetic strategy is to simplify the preparation techniques or to investigate a new technique to prepare nanocrystalline  $\text{TiO}_2(\text{B})$  materials which will be described in the next chapter.

## 2.5 References

- [1] N.N. Greenwood and A. Earnshaw, *Chemistry of the elements*, Second edi. Oxford, Boston: Butterworth-Heinemann, 1997, pp. 1–1341.
- [2] M.R. Hoffmann, S.T. Martin, W. Choi, and D.W. Bahnemann, “Environmental applications of semiconductor photocatalysis,” *Chem. Rev.*, vol. 95, pp. 69–96, 1995.
- [3] W.H. Baur and A.A. Khan, “Rutile-type compounds. IV.  $\text{SiO}_2$ ,  $\text{GeO}_2$  and a comparison with other rutile-type structures,” *Acta Crystallogr. Sect. B Struct. Crystallogr. Cryst. Chem.*, vol. 27, pp. 2133–2139, 1971.
- [4] M. Horn, C.F. Schwerdtfeger, and E.P. Meagher, “Refinement of the structure of anatase at several temperatures,” *Zeitschrift für Krist.*, vol. 136, pp. 273–281, 1972.
- [5] M. Tournoux, R. Marchand and L. Brohan, “Layered  $\text{K}_2\text{Ti}_4\text{O}_9$  and the open metastable  $\text{TiO}_2(\text{B})$  structure,” *Prog. Solid St. Chem.*, vol. 17, pp. 33-52, 1986.
- [6] M. Latroche, L. Brohan, R. Marchand, and M. Tournoux, “New hollandite oxides:  $\text{TiO}_2(\text{H})$  and  $\text{K}_{0.06}\text{TiO}_2$ ,” *J. Solid State Chem.*, vol. 81, no. 10, pp. 78–82, 1989.
- [7] V. Swamy, L.S. Dubrovinsky, N.A. Dubrovinskaia, F. Langenhorst, A.S. Simionovici, M. Drakopoulos, V. Dmitriev, and H.P. Weber, “Size effects on the structure and phase transition behavior of baddeleyite  $\text{TiO}_2$ ,” *Solid State Commun.*, vol. 134, pp. 541–546, 2005.

- [8] H. Zhang and J.F. Banfield, "Structural characteristics and mechanical and thermodynamic properties of nanocrystalline TiO<sub>2</sub>," *Chem. Rev.*, 2014.
- [9] J.F. Banfield and D.R. Veblen, "Conversion of perovskite to anatase and TiO<sub>2</sub>(B): a TEM study and the use of fundamental building blocks for understanding relationships among the TiO<sub>2</sub> minerals," *Am. Mineral.*, vol. 77, pp. 545–557, 1992.
- [10] J.F. Banfield, D.F. Veblen, and D.J. Smith, "The identification of naturally occurring TiO<sub>2</sub>(B) by structure determination using high-resolution electron microscopy, image simulation, and refinement," *Am. Mineral.*, vol. 76, pp. 343–353, 1991.
- [11] D.A.H. Hanaor and C.C. Sorrell, "Review of the anatase to rutile phase transformation," *J Mater Sci*, vol 46, pp 855–874, 2011.
- [12] X. Nie, S. Zhuo, G. Maeng and K. Sohlberg, "Doping of TiO<sub>2</sub> polymorphs for altered optical and photocatalytic properties," *Int J Photoenergy*, vol 2009, pp 1-22, 2009
- [13] T. Kamegawa, N. Suzuki, and H. Yamashita, "Design of macroporous TiO<sub>2</sub> thin film photocatalysts with enhanced photofunctional properties," *Energy Environ. Sci.*, vol. 4, no. 4, pp. 1411–1416, 2011.
- [14] Y. Paz, Z. Luo, L. Rabenberg, and A. Heller, "Photooxidative self-cleaning transparent titanium dioxide films on glass," *J. Mater. Res.*, vol. 10, no. 11, pp. 2842–2848, 2011.
- [15] X. Zhao, Q. Zhao, J. Yu, and B. Liu, "Development of multifunctional photoactive self-cleaning glasses," *J. Non. Cryst. Solids*, vol. 354, no. 12–13, pp. 1424–1430, 2008.
- [16] J.F. Jacobs, I. Van-De-Poel, and P. Osseweijer, "Sunscreens with Titanium dioxide (TiO<sub>2</sub>) nano-particles: A societal experiment," *nanoethics*, vol. 4, no. 2, pp. 103–113, 2010.
- [17] J.G. Li, T. Ishigaki, and X. Sun, "Anatase, brookite, and rutile nanocrystals via redox reactions under mild hydrothermal conditions: Phase-selective synthesis and physicochemical properties," *J. Phys. Chem. C*, vol. 111, pp. 4969–4976, 2007.
- [18] C.S. Kim, K. Nakaso, B. Xia, K. Okuyama, and M. Shimada, "A new observation on the phase transformation of TiO<sub>2</sub> nanoparticles produced by a CVD method," *Aerosol Sci. Technol.*, vol. 39, no. August 2015, pp. 104–112, 2005.
- [19] J. Huberty and H. Xu, "Kinetics study on phase transformation from titania polymorph brookite to rutile," *J. Solid State Chem.*, vol. 181, pp. 508–514, 2008.
- [20] U. Muller, *Inorganic Structural Chemistry*. New York: John Wiley & Sons, Ltd, 2007.

- [21] T.P. Feist and P.K. Davies, "The soft chemical synthesis of TiO<sub>2</sub>(B) from layered titanates," *J. Solid State Chem.*, vol. 101, pp. 275–295, 1992.
- [22] M. René, B. Luc, and T. Michel, "TiO<sub>2</sub>(B) a new form of titanium dioxide and the Potassium octatitanate K<sub>2</sub>Ti<sub>8</sub>O<sub>17</sub>," *Mater. Res. Bull.*, vol. 15, pp. 1129–1133, 1980.
- [23] A.G. Dylla, P. Xiao, G. Henkelman, and K.J. Stevenson, "Morphological dependence of lithium insertion in nanocrystalline TiO<sub>2</sub>(B) nanoparticles and nanosheets," *J. Phys. Chem. Lett.*, vol. 3, no. 15, pp. 2015–2019, 2012.
- [24] Y. Wang, Y. Huang, W. Ho, L. Zhang, Z. Zou, and S. Lee, "Biomolecule-controlled hydrothermal synthesis of C-N-S-tridoped TiO<sub>2</sub> nanocrystalline photocatalysts for NO removal under simulated solar light irradiation," *J. Hazard. Mater.*, vol. 169, pp. 77–87, 2009.
- [25] D. Galusek and K. Ghillányová, *Ceramic Oxides*, vol. 2. 2010, pp. 1–58.
- [26] T. Yazawa, F. Machida, N. Kubo, and T. Jin, "Photocatalytic activity of transparent porous glass supported TiO<sub>2</sub>," *Ceram. Int.*, vol. 35, no. 8, pp. 3321–3325, 2009.
- [27] T.N. Murakami, Y. Kijitori, N. Kawashima, and T. Miyasaka, "Low temperature preparation of mesoporous TiO<sub>2</sub> films for efficient dye-sensitized photoelectrode by chemical vapor deposition combined with UV light irradiation," *J. Photochem. Photobiol. A Chem.*, vol. 164, no. 1–3, pp. 187–191, 2004.
- [28] M.I. Dar, A.K. Chandiran, M. Grätzel, M.K. Nazeeruddin, and S.A. Shivashankar, "Controlled synthesis of TiO<sub>2</sub> nanoparticles and nanospheres using a microwave assisted approach for their application in dye-sensitized solar cells," *J. Mater. Chem. A*, vol. 2, pp. 1662, 2014.
- [29] P.S. Shinde and C.H. Bhosale, "Properties of chemical vapour deposited nanocrystalline TiO<sub>2</sub> thin films and their use in dye-sensitized solar cells," *J. Anal. Appl. Pyrolysis*, vol. 82, pp. 83–88, 2008.
- [30] C.J. Tavares, J. Vieira, L. Rebouta, G. Hungerford, P. Coutinho, V. Teixeira, J.O. Carneiro, and A J. Fernandes, "Reactive sputtering deposition of photocatalytic TiO<sub>2</sub> thin films on glass substrates," *Mater. Sci. Eng. B*, vol. 138, pp. 139–143, 2007.
- [31] A. Fujishima and K. Honda, "Electrochemical photolysis of water at a semiconductor electrode.," *Nature*, vol. 238, pp. 37–38, 1972.
- [32] H. Lin, A.K. Rumaiz, M. Schulz, D. Wang, R. Rock, C.P. Huang, and S.I. Shah, "Photocatalytic activity of pulsed laser deposited TiO<sub>2</sub> thin films," *Mater. Sci. Eng. B*, vol. 151, no. 2, pp. 133–139, 2008.
- [33] A.J. Cross, C.W. Dunnill, and I.P. Parkin, "Production of predominantly anatase thin films on various grades of steel and other metallic substrates from TiCl<sub>4</sub> and ethyl acetate by atmospheric pressure CVD," *Chem. Vap. Depos.*, vol. 18, no. 4–6, pp. 133–139, 2012.

- [34] M.M. Mohamed, B.H.M. Asghar, and H.A. Muathen, "Facile synthesis of mesoporous bicrystallized TiO<sub>2</sub>(B)/anatase (rutile) phases as active photocatalysts for nitrate reduction," *Catal. Commun.*, vol. 28, pp. 58–63, 2012.
- [35] A. Mattsson and L. Österlund, "Adsorption and photoinduced decomposition of acetone and acetic acid on anatase, brookite, and rutile TiO<sub>2</sub> nanoparticles," *J. Phys. Chem. C*, vol. 114, pp. 14121–14132, 2010.
- [36] W. Li, C. Liu, Y. Zhou, Y. Bai, X. Feng, Z. Yang, L. Lu, X. Lu and K.Y. Chan, "Enhanced photocatalytic activity in anatase/TiO<sub>2</sub>(B) core-shell nanofiber," *J. Phys. Chem. C*, vol. 112, no. 51, pp. 20539–20545, 2008.
- [37] G. Betz and H. Tributsch, "Hydrogen insertion (intercalation) and light induced proton exchange at TiO<sub>2</sub>(B)-electrodes," *J. Appl. Electrochem.*, vol. 14, pp. 315–322, 1984.
- [38] S. Yin, J. Wu, M. Aki, and T. Sato, "Photocatalytic hydrogen evolution with fibrous titania prepared by the solvothermal reactions of protonic layered tetratitanate (H<sub>2</sub>Ti<sub>4</sub>O<sub>9</sub>)," *Int. J. Inorg. Mater.*, vol. 2, pp. 325–331, 2000.
- [39] M. Søndergaard, Y. Shen, A. Mamakhel, M. Marinaro, M. Wohlfahrt-Mehrens, K. Wonsyld, S. Dahl, and B.B. Iversen, "TiO<sub>2</sub> nanoparticles for Li-ion battery anodes: mitigation of growth and irreversible capacity using LiOH and NaOH," *Chem. Mater.*, vol. 27, pp. 119–126, 2015.
- [40] A. Fujishima, T.N. Rao, and D.A. Tryk, "Titanium dioxide photocatalysis," *J. Photochem. Photobiol. C Photochem. Rev.*, vol. 1, pp. 1–21, 2000.
- [41] A.G. Dylla, G. Henkelman, and K.J. Stevenson, "Lithium insertion in nanostructured TiO<sub>2</sub>(B) architectures," *Acc. Chem. Res.*, vol. 46, no. 5, pp. 1104–1112, 2013.
- [42] V. Etacheri, R. Marom, R. Elazari, G. Salitra, and R. Aurbach, "Challenges in The development of advanced Li-ion batteries: a review," *Energy Environ. Sci.*, vol. 4, pp. 3243–3262, 2011.
- [43] Y. Qi, H. Guo, L.G. Hector, and A. Timmons, "Threefold increase in the Young's Modulus of graphite negative electrode during lithium intercalation," *J. Electrochem. Soc.*, vol. 157, pp. A558, 2010.
- [44] Y. Qi and S.J. Harris, "In Situ observation of strains during lithiation of a graphite electrode," *J. Electrochem. Soc.*, vol. 157, pp. A741, 2010.
- [45] Y. Reynier, R. Yazami, B. Fultz, and I. Barsukov, "Evolution of lithiation thermodynamics with the graphitization of carbons," *J. Power Sources*, vol. 165, pp. 552–558, 2007.
- [46] D. Liu and G. Cao, "Engineering nanostructured electrodes and fabrication of film electrodes for efficient lithium ion intercalation," *Energy Environ. Sci.*, vol. 3, pp. 1218, 2010.
- [47] B.J. Landi, M.J. Ganter, C.D. Cress, R.A. Di-Leo, and R.P. Raffaele, "Carbon nanotubes for lithium ion batteries," *Energy Environ. Sci.*, vol. 2, no. 6, pp. 638, 2009.

- [48] R. Giannuzzi, M. Manca, L. De Marco, M. R. Belviso, A. Cannavale, T. Sibillano, C. Giannini, P. D. Cozzoli, and G. Gigli, "Ultrathin TiO<sub>2</sub>(B) nanorods with superior lithium-ion storage performance," *ACS Appl. Mater. Interfaces*, vol. 6, no. 3, pp. 1933, 2014.
- [49] M. Fehse, F. Fischer, C. Tessier, L. Stievano, and L. Monconduit, "Tailoring of phase composition and morphology of TiO<sub>2</sub>-based electrode materials for lithium-ion batteries," *J. Power Sources*, vol. 231, pp. 23, 2013.
- [50] S. Liu, H. Jia, L. Han, J. Wang, P. Gao, D. Xu, J. Yang, and S. Che, "Nanosheet-constructed porous TiO<sub>2</sub>-B for advanced lithium ion batteries," *Adv. Mater.*, vol. 24, no. 24, pp. 3201–3204, 2012.
- [51] J. Li, W. Wan, H. Zhou, J. Li, and D. Xu, "Hydrothermal synthesis of TiO<sub>2</sub>(B) nanowires with ultrahigh surface area and their fast charging and discharging properties in Li-ion batteries.," *Chem. Commun.*, vol. 47, no. 12, pp. 3439–41, 2011.
- [52] J. Qu, J. E. Cloud, Y. Yang, J. Ding, and N. Yuan, "Synthesis of Nanoparticles deposited double walled TiO<sub>2</sub>-B nanotubes with enhanced performance for lithium-ion batteries," *ACS Appl. Mater. Interfaces*, vol. 6, pp. 22199–22208, 2014.
- [53] J.X.H. Xia, W. Xiong, C.K Lim, Q. Yao, Y. Wang, "Hierarchical TiO<sub>2</sub>-B nanowire@alpha-Fe<sub>2</sub>O<sub>3</sub> nanothorn core-branch arrays as superior electrodes for lithium-ion microbatteries," *Nano Res.*, vol. 7, No. 12, pp. 1797-1808, 2014.
- [54] Y. Ren, Z. Liu, F. Pourpoint, A.R. Armstrong, C.P. Grey, and P.G. Bruce, "Nanoparticulate TiO<sub>2</sub>(B): An anode for lithium-Ion batteries," *Angew. Chemie Int. Ed.*, vol. 51, pp. 2164–2167, 2012.
- [55] V. Etacheri, Y. Kuo, A. Van-der-Ven, and B.M. Bartlett, "Mesoporous TiO<sub>2</sub>-B microflowers composed of (1-10) facet-exposed nanosheets for fast reversible lithium-ion storage," *J. Mater. Chem. A*, vol. 1, pp. 12028, 2013.
- [56] Z. Guo, X. Dong, D. Zhou, Y. Du, Y. Wang, and Y. Xia, "TiO<sub>2</sub>(B) nanofiber bundles as a high performance anode for a Li-ion battery," *RSC Adv.*, vol. 3, no. 10, pp. 3352, 2013.
- [57] A.R. Armstrong, G. Armstrong, J. Canales, R. García, and P.G. Bruce, "Lithium-ion intercalation into TiO<sub>2</sub>-B nanowires," *Adv. Mater.*, vol. 17, no. 7, pp. 862–865, 2005.
- [58] G. Armstrong, A.R. Armstrong, J. Canales, and P.G. Bruce, "Nanotubes with the TiO<sub>2</sub>-B structure.," *Chem. Commun.*, no. 19, pp. 2454–6, 2005.
- [59] Z. Su, Y. Zhu, Z. Wu, X. Peng, C. Gao, K. Xi, C. Lai, and R.V. Kumar, "Introduction of 'lattice-voids' in high tap density TiO<sub>2</sub>-B nanowires for enhanced high-rate and high volumetric capacity lithium storage," *RSC Adv.*, vol. 4, pp. 22989, 2014.

- [60] D. Yang, H. Liu, Z. Zheng, Y. Yuan, J. Zhao, E.R. Waclawik, X. Ke, and H. Zhu, "An efficient photocatalyst structure: TiO<sub>2</sub>(B) nanofibers with a shell of anatase nanocrystals," *J. Am. Chem. Soc.*, vol. 131, no. 49, pp. 17885–17893, 2009.
- [61] Y. Bai, W. Li, C. Liu, Z. Yang, X. Feng, X. Lu, and K.Y. Chan, "Stability of Pt nanoparticles and enhanced photocatalytic performance in mesoporous Pt-(anatase/TiO<sub>2</sub>(B)) nanoarchitecture," *J. Mater. Chem.*, vol. 19, no. 38, pp. 7055, 2009.
- [62] Z. Zheng, H. Liu, J. Ye, J. Zhao, E. R. Waclawik, and H. Zhu, "Structure and contribution to photocatalytic activity of the interfaces in nanofibers with mixed anatase and TiO<sub>2</sub>(B) phases," *J. Mol. Catal. A Chem.*, vol. 316, no. 1–2, pp. 75–82, 2010.
- [63] X. Sun, W. Dai, G. Wu, L. Li, N. Guan, and M. Hunger, "Evidence of rutile to anatase photo-induced electron transfer in mixed phase TiO<sub>2</sub> by solid-state NMR spectroscopy," *Chem. Commun.*, 2015.
- [64] A.S. Aricò, P. Bruce, B. Scrosati, J.M. Tarascon, and W.V. Schalkwijk, "Nanostructured materials for advanced energy conversion and storage devices," *Nat. Mater.*, vol. 4, no. May, pp. 366–377, 2005.
- [65] J. Zhu, J. Zhang, F. Chen, and M. Anpo, "Preparation of high photocatalytic activity TiO<sub>2</sub> with a bicrystalline phase containing anatase and TiO<sub>2</sub>(B)," *Mater. Lett.*, vol. 59, no. 27, pp. 3378–3381, 2005.
- [66] S. K. Parayil, H. S. Kibombo, L. Mahoney, C. Wu, M. Yoon, and R. T. Koodali, "Synthesis of mixed phase anatase-TiO<sub>2</sub>(B) by a simple wet chemical method," *Mater. Lett.*, vol. 95, pp. 175–177, 2013.
- [67] C. Huang, K. Zhu, M. Qi, Y. Zhuang, and C. Cheng, "Preparation and photocatalytic activity of bicrystal phase TiO<sub>2</sub> nanotubes containing TiO<sub>2</sub>-B and anatase," *J. Phys. Chem. Solids*, vol. 73, no. 6, pp. 757–761, 2012.
- [68] G. Xiang, T. Li, J. Zhuang, and X. Wang, "Large-scale synthesis of metastable TiO<sub>2</sub>(B) nanosheets with atomic thickness and their photocatalytic properties," *Chem. Commun.*, vol. 46, no. 36, pp. 6801–3, 2010.
- [69] P. Wang, T. Xie, D. Wang, and S. Dong, "Facile synthesis of TiO<sub>2</sub>(B) crystallites/nanopores structure: A highly efficient photocatalyst," *J. Colloid Interface Sci.*, vol. 350, no. 2, pp. 417–420, 2010.
- [70] T. Hongo and A. Yamazaki, "Thermal influence on the structure and photocatalytic activity of mesoporous titania consisting of TiO<sub>2</sub>(B)," *Microporous Mesoporous Mater.*, vol. 142, no. 1, pp. 316–321, 2011.
- [71] B. Liu, A. Khare, and E.S. Aydil, "TiO<sub>2</sub>-B/anatase core-shell heterojunction nanowires for photocatalysis," *ACS Appl. Mater. Interfaces*, vol. 3, pp. 4444–4450, 2011.

- [72] C. Wang, X. Zhang, and Y. Liu, "Coexistence of an anatase/TiO<sub>2</sub>(B) heterojunction and an exposed (001) facet in TiO<sub>2</sub> nanoribbon photocatalysts synthesized via a fluorine-free route and topotactic transformation," *Nanoscale*, vol. 6, pp. 5329, 2014.
- [73] T. Guo, M.S. Yao, Y.H. Lin and C.W. Nana, "A comprehensive review on synthesis methods for transition-metal oxide nanostructures," *Cryst Eng Comm*, vol. 17, pp 3551, 2015.
- [74] T. Beuvier, M. Richard-Plouet, M.M.L. Granvalet, T. Brousse, O. Crosnier and L. Brohan, "TiO<sub>2</sub>(B) nanoribbons as negative electrode material for Lithium ion batteries with high rate performance," *Inorg. Chem*, vol 49, pp 8457, 2010
- [75] T. Beuvier, M. Richard-plouet, and L. Brohan, "Accurate methods for quantifying the relative ratio of anatase and TiO<sub>2</sub>(B) nanoparticles," *J. Phys. Chem. C*, vol. 113, no. 31, pp. 13703–13706, 2009
- [76] C.W. Peng, M. Richard-Plouet, T.Y. Ke, C.Y. Lee, H.T. Chiu, C. Marhic, E. Puzenat, F. Lemoigno, and L. Brohan, "Chimie douce route to sodium hydroxo titanate nanowires with modulated structure and conversion to highly photoactive titanium dioxides," *Chem. Mater.*, vol. 20, no. 23, pp. 7228–7236, 2008.
- [77] M. Tomiha, N. Masaki, S. Uchida, and T. Sato, "Hydrothermal synthesis of alkali titanates from nano size titania powder," *J. Mater. Sci.*, vol. 37, pp. 2341–2344, 2002.
- [78] H. Song, H. Jiang, T. Liu, X. Liu, and G. Meng, "Preparation and photocatalytic activity of alkali titanate nano materials A<sub>2</sub>Ti<sub>n</sub>O<sub>2n+1</sub> (A=Li, Na and K)," *Mater. Res. Bull.*, vol. 42, no. 2, pp. 334–344, 2007.
- [79] Y. Lei, J. Sun, H. Liu, X. Cheng, F. Chen, and Z. Liu, "Atomic mechanism of predictable phase transition in dual-phase H<sub>2</sub>Ti<sub>3</sub>O<sub>7</sub>/TiO<sub>2</sub>(B) nanofiber: an in situ heating TEM investigation," *Chem. - A Eur. J.*, vol. 20, pp. 11313–11317, 2014.
- [80] A.R. Armstrong, G. Armstrong, J. Canales, and P.G. Bruce, "TiO<sub>2</sub>-B Nanowires," *Angew. Chem Int Ed. Engl.*, vol. 43, pp. 2286–2288, 2004.
- [81] J. Li, Y. Yu, Q. Chen, J. Li, and D. Xu, "Controllable synthesis of TiO<sub>2</sub> single crystals with tunable shapes using ammonium-exchanged titanate nanowires as precursors," *Cryst. Growth Des.*, vol. 10, pp. 2111–2115, 2010.
- [82] K. Kiatkittipong, J. Scott, and R. Amal, "Hydrothermally synthesized titanate nanostructures: Impact of heat treatment on particle characteristics and photocatalytic properties," *ACS Appl. Mater. Interfaces*, vol. 3, pp. 3988–3996, 2011.
- [83] J.P. Huang, D.D. Yuan, H.Z. Zhang, Y.L. Cao, G.R. Li, H.X. Yang, and X.P. Gao, "Electrochemical sodium storage of TiO<sub>2</sub>(B) nanotubes for sodium ion batteries," *RSC Adv.*, vol. 3, no. 31, pp. 12593, 2013.

- [84] K. Kiatkittipong, A. Iwase, J. Scott, and R. Amal, "Photocatalysis of heat treated sodium- and hydrogen-titanate nanoribbons for water splitting, H<sub>2</sub>/O<sub>2</sub> generation and oxalic acid oxidation," *Chem. Eng. Sci.*, vol. 93, pp. 341–349, 2013.
- [85] S. Zhu, S. Xie, and Z. Liu, "Design and observation of biphasic TiO<sub>2</sub> crystal with perfect junction," *J. Phys. Chem. Lett.*, vol. 5, pp. 3162–3168, 2014.
- [86] Y. Wang, C. Wang, X. Zhang, P. Sun, L. Kong, Y. Wei, H. Zheng, and Y. Liu, "TiO<sub>2</sub>(B) nanosheets mediate phase selective synthesis of TiO<sub>2</sub> nanostructured photocatalyst," *Appl. Surf. Sci.*, vol. 292, pp. 937–943, 2014.

## **Chapter 3 Sample Preparations and Characterization methods**

The first section of this chapter describes two useful fabrication techniques to prepare TiO<sub>2</sub>(B) materials in this research: Hydrothermal and CVD methods including the basic principles. The following section presents the characterization methods: Powder X-ray Diffraction (PXRD), Scanning Electron Microscopy (SEM), Focused Ion Beam Scanning Electron Microscopy (FIB-SEM), Transmission Electron Microscopy (TEM), Raman Spectroscopy (Raman), and Ultraviolet-Visible diffuse reflectance spectroscopy (UV-VIS). This section details the principles of each technique, details of sample preparation and data analysis.

### **3.1 Fabrication Methods**

Two fabrication methods were used in this research. The first method is hydrothermal synthesis which has been used to synthesise TiO<sub>2</sub>(B) over the past decade. The second is Low Pressure Chemical Vapour Deposition (LPCVD) which is a novel technique to prepare TiO<sub>2</sub>(B) thin films. However this latter method aids study of the TiO<sub>2</sub>(B) phase formation.

#### **3.1.1 Hydrothermal Synthesis**

The general principles of hydrothermal synthesis including a hydrothermally experimental procedure to synthesis TiO<sub>2</sub>(B) in this research are described in this section.

##### **3.1.1.1 Background and theory of hydrothermal synthesis**

The general definitions of hydrothermal conditions are when the reaction temperature  $\geq 100^{\circ}\text{C}$  and reaction pressure  $\geq 1$  bar. A Carbolite oven fitted with a Eurotherm temperature controller was used as the external heat generator with air circulation. The reaction vessel in this work was a 4748 large capacity acid digestion bomb of 125 cm<sup>3</sup> volume composed of a metal body and a removable PTFE (Teflon) liner as shown in the diagrammatical representation in Figure 3-1.

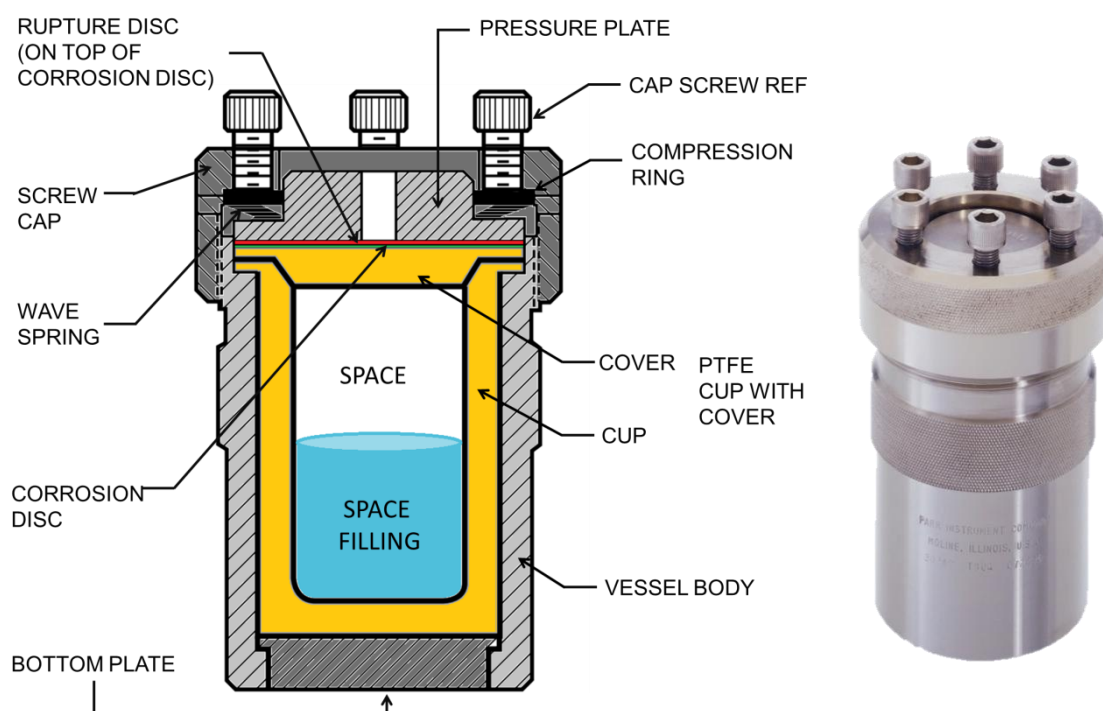


**Figure 3-1** (a) Diagram showing the components of a large capacity acid digestion vessel (b) an image of the large capacity acid digestion vessel employed in the hydrothermal synthesis for  $\text{TiO}_2(\text{B})$ . [Adapted from Parr Instrument Company, Illinois, US]

The standard operating procedures and precautions are provided in the Parr Operating Instructions (manufacturer). In order to prevent excessive pressure generated within the container, at least 33% of the bomb capacity (~40 mL) should be left as free space for volume expansion in the case of inorganic sample preparation reaction without any liberated gases. The filled Teflon cup with its Teflon cover is located inside the metal body and the correct position between the body and cup can be checked by slightly raising the bottom plate to avoid the air gap. A corrosion disc with a Rupture disc on top, is placed on the Teflon cover to protect the bomb and the operator from any dangers caused by unexpected high internal pressures. The pressure plate topped by the wave spring and compression ring is added on top of the rupture disc. The screw cap is turned down by hand to cover the pressure plate unit, finally the six cap screws between the screw cup unit and the pressure plate unit are tightened.

### 3.1.1.2 Experimental Procedure for Hydrothermal synthesis of the TiO<sub>2</sub>(B) phase

#### 3.1.1.2.1 Chemicals and Materials in Hydrothermal method

- Titanium(IV) isopropoxide, Ti[OCH(CH<sub>3</sub>)<sub>2</sub>]<sub>4</sub> or TTIP, 97%. Sigma Aldrich.
- Titanium(IV) dioxide, P25, nanopowder, ≥99.5% trace metals basis. Sigma Aldrich
- Titanium(IV) dioxide, rutile, nanopowder, ≥98.5% trace metals basis, Alfa Aesar.
- Titanium(IV) dioxide, Anatase, nanopowder, ≥ 99% trace metals basis, Sigma Aldrich.
- Sodium Hydroxide, NaOH, > 97.5% purity, Scientific Laboratory supplies
- Ethanol, 99.0%, A.R. grade, Alfa Aesar
- Nitric acid, 70%, A.R. grade, Sigma Aldrich
- Deionized (DI) water

#### 3.1.1.2.2 Hydrothermal synthesis of the TiO<sub>2</sub>(B) nanoparticles

A synthesis process *via* an alkali metal intermediate phase transformation was employed to prepare TiO<sub>2</sub>(B) nanoparticles. In order to study the TiO<sub>2</sub>(B) phase formation mechanism in the hydrothermal system *via* an effect of Na<sup>+</sup> on the phase formation which can be compared with the effect of Na<sup>+</sup> on the TiO<sub>2</sub>(B) phase formation prepared by LPCVD method. A range of Ti precursors (e.g. 1 g of P25, Anatase TiO<sub>2</sub> or rutile TiO<sub>2</sub> or, alternatively, 3 mL of TTIP) were used together with 75 mL of 10M NaOH, this was stirred for 30 min in a beaker followed by sonication at room temperature for 15 min. The solution was transferred into a Teflon cup before inserting it into the metal vessel body of the hydrothermal reactor. The vessel was placed in the Carbolite furnace, and heated at 180°C for 48 hr. The hydrothermal products were washed with deionised water several times to remove the excess NaOH until the pH of the washing water was below 8. The washed products were soaked in 100 mL of 0.1M HNO<sub>3</sub> for 1 day and dried at 70°C for 12 hours to form an intermediate phase of H<sub>2</sub>Ti<sub>n</sub>O<sub>2n+1</sub>. The intermediate sample was calcined at 400°C for 5 hours to obtain the final product (TiO<sub>2</sub>(B)).

### **3.1.2 Chemical Vapour Deposition (CVD)**

Typically, TiO<sub>2</sub> thin films have been prepared on substrates by a wide range of deposition methods such as sol-gel or wet chemical deposition [1]. However, those methods possess shortcomings concerned with the adhesion of TiO<sub>2</sub> on the surface of substrate, indicating a low life time of the material denseness. In order to overcome this problem, many methods that provide a stronger interaction between the substrate and TiO<sub>2</sub> thin film have been intensively studied and widely applied e.g. sputtering [2], pulsed laser deposition (PLD) [3], physical vapour deposition (PVD) and chemical vapour deposition. CVD is a low-cost method which is easy to set up and subsequently adjust. Furthermore, CVD permits a high degree of compatibility with a wide range of substrates and also has the potential for mass production.

The chemical vapour deposition technique has been used to synthesise a range of thin film materials with the thinnest layers around a few nanometres. In this research, it was employed for the preparation of nanocrystalline titanium dioxide thin films on substrates under low pressure. Low pressure chemical vapour deposition showed successful preparation of general TiO<sub>2</sub> polymorphs such as anatase and rutile as well as the rare phase TiO<sub>2</sub>(B).

#### **3.1.2.1 Background and Theory of CVD method**

Chemical vapour deposition (CVD) method has been used to prepare a large number of materials for almost 50 years. This is an efficient preparation method which can be scaled up from a laboratory tool to larger scale production with significant economic impact. CVD is one the most popular techniques to prepare thin film materials [4] including TiO<sub>2</sub> thin films [5]–[7]. As well as thin film fabrication, the CVD technique is also used to synthesise discrete TiO<sub>2</sub> ultrafine particles on the surface of several supports e.g. glass beads [8].

The basic principles of the CVD method for general metal oxide deposition are detailed in 7 steps as shown in Figure 3-2. The main mechanisms/steps occurring in the reactor chamber during the CVD process are described in detail below [9]:

- 1.) Liquid precursors are used to generate their active gaseous species by external thermal energy (e.g. heating mantles, hotplate with oil bath).
- 2.) The active gaseous species are mixed with a carrier gas (normally N<sub>2</sub> or Ar) and then transported into the reaction chamber.

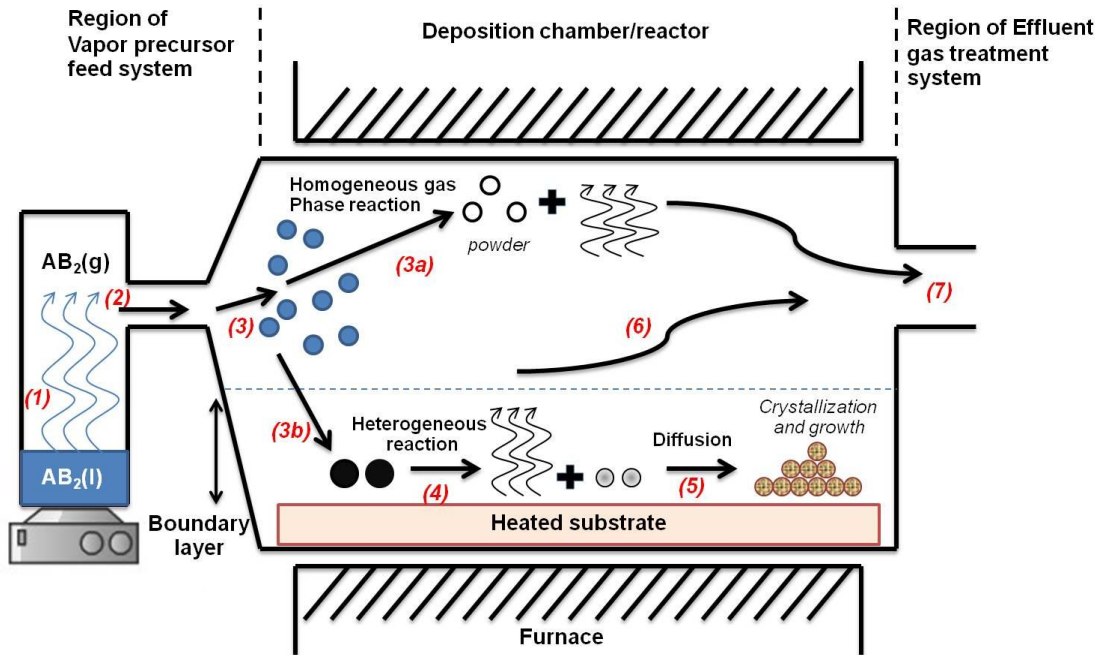


**Figure 3-2** The basic principles of the main steps occurring in the CVD process

- 3.) Thermal decomposition of the gas phase precursors occurs in the gas entry area to form intermediate phases. The intermediate species can sequentially react in two possible routes:
  - (3a) *Homogeneous Reaction Route*: occurring in a higher temperature region than the dissociation temperature of the intermediate species, the intermediate species thermally decompose and/or react with the carrier gas or itself to produce the desired powder product together with volatile byproducts. These byproducts flow away out of the reactor, and the desired powders are deposited on the substrate surface, some of them may act as nucleation centres (more details on this step is described in Figure 3-3);
  - (3b) *Heterogeneous Reaction Route*: occurring in a lower temperature region than dissociation temperature of the intermediate species, the intermediate species is transferred across the interlayer (a thin layer near the surface of substrate) as described in the following steps (4-7).
- 4.) The active species (from 3b) are absorbed onto the surface of the substrate which is heated by the surrounding furnace. The heterogeneous reaction between the gas species and solid-heated substrate occurs at the interface producing the deposit and byproducts in this region.

- 5.) The deposit diffuses along the surface of the substrate from a region of high vapour supersaturation to an area of low supersaturation, forming crystalline and/or amorphous materials by nucleation and sequential growth of the thin film. A low nucleation rate produces a single crystal thin film, whereas a higher nucleation rate results in a polycrystalline film or possibly discrete particles.
- 6.) The volatile byproducts and unreacted gaseous precursor flow away out of the reactor with the carrier gas to the exhaust line.

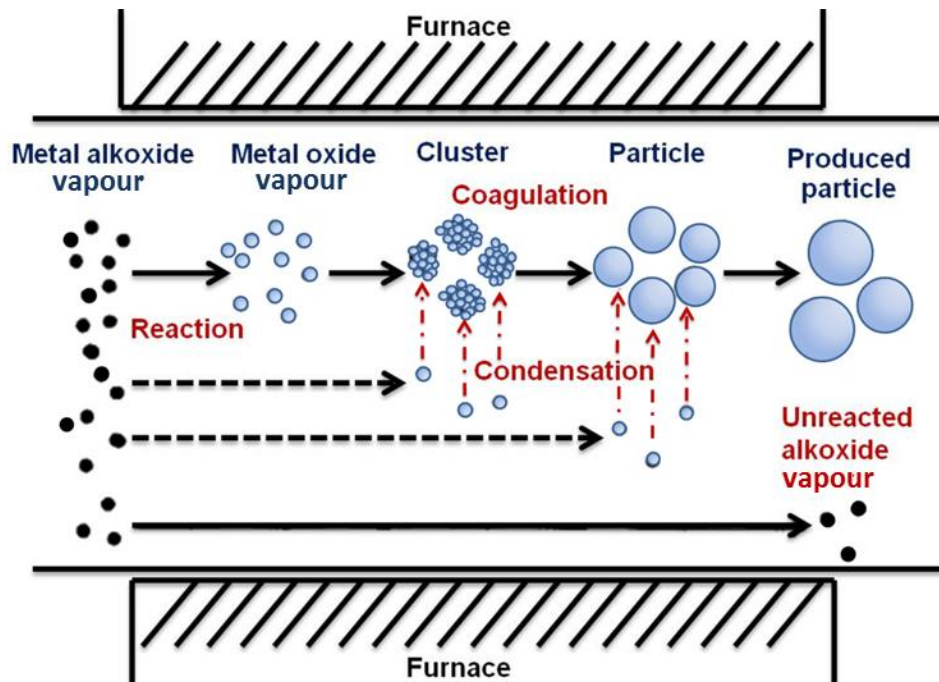


**Figure 3-3** Particle formation in the furnace via Homogeneous Reaction Route (adapted from [32])

Figure 3-3, shows the general mechanism in the CVD reaction chamber using an example of an active gaseous species generated from metal-alkoxide precursors that is predicted to occur at a higher temperature region than the dissociation temperature of the active gaseous species: firstly, metal alkoxide vapour is thermally decomposed at some suitable temperature area in the reactor to provide a supersaturated metal oxide vapour; secondly, if the amount of this oxide vapour reaches a sufficient level to cause a homogeneous nucleation (i.e. in atmospheric pressure CVD), ultrafine primary clusters of metal oxide nucleate; thirdly, some of this ultrafine primary cluster agglomerate to form bigger secondary particles and clusters also grow by heterogeneous condensation from the metal oxide vapour. When the particles are heavy enough, they will drop on to the surface of the substrate by gravity. Finally, the unreacted metal alkoxide vapour flows away from the reactor by the carrier gas into the exhaust line [10]. Note if low pressure CVD is employed thin films are favoured via a heterogeneous nucleation route.

### 3.1.2.2 CVD for TiO<sub>2</sub> synthesis

During preparation of TiO<sub>2</sub> nanoparticles by CVD, it has been found that control of the size of primary particles and their agglomeration are difficult. Many researchers have studied the size and crystallinity of TiO<sub>2</sub> nanoparticles including their physical morphology, prepared by several different CVD methods. There are many factors which can control the size, crystallinity, phase and physical morphology of TiO<sub>2</sub> particles, e.g. choice of titanium precursors, precursor concentration, reaction temperature and residence time. Two main titanium precursors have been regularly used: titanium tetrachloride (TiCl<sub>4</sub>) and titanium tetraisopropoxide (TTIP). Literature articles are briefly summarized in in Table 3-1 in terms of synthesis parameters and the nature of the TiO<sub>2</sub> final product.

For the case of TiCl<sub>4</sub> acting as the precursor, TiCl<sub>4</sub> can be oxidized [11]–[14] and/or hydrolysed [11], [15], [16] under the CVD system to form the TiO<sub>2</sub> fine particles. Using TTIP as titanium source, the thermal decomposition of TTIP is the main reaction to prepare TiO<sub>2</sub> particles [10], [17]–[19].

From Table 3-1, literature articles can be divided into at least three groups. The first group focuses on TiO<sub>2</sub> fine particles and/or thin films supported on appropriate substrates such as SiO<sub>2</sub>, Al<sub>2</sub>O<sub>3</sub>, activated carbon, porous glass, silica gel and glass beads [6], [8], [20]–[23]. The second group of literature has studied the powder preparation of TiO<sub>2</sub> nano/micro particles [10], [24]–[30]. Both of these groups have utilized TTIP as the precursor. The last group of literature has synthesised TiO<sub>2</sub> fine particles by using TiCl<sub>4</sub> as the titanium source instead of the general TTIP precursor [12], [22], [27], [31]. An inert gas e.g. Ar or N<sub>2</sub> is usually used as the carrier gas, however mixing O<sub>2</sub> gas (from the pure commercial O<sub>2</sub> or Air) with the carrier (inert) gas helps the active gas species complete their reaction sooner, especially the decomposition reaction. Most of the tube furnace reactors were set in either a vertical or horizontal direction. The observed reaction temperature normally ranged from 300°C to 1000°C, but in the optimum reaction conditions it ranged from 300°C to 600°C. The particle size of TiO<sub>2</sub>, varied significantly with preparation conditions especially the reaction temperature and reaction time.

**Table 3-1** Literature articles which have used the CVD method to synthesise TiO<sub>2</sub> materials. This table shows the synthesis parameters and physical appearance of TiO<sub>2</sub> final product.

| Ref. | Final Products  | Reactor Shape and Furnace  | Reaction Pressure  | Carrier Gas/<br>Flow rate              | Deposition Conditions |              | Precursors                              |  |
|------|---|--|--------------------|--|-----------------------|--------------|---|--|
|      |   |  |                    |  | Temperature           | Time         | Ti sources and Temp of bubbling chamber | Gas precursor/<br>flow rate                                    |
| [10] | Ultrafine spherical TiO <sub>2</sub> particles, 10-60 nm  | Tube furnace, Quartz tube L=30 cm, $\theta=1.3$ cm (horizontal)                                      | A few <i>mTorr</i> | N <sub>2</sub> /<br>(300-4,000 mL/min) | 400-900°C             | -            | TTIP                                    | -  |
| [20] | TiO <sub>2</sub> particles supporting on transparent porous glass   | Furnace with porous glass tube inside  | Reduced pressure   | N <sub>2</sub>                         | 570, 600°C            | 32 and 70 hr | TTIP                                    | O <sub>2</sub> was add to the mixer of TTIP and N <sub>2</sub> |
| [21] | Anatase TiO <sub>2</sub> nanoparticles on supporter (SiO <sub>2</sub> , Al <sub>2</sub> O <sub>3</sub> and Activated Carbon), ~50 nm        | Tube furnace, Quartz tube (vertical) with porous quartz disk annealed at the end of tube             | Under vacuum       | N <sub>2</sub> /<br>(30,60 mL/min)     | 300°C                 | 3-5 hr.      | TTIP/ 80°C                              | -  |
| [8]  | Anatase TiO <sub>2</sub> nanoparticles (10-20 nm), Thin TiO <sub>2</sub> layer and Thick TiO <sub>2</sub> layer on a supporter (silica gel) | Tube furnace, Quartz tube (vertical, horizontal) with porous quartz disk annealed at the end of tube | Under vacuum       | N <sub>2</sub>                         | 300°C                 | -            | TTIP/ 80°C                              | -  |

| Ref.        | Final Products  | Reactor Shape and Furnace   | Reaction Pressure | Carrier Gas/ Flow rate        | Deposition Conditions                 |  | Precursors  |                          |
|-------------|---|---|-------------------|-------------------------------|---------------------------------------|--|---|--------------------------|
|             |   |   |                   |                               | Temperature                           | Time   | Ti sources and Temp of bubbling chamber   | Gas precursor/ flow rate |
| [6]         | TiO <sub>2</sub> nanoparticles, 20-30 nm coated on glass beads  | Tube furnace, Alumina tube L=80 cm $\theta$ =1.0 cm (horizontal)                    | Atmosphere        | Ar                            | 900°C                                 | 10,30,60, 120 min (Effective time is 60 min) | TTIP/ 90°C  | -                        |
|             |   |   |                   |                               |                                       |  | Adding N <sub>2</sub> gas in the mixer of Ar gas and TTIP before feeding into the reactor |                          |
| [22]        | Anatase TiO <sub>2</sub> nanoparticles on supporter (Activated Carbon), 10-50 nm  | Furnace, Quartz tube (vertical) with porous quartz disk annealed at the end of tube | Atmosphere        | N <sub>2</sub> / (400 mL/min) | 500°C                                 | < 120 min                                    | TBOT/ 100, 200°C  | -                        |
| [24] – [26] | TiO <sub>2</sub> nanoparticles, nano- to submicrometer, mean= 10 nm at optimal condition                                      | Tube furnace, Alumina tube L=80 cm $\theta$ =1.0 cm (horizontal)                    | Atmosphere        | Ar                            | 700,900, 1100, 1300°C                 | Collected sample after pass from the reactor | TTIP/ 80, 95 and 110°C  | Air                      |
| [27]        | Polycrystalline anatase TiO <sub>2</sub> nanoparticles, diameter of 1° particles is between 6-16 nm varied with reaction Temp | Quartz tube, L=60 cm $\theta$ =1.3 cm (vertical) (Effective zone from 20 cm-33 cm)  | Atmosphere        | N <sub>2</sub> / (2 L/min)    | 250-1000°C, Effective temp= 600,800°C | -  | [TTIP]= 7.68x10 <sup>-7</sup> mol/L   | -                        |

| Ref. | Final Products   | Reactor Shape and Furnace  | Reaction Pressure | Carrier Gas/ Flow rate          | Deposition Conditions                 |                 | Precursors  |   |
|------|--|--|-------------------|---------------------------------|---------------------------------------|-----------------|---|---|
|      |  |  |                   |                                 | Temperature                           | Time            | Ti sources and Temp of bubbling chamber                   | Gas precursor/ flow rate  |
| [27] | Polycrystalline anatase TiO <sub>2</sub> nanoparticles, 8-15 nm varied with Reaction Temp.         | Quartz tube, L=60 cm, $\theta$ =1.3 cm (vertical) (Effective zone from 20-33 cm) | Atmosphere        | N <sub>2</sub> / (2 L/min)      | 550-1200°C effective temp= 800,1000°C | -               | [TiCl <sub>4</sub> ]= 7.64x10 <sup>-7</sup> mol/L         | O <sub>2</sub> (0.5 L/min) was added to the mixture of TiCl <sub>4</sub> and N <sub>2</sub> before feeding into the reactor   |
| [23] | TiO <sub>2</sub> thin films with thickness about 420 nm on the inner surface of porous glass tubes | Tube furnace, Quartz tube (horizontal)   | Atmosphere        | N <sub>2</sub> / (200 mL/min)   | 200-400°C                             | -               | TTIP/ 70°C  | Mixed O <sub>2</sub> and N <sub>2</sub> (700 L/min) was added into the TTIP/N <sub>2</sub> stream before feeding into the reactor   |
| [28] | TiO <sub>2</sub> nanoparticles, 5-50 nm, mean= 10 nm   | Stainless tube L=49 cm, $\theta$ =3.5 cm (horizontal)                            | -                 | N <sub>2</sub> / (10-30 mL/min) | 300-400°C                             | 14 sec          | TTIP/ 40°C  | High temperature N <sub>2</sub> gas was mixed with a mixture of N <sub>2</sub> gas and TTIP before being transferred into the reactor (to prevent a condensation of TTIP) |
| [29] | TiO <sub>2</sub> nanoparticles, < 30 nm  | Tube furnace, $\theta$ =2.7 cm (horizontal)                                      | -                 | N <sub>2</sub>                  | 100-500°C                             | Minimum is 20 s | TTIP [8.8x10 <sup>-8</sup> to 7.1x10 <sup>-7</sup> mol/L] | N <sub>2</sub> , Air & TTIP was mixed before feeding into the reactor   |

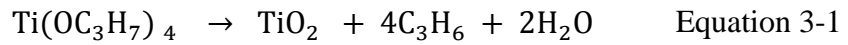
| Ref. | Final Products   | Reactor Shape and Furnace   | Reaction Pressure | Carrier Gas/ Flow rate | Deposition Conditions     |        | Precursors  |  |
|------|--|---|-------------------|------------------------|---------------------------|--------|---|--|
|      |  |   |                   |                        | Temperature               | Time   | Ti sources and Temp of bubbling chamber   | Gas precursor/ flow rate   |
| [30] | Polycrystalline anatase TiO <sub>2</sub> nanoparticles, 20-25 nm | Quartz tube<br>L=12.5 cm $\theta$ =1.3 cm (horizontal)  | A few mTorr       | Ar / (30 mL/min)       | 600°C                     | -      | TTIP/ 220°C   | O <sub>2</sub> (3 mL/min) was add into the mixture of TTIP and Ar  |
| [12] | Anatase and Rutile TiO <sub>2</sub> particles, 0.13-0.35 $\mu$ m | Tube furnace, Alumina tube<br>L=152.4 cm $\theta$ =3.175 cm (horizontal)  | Atmosphere        | Ar                     | 927,1127, 1327 and 1450°C | 1.6 S  | TiCl <sub>4</sub> [9.34-15.6x10 <sup>-5</sup> mol/L], RT.   | O <sub>2</sub> was added into the mixture of TiCl <sub>4</sub> +Ar before feeding into the reaction  |
| [31] | Anatase and Rutile TiO <sub>2</sub> particles, ~ 0.5 $\mu$ m     | Tube furnace, Quartz tube (horizontal)<br>L=143 cm $\theta$ =2.7 cm ( having a quartz rods inside with L=100 cm $\theta$ =0.6 cm) | -                 | Ar / (1.5-3.5 L/min)   | 1100°C                    | 50 min | TiCl <sub>4</sub> (l) [99.5% pure], at 90±1 °C  | O <sub>2</sub> was added into the mixture of TiCl <sub>4</sub> +Ar before feeding into the reaction (O <sub>2</sub> was preheated at 300°C before feeding) |
|      |  |   |                   |                        |                           |        | To prevent condensation of TiCl <sub>4</sub> all of the transport lines of TiCl <sub>4</sub> were maintained at 150°C |  |

TTIP = Titanium Tetraisopropoxide, TBOT = Tetrabutyl Titanate

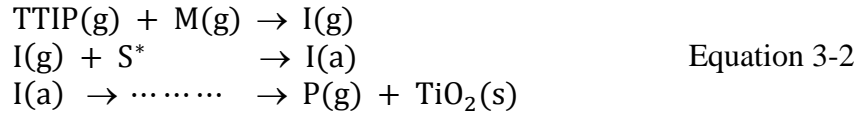
Moreover, the second group of literature shows that TiO<sub>2</sub> nanoparticles can be prepared without a support by using reaction temperatures over a similar range to the first group (involving deposition of TiO<sub>2</sub> on substrates). Using a TiCl<sub>4</sub> precursor, these CVD methods need an additional gas e.g. O<sub>2</sub> to help the precursor complete the reaction. In addition, the phase/s of TiO<sub>2</sub> products depend on the reaction temperature inside the chamber. A temperature higher than 700°C usually promotes the rutile phase of TiO<sub>2</sub> whereas a temperature lower than 600°C leads to the formation of the anatase phase. To access the best parameters for depositing TiO<sub>2</sub> nanocrystalline thin films onto substrates by the CVD method, I can conclude the following:

- The carrier gases are normally N<sub>2</sub> or Ar. Additionally, O<sub>2</sub> gas can be introduced into the reactor to complete the reaction. The gas flow rate is range in 30 mL/min to 3.5 L/min depending on the other parameters and desired final products.
- An alumina/silica tube furnace is mostly used. Moreover, this reactor can be set in either a vertical or horizontal direction.
- The reaction time can be varied from a few minutes to hours.
- A good position for setting a substrate is centred in the alumina/silica tube in the case of horizontal reactor or on a porous quartz disk at the end of the tube in the case of a vertical reactor.
- A low pressure system has been used with chemical vapour deposition to encourage a uniform film thickness. The main reason for using Low Pressure Chemical Vapour Deposition (LPCVD) instead of atmospheric pressure CVD is to control the ratio of the mass transport velocity of active gaseous precursors and their reaction kinetics on the substrate surface [32]–[35]. This process results in better uniformity and homogeneity including smaller particles sizes of deposited thin films. However, the major disadvantages of LPCVD are: (1) the walls of reactor chamber can easily get heavily coated, meaning it requires frequent cleaning; (2) the system involves higher energy usage for the vacuum pumping system; (3) A chemical trapping unit and cooling system are required in the exhaust line before the vacuum pump.
- TTIP is the best titanium precursor due to its low temperature use for the TiO<sub>2</sub> deposition process (300-900°C), as compared to TiCl<sub>4</sub> (more than 1000°C). TTIP is safer and produces no hazardous by-products. The thermal decomposition of TTIP is the main reaction occurring in the deposition chamber.
- The thermal decomposition reaction of TTIP, summarised in Equation 3-1, produces water vapour, gaseous propylene and gaseous TiO<sub>2</sub> [10]. The gaseous

TiO<sub>2</sub> sequentially deposits onto the substrate due to gravity. In the meantime, propylene and water are evacuated with the carrier gas *via* an exhaust line.



The details of the thermal-decomposition reaction of the TTIP precursor for TiO<sub>2</sub> coating process in the CVD system can be described by the following equations [21].



- I(g) is the active intermediate species;
- I(a) is the intermediate species coating on the substrate;
- S\* is the vacant surface on the substrate;
- P is the gas phase by-product;
- M is a collision partner (TTIP and/or carrier gas e.g. N<sub>2</sub>)

The first step of this reaction is the collision between two gas phase molecules: these can be TTIP with TTIP or TTIP with the carrier gas, providing an intermediate species as the product. This active species will continuously interact with the active sites on the surface of substrate, followed by pyrolysis to generate deposited TiO<sub>2</sub> and the gaseous by-products.

### 3.1.2.3 Experimental Procedure on LPCVD method for TiO<sub>2</sub>(B) phase preparation

In order to prepare TiO<sub>2</sub> nanoparticulate thin films, the LPCVD method is one of the best techniques. In this research, the LPCVD system was set up at the School of Chemical and Process Engineering (SCAPE) at the University of Leeds. The components for LPCVD rig are presented in Figure 3-4 with labels for each component. This LPCVD rig can be separated into three main systems: (1) the vapour precursor system; (2) the reactor system; (3) the exhaust system.

The vapour precursor system is composed of a nitrogen gas container, a set of gas valves, a rotameter, a dreschel bottle centrally located into a silicon oil bath. A premeasured amount of titanium precursor e.g. TTIP, is loaded into the heated dreschel bottle of 90°C through an opening using a syringe. Titanium vapour precursors are generated and mixed with the inert gas carrier before being transported into the reaction chamber.

In part of the reactor system, a quartz cylinder tube with a centrally loaded substrate is placed inside the tube furnace. The reactor is connected with the chemical vapour precursor supply system and the exhaust system. The reactor is pre-heated at desired temperature for 10 min before starting the reaction. The furnace temperature is normally varied between 400°C to 700°C. The generated vapour precursors (TTIP + Carrier gas) are carried into the reaction chamber on opening the valve V4. The decomposition/oxidation reactions and deposition processes occur inside the quartz tube for the set reaction time. The non-reacted precursors, by-products, un-deposited materials and heated inert gas is continuously transferred to the cooling system.

The exhaust system is composed of a cooling trap, a chemical trap and a vacuum pump sequentially. All wastes except the N<sub>2</sub> gas carrier, is trapped in the condenser and the cooling glass beads and should not enter to the downstream pipe-work. However, if there are still some remaining chemicals in the exhaust gas, the chemical trap will help to completely capture those chemicals before reaching the vacuum pump.

Before starting the experiment, the LPCVD rig was completely checked in terms of the gas circulation system, the vacuum pressure system, the cooling system and the heating system to ensure all equipment was operating correctly. The LPCVD rig's standard operating procedure was written with the assistance of Mr. Robert Simpson as shown in the Appendix(I). The TiO<sub>2</sub> thin film preparation in this research is described below.

#### 3.1.2.3.1 Chemicals and Materials in LPCVD method for TiO<sub>2</sub> thin film deposition

- Soda-lime glass slide (with wt% composition of 72.00 SiO<sub>2</sub>, 14.50 Na<sub>2</sub>O, 7.05 CaO, 3.95 MgO, 1.65 Al<sub>2</sub>O<sub>3</sub>, 0.30 K<sub>2</sub>O and 0.06 Fe<sub>2</sub>O<sub>3</sub>)
- Fused-quartz (pure amorphous silica of the same dimensions)
- Highly ordered pyrolytic graphite (HOPG)
- Grafoil (pressed, pure natural graphite flake)
- <100> oriented silicon wafer (Sigma Aldrich)
- Lithium Hydroxide, LiOH, > 98% purity, Sigma Aldrich
- Sodium Hydroxide, NaOH, > 97.5% purity, Sciencetific Laboratory supplies
- Sodium Ethoxide, NaOEt, 99.0% purity, Sigma Aldrich
- Potassium Hydroxide, KOH, > 90% purity, Sigma Aldrich
- Titanium Tetraisopropoxide, TTIP, 97% purity, Sigma Aldrich
- Ethanol, EtOH, 99.00%, Sigma Aldrich
- Deionized (DI) water

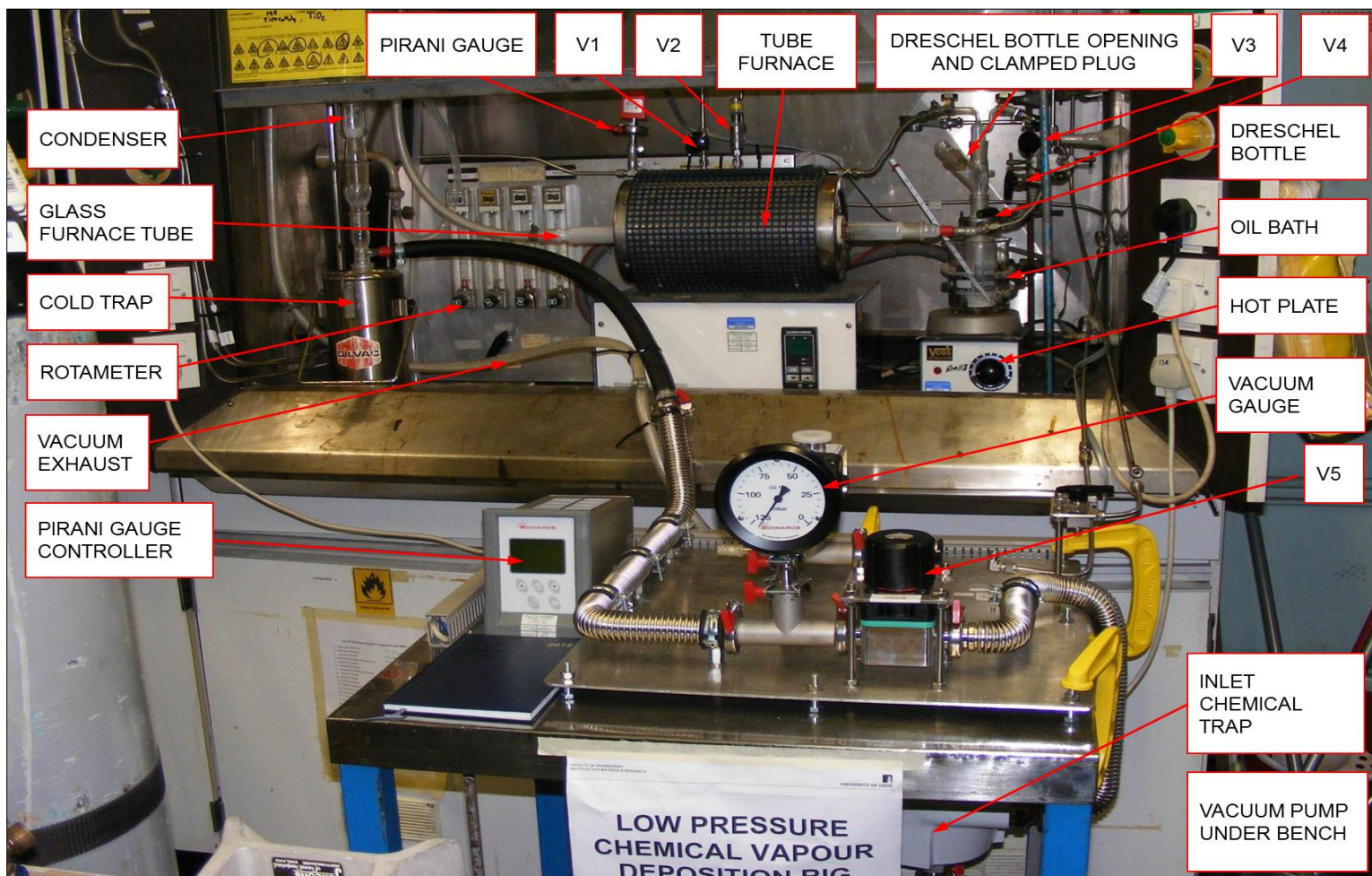


**Figure 3-4** Low Pressure Chemical Vapour Deposition (LPCVD) rig at SCAPE, the University of Leeds

### 3.1.2.3.2 TiO<sub>2</sub> Thin film deposition

Low pressure chemical vapour deposition (i.e. thermal decomposition and oxidation of a precursor) at 25 mbar was used to synthesize TiO<sub>2</sub> thin films on substrates as shown schematically in Figure 3-5(a). Titanium tetra-isopropoxide (TTIP, 97%) was used as the titania precursor, 5 mL being placed in a bubbling chamber which was set in an oil bath at 90°C. The reactor was a quartz cylinder tube placed in a tube furnace and was pre-heated from room temperature up to the desired reaction temperature. N<sub>2</sub> gas with a flow rate of 1 L/min was used to carry the TTIP vapour into the reactor. Titania thin films were deposited onto different substrates of dimensions 11 mm × 11 mm × 1.0 mm (width × length × thickness) including: soda-lime glass slides, fused quartz, Si-wafers, HOPG and grafoil. The reaction temperature in the tube furnace was varied between 450 and 600°C with a reaction time of typically 15 min. However, I note that this is only a nominal temperature as there will exist a temperature gradient inside the reaction tube. This temperature gradient was measured in air as a function of position inside the reaction tube using a moveable thermocouple and the results for a nominal furnace temperature of 600°C are shown in Figure 3-5(b).

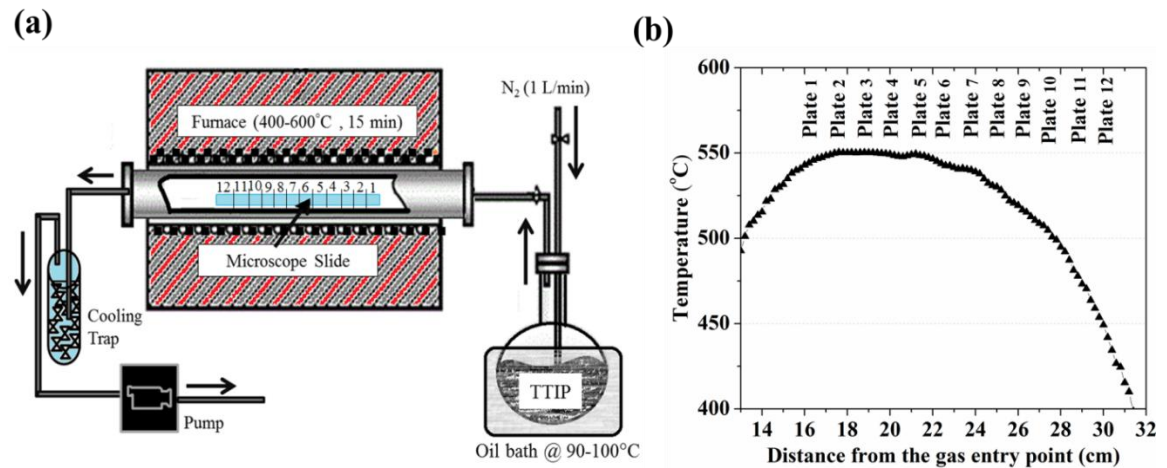


**Figure 3-5** (a) Schematic representation showing the LPCVD system for preparing TiO<sub>2</sub> (b) temperature profile in the tube furnace for a nominal reaction temperature of 600°C

### 3.1.2.3.3 Pre-treatment of the substrate

Pre-treatment of a substrate prior to TiO<sub>2</sub> thin film deposition is a modification of the general LPCVD method. The pre-treatment process involved thin film deposition of an alkali metal solution onto the substrates as schematically illustrated in Figure 3-6.

The substrates used were: fused quartz, silicon wafer, HOPG and grafoil. These were cut into dimensions of 11 mm × 11 mm × 1.0 mm (width × length × thickness).

The substrates were initially cleaned by sonication in ethanol and then pre-treated by spraying onto the surface 0.5 mL of an alkali ion-containing solution, i.e. sodium ethoxide (NaOEt) dissolved in Ethanol (99.00%) in varying concentrations between 0.1-5.0 %<sup>W</sup>/<sub>V</sub> of Na. Following investigation, the distance between the substrate surface and the spray nozzle (Adjustable sprayer tube length 813 mm; Fisher Scientific Ltd) was fixed at 15 cm and after spraying, the Na-coated substrates were slowly dried in air at 50°C for 12 hr.

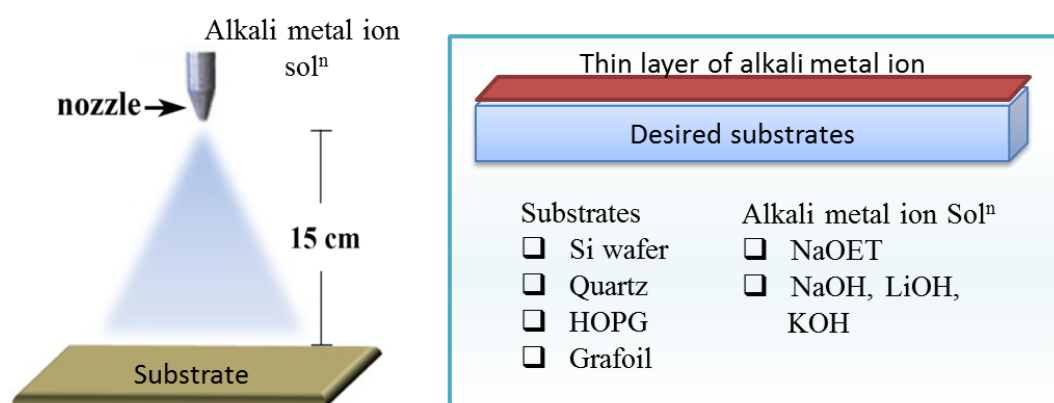


**Figure 3-6** Schematic of pre-treatment process by spraying alkali metal solution onto a Si-wafer substrate

## 3.2 Characterisation methods

### 3.2.1 Powder X-Ray Diffraction (PXRD) [36]

X-ray diffraction has been used to determine the phase composition of the crystalline TiO<sub>2</sub> thin films deposited by LPCVD and the crystalline TiO<sub>2</sub> nanoparticles synthesised by the hydrothermal method in this research.

#### 3.2.1.1 XRD methodology

Crystals are formed of unit cells, which is the repeatable unit containing the smallest number of atoms able to form the 3-dimensional structure. The lattice parameter is employed to define the dimensions of the unit cell. Measurement of the inter-planar distances ( $d_{hkl}$ ) can be used to determine the lattice parameter by using Bragg's law. The set of  $d_{hkl}$  data can be used to characteristically identify an individual crystal structure.

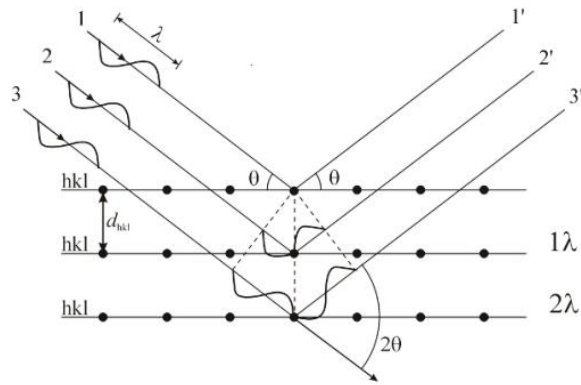


**Figure 3-7** X-ray diffraction from parallel planes of atoms in a crystalline material

Bragg's law is based on the path difference between (X-ray) waves scattered by two neighbouring lattice planes. For strong constructive interference and hence diffraction to occur, the following equation.

$$\text{Bragg's law: } n\lambda = 2 d_{hkl} \sin\theta \quad \text{Equation 3-3}$$

Where:  $n$  is the diffraction index;  
 $\lambda$  is the wavelength of the X-ray source ( $\text{\AA}$ );  
 $d_{hkl}$  is the inter-planar spacing corresponding to the  $hkl$  Miller indices;  
 $\theta$  is the scattering angle between the incident and diffracted beams

Besides determination of the lattice parameter, X-ray diffraction also can provide an estimate of the crystallite size *via* Scherrer's equation by using the line broadening at half-maximum intensity of a XRD peak.

$$\text{Scherrer's equation: } \tau = \frac{K\lambda}{\beta \cos\theta} \quad \text{Equation 3-4}$$

Where:  $\tau$  is the estimated crystallite size;  
 $K$  is the dimensionless shape factor;  
 $\lambda$  is the wavelength of the X-ray source ( $\text{\AA}$ );  
 $\beta$  is the full width at half maximum height of a Bragg XRD peak;  
 $\theta$  is the scattering angle in radians.

The calculated crystallite size may be smaller or equal to the particle size depending on physical morphology of the sample. Scherrer's equation is appropriate for a range of nanoparticles, however, it usually provides an big error in measurement when the crystallite size is larger than 200 nm.

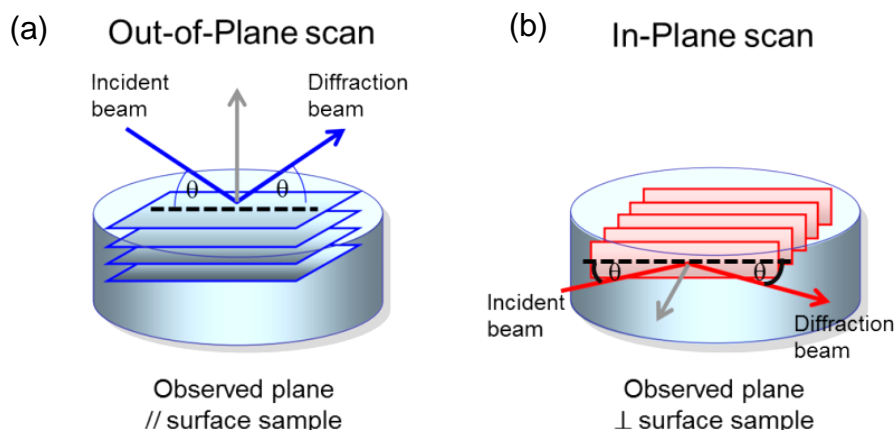


**Figure 3-8** The orientation of observed crystal plane depend on scanning mode: (a) Out-of-Plane scanning; (b) In-Plane scanning.

In general, it is usual to set the scanning of the X-ray incident beam and/or detector parallel to the specimen stage/surface as shown in Figure 3-8(a). X-ray diffraction of crystalline materials normally shows all of the crystal planes (XRD peaks), if the samples are randomly oriented polycrystals. The intensities of each crystal plane should occur in the same relative proportion as in the XRD powder diffraction database (ICDD PDF4+2014). However, if the crystals are not randomly oriented (i.e. there is a preferred orientation), the diffracted intensity from each crystal plane will not be uniform. In some cases, if a crystal plane is not properly aligned to generate a diffracted beam, it might be absent in a XRD pattern. This problem usually occurs for the case of thin film crystalline materials on substrates, i.e. TiO<sub>2</sub> thin films on a glass substrate as shown in Figure 3-9 (a). The absence of peaks in the out of plane XRD pattern can be understood with reference to Figure 3-10. In-Plane scanning mode has been used to complete the XRD diffraction data as shown in Figure 3-9 (b); here the specimen surface is oriented perpendicular to the plane of the incident beam during scanning as shown in Figure 3-8 (b).

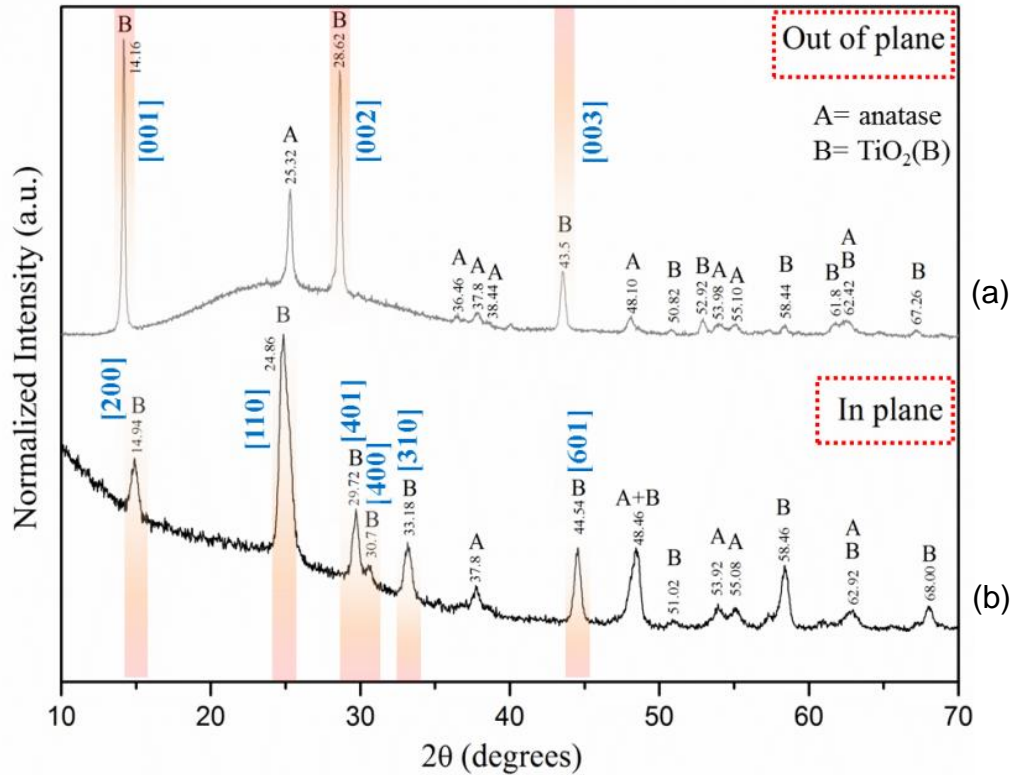


**Figure 3-9** The In-plane and Out-of-plane XRD patterns of mixed phase TiO<sub>2</sub>(B) and anatase thin films on soda-lime glass substrate with a preferred [001] orientation of TiO<sub>2</sub>(B) parallel to the substrate.

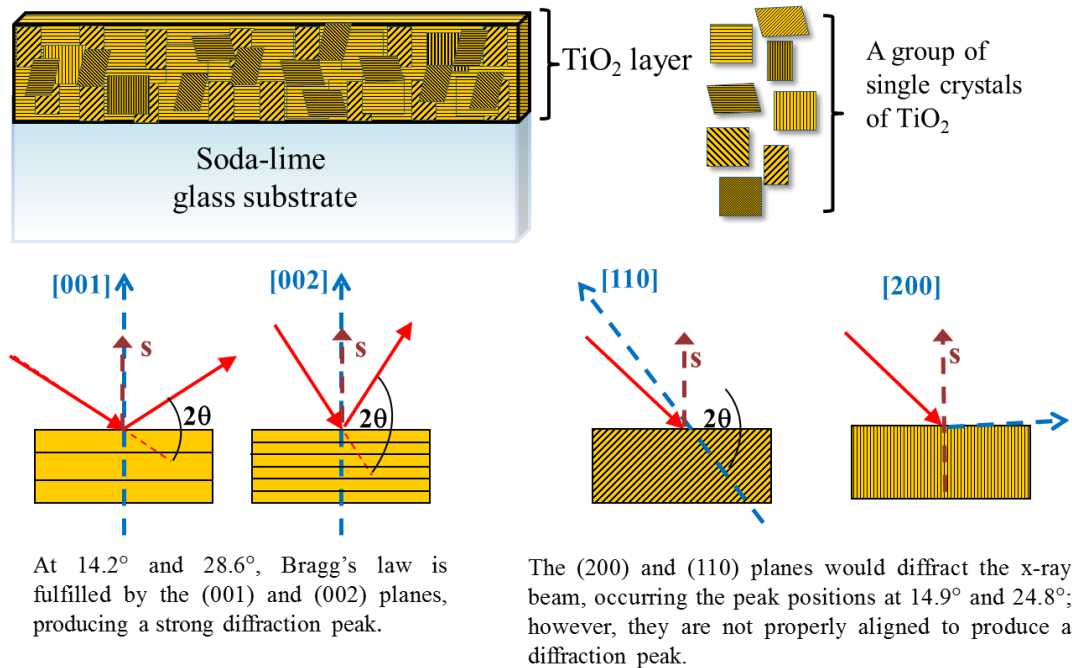


**Figure 3-10** Schematic showing the internal polygrains and/or polycrystals of TiO<sub>2</sub> thinfilms deposited on a glass substrate with their X-ray diffraction of lattice planes in individual single crystals. It shows the absence of peaks when planes are not properly aligned to produce diffraction peaks such as (110), (200) as illustrated in Figure 3-9.

### 3.2.1.2 XRD experimental details

#### 3.2.1.2.1 XRD instrumentation

XRD patterns of all thin films samples prepared by LPCVD were characterized by a P'Analytical X'pert MPD diffractometer working in the  $2\theta$  scanning mode of Bragg geometry as shown in Figure 3-11(a). The spinner PW3064 was employed to rotate the sample whilst correcting XRD data. The diffraction patterns of fine powder samples synthesised by the hydrothermal method were recorded using a Bruker D8 X-ray diffractometer (XRD) as shown in Figure 3-11(b). Both diffractometers employ a Cu  $K\alpha$  tube with  $\lambda = 1.545 \text{ \AA}$  as the X-ray source, and are located in SCAPE at the University of Leeds.

During the investigation of the  $\text{TiO}_2$  thin films on substrates, the effect of the crystalline substrate can overwhelm the thin film pattern, making it difficult to observe the  $\text{TiO}_2$  thin film sample. Therefore, the thin film sample was tilted to an angle of 2 degrees with respect to a normal  $2\theta$  scan during X-ray scanning, so as to reduce the strength of the single hkl substrate reflection which would otherwise dominate the pattern.



**Figure 3-11** The XRD machines operated in this research: (a) Bruker D8 X-ray diffractometer and (b) Philips Analytical X'pert MPD diffractometer

#### 3.2.1.2.2 Preparation of XRD samples

There are two physical forms of the synthesised samples in this research: TiO<sub>2</sub> thin films on substrates and fine solid powders. In case of TiO<sub>2</sub> thin films on substrates, 3 mm diameter plasticine was centrally placed on the back of a square centimetre sample slide and then stuck onto the sample holder. It is very important to make sure that the surface of sample slide and the edge of sample holder are in the same plane. The sample holder was mounted onto the spinner stage with insertion of a 10 mm slit to collimate the radiation. The measurement was undertaken using X-pert Data Collection software. In contrast TiO<sub>2</sub> fine powder samples were ground before loading a small amount of powder onto a silicon wafer sample holder. The sample was gently pressed to get a smooth and flat surface. The X-ray data was collected by the Bruker D8 machine with XRD commander software. All XRD-data was interpreted using X-pert high score plus software with the updated 2014 powder diffraction data base (ICDD PDF4+2014).

### 3.2.2 Electron Microscopy [37]

One of the benefits of using high energy electrons to analyse materials is the production of a wide range of secondary signals from the interaction of the electron with the material. These secondary signals are summarized in Figure 3-12. The direction of each signal indicates where the signal should be strongest and where it should be detected. The quality of the signals is directly dependent on the quality of the incident beam so the electron source should be critical.

#### 3.2.2.1 Scanning Electron Microscopy (SEM)

SEM is one of the best techniques to investigate the 3D morphology of a sample. The best resolution of a SEM image can be in the range of a few nanometers however, it depends on many physical and chemical factors such as the intensity of the incident beam, the electron accelerating voltage, the type of sample and also the SEM lenses.

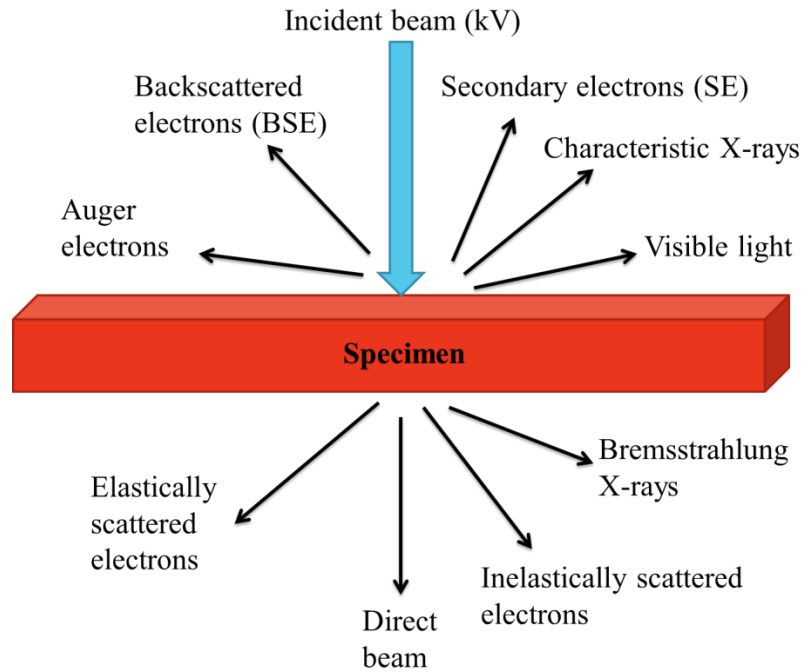


**Figure 3-12** Secondary signals generated by high-energy electrons interaction with the specimen materials

#### 3.2.2.1.1 SEM methodology

The general SEM process starts by accelerating electrons produced under vacuum from a filament by applying a high voltage. The accelerated electrons are focused to a very small beam with a very high intensity by using electromagnetic lenses. The focused accelerated electrons are scanned across the specimen surface, generating different types of secondary signals.

The main imaging signals in a SEM are backscattered and secondary electrons, these can provide the information on average atomic number and surface topology respectively. Moreover, during the interaction between the accelerated electron and the specimen, characteristic X-rays are also produced, providing information on elemental composition of the sample. A SEM system is diagrammatically shown in Figure 3-13.

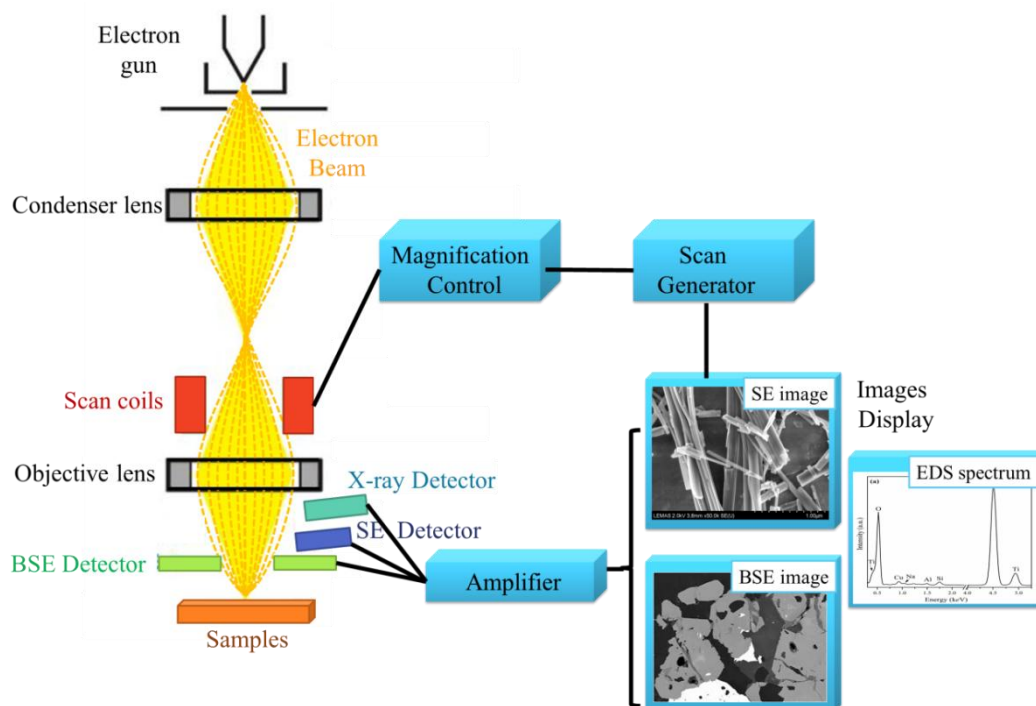


**Figure 3-13** Schematic representation of the basic operation of a scanning electron microscope

For non-conductive materials, coating with a very thin conductive film e.g. carbon, gold and platinum is necessary to get the best SEM performance. In this work, nanoparticles of  $\text{TiO}_2$  are poorly conducting so require sputter coating by Carbon or Platinum (5 nm thickness) to prevent charging on the specimen when irradiated with an electron beam.

### 3.2.2.1.2 The SEM machines

In the present work, the morphologies of all the  $\text{TiO}_2$  thin films supported on soda-lime glass substrate and  $\text{TiO}_2$  nanotubes were studied by using a LEO 1530 “Gemini” (Carl Zeiss, Cambridge) field emission gun scanning electron microscope (FEG-SEM). Secondary electron images were produced at an operating voltage of 5 kV, these were collected by an in-lens detector. In the case of  $\text{TiO}_2$  thin film samples deposited on other substrates e.g. Si-wafer, Fused quartz, HOPG and Grafoil, these were examined using a Hitachi SU8230 Cold-FESEM with an operating voltage of 2 kV. Both SEMs were fitted with energy dispersive X-ray (EDX) detectors (80mm X-Max SDD detector), Oxford Instruments and AZtecEnergy EDX software and were located at SCAPE, Faculty of Engineering, University of Leeds

### 3.2.2.1.3 Preparation of SEM samples

Three type of sample were investigated by SEM: 1.)  $\text{TiO}_2$  thin films on substrates in plan view; 2.) cross-sectional samples of  $\text{TiO}_2$  thin films on substrates; and 3.) fine powders of  $\text{TiO}_2$  nanotubes/nanowires. Both thin film samples were stuck onto Al

stubs with an adhesive carbon paste. The nanoparticulate TiO<sub>2</sub> was dispersed in isopropanol, stirred and sonicated for 10 minutes. Then, the suspension was drop casted onto the Al stubs. All of the samples were dried in a vacuum desiccator at least 1 day before SEM investigation.

### 3.2.2.2 Transmission Electron Microscopy (TEM) [37]

The concept of TEM is quite similar to a general transmission light microscope with electromagnetic lenses instead of optical lenses. Accelerated electrons generated from an electron gun travel within the microscope column with a specific energy which is dependent on the applied accelerating voltage. The resolution of the TEM is directly related to the accelerating voltage as described by the following equation: for example, an accelerating voltage of 200 keV can provide the electron wavelength of 0.0251 Å which is smaller than a diameter of the smallest atom.

$$\lambda = \frac{h}{\sqrt{2m_0 eV}} \quad \text{Equation 3-5}$$

Where:  $\lambda$  is the wavelength of accelerated electrons (Å);  
 $V$  is the accelerating voltage of electron microscope (V);  
 $m$  is the electron mass;  
 $e$  is the electron charge (- 1.602x10<sup>-19</sup> C).

TEM techniques commonly involve the forward scattered secondary signals from a thin sample. The TEM is usually operated in one of two fundamental modes: imaging mode or diffraction mode as illustrated in Figure 3-14. In each TEM mode, an intermediate lens selects either the intermediate image 1 of the objective lens or the diffraction pattern in the back focal plane.

#### 3.2.2.2.1 Electron Diffraction Mode

When electron waves are transmitted across the periodic arrangement of crystal planes of the specimen, elastic scattering of the electron wave is generated at various different angles according to Bragg's Law forming an electron diffraction pattern in the back focal plane. The diffracting area is defined by inserting a selected area (SA) aperture in the plane of the first intermediate image formed (Figure 3-14 (b)). Spot diffraction patterns are generated when the sample is a single crystal material, whereas rings diffraction patterns are produced from polycrystalline materials. The SA electron diffraction pattern can also provide crystallographic information such as the crystallographic lattice spacing, the crystal growth direction and the exact crystalline phase.

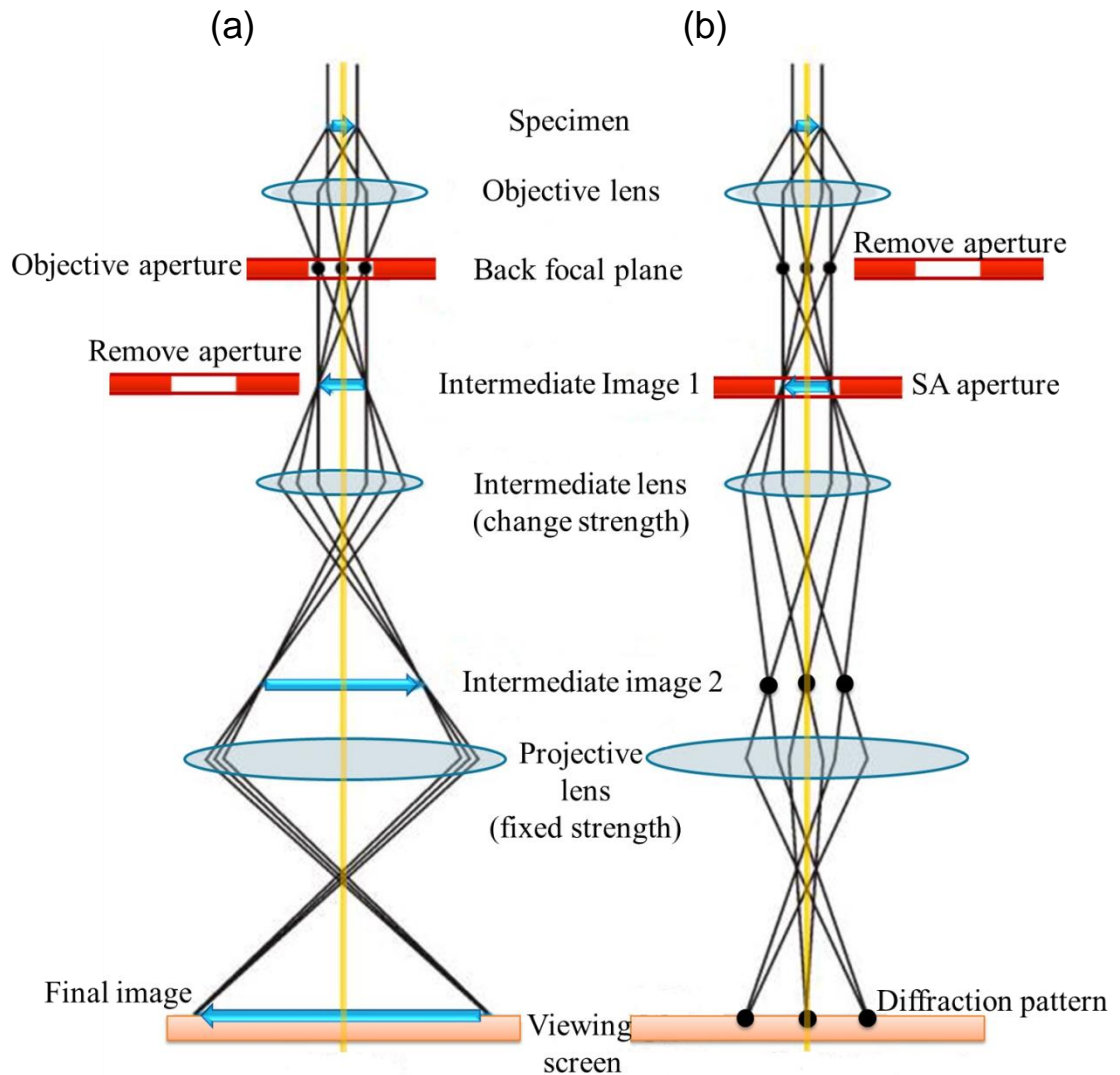


**Figure 3-14** Two ray diagrams showing two main operating modes of the TEM: (a) The imaging mode and (b) the diffraction mode.

#### 3.2.2.2.2 Imaging mode

There are two kinds of image contrast which contribute to TEM images: amplitude contrast and phase contrast. Amplitude contrast is a combination of mass-thickness contrast and diffraction contrast which affects the scattered electron amplitude and hence intensity. Phase contrast arises from the change in phase of the electron wave as it is transmitted through a sample. It is difficult to interpret this contrast mechanism due to its high sensitivity to many factors such as the focus and astigmatism of the objective lens, the orientation or scattering factor and even the small changes in thickness of the sample. All of these factors can be exploited to produce atomic resolution TEM images arising from the interference between different diffracted beams and the unscattered beam.

Diffraction contrast is employed to form two types of images: Bright Field (BF) and Dark Field (DF) images. The objective aperture is inserted in the back focal plane

to allow only unscattered beams to pass through the TEM column constructing a BF image on the screen (Figure 3-14(a)). In case of a DF image, the inserted aperture permits only specific diffracted beams to pass and also blocks the unscattered beam at the same time. BF and DF images show a reversal of contrast and generally, DF images are of interest when studying defects or special structures within a specimen.

High Resolution TEM (HRTEM) images are very useful for studying the lattice images at atomic resolution of crystalline samples. Generally no objective aperture is used and both the scattered and unscattered electron waves are used to form HRTEM images. Examples of BF, DF and phase contrast TEM images are shown in Figure 3-15.

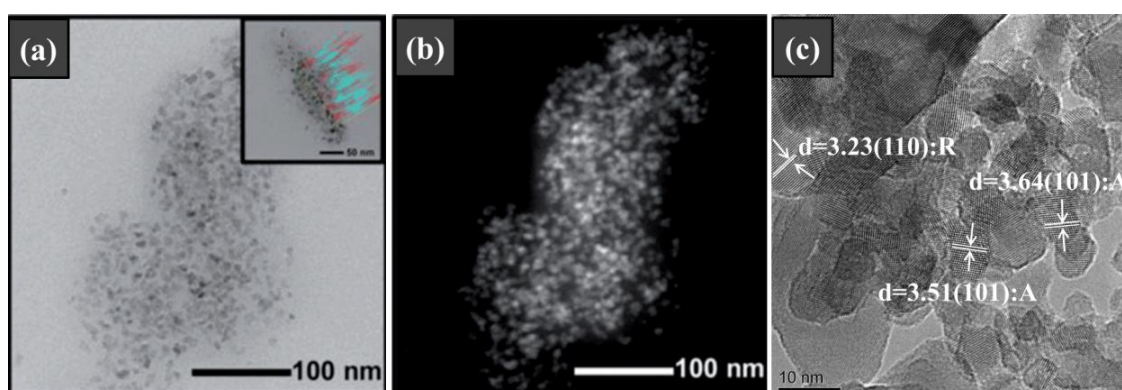


**Figure 3-15** Example TEM images of: (a) BF image of  $\text{TiO}_2$  nanoparticles ;(b) DF image of  $\text{TiO}_2$  nanoparticles at the same area as Figure 3-15(a) and ;(c) HRTEM of nanoparticles mixed phase anatase and Rutile  $\text{TiO}_2$  [59]

#### 3.2.2.2.3 TEM specimen preparation

In this work, the fine powder samples prepared by the hydrothermal method were prepared as TEM specimens by adding a few milligrams of  $\text{TiO}_2$  powder into 2 mL of isopropanol, stirring and then sonicating for 3 minutes. The suspension was dropped casted onto a holey carbon film supported on a 400 mesh Cu TEM grid. The specimen was dried under a warm light and stored in a vacuum desiccator.

TEM specimen preparation of initial  $\text{TiO}_2$  thin film samples on substrates was achieved by using a scalpel to scrape off deposited material from the substrate onto a holey carbon film supported on a Cu TEM grid. In addition, a Focused Ion Beam (FIB–FEI Nova 200) was used to prepare directly thin cross-sections of the materials on the substrates.

#### 3.2.2.2.4 TEM instrumentation

TEM analysis using imaging, selected area electron diffraction (SAED), and high resolution TEM imaging was performed in SCAPE, University of Leeds using a FEI

Tecnai G2 TEM/STEM operated at 200 kV. This machine has an EDX detector and Scanning system for EDX mapping and quantification (Oxford Instruments AZTEC). Images were recorded and processed using Digital Micrograph software.

### 3.2.3 Energy Dispersive X-ray Spectroscopy (EDX)

Inelastic electron interactions with the specimen involve an energy transfer between the incident electron and the target atom. This energy may cause ejection of an electron from the inner shell of a target atom, if this energy transfer is adequate. To maintain the equilibrium in the atomic structure after an inner shell electron has been ejected, an outer shell electron will transfer to the hole (created) with the release of energy in terms of X-ray emission as seen in Figure 3-16. The X-ray energy is characteristic of the elemental atom in the target sample. The released X-ray energy can be employed to investigate both qualitative (characteristic peak positions) and quantitative (relative peak area) analysis of the materials as illustrated in Figure 3-17. Practically, the EDX detector is connected with a SEM or TEM to identify the types and amount of the elements in a specific region of a sample.

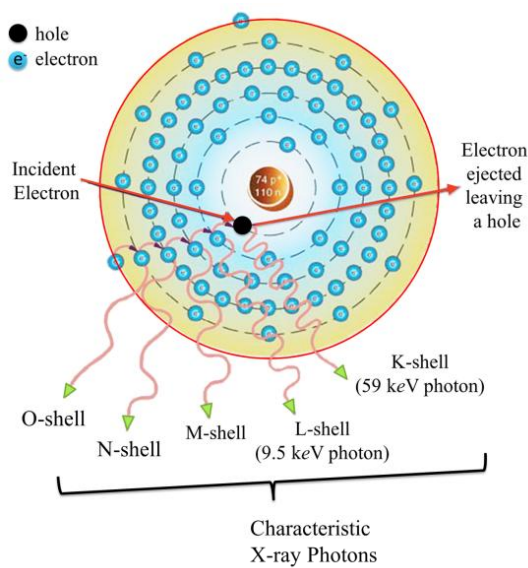


**Figure 3-16** The possible electron transitions in the electron energy levels of Tungsten atom showing the characteristic X-ray energy after an electron releases its energy to replace a hole at lower energy level.

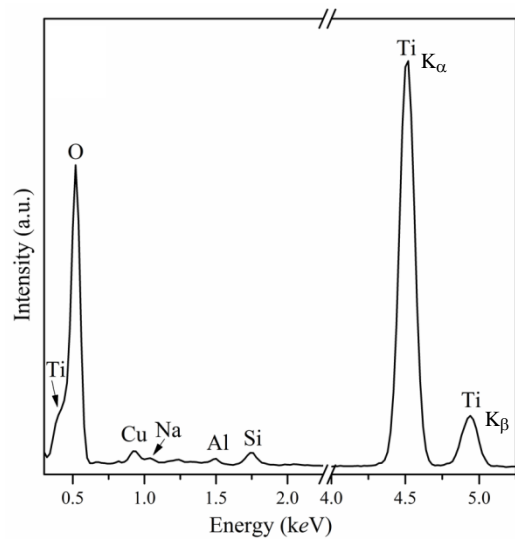


**Figure 3-17** TEM-EDX spectrum of a group of TiO<sub>2</sub>(B) needle particles on the holey carbon film supported on a Cu TEM grid showing the characteristic peak position of each of the elements in the sample and their peak areas which can be used to calculate the weight% and also atomic% of each element in the whole mixture.

### 3.2.4 Raman Spectroscopy

The principle of Raman spectroscopy is to investigate different modes of excitation, including characteristic vibrational and rotational excitations of the chemical bonds in materials. The sample is illuminated by a monochromatic laser, providing scattering and absorption of photons which can absorb or release energy either in the near-IR, Visible or UV region of the electromagnetic spectrum. This produces inelastic sidebands on a very intense elastically scattered peak. The laser beam focuses on the sample *via* the lens system of an optical microscope. The scattering signals return to the microscope through the same ray path. At the end of the ray path, the filtered signals are measured by a highly sensitive detector and transformed to a Raman spectrum as illustrated in Figure 3-18 (a). In this work, all Raman results were collected at room temperature and conducted on a Renishaw inVia Raman microscope machine with a green Ar/Kr ion laser of wavelength 514 nm and laser power of 25 mWatt. The machine is composed of a Raman spectrometer connected to a modified optical microscope of  $\sim 1 \mu\text{m}$  resolution and a CCD detector as shown in Figure 3-18 (b).

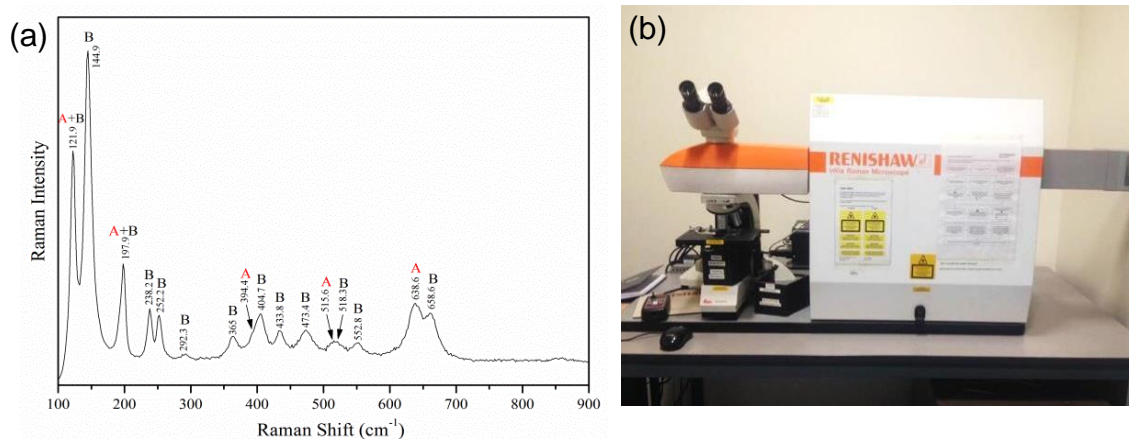


**Figure 3-18** (a) Raman spectrum of mixed phase TiO<sub>2</sub>(B) and anatase thin films on soda-lime glass substrate showing characteristic patterns of anatase and TiO<sub>2</sub>(B) [38]; A and B refer to anatase and TiO<sub>2</sub>(B) and (b) The Renishaw's inVia Raman microscope machine proceeding at SCAPE, Faculty of Engineering, University of Leeds.

### 3.2.5 UV-Visible Diffuse Reflectance Spectroscopy

One of the most useful measurements in relation to solar energy harvesting is UV-Vis spectroscopy. Here the material is a thin film coating of an opaque semiconductor materials and reflection mode geometry is appropriate because light cannot pass through the sample. There are two types of reflection modes: specular and diffuse which have been applied to investigate the band gap of semiconductor materials as shown in Figure 3-19 (a). Diffuse reflection is generally generated by a rough surface

as is the case for the materials in this research. In this case, an incident beam (from a light source) illuminates the thin film sample at one specific angle, generating a range of reflection angles. The diffuse reflection is measured by a 150 mm diameter integrating sphere with internal detectors.

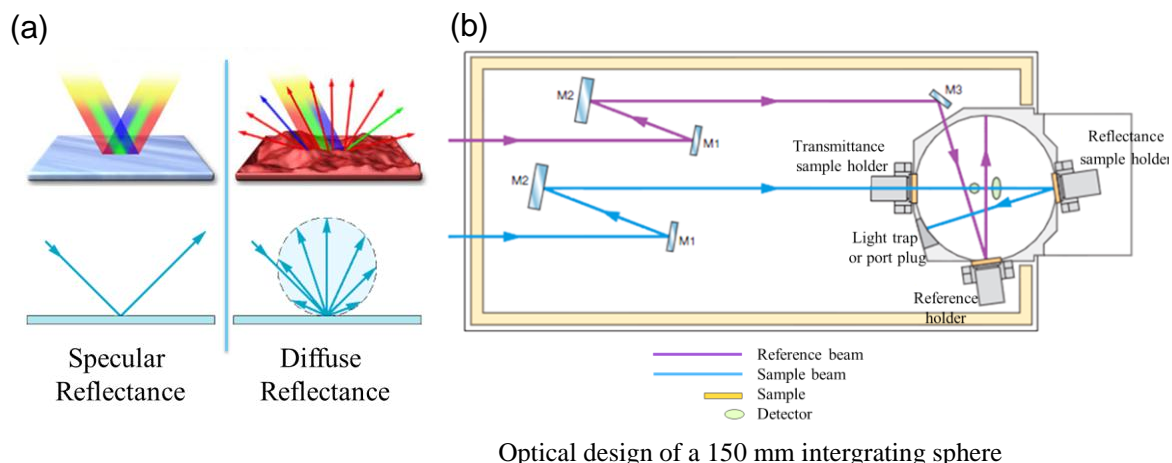


**Figure 3-19** (a) two types of reflections, a smooth surface usually provides specular reflection whereas a rough surface prefers to generate diffuse reflection (b) basic optical layout for a double beam 150 mm integrating sphere of Perkin Elmer UV-Vis Lambda 900

UV-Vis diffuse reflectance spectroscopy (Perkin Elmer UV-vis Lambda 900) was used to characterise the thin film materials in this work, and was undertaken at SCAPE, Faculty of Engineering, University of Leeds. The raw spectra were directly generated by the Perkin Elmer UV-Vis Win Lab software. However, the band gap energies of the samples can be investigated by Kubelka-Munk transformation of the raw spectra [39], [40] and the band gaps were calculated by extrapolating the linear portion of data.

### 3.3 Reference

- [1] A. Bittner, R. Jahn, and P. Löbmann, "TiO<sub>2</sub> thin films on soda-lime and borosilicate glass prepared by sol-gel processing: influence of the substrates," *J. Sol-Gel Sci. Technol.*, vol. 58, no. 2, pp. 400–406, 2011.
- [2] P. Löbl, M. Huppertz, and D. Mergel, "Nucleation and growth in TiO<sub>2</sub> films prepared by sputtering and evaporation," *Thin Solid Films*, vol. 251, pp. 72–79, 1994.
- [3] J.D. Kwon, J.J. Rha, K.S. Nam, and J.S. Park, "Photocatalytic functional coating of TiO<sub>2</sub> thin film deposited by cyclic plasma chemical vapor deposition at atmospheric pressure," *Jpn. J. Appl. Phys.*, vol. 50, no. 8, pp. 085502, 2011.

- [4] J.M. Blocher, "Chemical vapor deposition for surface conditioning: Opportunities and cautions," *Mater. Sci. Eng. A*, vol. 105–106, pp. 435–441, 1988.
- [5] P.S. Shinde and C.H. Bhosale, "Properties of chemical vapour deposited nanocrystalline TiO<sub>2</sub> thin films and their use in dye-sensitized solar cells," *J. Anal. Appl. Pyrolysis*, vol. 82, pp. 83–88, 2008.
- [6] H. Lee, M.Y. Song, J. Jurng, and Y.K. Park, "The synthesis and coating process of TiO<sub>2</sub> nanoparticles using CVD process," *Powder Technol.*, vol. 214, no. 1, pp. 64–68, 2011.
- [7] G.A Battiston, R. Gerbasi, M. Porchia, and L. Rizzo, "TiO<sub>2</sub> coating by atmospheric pressure MOCVD in a conveyor belt furnace for industrial applications," *Chem. Vap. Depos.*, vol. 5, pp. 73, 1999.
- [8] Z. Ding, X. Hu, G.Q. Lu, P. Yue, and P.F. Greenfield, "Novel silica gel supported TiO<sub>2</sub> photocatalyst synthesized by CVD method," *Langmuir*, vol. 16, pp. 6216–6222, 2000.
- [9] K.L. Choy, "Vapor processing of nanostructured materials," in *Handbook of Nanostructured Materials and Nanotechnology*, H.S. Nalwa, Ed. Burlington: Academic Press, 2000, pp. 533–577.
- [10] K. Okuyama, Y. Kousak, N. Tohge, S. Yamamoto, J.J. Wu, "Production of ultrafine metal oxide aerosol by thermal deposition of metal alkoxide vapors," *AIChE J.*, vol. 32, no. 12, pp. 2010–2019, 1986.
- [11] M.K. Akhtar, S. Vemury, and S.E. Pratsinis, "Corn petition between TiCl<sub>4</sub> hydrolysis and oxidation and its effect on product TiO<sub>2</sub> powder," *Mater. Interfaces Electrochem. Phenom.*, vol. 40, no. 7, pp. 1183–1192, 1994.
- [12] M.K. Akhtar, Y. Xiong, and S.E. Pratsinis, "Vapor synthesis of titania powder by titanium tetrachloride oxidation," *AIChE J.*, vol. 37, no. 10, pp. 1561–1570, 1991.
- [13] H.D Jang and J. Jeong, "The effects of temperature on particle size in the gas-phase production of TiO<sub>2</sub>," *Aerosol Sci. Technol.*, vol. 23, no.4, pp. 553–560, 1995.
- [14] R.S. Windeler, S.K. Friedlander, and K.E.J. Lehtinen, "Production of nanometer-sized metal oxide particles by gas phase reaction in a free jet. I: experimental system and results," *Aerosol Sci. Technol.*, vol. 27, no. 2, pp. 174–190, 1997.
- [15] A.K. John and G.D. Surender, "Low temperature process for the synthesis of rutile phase titania through vapor phase hydrolysis," *J. Mater. Sci.*, vol. 40, pp. 2999–3001, 2005.
- [16] C.S. Kim, K. Nakaso, B. Xia, K. Okuyama, and M. Shimada, "A new observation on the phase transformation of TiO<sub>2</sub> nanoparticles produced by a CVD method," *Aerosol Sci. Technol.*, vol. 39, no. 2, pp. 104–112, 2005.

- [17] K.Y. Park, M. Ullmann, Y.J. Suh, and S.K. Friedlander, "Nanoparticle microreactor: Application to synthesis of titania by thermal decomposition of titanium tetraisopropoxide," *J. Nanoparticle Res.*, vol. 3, pp. 309–319, 2001.
- [18] F. Kirkbir and H. Komiyama, "Formation and Growth Mechanism of Porous, Amorphous, and Fine Particles Prepared by Chemical Vapor Deposition: Titania from Titanium Tetraisopropoxide," *Can. J. Chem. Eng.*, vol. 65, 1987.
- [19] H. Komiyama, T. Kanai, and H. Inoue, "Preparation of porous, amorphous, and ultrafine TiO<sub>2</sub> particles by chemical vapor deposition," *Chem. Lett.*, vol. 13, no. 8, pp. 1283–1286, 1984.
- [20] T. Yazawa, F. Machida, N. Kubo, and T. Jin, "Photocatalytic activity of transparent porous glass supported TiO<sub>2</sub>," *Ceram. Int.*, vol. 35, no. 8, pp. 3321–3325, 2009.
- [21] Z. ding, X. Hu, P.L. Yue, G.Q. Lu, and P.F. Greenfield, "Synthesis of anatase TiO<sub>2</sub> supported on porous solids by chemical vapor deposition," *Catal. today*, vol. 68, pp. 173–182, 2001.
- [22] X. Zhang, M. Zhou, and L. Lei, "Preparation of photocatalytic TiO<sub>2</sub> coatings of nanosized particles on activated carbon by AP-MOCVD," *Carbon*, vol. 43, no. 8, pp. 1700–1708, 2005.
- [23] H.Y. Ha, S.W. Nam, T.H. Lim, I. Oh, and S. Hong, "Properties of the TiO<sub>2</sub> membranes prepared by CVD of titanium tetraisopropoxide," *J. Memb. Sci.*, vol. 111, pp. 81–92, 1996.
- [24] S. Chin, E. Park, M. Kim, and J. Jurng, "Photocatalytic degradation of methylene blue with TiO<sub>2</sub> nanoparticles prepared by a thermal decomposition process," *Powder Technol.*, vol. 201, no. 2, pp. 171–176, 2010.
- [25] S. Chin, E. Park, M. Kim, J. Jeong, G.N. Bae, and J. Jurng, "Preparation of TiO<sub>2</sub> ultrafine nanopowder with large surface area and its photocatalytic activity for gaseous nitrogen oxides," *Powder Technol.*, vol. 206, no. 3, pp. 306–311, 2011.
- [26] Y.S. Kim, L.T. Linh, E.S. Park, S. Chin, G.N. Bae, and J. Jurng, "Antibacterial performance of TiO<sub>2</sub> ultrafine nanopowder synthesized by a chemical vapor condensation method: Effect of synthesis temperature and precursor vapor concentration," *Powder Technol.*, vol. 215–216, pp. 195–199, 2012.
- [27] K. Nakaso, K. Okuyama, M. Shimada, and S.E. Pratsinis, "Effect of reaction temperature on CVD-made TiO<sub>2</sub> primary particle diameter," *Chem. Eng. Sci.*, vol. 58, no. 15, pp. 3327–3335, 2003.
- [28] K. Okuyama, J.T. Jeung Y. Kousaka, "Experimental control of ultrafine TiO<sub>2</sub> particle generation from thermal decomposition of titanium tetraisopropoxide vapor," *Chem. Eng. Sci.*, vol. 44, no. 6, pp. 1369–1375, 1989.
- [29] P. Moravec, J. Smolik, and V.V. Levdansky, "Synthesis of titania particles by vapour-phase decomposition of titanium tetraisopropoxide," *J. Aerosol Sci.*, vol. 31, pp. s927–s928, 2000.

- [30] W. Li, S.I Shaa, C.P. Huang, O. jung, and C. Ni, "Metallorganic chemical vapor deposition and characterization of TiO<sub>2</sub> nannoparticles," *Mater. Sci. Eng. B*, vol. 96, pp. 247–253, 2002.
- [31] E. Zhou, Z. Yuan, Z. Wang, X.G. Fang, and J.Z. Gong, "Mechanism of scaling on oxidation reactor wall in TiO<sub>2</sub> synthesis by chloride process," *Trans. Nonferrous Met. Soc. China*, vol. 16, pp. 426–431, 2006.
- [32] S.C. Jung, S.J. Kim, N. Imaishi, and Y.I. Cho, "Effect of TiO<sub>2</sub> thin film thickness and specific surface area by low-pressure metal–organic chemical vapor deposition on photocatalytic activities," *Appl. Catal. B Environ.*, vol. 55, pp. 253–257, 2005.
- [33] A.J. Cross, C.W. Dunnill, and I.P. Parkin, "Production of predominantly anatase thin films on various grades of steel and other metallic substrates from TiCl<sub>4</sub> and ethyl acetate by atmospheric pressure CVD," *Chem. Vap. Depos.*, vol. 18, no. 4–6, pp. 133–139, 2012.
- [34] S.A. O'Neill, R.J.H. Clark, I.P. Parkin, N. Elliott, and A. Mills, "Anatase thin films on glass from the chemical vapor deposition of Titanium(IV) Chloride and Ethyl Acetate," *Chem. Mater.*, vol. 15, no. 1, pp. 46–50, 2003.
- [35] V.K. Singh, "Effect of surface re-emission on the surface roughness of film growth in low pressure chemical vapor deposition," *J. Vac. Sci. Technol. A Vacuum, Surfaces, Film.*, vol. 11, no. 1993, pp. 557, 1993.
- [36] C. Hammond, *The basics of crystallography and diffraction*. New York: Oxford University Press, Inc, 2009
- [37] D.B. Williams and C.B. Carter, *Transmission electron microscopy*. New York and London: Plenum press, 1996.
- [38] B. Thomas, R.P. Mireille and B. Luc, *Accurate methods for quantifying the relative ratio of anatase and TiO<sub>2</sub>(B) nanoparticles*. *J. Phys. Chem. C*, vol. 113, No 31, pp.13703, 2009.
- [39] A.E. Morales, E.S. Mora, and U. Pal, "Use of diffuse reflectance spectroscopy for optical characterization of un-supported nanostructures," *Resvista Mex. Física s*, vol. 53, no. 5, pp. 18–22, 2007.
- [40] D. Yang, H. Liu, Z. Zheng, Y. Yuan, J. Zhao, E.R. Waclawik, X. Ke, and H. Zhu, "An efficient photocatalyst structure: TiO<sub>2</sub>(B) nanofibers with a shell of anatase nanocrystals," *J. Am. Chem. Soc.*, vol. 131, no. 49, pp. 17885–17893, 2009.

## **Chapter 4 Hydrothermal Synthesis of TiO<sub>2</sub>(B) Nanorods *via* Alkali Metal Titanate Phase Transformation**

Prior to using CVD, in order to clearly understand the effect of alkali metal cation on TiO<sub>2</sub>(B) phase formation, a general TiO<sub>2</sub>(B) preparation method involving Na<sup>+</sup> has been studied and is presented in this chapter. An alkali hydrothermal synthesis method combined with a post ion-exchange process and calcination has been used to synthesise the TiO<sub>2</sub>(B) phase. A mechanism for TiO<sub>2</sub>(B) phase formation is proposed in this chapter and the effect of different types of titanium precursors on the phase formation and physical morphology were investigated. Finally, the stability of TiO<sub>2</sub>(B) phase and the effect of calcination temperature was also analysed.

### **4.1 Experimental Procedure**

#### **4.1.1 Hydrothermal synthesis method**

The hydrothermal method was used to prepare an intermediate sodium titanate product using the preparation procedure described in chapter 3. The primary hydrothermal products after washing with DI water to remove the excess NaOH, were designated as P<sub>1</sub>, T<sub>1</sub>, R<sub>1</sub> and A<sub>1</sub> corresponding to the type of Ti precursor: P25, TTIP, rutile and anatase respectively. After washing the hydrothermal products with DI water until the pH of the suspension was approximately 7, a proton-exchange process was conducted with 0.1M HNO<sub>3</sub> solution. The suspensions were dried at 80°C and were named as P<sub>2</sub>, T<sub>2</sub>, R<sub>2</sub> and A<sub>2</sub> representing an intermediate phase of hydrogen titanate. The secondary intermediate products were calcined at 400°C for 5 hr with a heating rate of 5°C. The nomenclatures of final products were X@Y, where X and Y were type of Ti precursors and calcination temperature respectively.

#### **4.1.2 Materials Characterization**

X-ray diffraction (XRD), undertaken using the Bruker D8 diffractometer, was used to investigate the samples. In-situ hot-stage XRD was also employed to study the phase transformation of the sample; using a Philips X-pert MPD diffractometer. Raman spectra were collected in the range of 3200-100 cm<sup>-1</sup> to investigate the phases present in the sample. The Hitachi Cold-FESEM with EDX was operated with platinum coated samples to study the morphology and elemental composition of the samples. Finally, TEM was used to investigate the phase formation, growth direction and particle morphology. All specimen preparation for all characterization techniques has been described in chapter 3.

## 4.2 Results

### 4.2.1 X-ray Diffraction

The primary intermediate products from all titanium precursors after hydrothermal treatment were fine white powders. A<sub>1</sub> is used as a representative to characterise phase formation by XRD. The XRD pattern of Sodium Titanium Oxide Hydroxide Hydrate (NaTi<sub>3</sub>O<sub>6</sub>(OH)(H<sub>2</sub>O)<sub>2</sub>) with a monoclinic structure (JCPDS 04-018-2801) matches well with the XRD pattern from the A<sub>1</sub> sample as shown in Figure 4-1. In this work, the NaTi<sub>3</sub>O<sub>6</sub>(OH)(H<sub>2</sub>O)<sub>2</sub> phase occurs instead of NaTi<sub>6</sub>O<sub>13</sub> which is a typical hydrothermal product in the literature [1]–[3], this might suggest that the removal process of excess NaOH by washing with Di water was not complete in that the sample was not dry enough, retaining hydroxide ions and water molecules inside the crystal structure. However, this compound is easily changed to NaTi<sub>6</sub>O<sub>13</sub> when the water molecules are removed out of its structure by heating as shown in the following equation.

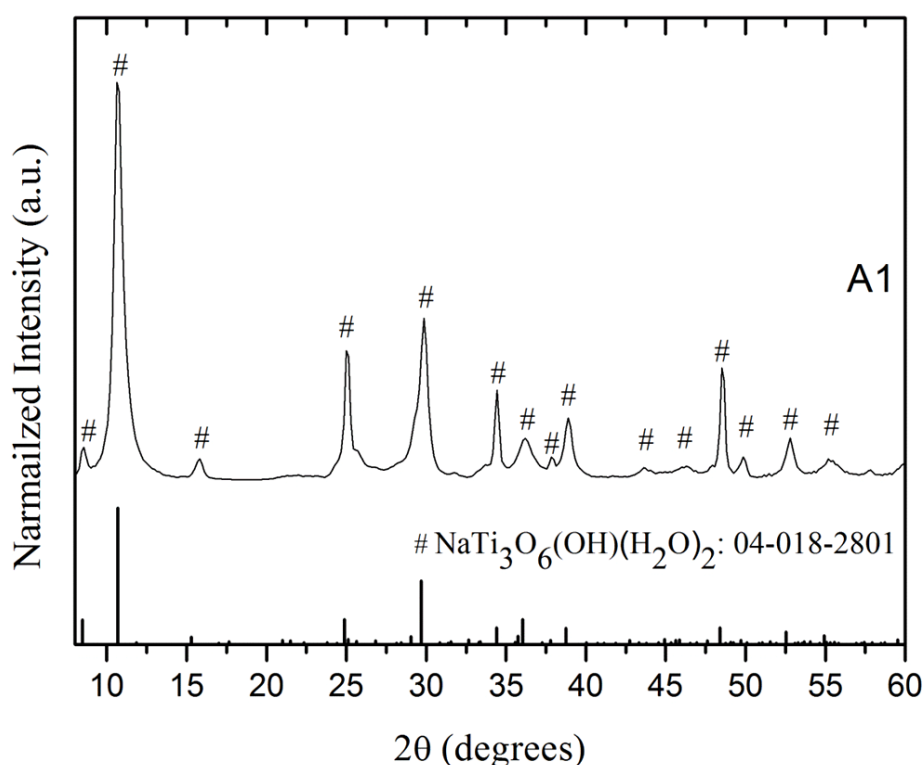
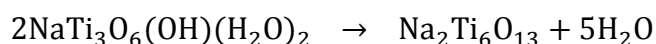


**Figure 4-1** XRD pattern of A1; the first intermediate product from the hydrothermal procedure.

The three other hydrothermal samples from rutile ( $R_1$ ), P25 ( $P_1$ ) and TTIP ( $T_1$ ) precursors also exhibited hydroxide contamination. However there was evidence for a complete ion exchange process between  $Na^+$  and  $H^+$  during the acid soaking & washing as confirmed by the XRD pattern shown in Figure 4-2.

All of the second intermediate samples,  $A_2$ ,  $R_2$ ,  $T_2$  and  $P_2$ , exhibit the same trend in their diffraction patterns. The XRD patterns do not match well with only one reference pattern but seem to match with two candidates:  $H_2Ti_3O_6$  (JCPDS: 00-041-4192) and  $H_2Ti_3O_7$  (JCPDS:00-036-0656), both of which show a similar layered structure of the monoclinic system. The absence of sodium titanate peaks suggests that all of the  $Na^+$  ions which act as counterions between the titania layers were substituted by  $H^+$  and the remaining  $OH^-$  were also removed during this process.

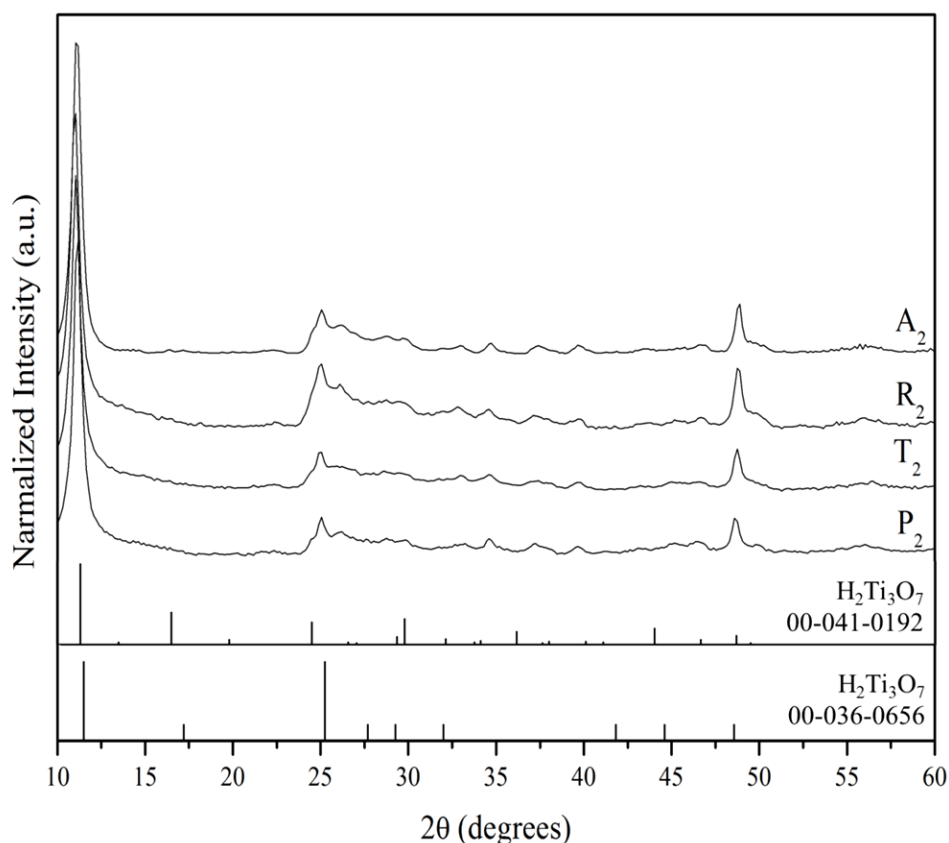


**Figure 4-2** XRD patterns of  $A_2$ ,  $R_2$ ,  $T_2$  and  $P_2$ ; the second intermediate products after the ion-exchange process.

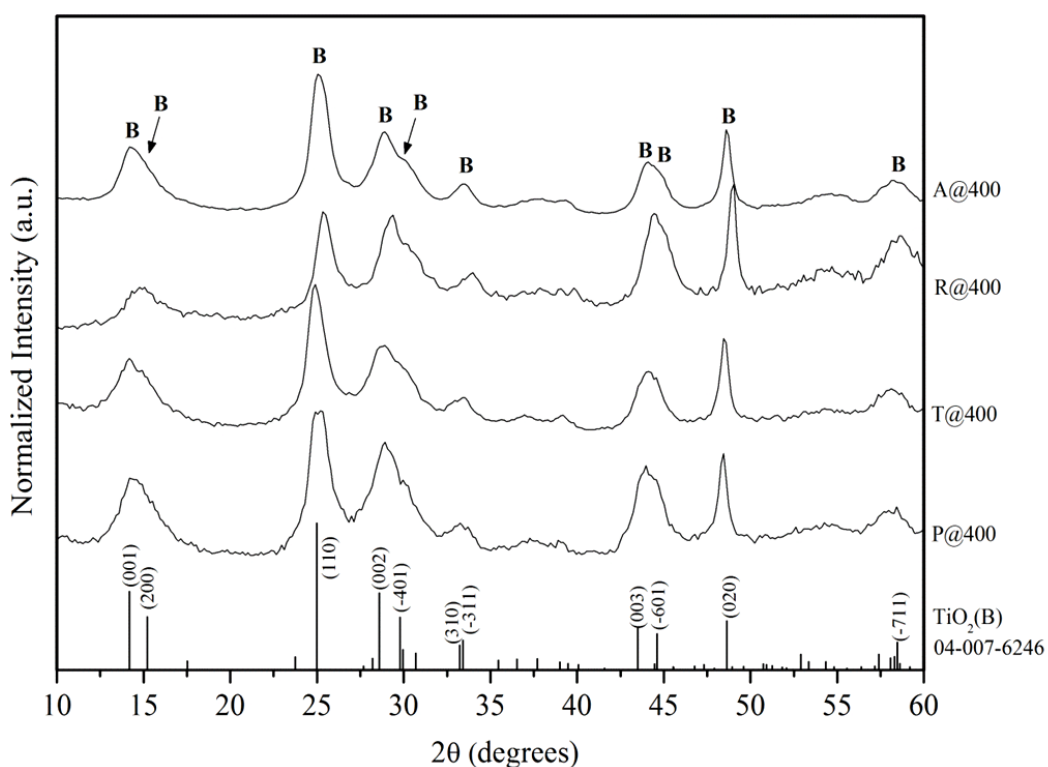


**Figure 4-3** XRD patterns of A@400, R@400, T@400 and P@400; the final products after calcination of the second intermediate phase at 400°C for 5 hr.

**Table 4-1** List of synthesised samples with results of SEM/EDX quantitative elemental analysis, XRD crystallite size and primary particle size derived from SEM

| Sample | Composition in Atom% from SEM/EDX |       |       | Calculated crystallite size by Scherrer's equation (nm) | Measured primary particle size (nm) from SEM images (widths) |
|--------|-----------------------------------|-------|-------|---|--|
|        | Na                                | O     | Ti    | TiO <sub>2</sub> (B)                                    |  |
| P@400  | 0.00                              | 74.52 | 25.48 | 6.4±0.6   | 128.4±1.2<br>(S.D=46.7)                                      |
| T@400  | 0.00                              | 79.99 | 20.01 | 4.3±0.3   | 130.8±1.2<br>(S.D=78.9)                                      |
| R@400  | 0.00                              | 86.40 | 13.60 | 5.6±0.5   | 112.9±1.2<br>(S.D=52.6)                                      |
| A@400  | 0.00                              | 75.38 | 24.62 | 4.3±0.3   | 112.8±1.2<br>(S.D=45.1)                                      |

Figure 4-3 presents the XRD patterns of the final products after the second intermediate products of each of the Ti precursors were calcined at 400°C for 5 hr. All can be indexed to the monoclinic structure of TiO<sub>2</sub>(B) (JCPDS: 04-007-6246). This shows the phase transformation from H<sub>2</sub>Ti<sub>3</sub>O<sub>7</sub> to TiO<sub>2</sub>(B) using thermal energy. The broad peaks of the XRD pattern reflect the nano-crystalline nature of the samples and the crystallite sizes of the TiO<sub>2</sub>(B) phase were calculated by Scherrer's equation and the FWHM of the (110) peak at around 2θ= 24.9°. The crystallite sizes of P@400, T@400, R@400 and A@400 are in a similar range of 4-7 nm as presented in Table 4-1. The XRD pattern of final products also suggest a preferred crystallographic orientation of the TiO<sub>2</sub>(B) morphology as the (020) XRD peak is a sharp peak at around 2θ=48° whereas the other peaks are all broad. Thus suggests [020] oriented nanorods.

The influence of calcination temperature on phase formation was studied using in-situ hot-stage XRD analysis in the temperature range 300°C to 800°C. The second intermediate sample (A<sub>2</sub>) was placed on the hot-stage sample holder and data first collected at 25°C. Then the sample was heated with a heating rate, a heating step and a holding time of 5°C.min<sup>-1</sup>, 25°C/step and 30 min/step respectively. All of the XRD patterns at each holding temperature were characterized with the same parameters. The phase transformation of H<sub>2</sub>Ti<sub>3</sub>O<sub>7</sub> is shown in Figure 4-4. The H<sub>2</sub>Ti<sub>3</sub>O<sub>7</sub> structure transforms to TiO<sub>2</sub>(B) as the temperature reaches 300°C with an increase in TiO<sub>2</sub>(B) crystallinity with increasing temperature. However at 400°C, some small intense peaks of anatase are observed indicating that the TiO<sub>2</sub>(B) crystal structure transformations to anatase at temperatures higher than 400°C. The relative proportion of anatase in the mixed phase sample gradually increases with increasing temperature in the range 400-675°C. The TiO<sub>2</sub>(B)-anatase phase transformation is complete at 700°C, leaving only the anatase phase at temperatures ≥700°C.

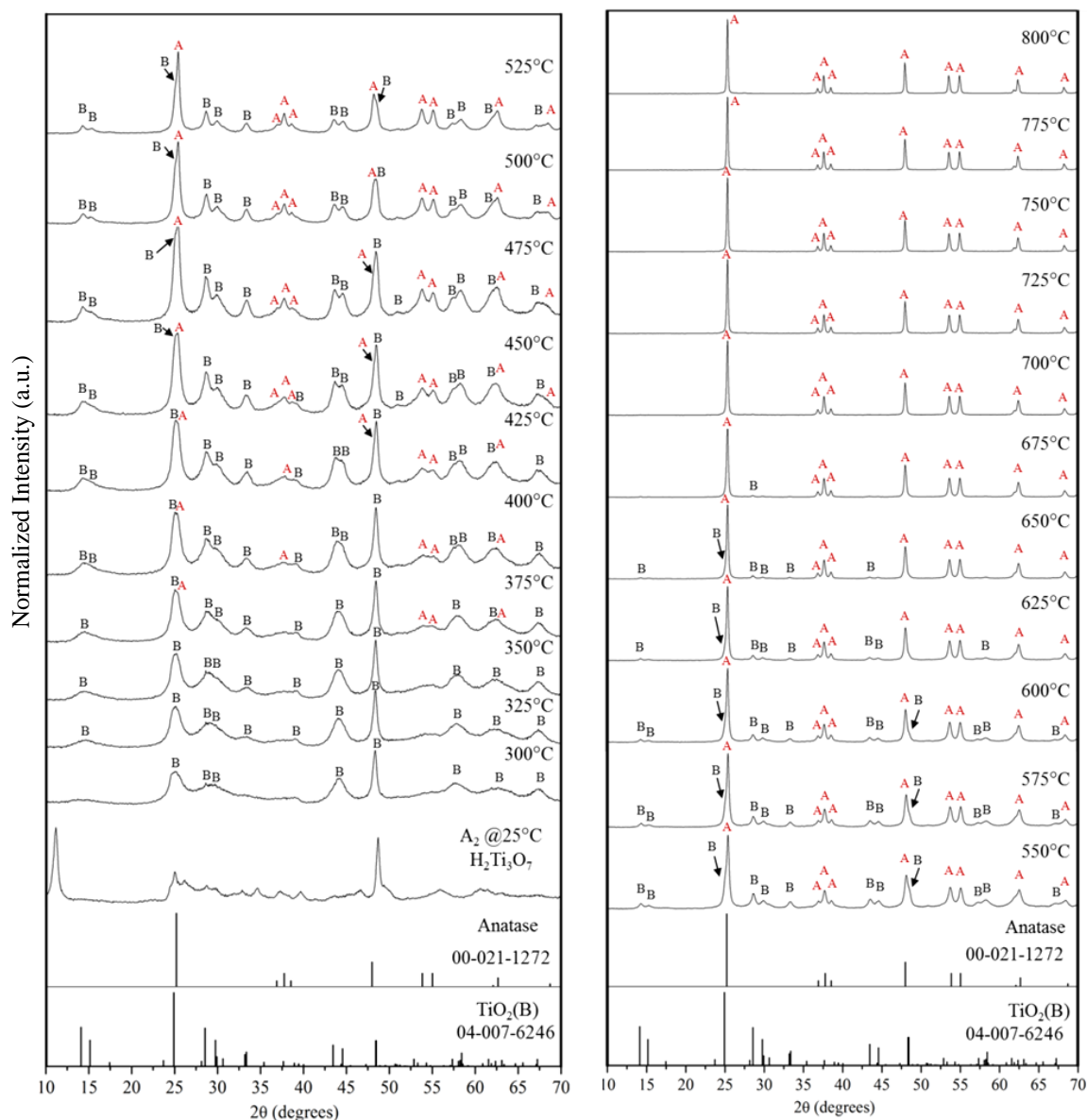


**Figure 4-4** In-situ hot-stage XRD characterization of A<sub>2</sub>, heating rate: 5 °C min<sup>-1</sup>

## 4.2.2 Raman Spectroscopy

Owing to the broad XRD peaks arising from the nanoscale crystallites, the main peaks of TiO<sub>2</sub>(B) phase and anatase can overlap especially at 2θ around 25° and 48°. Therefore, the final products were also characterized by Raman spectroscopy to complement the XRD results as shown in Figure 4-5. A@400 and P@400 are representative of the final product after calcination at 400°C, and exhibit Raman active modes at 122, 145, 196, 236, 249, 293, 366, 406, 432, 469, 510, 551, 635 and 656 cm<sup>-1</sup>. This implies the presence of pure phase TiO<sub>2</sub>(B) without any evidence of anatase peaks which normally occur at 143, 396, 517 and 637 cm<sup>-1</sup> with 6 times higher intensity than for TiO<sub>2</sub>(B). This supports the results from XRD that all of the final products are pure TiO<sub>2</sub>(B) phase at this temperature.

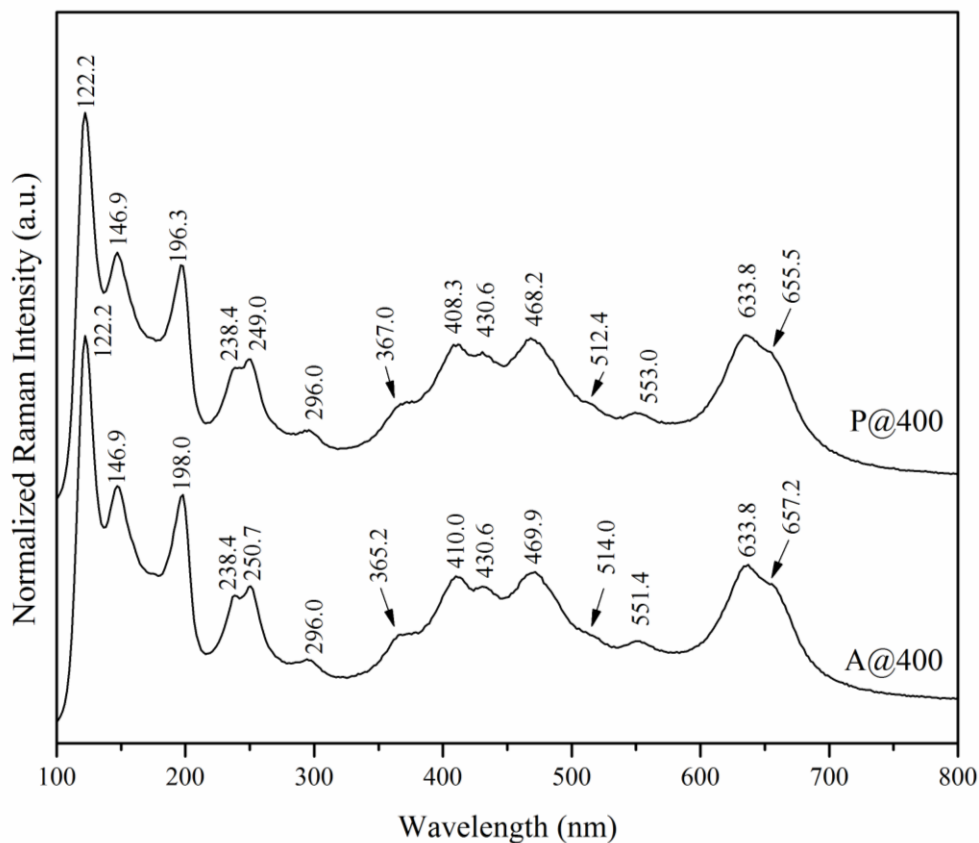


**Figure 4-5** Raman spectra of A@400 and P@400

### 4.2.3 Scanning electron microscopy (SEM)

SEM analysis was used to study the physical morphology of the final products. In the SEM specimen preparation process, the samples were deposited on an Al stub and coated with Pt thin layer. The SEM images of P@400, T@400, R@400 and A@400 samples are shown in Figure 4-6. Generally, one-dimensional particle morphologies such as tube, rod and wire are the main physical forms of the TiO<sub>2</sub> products after hydrothermal synthesis using a high concentration of alkali metal hydroxide solution as previously summarized in Table 3-1 in chapter 3.

In this research, P@400, R@400 and A@400 mostly appear as discrete nanorods, whereas the particle morphology of T@400 shows an elongation of nanorods as illustrated in Figure 4-6. Average particle sizes were manually measured from the SEM images and displayed in Table 4-1. The average particle sizes (widths) in P@400, T@400, R@400 and A@400 are 128.4±47, 130.9±44, 112.9±41 and 112.8±52 nm respectively. The average particle widths and lengths of the four samples are in the same range but T@400 shows an obvious difference in length from the others (in that it is longer than 1 μm whereas the other lengths are in range of nanoscale). A possible reason for this is the different state of matter of the titanium precursor. T@400 used TTIP in the liquid state whereas the other three are solid

precursors (P25, anatase and rutile). The liquid phase may promote increased growth due to increased availability.

The chemical composition of the  $\text{TiO}_2(\text{B})$  samples were investigated by SEM/EDX analysis and the results are also presented in Table 4-1. EDX results suggest the presence of Titanium and Oxygen and the absence of Na, indicating that all of the intermediate samples were completely transformed to a final product of  $\text{TiO}_2$ . The lower atomic ratios than the theoretical ratio of  $\text{TiO}_2$  ( $\text{Ti}/\text{O}=0.5$ ) may result from an interference of oxygen signals from the SEM stub (Al) which will be oxidised.

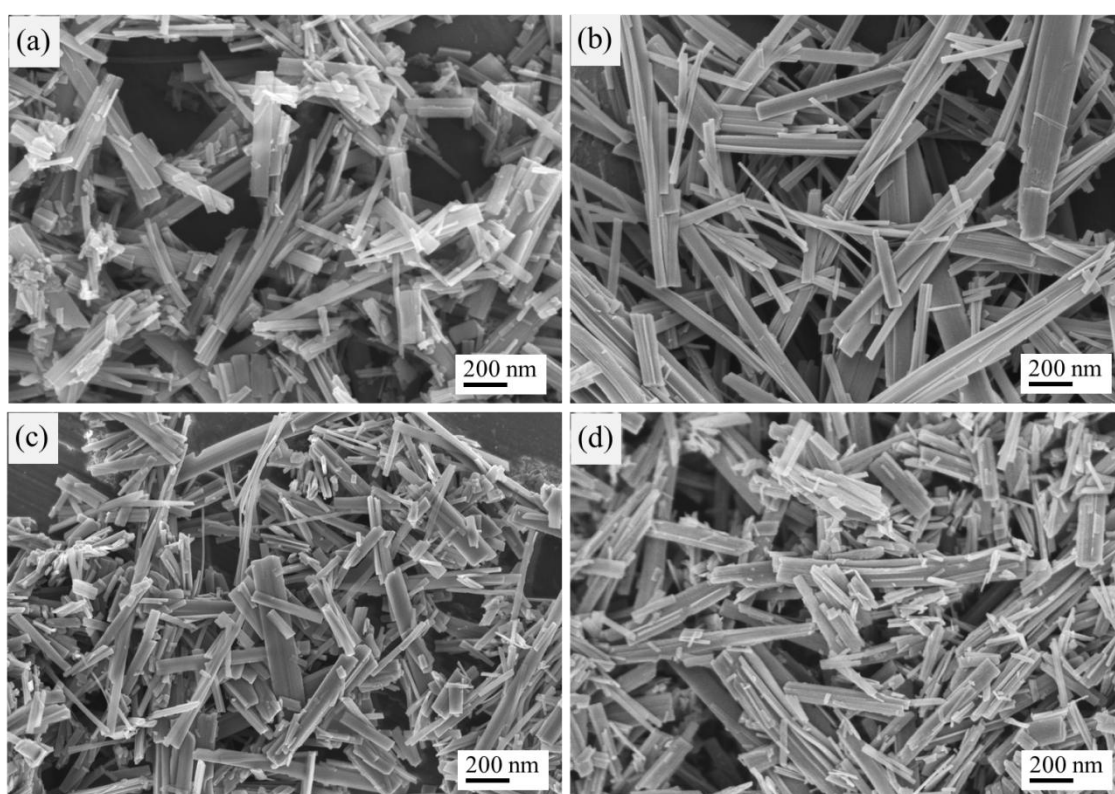


**Figure 4-6** SEM secondary electron images of  $\text{TiO}_2(\text{B})$  final products from the four different Ti precursors: (a) P25, P@400 (b) TTIP, T@400 (c) Rutile, R@400 and (d) Anatase, A@400.

#### 4.2.4 Transmission electron microscopy (TEM)

The  $\text{TiO}_2(\text{B})$  1D structure (nanorods) was indicated by the evidence of preferred orientation in XRD patterns and also SEM images. The particle morphology, the phase formation and the growth direction of  $\text{TiO}_2(\text{B})$  structures in samples P@400, T@400, R@400 and A@400 were also evident in HRTEM images and electron diffraction patterns shown in Figure 4-7, Figure 4-8, Figure 4-9 and Figure 4-10 respectively.

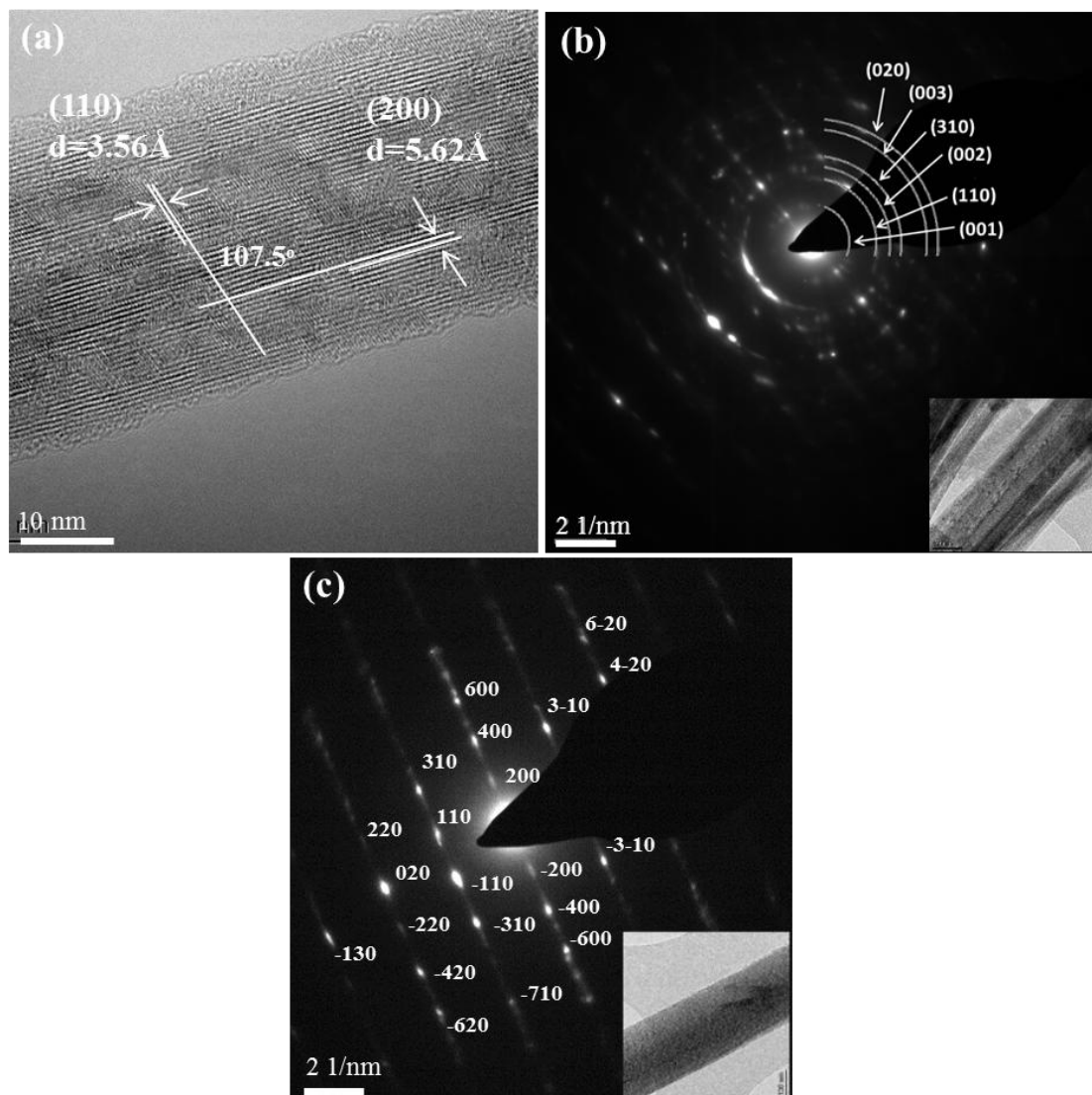


**Figure 4-7** (a) A HRTEM image taken from P@400 (b) a ring diffraction pattern taken from a group of particles shown in the image inset, (c) a spot diffraction pattern of a single particle shown in the image inset.

HRTEM images from all samples clearly revealed the lattice spacings in single crystal nanorods of 5.6 and 3.5 Å corresponding to the (200) and (110) spacings of the TiO<sub>2</sub>(B) phase respectively. An interplanar angle between both lattice spacings is in the range of 107.5-109.5° being in agreement with the theoretical value of 107.8°. Moreover, all TEM selected area diffraction patterns from groups of particles shown inset in the figures as (b), illustrated a set of rings spacings characteristic of TiO<sub>2</sub>(B) corresponding to the (001), (110), (002), (310), (003) and (020) lattice spacings. Spot diffraction patterns taken from nanorods indicated a growth direction along [020] in all samples in agreement with the preferred [020] orientation evident in XRD patterns.

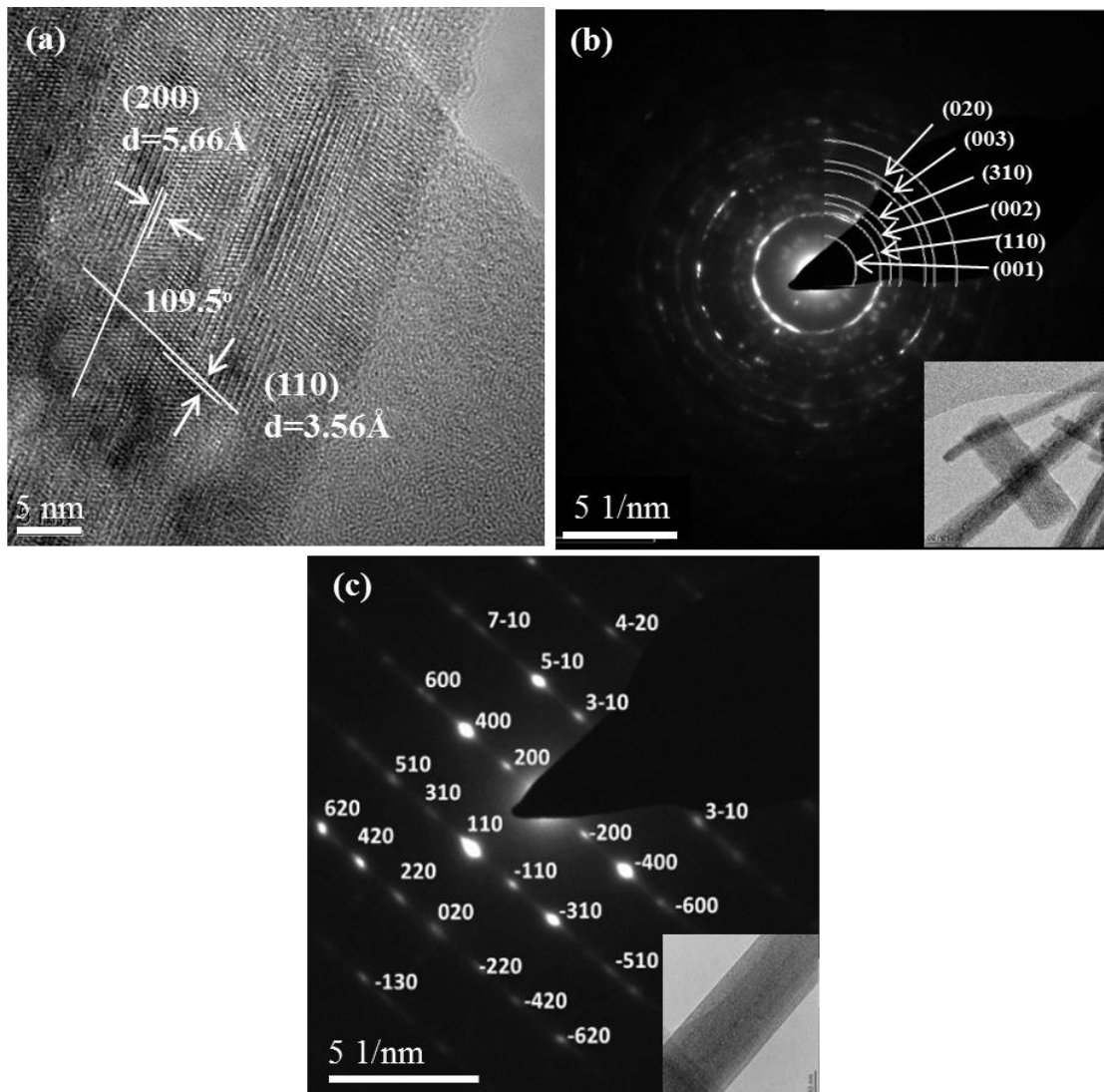


**Figure 4-8** (a) A HRTEM image taken from T@400 (b) a ring diffraction pattern taken from a group of particles shown in the image inset, (c) a spot diffraction pattern of a single particle shown in the image inset.

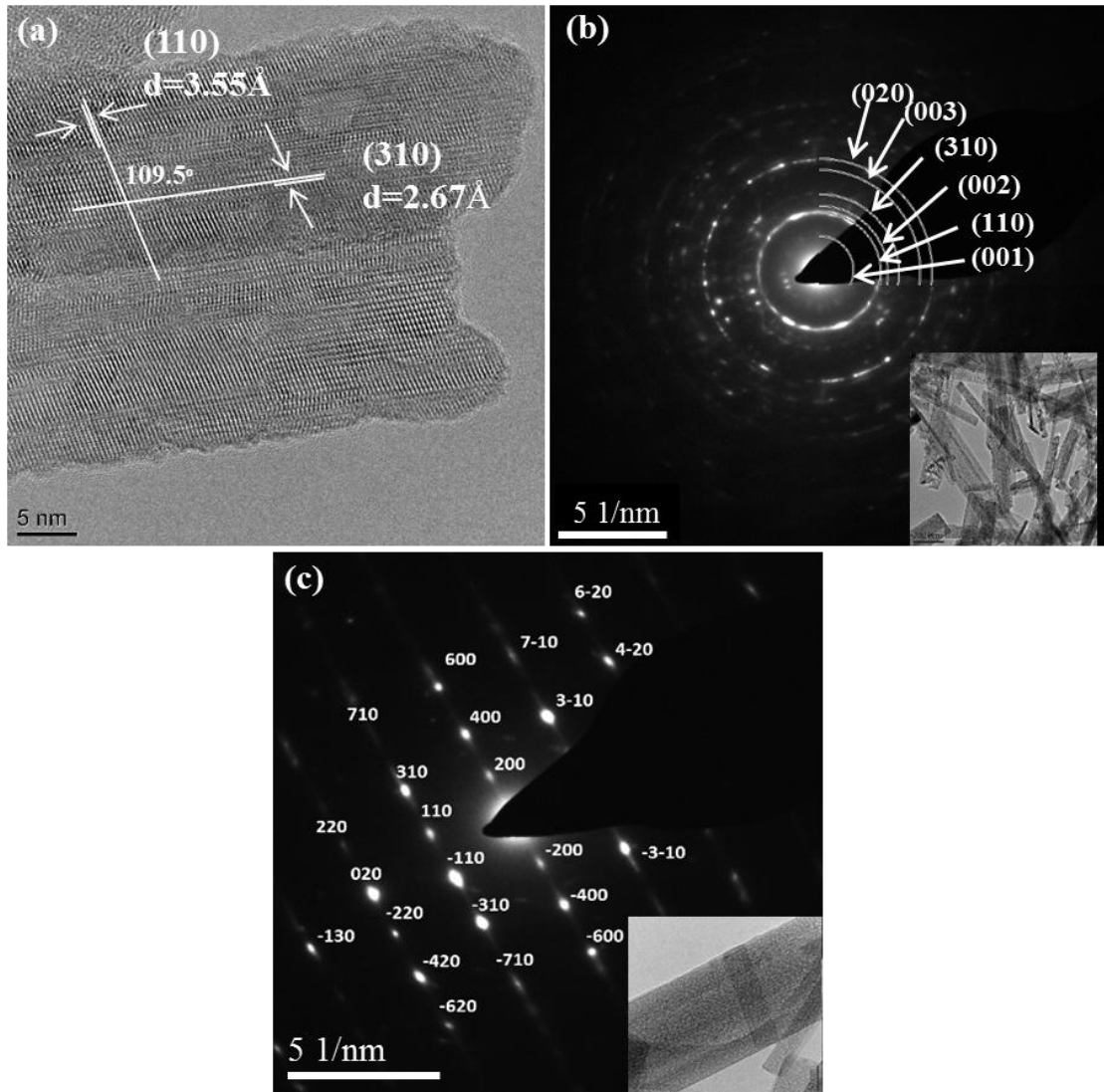


**Figure 4-9** (a) A HRTEM image taken from R@400 (b) a ring diffraction pattern taken from a group of particles shown in the image inset, (c) a spot diffraction pattern of a single particle shown in the image inset.

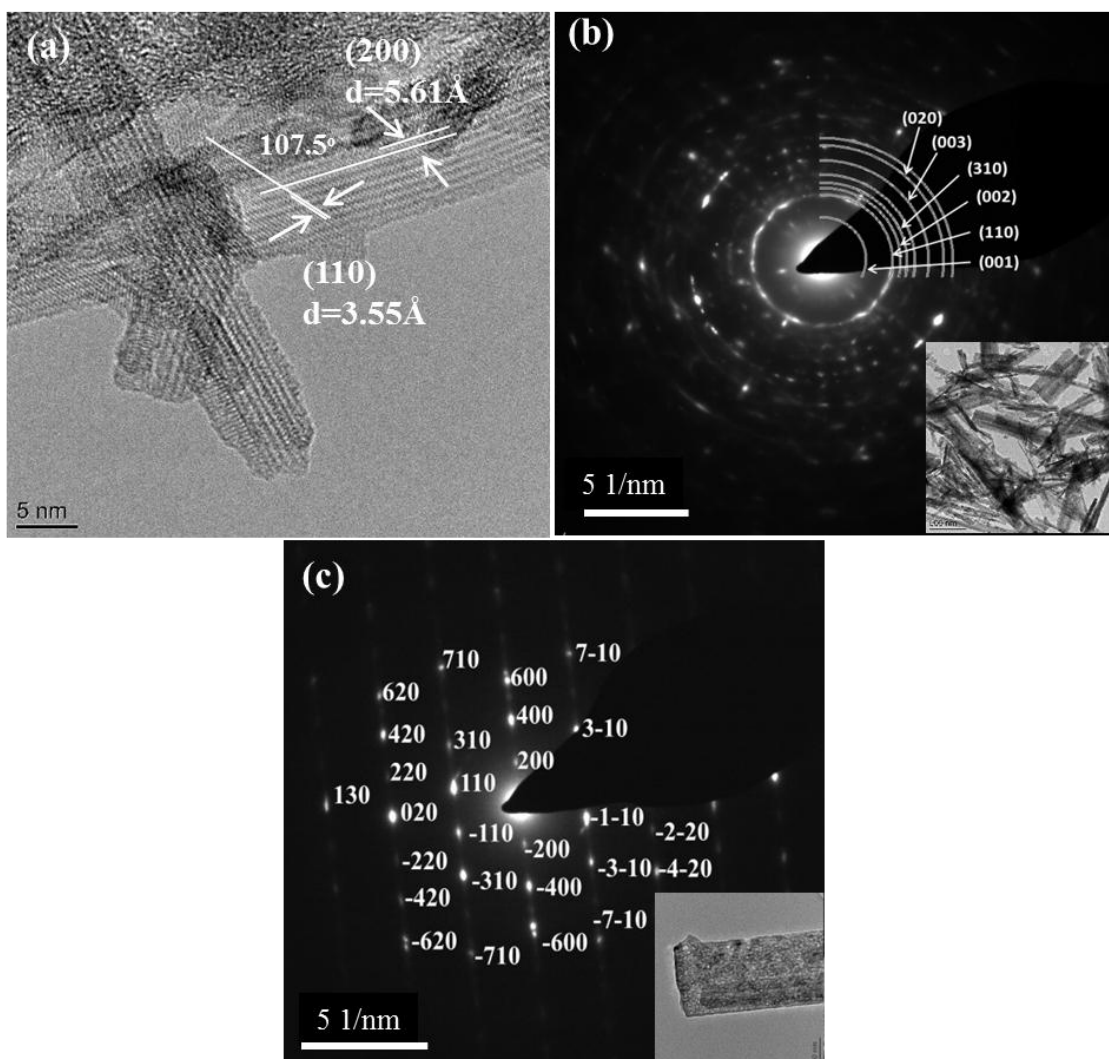


**Figure 4-10** (a) A HRTEM image taken from A@400 (b) a ring diffraction pattern taken from a group of particles shown in the image inset, (c) a spot diffraction pattern of a single particle shown in the image inset.

### 4.3 Discussion

All results from alkali hydrothermal synthesis route for the different precursors are in agreement with results in the literature [3]–[7] which suggested 1-D structures of TiO<sub>2</sub>(B) nanorods and the same phase transformation mechanism.

The morphology of TiO<sub>2</sub>(B) particles synthesized using the alkali hydrothermal method are typically 1-D structures which depend on the synthesis parameters such as alkali metal type, concentration of alkali metal hydroxide and hydrothermal reaction temperature. In this research, an elongation of nanorods was promoted by using liquid titania precursor (TTIP) whereas short nanorods occurred when solid titania precursors were used such as anatase, rutile and P25. In section 4.2.3, a possible reason why TTIP supports an elongation of particle morphology was proposed. Moreover, It was found by C-W. Peng [8] that use of amorphous TiO<sub>2</sub> instead of crystalline TiO<sub>2</sub> as alkali

hydrothermal precursors provided thinner diameter alkaline titanate products resulting in an increase in the length/width ratio. This result supports an elongation of nanorods if amorphous  $\text{TiO}_2$  is generated from the hydrolysis of TTIP.

Naturally, sodium titanates prefer to construct a layered intermediate structure (nanosheet). When treated with highly concentrated NaOH solution, the Ti-O-Ti bonds at the surface of nanosheet are broken and replaced by Ti-O-Na or Ti-OH [9]. Upon washing with water,  $\text{Na}^+$  and  $\text{OH}^-$  are removed from the sheet surfaces, leaving an imbalance of surface charge. This charge imbalance is the driving force for the rearrangement of nanosheet morphology by either rolling up to form a nanotube or stacking with other sheets to form a nanorod [3]. The concentration of NaOH (Na/Ti ratio) primarily affects the level of charge imbalance, controlling the morphology of the resulting sodium titanate [10]. Thus, it can be concluded that the concentration of alkali hydroxide and the washing of the alkali-hydrothermal samples with water followed by acid treatment (washing and soaking) are the crucial factors to promote different types of 1-D morphology [9],[11].

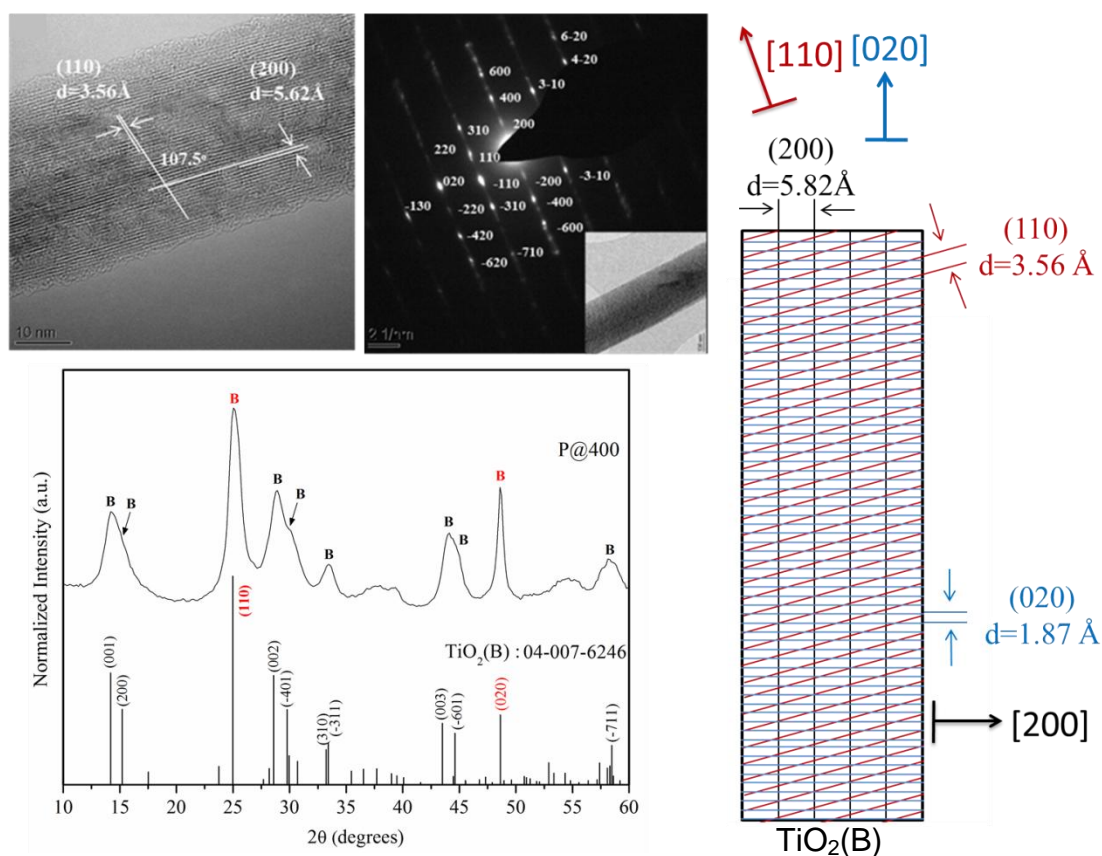


**Figure 4-11** Schematic view of a  $\text{TiO}_2(\text{B})$  nanorod (P@400) with an orientation corresponding to the evidence from XRD, HRTEM and SADP.

However, many researchers have reported an influence of hydrothermal conditions on morphological form. It was found that a hydrothermal reaction temperature of 150°C normally promotes the formation of nanotubes [3], [5], [7], [12], [13], whereas nanorods, nanowires and nanoribbons have been prepared at temperatures in the range of 170-220°C. Furthermore, a higher % filling of the hydrothermal reactor also promotes the elongation of particles, forming nanowire structures instead of nanotubes [7]. These practical suggestions support the observed nanorod formation in this research which used a hydrothermal temperature of 180°C and 75% filling of the reactor.

The fabricated TiO<sub>2</sub>(B) nanorods, reveal a preferred growth direction along [020] which is evidenced by XRD patterns and SADP images and is depicted schematically in Figure 4-11.

The investigation of TiO<sub>2</sub>(B) phase formation *via* the hydrothermal process indicates a mechanism involving phase transformation *via* an alkali metal titanate intermediate phase. This may correlate with the proposed mechanism for TiO<sub>2</sub>(B) phase formation by the LPCVD method in the next chapter.

I propose a three-step hydrothermal mechanism for TiO<sub>2</sub>(B) formation as diagrammatically illustrated in Figure 4-12 [3], [5], [8], [13]–[16] with a brief description of each of the steps as follows:

- (1) The titanium precursor: P25, TTIP, Rutile or Anatase, hydrothermally reacts with NaOH, providing the dissociation of TiO<sub>2</sub> starting materials into linked titanate building blocks. Na<sup>+</sup> ions are incorporated into the titanate building units forming the first intermediate sample of a sodium titanate layered structure. The monoclinic crystal structure of Na<sub>2</sub>Ti<sub>6</sub>O<sub>13</sub> generally comprises Na<sup>+</sup> ions (in yellow) located in the interlayers between the Ti<sub>n</sub>O<sub>2n+1</sub> planes;
- (2) The Na<sup>+</sup> ions in the Na<sub>2</sub>Ti<sub>6</sub>O<sub>13</sub> structure are ion-exchanged with H<sup>+</sup> during the acid soaking & washing processes, and then the structure transforms into the H<sub>2</sub>Ti<sub>3</sub>O<sub>7</sub> structure which is an analogous structure to Na<sub>2</sub>Ti<sub>3</sub>O<sub>7</sub>. The monoclinic H<sub>2</sub>Ti<sub>3</sub>O<sub>7</sub> structure is constructed from a titanate layered structure with an interlayer counteraction of H<sup>+</sup> (in black);
- (3) Under heat treatment at a suitable temperature (in this case at 400°C), the H<sub>2</sub>Ti<sub>3</sub>O<sub>7</sub> dehydrates via an evaporation of H<sub>2</sub>O molecules, and structurally rearranges to form TiO<sub>2</sub>(B).

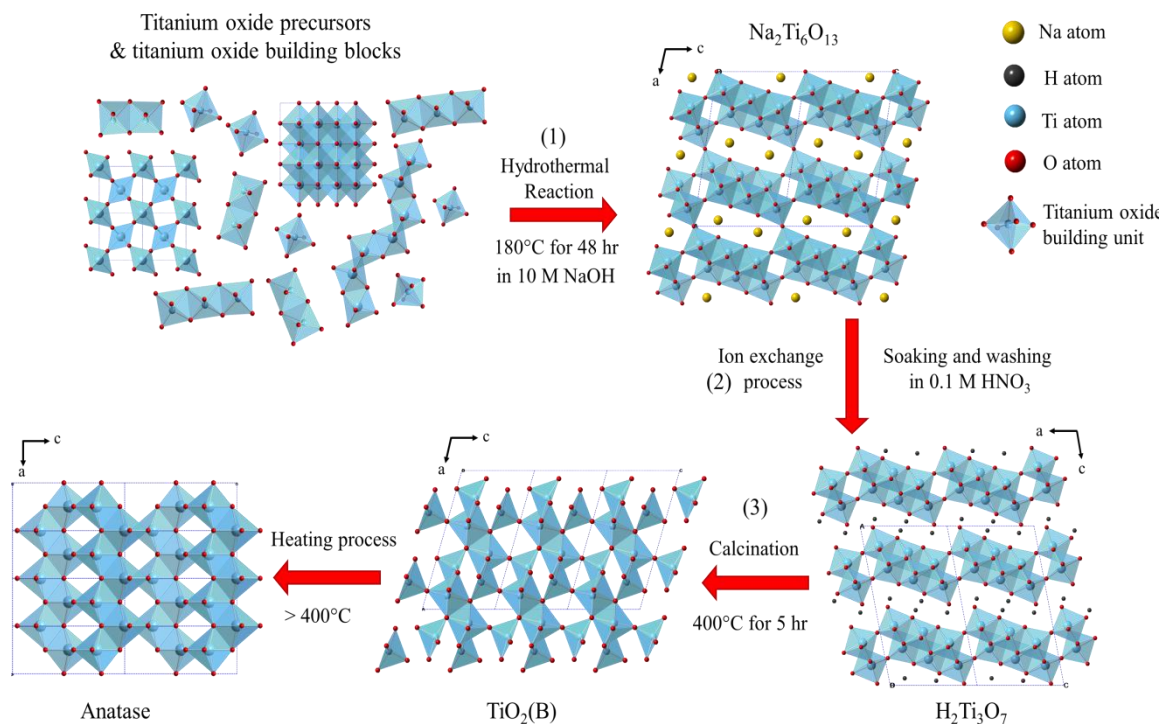


**Figure 4-12** Schematic diagram depicting the hydrothermal phase transformation mechanism for preparing the  $\text{TiO}_2(\text{B})$  phase.

This proposed mechanism is similar to that proposed in the literature [3], [5], [8], [13]–[16], all of which suggest a phase transformation mechanism through the sequential steps  $\text{Ti}_x\text{O}_y \rightarrow \text{Na}_2\text{Ti}_n\text{O}_{2n+1} \rightarrow \text{H}_2\text{Ti}_n\text{O}_{2n+1} \rightarrow \text{TiO}_2(\text{B})$ .

Owing to the fact that  $\text{TiO}_2(\text{B})$  is a metastable phase, it is easy to transform to the anatase phase when the temperature is higher than  $400^\circ\text{C}$  (the stability of  $\text{TiO}_2(\text{B})$  phase is reported to be below  $600^\circ\text{C}$  [17]). Many research studies have proposed an interface structural transformation in the mixed-phase nanostructure. In which the interface between anatase and  $\text{TiO}_2(\text{B})$  phase should relate to a well-matched arrangement at the atomic level of their crystal structures which is a so-called lattice-directed topotactic transformation. However, the interfacial lattice planes are still a matter of debate. For example, the practical study by Zheng [4] proposed that the interfacial lattice planes are between (202) of  $\text{TiO}_2(\text{B})$  and (202) of anatase with the lattice spacings of 1.76 and  $1.78\text{\AA}$  respectively, whereas, the theoretical study by Zhu [18] suggested a possible habit plane of the phase transition between (-201)  $\text{TiO}_2(\text{B})$  and (103) Anatase.

## 4.4 Conclusion

Titanium dioxide 1-D structures were successfully fabricated via a hydrothermal method with a subsequent ion-exchange process and calcination. P25, TTIP, rutile and also anatase were used as Ti precursors in the alkali hydrothermal system. TTIP promoted an elongation of nanorod morphology whereas the other precursors produced short nanorod structures. The different types of titanium precursors did not have any influence on the phase transformation during the fabrication process.  $\text{Na}_2\text{Ti}_6\text{O}_{13}$  is the primary intermediate product after washing the hydrothermal sample.  $\text{H}_2\text{Ti}_3\text{O}_7$  is the secondary intermediate phase obtained following proton-exchange of  $\text{Na}_2\text{Ti}_6\text{O}_{13}$  in 0.1 M  $\text{HNO}_3$  solution. Finally, the  $\text{TiO}_2(\text{B})$  phase was the product of calcination of the secondary intermediate product at  $400^\circ\text{C}$  for 5 hr. A phase transformation mechanism is presented *via* an investigation of products at each of the steps which corresponds with the literature. The effects of the synthesis condition on tailoring of crystal morphology are discussed. The growth direction of the nanorods of  $\text{TiO}_2(\text{B})$  is investigated including a schematic representation of crystal plane directions in the nanorods structure. Finally, the metastable phase of  $\text{TiO}_2(\text{B})$  is shown to be transformed to anatase during thermal treatment at temperatures higher than  $400^\circ\text{C}$ .

## 4.5 References

- [1] H. Song, H. Jiang, T. Liu, X. Liu, and G. Meng, "Preparation and photocatalytic activity of alkali titanate nano materials  $\text{A}_2\text{Ti}_n\text{O}_{2n+1}$  ( $\text{A}=\text{Li}$ ,  $\text{Na}$  and  $\text{K}$ )," *Mater. Res. Bull.*, vol. 42, no. 2, pp. 334–344, 2007.
- [2] K. Kiatkittipong, C. Ye, J. Scott, and R. Amal, "Understanding hydrothermal titanate nanoribbon formation," *Cryst. Growth Des.*, vol. 10, no. 3, pp. 3618–3625, 2010.
- [3] K. Kiatkittipong, J. Scott, and R. Amal, "Hydrothermally synthesized titanate nanostructures: Impact of heat treatment on particle characteristics and photocatalytic properties," *ACS Appl. Mater. Interfaces*, vol. 3, pp. 3988–3996, 2011.
- [4] Z. Zheng, H. Liu, J. Ye, J. Zhao, E.R. Waclawik, and H. Zhu, "Structure and contribution to photocatalytic activity of the interfaces in nanofibers with mixed anatase and  $\text{TiO}_2(\text{B})$  phases," *J. Mol. Catal. A Chem.*, vol. 316, no. 1–2, pp. 75–82, 2010.
- [5] C. Huang, K. Zhu, M. Qi, Y. Zhuang, and C. Cheng, "Preparation and photocatalytic activity of bicrystal phase  $\text{TiO}_2$  nanotubes containing  $\text{TiO}_2\text{-B}$  and anatase," *J. Phys. Chem. Solids*, vol. 73, no. 6, pp. 757–761, 2012.
- [6] A.R. Armstrong, G. Armstrong, J. Canales, and P.G. Bruce, " $\text{TiO}_2\text{-B}$  Nanowires," *Angew. Chem Int. Ed. Engl.*, vol. 43, pp. 2286–2288, 2004.
- [7] G. Armstrong, A.R. Armstrong, J. Canales, and P.G. Bruce, "Nanotubes with the  $\text{TiO}_2\text{-B}$  structure.," *Chem. Commun.*, no. 19, pp. 2454–2456, 2005.

- [8] C.W. Peng, M. Richard-Plouet, T.Y. Ke, C.Y. Lee, H.T. Chiu, C. Marhic, E. Puzenat, F. Lemoigno, and L. Brohan, "Chimie douce route to sodium hydroxo titanate nanowires with modulated structure and conversion to highly photoactive titanium dioxides," *Chem. Mater.*, vol. 20, no. 23, pp. 7228–7236, 2008.
- [9] T. Kasuga, M. Hiramatsu, A. Hoson, T. Sekino, and K. Niihara, "Titania nanotubes prepared by chemical processing," *Adv. Mater.*, vol. 11, no. 15, pp. 1307–1311, 1999.
- [10] M. Fehse, F. Fischer, C. Tessier, L. Stievano, and L. Monconduit, "Tailoring of phase composition and morphology of TiO<sub>2</sub>-based electrode materials for lithium-ion batteries," *J. Power Sources*, vol. 231, pp. 23–28, 2013.
- [11] Q. Chen, W. Zhou, G.H. Du, and L.M. Peng, "Trititanate nanotubes made via a single alkali treatment," *Adv. Mater.*, vol. 14, no. 17, pp. 2000–2003, 2002.
- [12] A R. Armstrong, G. Armstrong, J. Canales, and P.G. Bruce, "TiO<sub>2</sub>-B nanowires," *Angew. Chem. Int. Ed. Engl.*, vol. 43, no. 17, pp. 2286–2288, 2004.
- [13] J.P. Huang, D.D. Yuan, H.Z. Zhang, Y.L. Cao, G.R. Li, H.X. Yang, and X.P. Gao, "Electrochemical sodium storage of TiO<sub>2</sub>(B) nanotubes for sodium ion batteries," *RSC Adv.*, vol. 3, no. 31, pp. 12593, 2013.
- [14] Y. Lei, J. Sun, H. Liu, X. Cheng, F. Chen, and Z. Liu, "Atomic mechanism of predictable phase transition in dual-phase H<sub>2</sub>Ti<sub>3</sub>O<sub>7</sub> /TiO<sub>2</sub>(B) nanofiber: An in situ heating TEM investigation," *Chem. - A Eur. J.*, vol. 20, pp. 11313–11317, 2014.
- [15] K. Kiatkittipong, A. Iwase, J. Scott, and R. Amal, "Photocatalysis of heat treated sodium- and hydrogen-titanate nanoribbons for water splitting, H<sub>2</sub>/O<sub>2</sub> generation and oxalic acid oxidation," *Chem. Eng. Sci.*, vol. 93, pp. 341–349, 2013.
- [16] B. Liu, A. Khare, and E.S. Aydil, "TiO<sub>2</sub>-B/anatase core-shell heterojunction nanowires for photocatalysis," *ACS Appl. Mater. Interfaces*, vol. 3, pp. 4444–4450, 2011.
- [17] W. Zhuang, L. Lu, X. Wu, W. Jin, M. Meng, Y. Zhu, and X. Lu, "TiO<sub>2</sub>-B nanofibers with high thermal stability as improved anodes for lithium ion batteries," *Electrochem. commun.*, vol. 27, pp. 124–127, 2013.
- [18] S. Zhu, S. Xie, and Z. Liu, "Design and observation of biphasic TiO<sub>2</sub> crystal with perfect junction," *J. Phys. Chem. Lett.*, vol. 5, pp. 3162–3168, 2014.

## **Chapter 5 Synthesis and characterization of mixed phase anatase TiO<sub>2</sub> and sodium-doped TiO<sub>2</sub>(B) thin films by low pressure chemical vapour deposition (LPCVD)**

Thin films based on the crystalline anatase phase of TiO<sub>2</sub> are used in self-cleaning glass/windows [1] as this polymorph possesses a higher photocatalytic activity than rutile. Current improvement strategies focus on the production of phase mixtures in the thin films which may provide higher photocatalytic activities. Mixing two different phases of TiO<sub>2</sub> such as anatase/rutile [2] or anatase/TiO<sub>2</sub>(B) [3], directly affects the charge transfer process between the different phases possibly reducing recombination of photo-generated electrons and so enhancing the photocatalytic activity [4]–[7]. This directly improves the efficiency of oxidative stripping of organic molecules from water or air.

Commonly, alkali metal titanates have been used as precursors for TiO<sub>2</sub>(B) preparation in many synthetic methods such as sol-gel [8], hydrothermal [9] and solid-state reaction [10]. In this chapter, the LPCVD method was employed to synthesize (for the first time) dual phase anatase and sodium-doped TiO<sub>2</sub>(B) thin films on glass substrates.

### **5.1 Experimental Procedure**

#### **5.1.1 Thin Film Preparation**

TiO<sub>2</sub> thin films were deposited onto either a soda-lime glass slide or a fused quartz slide. The reaction temperature was varied between 450 and 600°C with a reaction time of typically 15 min. The LPCVD process is detailed in chapter 3 section 3.1.2.3.

#### **5.1.2 Materials Characterization**

Before being characterized, the TiO<sub>2</sub> film deposited onto the substrate (e.g. a soda-lime glass slide) was divided into 12 plates each of dimensions 12 mm × 12.6 mm × 1 mm. These samples represented different reactor positions relative to the gas entry point at plate1 (Fig 3-5). In-plane and out of plane X-ray diffraction (XRD) with a Philips X'Pert MPD diffractometer, were employed to characterise the crystalline phases in the samples. The surface morphology and thickness of TiO<sub>2</sub> thin films were investigated by SEM (Carl Zeiss LEO 1530 Gemini FEGSEM) and EDX spectroscopy both in plan-view and in cross-section. Raman spectroscopy and UV-Vis diffuse reflectance spectroscopy were also used to characterise these materials. The materials

were analysed by TEM using imaging, SAED and EDX spectroscopy, mapping and quantification.

## 5.2 Results

### 5.2.1 X-ray Diffraction

The optimum synthesis condition to achieve thin films composed of mixed phase TiO<sub>2</sub>(B) and anatase was found to be a nominal reaction temperature of 600°C for 15 min reaction time with 5 mL of TTIP. The mixed phase of TiO<sub>2</sub> only occurred when the nominal reaction temperature reached 600°C. At lower nominal temperatures such as 400°C and 500°C, thin films tended to be composed of pure anatase with an equiaxed particle morphology exhibiting extensive particle aggregation, whilst at high temperatures (700°C) it was observed that the substrate began to deform and the deposit consisted of pure anatase with a non-aggregated spherical particle morphology (The XRD results of the higher and lower temperatures than 600°C are shown in the appendix II). Here, I focus solely on the results obtained at a nominal temperature of 600°C as these conditions appear to promote the formation of the TiO<sub>2</sub>(B) phase. As shown in Figure 3-5(b) in chapter 3 the actual temperature in the reaction tube had a maximum of *ca.* 550°C at the position of plates 2-5 and decreased towards each end of the tube.

For these conditions, the out of plane XRD patterns of a selection of 12 plates on a soda-lime glass substrate are shown in Figure 5-1, and are compared to the corresponding thin film on a fused quartz substrate (referred to as TiO<sub>2</sub>-Quartz) prepared under identical conditions and reactor position for Plate 4. The XRD patterns show that almost all of 600°C synthesized thin films on soda lime glass substrate consist of a combination of both TiO<sub>2</sub>(B) (JCPDS 04-007-6246) and anatase phases (JCPDS 00-021-1272) in different relative proportions depending on the distance from the gas entry point. As will become clear later, it is important to note that the XRD peaks assigned to the TiO<sub>2</sub>(B) phase do not match with any sodium titanate Na<sub>x</sub>TiO<sub>2+0.5x</sub> phase or any other related sodium-containing phase in the JCPDS database. In Plate 1 anatase is the majority component, nevertheless in other reactor positions (as shown in Plates 2, 4, 5 and 8) XRD indicates the main component is the TiO<sub>2</sub>(B) phase. In the case of Plate 10, the patterns show only one peak at  $2\theta = 25.30^\circ$  indicating the anatase phase and two very broad features lying between  $15-35^\circ$  and  $60-70^\circ$  characteristic of amorphous SiO<sub>2</sub> from the glass substrates. The influence of the substrate was more evident at larger distances from the gas entry point possibly indicating the presence of a thinner crystalline deposit.

The influence of the substrate on the film was studied using a fused-quartz plate (at the same position as Plate 4) instead of the normal soda-lime glass substrate under the same synthesis conditions. The differences can be seen in Figure 5-1 by comparing the XRD patterns labeled Plate 4 and Quartz-plate 4 respectively. These results indicate that a mixed phase of anatase and  $\text{TiO}_2(\text{B})$  can be indexed on Plate 4, whilst only the anatase phase is evident on a fused quartz substrate indicating that the soda-lime glass substrate promotes the formation of  $\text{TiO}_2(\text{B})$  by LPCVD.

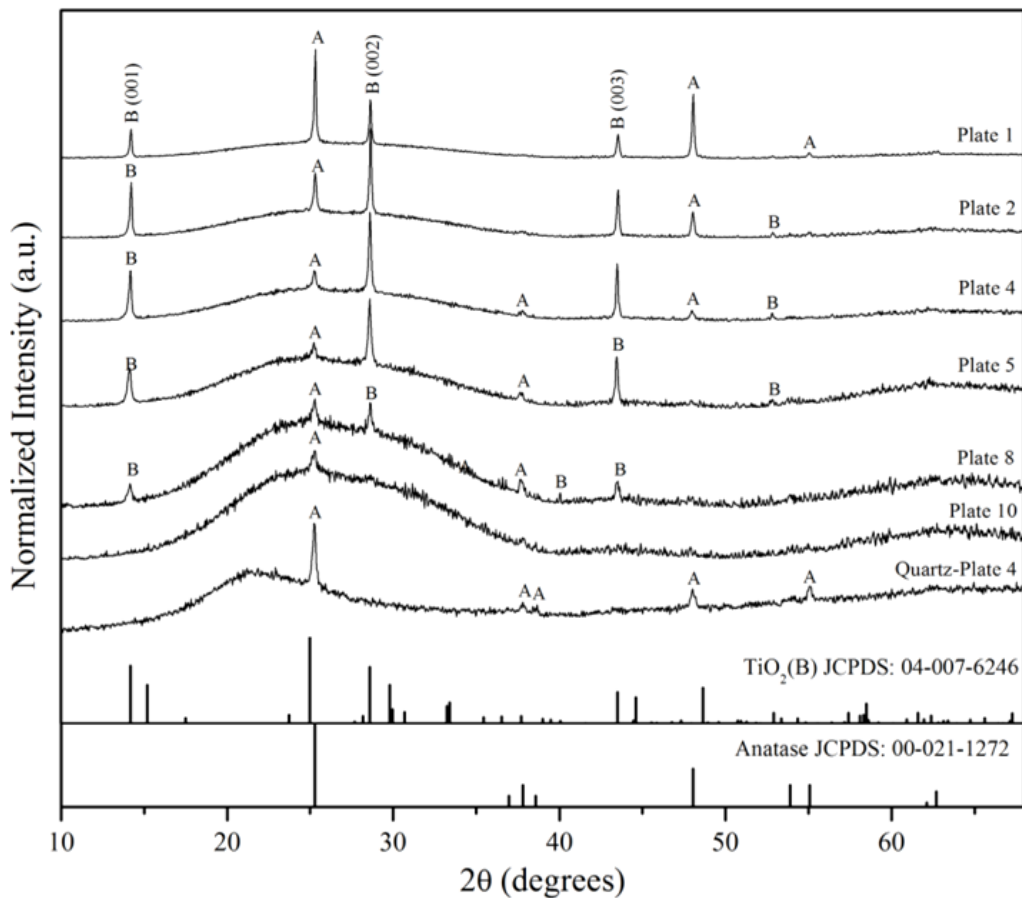


**Figure 5-1** Out of plane XRD patterns of  $\text{TiO}_2$  thin film deposited onto soda-lime glass substrates and a quartz substrate at position Plate 4 prepared by LPCVD at  $600^\circ\text{C}$ : A and B refer to the assignment of the anatase and  $\text{TiO}_2(\text{B})$  phases respectively

The (101) and (200) peaks of the anatase phase (at  $2\theta = 25.28^\circ$  and  $48.05^\circ$  respectively) are very close to the (110) and (020) peaks of the  $\text{TiO}_2(\text{B})$  phase at  $2\theta=24.98^\circ$  and  $48.63^\circ$ . The crystallite size derived from XRD line broadening in Figure 5-1 was estimated to be in the range 40-60 nm for both phases. In order to clarify the results, both in-plane and out-of-plane XRD were recorded for Plate 4 to confirm the existence of both phases, as illustrated in Figure 5-2. The in-plane XRD

pattern shows additional peaks of the TiO<sub>2</sub>(B) phase when compared to the TiO<sub>2</sub>(B) peaks evident in the out-of-plane pattern. Not only does this confirm the existence of the TiO<sub>2</sub>(B) phase it also reveals a preferred [001] crystallographic orientation of TiO<sub>2</sub>(B) as illustrated by the strong (001), (002) and (003) hkl reflections at 2θ = 14.16°, 28.62° and 43.5° in the out-of-plane pattern.

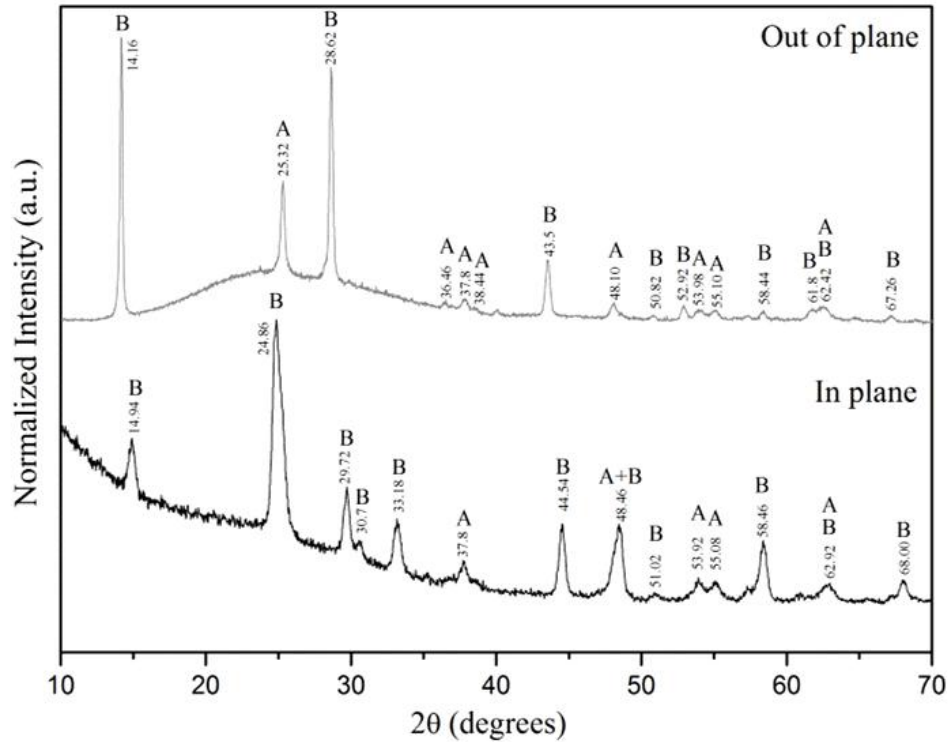


**Figure 5-2** In plane and out of plane XRD patterns of Plate 4: A and B refer to anatase and TiO<sub>2</sub>(B) phases respectively.

### 5.2.2 Raman Spectroscopy

Raman spectroscopy was employed to confirm the phases on Plate 4 and Quartz-plate 4. The Raman active modes for anatase are evident as an intense peak around 144 cm<sup>-1</sup> as well as three other peaks at 395, 517 and 637 cm<sup>-1</sup> present in both samples and indicating solely pure anatase on Quartz-plate 4 (Figure 5-3). The remaining peaks, especially two strong peaks at 121.9 and 144.96 cm<sup>-1</sup> signify the Raman active modes of the TiO<sub>2</sub>(B) phase [11], [12] indicating the presence of the mixed phase on Plate 4.

### 5.2.3 UV-Visible Spectroscopy

UV-Visible diffuse reflectance spectroscopy was used to study optical properties of the thin films and raw spectra are shown in Figure 5-4(a) and the same data after a transformation to transformed reflectance in Figure 5-4(b) [4]. Here, I have plotted transformed reflectance according to Kubelka-Munk function against photon energy as anatase and TiO<sub>2</sub>(B) are an indirect band gap semiconductor.

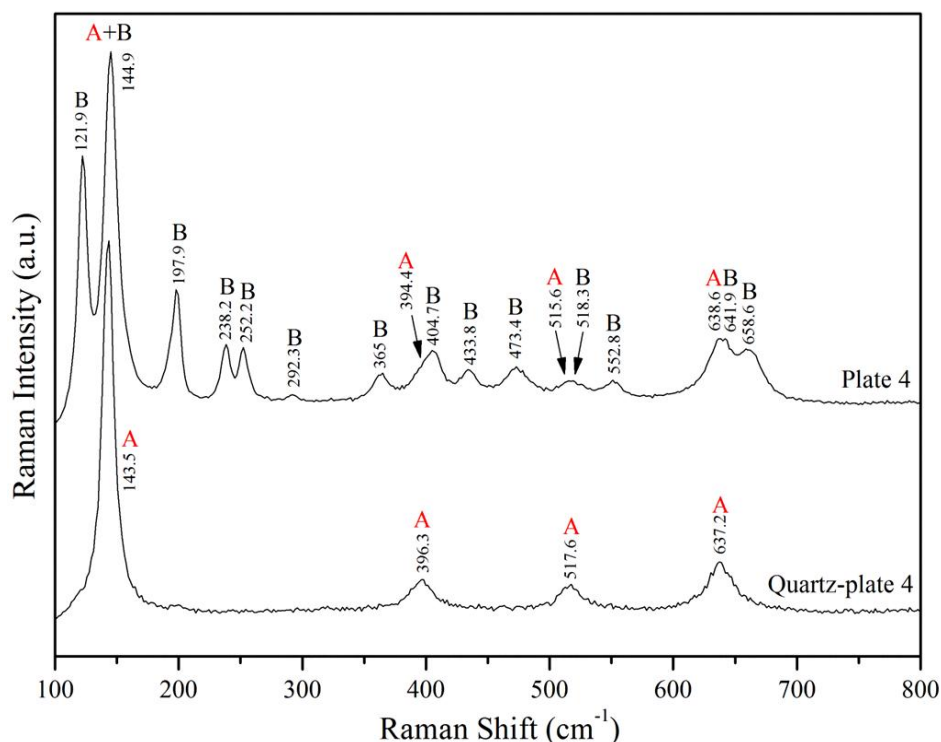


**Figure 5-3** Raman spectra of Plate 4 and Quartz-plate 4: A and B indicate the anatase and TiO<sub>2</sub>(B) phases respectively.

The band gaps of these materials were calculated by extrapolating the linear portion of the slopes in Figure 5-4(b) and determining the intercept with the background. The band gap energies of anatase and TiO<sub>2</sub>(B) are experimentally reported as being 3.2 eV and 3.0-3.2 eV respectively [12]–[15]. The present results curiously show a energy band gap of between 3.25 and 3.31 eV which increased with an increasing proportion of the TiO<sub>2</sub>(B) phase. It might be expected that the presence of any dopants in the thin film may cause changes including possible increases in the band gap energy. In contrast, the anatase thin film on Quartz-plate 4 showed a band gap of 3.275 eV.

#### 5.2.4 Scanning Electron Microscopy

A SEM plan-view image of Plate 4 is shown in Figure 5-5(a) and illustrates the presence of two types of particle morphology: large polygonal plates 100-200 nm in diameter and smaller, more spherical particles with a diameter of around 20 nm. The average primary particle size of this bimodal distribution at the film surface is 73±42 nm. A composition derived from SEM/EDX, shown inset in Figure 5-5(a), confirms the existence of titanium and oxygen in the thin film.

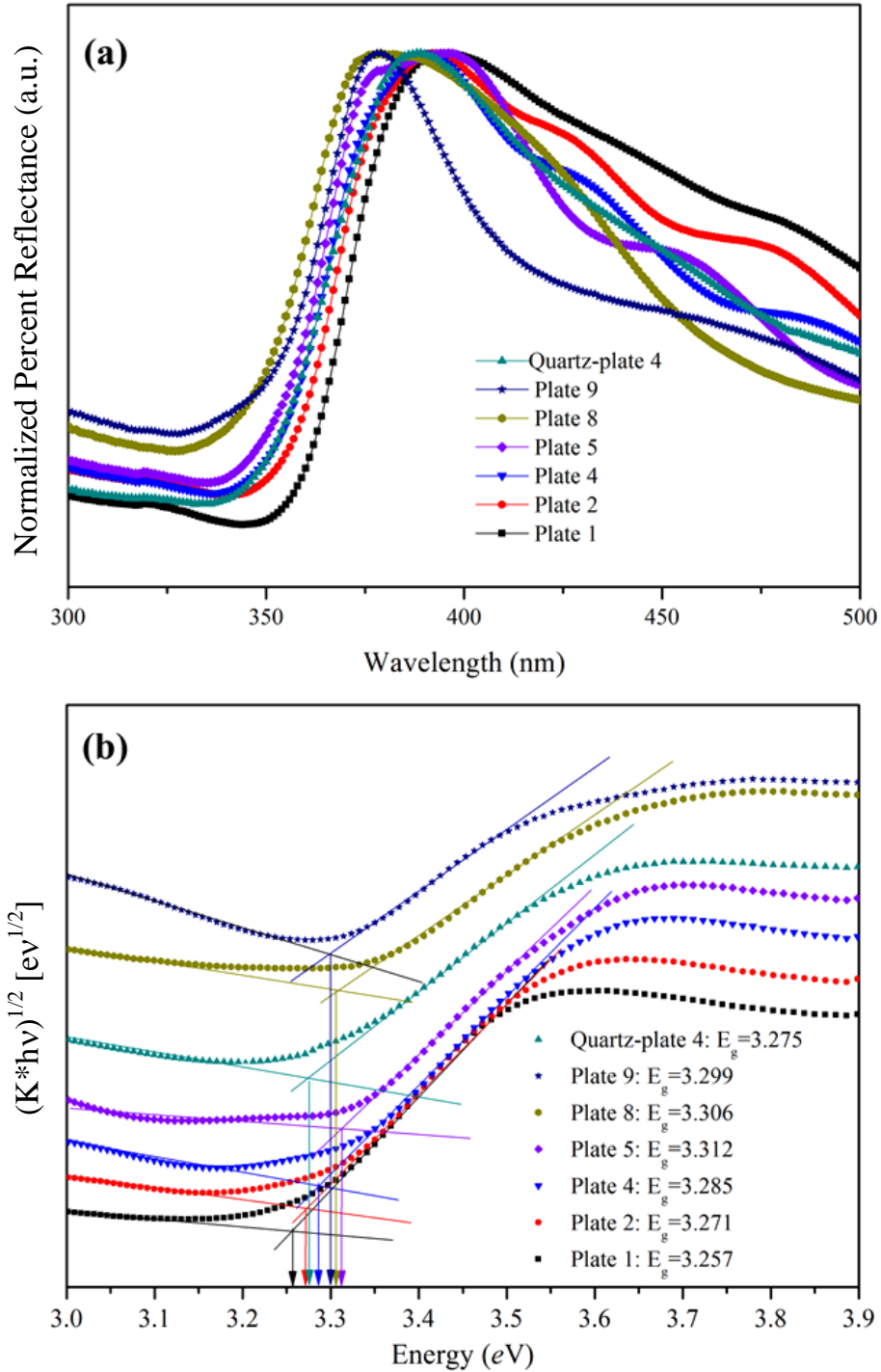


**Figure 5-4** (a) UV-Vis diffuse reflectance spectra of the samples prepared at optimum LPCVD condition (b) Estimation of the band gap energy by plotting the corresponding graph of photon energy (eV) versus transformed Kubelka-Munk function.

As the TiO<sub>2</sub> film thickness is only around 200 nm, as shown in the SEM cross-section in Figure 5-6(a), the electron beam interaction volume also samples the glass substrate and hence the Ti:O ratio is less than 1:2 and this is also presumably why Na, Si, Ca and Mg are detected. Inspection of Figure 5-6(a), reveals that the film cross-section also contains two kinds of particles: smaller columnar or needle-shaped

particles present predominantly at the glass substrate/film boundary and the larger plate-like particles predominantly deposited on the film surface. This may suggest that the small needle-shaped particles are acting as a seeding layer on the substrate or arise from some sort of interfacial reaction with the substrate.

As shown in the graph in Figure 5-6(c) and in the images in Figure 5-6(d), the film thickness decreases from 400 to 50 nm dependent on the distance from the carrier gas entry point, most likely due to precursor depletion. Thus both the thickness and the relative proportion of the different crystalline phases are directly dependent on the position of the substrate in the reactor. Interestingly from the plan-view image of the Quartz-plate 4 sample shown in Figure 5-5(b), the pure anatase particles so produced exhibit a size of 30 nm and a different spherical morphology, similar to anatase samples synthesized at reaction temperatures below 500°C and above 700°C on soda-lime glass substrates. A SEM cross section image of Quartz-plate 4 (Figure 5-6(b)) shows a unique columnar morphology across the thin film with no apparent phase at the film-substrate interface.

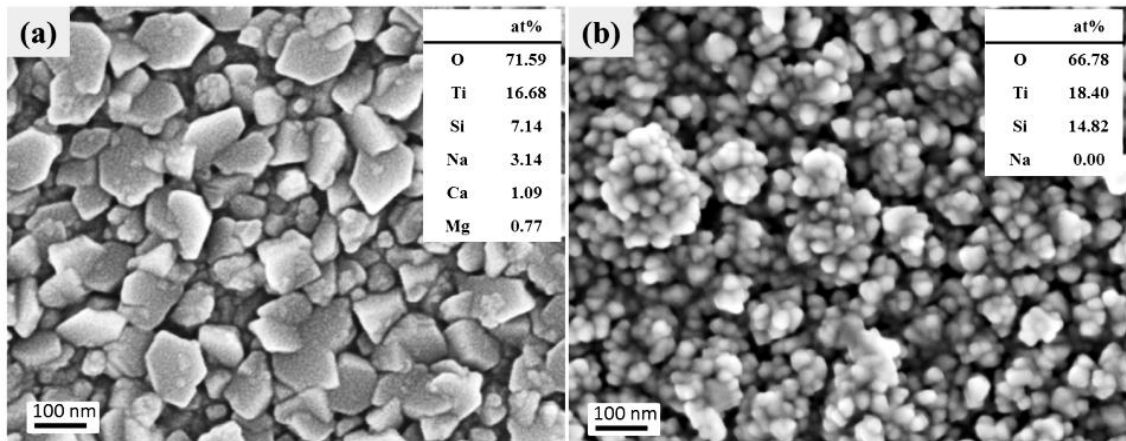


**Figure 5-5** (a) SEM secondary electron image of TiO<sub>2</sub> thin film from the top surface of Plate 4; (b) SEM secondary electron image of TiO<sub>2</sub> thin film from the top surface of Quartz-plate 4.

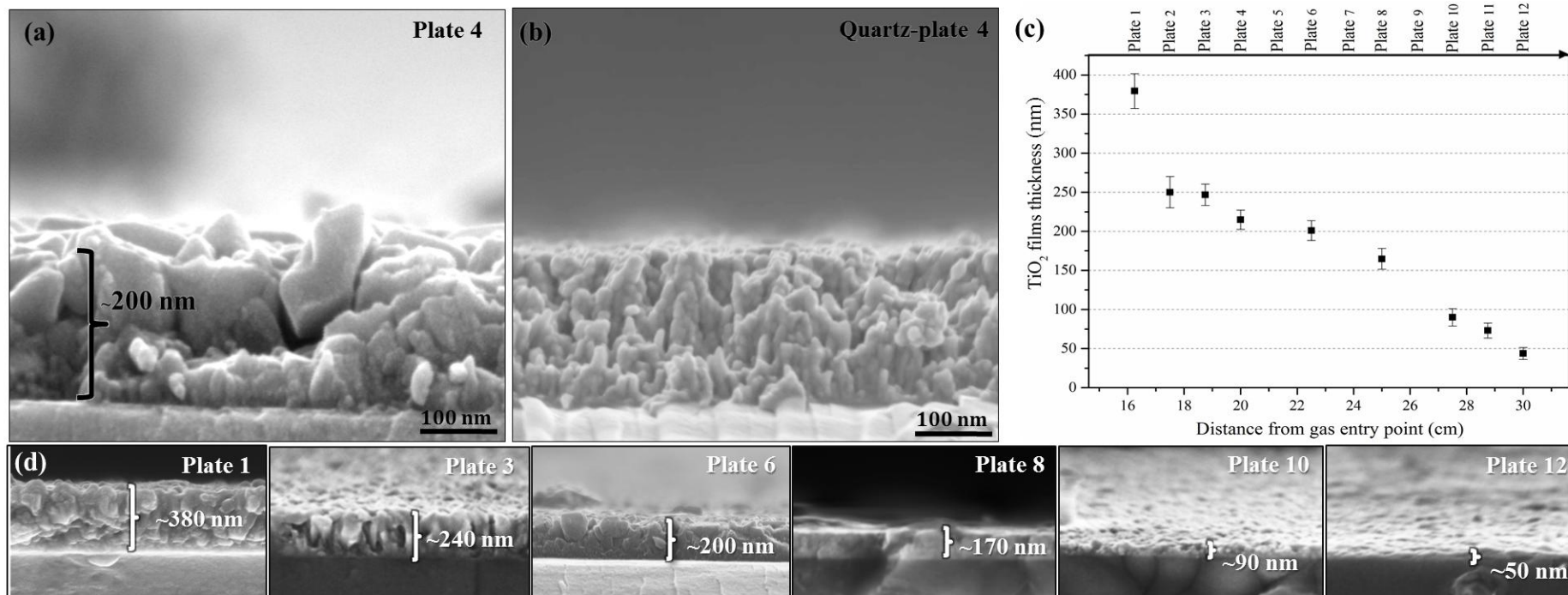


**Figure 5-6** SEM cross-sectional images of thin film fracture surfaces of Plate 4 on: (a) soda lime glass and (b) fused quartz substrates; (c) Plot of the film thickness relative to the gas entry point observed from SEM cross-sectional images of thin films on soda lime glass substrates shown in Figure 5-6(d); (d) The decreasing of TiO<sub>2</sub> film thickness on Soda lime glass substrate relative to the gas entry point.

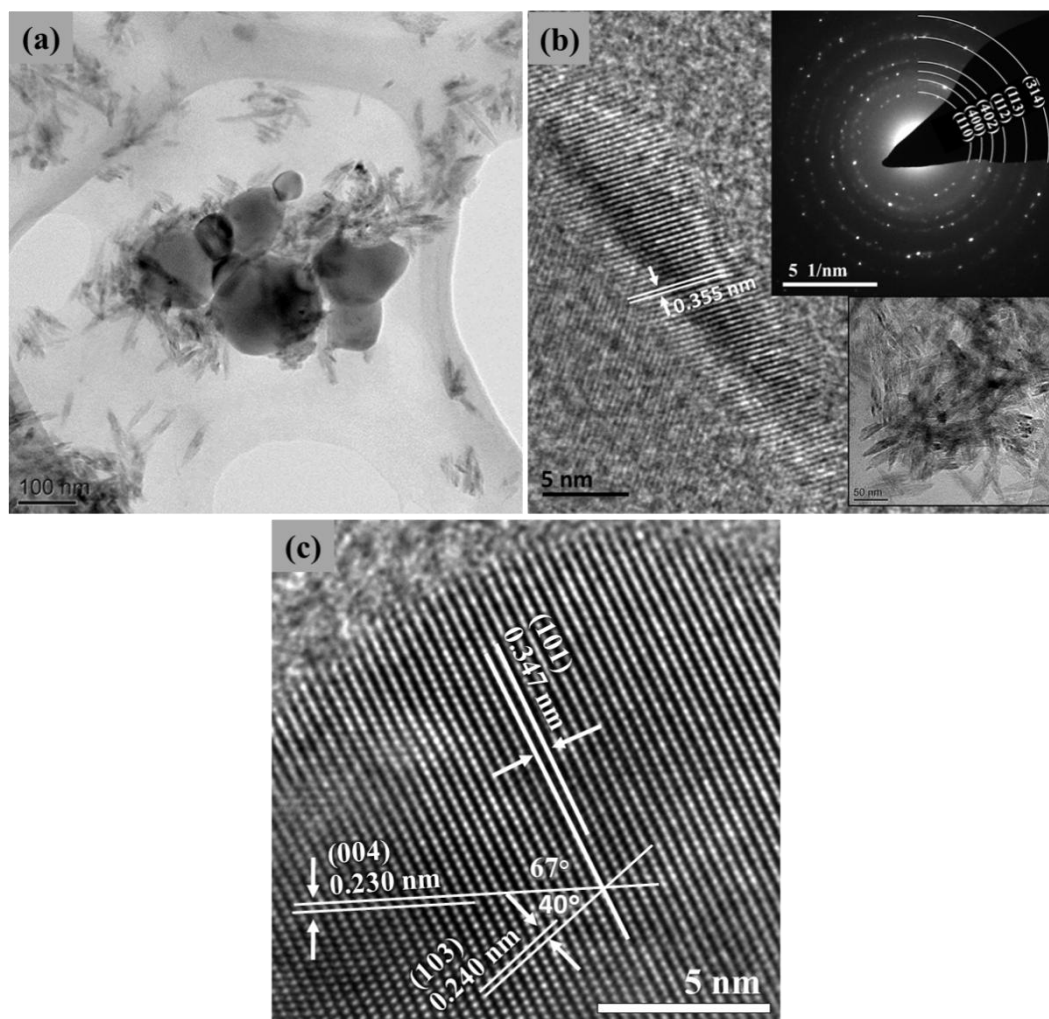


**Figure 5-7** (a) A TEM image taken from Plate 4, showing both anatase polygonal plates and TiO<sub>2</sub>(B) needle-shaped particles; (b) HRTEM and diffraction pattern of a TiO<sub>2</sub>(B) needle; (c) HRTEM image of an anatase polygonal plate.

### 5.2.5 Transmission Electron Microscopy

The coexistence of TiO<sub>2</sub>(B) and anatase phases in the thin films confirmed by XRD and Raman results may explain the two types of particle morphology observed in SEM images. These two distinct types of particle morphology (small needle-shaped and larger polygonal plate-like) are also evident in TEM of thin film material scraped from the surface of Plate 4, a typical TEM image being shown in Figure 5-7(a). The particle size of the polygonal plates are in the range 40-220 nm with an average of around 150 nm, significantly bigger than the needles which are in the range 5-10 nm in width and 50-80 nm in length. These values are consistent with the XRD results on the assumption that the short axis of the polygonal plates lies parallel to the substrate. HRTEM and SAED were employed to investigate the relationship between physical appearance and the nanostructure of these morphologies as illustrated in Figure 5-7(b) and Figure 5-7(c). In Figure 5-7(b), the needle-like crystals clearly show a lattice

spacing of  $3.55\text{\AA}$  which can be tentatively assigned to the (110) lattice spacing of  $\text{TiO}_2(\text{B})$ . Moreover, a TEM selected area diffraction pattern of a group of needles, shown inset in Figure 5-7(b), shows rings corresponding to the (110), (400), (-402), (112), (113) and (-314) spacings of  $\text{TiO}_2(\text{B})$ . TEM/EDX spectra (Figure 5-8(a)) of the same area reveals the presence of Ti, O and also a very small amount of Na typically less than 1% atomic, however interference between the Cu  $L\alpha$ - (from the TEM support grid) and Na  $K\alpha$ -X-ray emission peaks makes this quantification unreliable. Figure 5-7(c) demonstrates that the polygonal plate is anatase as it reveals lattice spacings of  $3.47\text{\AA}$ ,  $2.38\text{\AA}$  and  $2.28\text{\AA}$  which correspond to the (101), (103) and (112) interplanar spacings respectively. TEM/EDX on the anatase plates reveals the presence of solely Ti and O (Na, if present, is below the level of detectability following quantification), as shown in Figure 5-8(b).

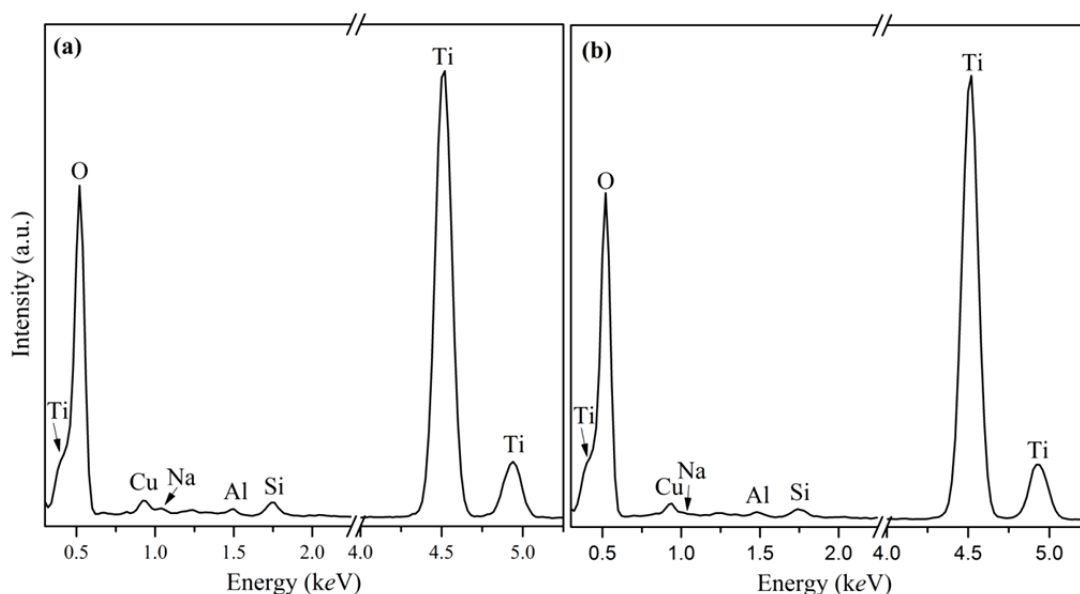


**Figure 5-8** TEM-EDS spectrum of: (a) a group of needles particles investigated in the same area of Figure 5-7(b); (b) a polygonal plate particle correlated with Figure 5-7(b)

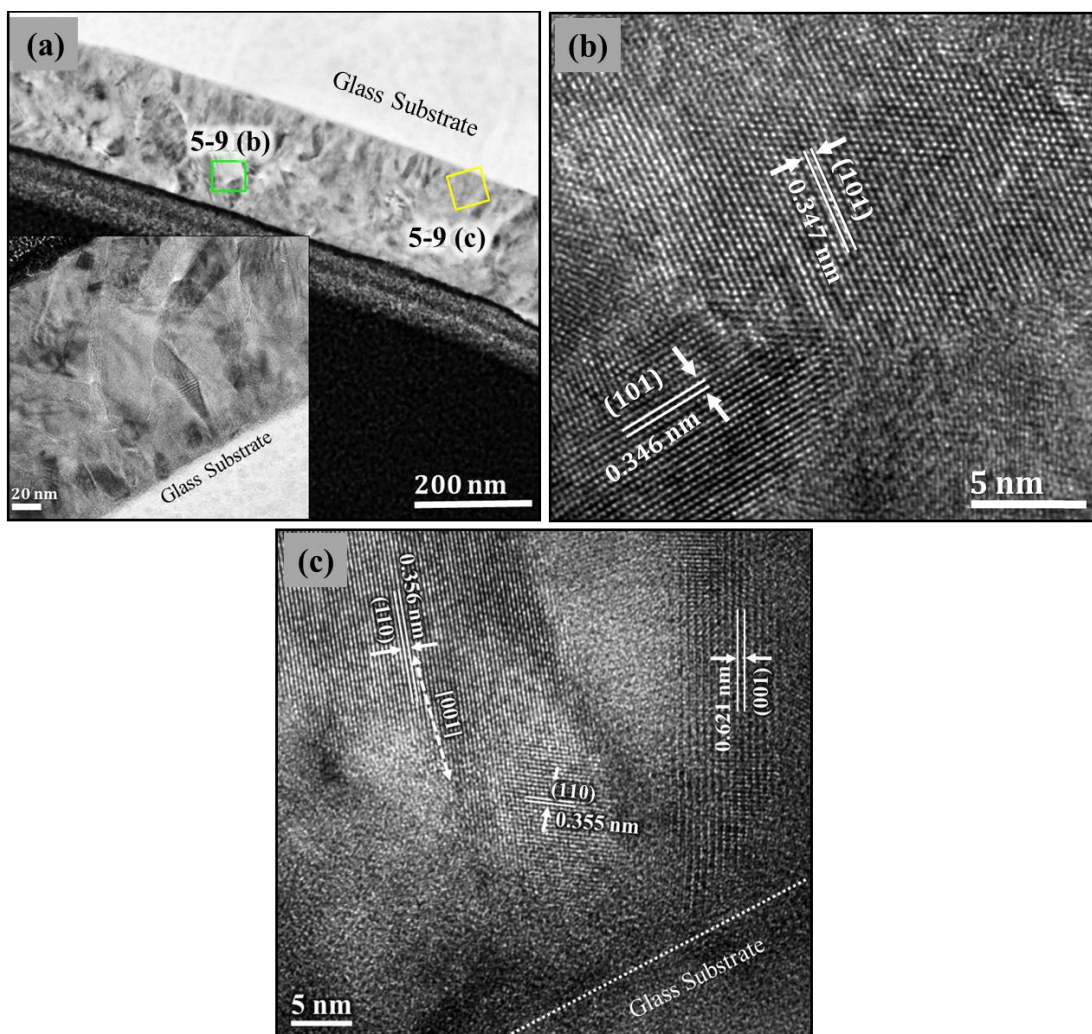


**Figure 5-9** (a) A TEM image of FIB cross section of Plate 4;(b) A HRTEM image taken from FIB-section at a square area labelled as 5-9(b) on the Figure 5-9(a), showing lattice spacings of anatase polygonal plates; (c) A HRTEM image taken from different square area of the Figure 5-9(a), labelled as 5-9(c) of TiO<sub>2</sub>(B) needle-shaped particles illustrates (110) and (001) spacings.

The FIB lift out method was used to prepare a thin cross-sectional TEM sample of Plate 4 as shown in Figure 5-9(a). HRTEM images are presented from two different areas on this cross section: one in a region near the top surface of thin film (Figure 5-9(b)) showing the lattice spacings of anatase TiO<sub>2</sub>; whilst the other is from an area close to the interface between the TiO<sub>2</sub> film and the substrate shown in Figure 5-9(c). In Figure 5-9(a) (inset) and Figure 5-9(c), a number of needle particles are observed at the interface between the glass substrate and the TiO<sub>2</sub> thin film deposit, these exhibit lattice spacings of 3.59Å and 6.21Å consistent with the (110) and (001) spacings of TiO<sub>2</sub>(B) respectively. The majority of needle particles exhibited a preferred growth direction along [001] (as suggested by XRD), however some showed orientations corresponding to [110] and close to [111].

When combined with the XRD results, this suggests that predominantly the needles grow preferentially along their long axis ([001] direction) perpendicular to the substrate, i.e. oriented vertically as illustrated schematically in Figure 5-12. Note this is different to the findings of Li et al. (2011) on powders of  $\text{TiO}_2(\text{B})$  nanowires grown by hydrothermal synthesis who propose a preferred [110] orientation in the nanowires [16] and also different to chapter 4 where it was a [020] preferred orientation.

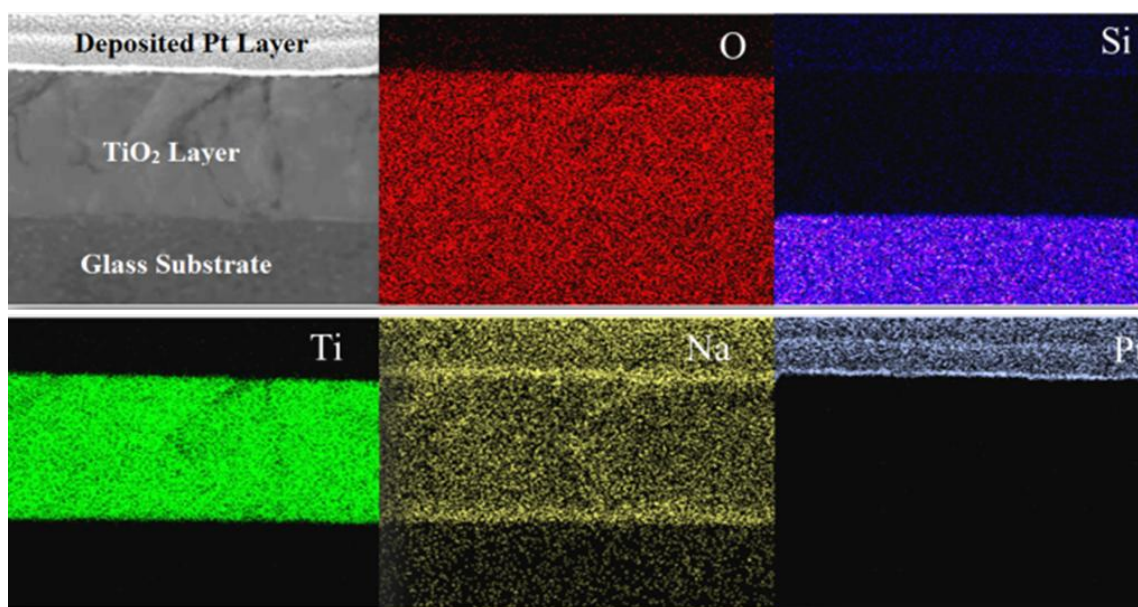


**Figure 5-10** STEM-EDS elemental maps of FIB cross section of Plate 4

Phase-formation in the thin film was investigated by Scanning TEM (STEM) and EDX spectroscopy on the FIB cross-section. STEM/EDX elemental maps, shown in Figure 5-10, indicate the presence of relatively high concentrations of Na (typically a Na/Ti elemental ratio of ca. 0.2) at the interface between the glass substrate and the  $\text{TiO}_2$  film. STEM/EDX line scans also confirm a concentration gradient of Na presumably arising as a result of diffusion from the glass substrate as shown in Figure 5-11. Generally the level of Na gradually decreases with increasing distance from the substrate interface, however there also seems to be a build-up of Na at the top film surface evident in both the maps and the line scans. The present results all indicate that the presence of Na arising from diffusion from the soda lime glass substrate is associated with the formation of a reaction layer of the  $\text{TiO}_2(\text{B})$  phase at the film/substrate interface. This interfacial layer is absent when the thin film is grown on fused quartz, which does not contain sodium. From the pXRD data it is clear that anatase is present even when  $\text{TiO}_2(\text{B})$  is absent and thus the  $\text{TiO}_2(\text{B})$  layer does not appear necessary to seed growth of anatase.

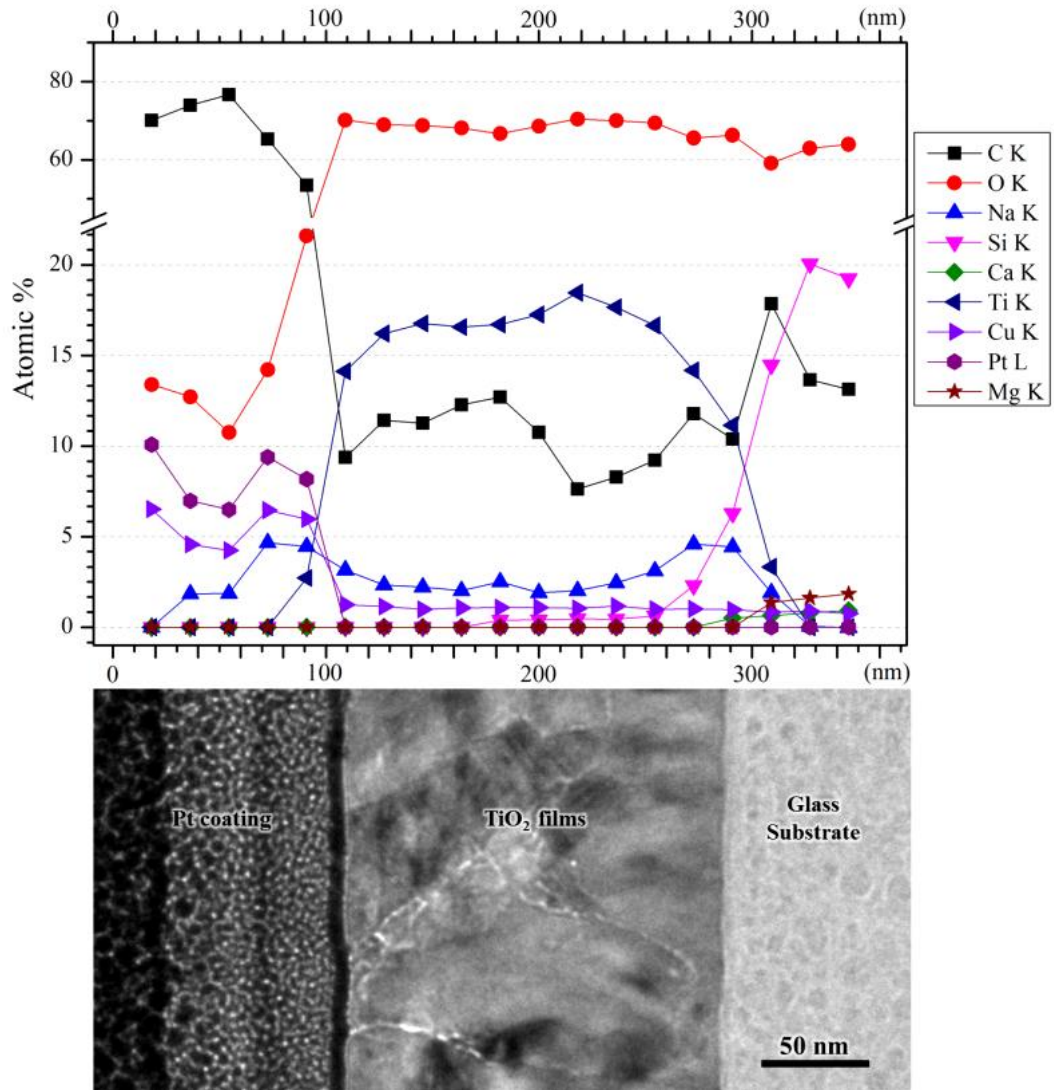


Figure 5-11 STEM-EDS line scanning of FIB cross section of Plate 4.

### 5.3 Discussion

The literature for the preparation of TiO<sub>2</sub>(B) has, until now, concentrated exclusively on the production of powders using synthesis routes such as hydrothermal and sol-gel methods and there is no mention of CVD. All these synthesis routes utilise the same key concept, involving the use of NaOH in addition to the main titanium precursor [17], [18]. All propose similar steps in the synthesis mechanism involving: (1) incorporation of Na<sup>+</sup> into the TiO<sub>2</sub> crystallite forming Sodium Titanate as a first intermediate material; (2) Na<sup>+</sup> in the Sodium Titanate structure is exchanged with H<sup>+</sup> from an acidic solution during post-synthesis processing, producing a second intermediate phase of Hydrogen Titanate; (3) finally a thermal treatment is used to transform the unstable phase of H<sub>x</sub>TiO<sub>y</sub> to the more stable phases of TiO<sub>2</sub> depending on the heat treatment temperature [19].

However, NaOH was not used as a precursor during the present LPCVD deposition of the thin films. However Na is a major constituent of soda lime glass and may contain up to 5 atomic% Na [1]. The silicon-oxygen tetrahedron is the basic building block of the glass framework however cations such as Na<sup>+</sup> ions usually perform the function of cationic counterparts at non-bridging oxygen units. Thus, the Na<sup>+</sup> ions are considered to be mobile. Diffusion of Na<sup>+</sup> from the glass substrate could occur at deposition temperatures of 600°C which is higher than the range of glass transition temperatures of commercial soda-lime glass slides – usually between 564 to 573°C [20]. We calculate the diffusion coefficient of Na<sup>+</sup> in soda-lime glass at 600°C to be of the order of  $4 \times 10^{-7}$  cm<sup>2</sup>/s [21], furthermore the diffusivity of Na<sup>+</sup> increases as pressure is decreased [22], which implies that during reaction sodium ions could diffuse hundreds of microns and hence throughout the film.

From these results it can be concluded that LPCVD deposition method at 600°C with a TTIP precursor normally promotes the formation of the TiO<sub>2</sub> anatase phase on a general substrate, however the existence of Na<sup>+</sup> ions which have diffused from a substrate such as a soda lime glass slide encourages the formation of an oriented TiO<sub>2</sub>(B) reaction layer during TiO<sub>2</sub> thin film deposition. This potential mechanism for TiO<sub>2</sub>(B) formation in the LPCVD process is shown in Figure 5-12. Here I propose three steps for the TiO<sub>2</sub>(B) formation: (1) Na<sup>+</sup> ions migrate to the surface of the substrate during the pre-heat treatment process [23]; (2) owing to higher negative charge of non-bridging oxygen units of TiO<sub>2</sub> than SiO<sub>2</sub>, the Na<sup>+</sup> ions prefer to diffuse from the surface of the substrate into the nascent TiO<sub>2</sub> films leaving a Na-depleted zone in the region of glass neighboring the TiO<sub>2</sub> film [24]; (3) a seeding intermediate phase is formed and this decomposes at temperature so forming TiO<sub>2</sub>(B) needles and leaving Na<sup>+</sup> ions to continuously migrate to the upper surface of the thin film. Further into the film and in the absence of significant amounts of Na, the titania deposits and forms anatase instead of TiO<sub>2</sub>(B) depending on the reaction temperature. This assumption is partially supported by previously reported research where migration from soda glass slide to the initial stages of growth of TiO<sub>2</sub> films produced only brookite TiO<sub>2</sub> or an incomplete phase referred to as Na<sub>2</sub>O.xTiO<sub>2</sub> [25], [26]. Finally it has been reported that TiO<sub>2</sub>(B) synthesized from sodium-containing starting materials promotes particle needle, tube- and rod-shaped morphologies with a preferred growth direction [4], [8], [9], [27] consistent with the needle-morphologies observed in this research.

A number of research reports have indicated improved efficiencies of mixed-phase anatase and TiO<sub>2</sub>(B) over single phase material (either anatase or TiO<sub>2</sub>(B)) for the case of a number of photocatalyst reactions including: methyl

orange degradation [5], sulforhodamine B degradation [4], methylene blue degradation [28], active yellow XRG dye degradation [29], nitrate reduction [3] and the water splitting reaction [30]. As far as I am aware, there have been no reports of the application of mixed-phase materials in self-cleaning glass, however such materials could in principle lead to improved photocatalytic efficiencies. Furthermore,  $\text{TiO}_2(\text{B})$  nanocrystalline thin films have been fabricated using spin-dip coating onto conductive glass substrates for use as a replacement for graphite anodes in lithium ion batteries. Potentially the high surface area and mesoporosity of such nanostructured films could lead to improved storage capacities and the present CVD route may offer a potential alternative route for their fabrication provided a sodium source could be incorporated in the substrate.

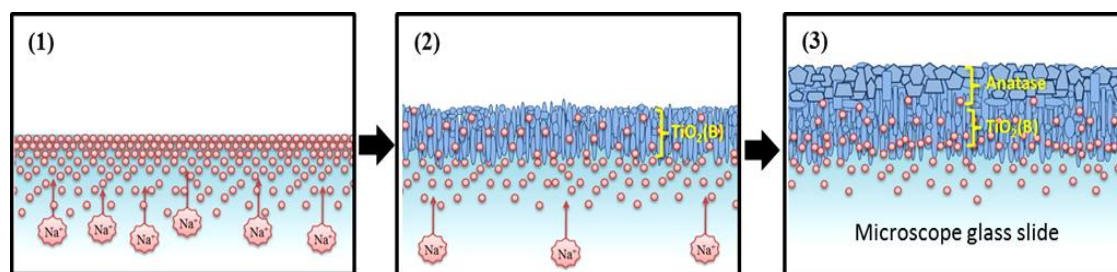


**Figure 5-12** Proposed mechanism for synthesis of mixed phase  $\text{TiO}_2$  thin films by LPCVD method

## 5.4 Conclusions

Titania films have been prepared by low pressure chemical vapour deposition on soda-lime glass substrates. Using 5 mL of a TTIP precursor deposited for 15 min at  $550^\circ\text{C}$  (actual temperature) on the substrate, around 200 nm thick  $\text{TiO}_2$  thin films consisting of dual phase monoclinic  $\text{TiO}_2(\text{B})$  needles and larger anatase polygonal plates were observed. The small nano-needles of the  $\text{TiO}_2(\text{B})$  phase were located at the interface with the substrate and exhibited a preferred orientation along [001]. These needles were absent when the substrate was fused quartz. A mechanism for the CVD synthesis of  $\text{TiO}_2(\text{B})$  is presented involving diffusion of Na from the glass substrates. To my knowledge, this is the first time the monoclinic  $\text{TiO}_2(\text{B})$  phase has been prepared by a CVD method. Potentially this fabrication route could be of benefit for production of photocatalytic devices and replacement anodes for lithium ion batteries.

## 5.5 References

- [1] Y. Paz, Z. Luo, L. Rabenberg, and A. Heller, "Photooxidative self-cleaning transparent titanium dioxide films on glass," *J. Mater. Res.*, vol. 10, no. 11, pp. 2842–2848, 2011.
- [2] A.J. Cross, C.W. Dunnill, and I.P. Parkin, "Production of predominantly anatase thin films on various grades of steel and other metallic substrates from  $\text{TiCl}_4$  and ethyl acetate by atmospheric pressure CVD," *Chem. Vap. Depos.*, vol. 18, no. 4–6, pp. 133–139, 2012.
- [3] M.M. Mohamed, B.H.M. Asghar, and H.A. Muathen, "Facile synthesis of mesoporous bicrystallized  $\text{TiO}_2(\text{B})$ /anatase(rutile) phases as active photocatalysts for nitrate reduction," *Catal. Commun.*, vol. 28, pp. 58–63, 2012.
- [4] D. Yang, H. Liu, Z. Zheng, Y. Yuan, J. Zhao, E.R. Waclawik, X. Ke, and H. Zhu, "An efficient photocatalyst structure:  $\text{TiO}_2(\text{B})$  nanofibers with a shell of anatase nanocrystals," *J. Am. Chem. Soc.*, vol. 131, no. 49, pp. 17885–17893, 2009.
- [5] C. Huang, K. Zhu, M. Qi, Y. Zhuang, and C. Cheng, "Preparation and photocatalytic activity of bicrystal phase  $\text{TiO}_2$  nanotubes containing  $\text{TiO}_2\text{-B}$  and anatase," *J. Phys. Chem. Solids*, vol. 73, no. 6, pp. 757–761, 2012.
- [6] Z. Zheng, H. Liu, J. Ye, J. Zhao, E.R. Waclawik, and H. Zhu, "Structure and contribution to photocatalytic activity of the interfaces in nanofibers with mixed anatase and  $\text{TiO}_2(\text{B})$  phases," *J. Mol. Catal. A Chem.*, vol. 316, no. 1–2, pp. 75–82, 2010.
- [7] Y. Bai, W. Li, C. Liu, Z. Yang, X. Feng, X. Lu, and K.Y. Chan, "Stability of Pt nanoparticles and enhanced photocatalytic performance in mesoporous Pt-(anatase/ $\text{TiO}_2(\text{B})$ ) nanoarchitecture," *J. Mater. Chem.*, vol. 19, no. 38, pp. 7055, 2009.
- [8] R. Giannuzzi, M. Manca, L. De-Marco, M.R. Belviso, A. Cannavale, T. Sibillano, C. Giannini, P.D. Cozzoli, and G. Gigli, "Ultrathin  $\text{TiO}_2(\text{B})$  nanorods with superior lithium-Ion storage performance," *ACS Appl. Mater. Interfaces*, vol. 6, no. 3, pp. 1933–1943, 2014.
- [9] A.R. Armstrong, G. Armstrong, J. Canales, R. García, and P.G. Bruce, "Lithium-Ion Intercalation into  $\text{TiO}_2\text{-B}$  Nanowires," *Adv. Mater.*, vol. 17, no. 7, pp. 862–865, 2005.
- [10] M. René, B. Luc, and T. Michel, " $\text{TiO}_2(\text{B})$  a new form of titanium dioxide and the Potassium octatitanate  $\text{K}_2\text{Ti}_8\text{O}_{17}$ ," *Mater. Res. Bull.*, vol. 15, pp. 1129–1133, 1980.
- [11] T. Beuvier, M. Richard-plouet, and L. Brohan, "Accurate methods for quantifying the relative ratio of anatase and  $\text{TiO}_2(\text{B})$  nanoparticles," *J. Phys. Chem. C*, vol. 113, no. 31, pp. 13703–13706, 2009.
- [12] M.B. Yahia, F. Lemoigno, T. Beuvier, J.S. Filhol, M. Richard-Plouet, L. Brohan, and M.L. Doublet, "Updated references for the structural, electronic, and vibrational properties of  $\text{TiO}_2(\text{B})$  bulk using first-principles density functional theory calculations.," *J. Chem. Phys.*, vol. 130, no. 20, pp. 204501, 2009.

- [13] F.P. Koffyberg, K. Dwight, and A. Wold, "Interband transition of semiconducting oxides determined from photoelectrolysis spectra," *Solid State Commun.*, vol. 30, pp. 433–437, 1979.
- [14] G. Betz and H. Tributsch, "Hydrogen insertion (intercalation) and light induced proton exchange at TiO<sub>2</sub>(B)-electrodes," *J. Appl. Electrochem.*, vol. 14, pp. 315–322, 1984.
- [15] G. Nussli, K. Yoshizawa, and T. Yamabe, "Lithium intercalation in TiO<sub>2</sub> modifications," *J. Mater. Chem.*, vol. 7, no. 12, pp. 2529–2536, 1997.
- [16] J. Li, W. Wan, H. Zhou, J. Li, and D. Xu, "Hydrothermal synthesis of TiO<sub>2</sub>(B) nanowires with ultrahigh surface area and their fast charging and discharging properties in Li-ion batteries," *Chem. Commun. (Camb.)*, vol. 47, no. 12, pp. 3439–3441, 2011.
- [17] C.W. Peng, T.Y. Ke, L. Brohan, M. Richard-Plouet, J.C. Huang, E. Puzenat, H.T. Chiu, and C.Y. Lee, "(101)-Exposed anatase TiO<sub>2</sub> nanosheets," *Chem. Mater.*, vol. 20, no. 7, pp. 2426–2428, 2008.
- [18] T. Beuvier, M. Richard-Plouet, and L. Brohan, "Ternary morphological diagram for nano(tube–ribbon–sphere) sodium titanate deduced from raman spectra analysis," *J. Phys. Chem. C*, vol. 114, no. 17, pp. 7660–7665, 2010.
- [19] V. Gentili, S. Brutti, L.J. Hardwick, A.R. Armstrong, S. Panero, and P.G. Bruce, "Lithium insertion into anatase nanotubes," *Chem. Mater.*, vol. 24, no. 22, pp. 4468–4476, 2012.
- [20] A. Fluegel, D.A. Earl, A.K. Varshneya, and D. Oksoy, "Statistical analysis of viscosity, electrical resistivity, and further glass melt properties," in *High temperature glass melt property database for process modeling*, vol. 72, T. P. Seward and T. Vascott, Eds. Ohio: Wiley, 2006.
- [21] M. Braedt and G.H. Frischat, "Sodium self-diffusion coefficients in alkali silicate glass melts as obtained by a microgravity experiment," *Commun. Am. Ceram. Soc.*, pp. c54–56, 1984.
- [22] J.G. Bryce, F.J. Spera, and D.J. Stein, "Pressure dependence of self-diffusion in the NaAlO<sub>2</sub>-SiO<sub>2</sub> system: Compositional effects and mechanisms," *Am. Mineral.*, vol. 84, pp. 345–356, 1999.
- [23] G.H. Frischat, "Sodium diffusion in SiO<sub>2</sub> glass," *J. Am. Ceram. Soc.*, vol. 51, no. 9, pp. 528–530, 1968.
- [24] E. Aubry, J. Lambert, V. Demange, and A. Billard, "Effect of Na diffusion from glass substrate on the microstructural and photocatalytic properties of post-annealed TiO<sub>2</sub> films synthesised by reactive sputtering," *Surf. Coatings Technol.*, vol. 206, no. 23, pp. 4999–5005, 2012.
- [25] H. Schroeder, "Oxide Layer deposited from organic solution," in *Physics of thin films*, 5th ed., vol. 5, G. Hass and R. E. Thun, Eds. New York and London: Academic press, 1969, pp. 87–140.
- [26] C. Ohara, T. Hongo, A. Yamazaki, and T. Nagoya, "Synthesis and characterization of brookite/anatase complex thin film," *Appl. Surf. Sci.*, vol. 254, no. 20, pp. 6619–6622, 2008.

- [27] Z. Liu, Y.G. Andreev, A.R. Armstrong, S. Brutti, Y. Ren, and P.G. Bruce, "Nanostructured TiO<sub>2</sub>(B): the effect of size and shape on anode properties for Li-ion batteries," *Prog. Nat. Sci. Mater. Int.*, vol. 23, no. 3, pp. 235–244, 2013.
- [28] C.W. Peng, M. Richard-Plouet, T.Y. Ke, C.Y. Lee, H.T. Chiu, C. Marhic, E. Puzenat, F. Lemoigno, and L. Brohan, "Chimie Douce Route to Sodium Hydroxo Titanate Nanowires with Modulated Structure and Conversion to Highly Photoactive Titanium Dioxides," *Chem. Mater.*, vol. 20, no. 23, pp. 7228–7236, 2008.
- [29] J. Zhu, J. Zhang, F. Chen, and M. Anpo, "Preparation of high photocatalytic activity TiO<sub>2</sub> with a bicrystalline phase containing anatase and TiO<sub>2</sub>(B)," *Mater. Lett.*, vol. 59, no. 27, pp. 3378–3381, 2005.
- [30] S.K. Parayil, H.S. Kibombo, L. Mahoney, C. Wu, M. Yoon, and R.T. Koodali, "Synthesis of mixed phase anatase-TiO<sub>2</sub>(B) by a simple wet chemical method," *Mater. Lett.*, vol. 95, pp. 175–177, 2013.

## **Chapter 6 Universal synthesis method for mixed phase TiO<sub>2</sub>(B) and anatase TiO<sub>2</sub> thin films on substrates via a modified low pressure chemical vapour deposition (LPCVD) route**

In the previous chapter I reported the formation of mixed phase TiO<sub>2</sub>(B) and anatase thin films containing a majority phase of TiO<sub>2</sub>(B) using low pressure chemical vapour deposition (LPCVD) at 600°C on soda-lime glass substrates. It was suggested that TiO<sub>2</sub>(B) formed as a result of diffusion of Na from the soda-lime glass substrate which encouraged phase formation during the deposition process. This finding is promising as it may lead to LPCVD being selected for the synthesis of TiO<sub>2</sub>(B) thin films providing they can be deposited on conducting substrates for application in Li ion battery anodes.

To address this issue, I propose a new method involving pre-treatment of substrates with Na from external sources prior to LPCVD deposition in order to promote TiO<sub>2</sub>(B) formation as a result of Na diffusion from this pre-treated surface layer. I demonstrate the success of this method using Si wafer, fused quartz, HOPG and grafoil substrates. I speculate that this could be of use for not only lithium battery electrodes but also mixed TiO<sub>2</sub> phase photocatalysts with higher efficiency than the pure anatase phase [1]–[4].

### **6.1 Experimental Procedure**

#### **6.1.1 Substrate Pre-treatment**

The substrates used were: fused quartz, silicon wafer, HOPG and grafoil. The cleaned substrates pre-treated by spraying onto the surface 0.5 mL of a NaOEt solution in varying concentrations between 0.1-5.0 %<sup>W</sup>/<sub>V</sub> of Na. The details of the substrate pre-treatment were described in chapter 3, section 3.1.2.3.3.

#### **6.1.2 TiO<sub>2</sub> Thin Film Deposition**

LPCVD was used to prepare TiO<sub>2</sub> thin films on the desired pre-treated substrate; details of this equipment being described in chapter 3, section 3.1.2.3. From the previous studies, the optimum conditions for the synthesis of the TiO<sub>2</sub>(B) phase on soda-lime glass substrates was 600°C at a pressure of 25 mbar and hence the same conditions as describe in chapter 5 were applied here. Sample nomenclature was x%\_Substrate, where x and Substrate are the %<sup>W</sup>/<sub>V</sub> of the sprayed Na solution and type of substrate respectively.

### 6.1.3 Materials Characterization

All thin film samples were characterized using the same methods as described in chapter 3 and chapter 5.

## 6.2 Results and Discussion

### 6.2.1 X-ray Diffraction

The XRD patterns of the films on the 4 different substrates are shown in Figure 6-1. XRD of the 0.5%\_Si and 0.5%\_Fused quartz samples clearly show peaks which can be assigned to  $\text{TiO}_2(\text{B})$  (JCPDS 04-007-6246) and anatase (JCPDS 00-021-1272) phases together with peaks from the Si wafer substrate (labelled S) and a broad peak lying between  $20\text{-}23^\circ$   $2\theta$  from the amorphous quartz substrate respectively. Calculated crystallite (grain) sizes of the  $\text{TiO}_2(\text{B})$  and anatase phases derived using XRD line broadening and Scherrer's equation are  $42\pm 5$  and  $30\pm 5$  nm respectively on 0.5%\_Si, while for 0.5%\_ Fused quartz the corresponding values are  $40\pm 5$  nm and  $35\pm 5$  nm. However, for both the 0.5%\_HOPG and 0.5%\_Grafoil samples only intense peaks at  $26.48^\circ$  and  $54.57^\circ$  are observed corresponding to the (002) and (004) spacings of the highly oriented graphite substrates (JCPDS 00-041-1487), with no obvious diffraction peaks of  $\text{TiO}_2(\text{B})$  or anatase evident; this was the case even if the substrate was oriented slightly off axis.

### 6.2.2 Raman Spectroscopy

Owing to the sensitivity issue with XRD when in the presence of a highly oriented substrate, the thin films on all four substrates were also characterized by Raman spectroscopy and the results are displayed in Figure 6-2. It may be seen that Raman active modes of both  $\text{TiO}_2(\text{B})$  and anatase phases are present in all samples, in addition to the characteristic peaks from the substrates which are  $520.80\text{ cm}^{-1}$  for the Si wafer and  $1584.71\text{ cm}^{-1}$  for graphitic substrates (both HOPG and Grafoil) [5]. The Raman active modes for anatase appear as an intense peak at  $141.53\text{ cm}^{-1}$  with three other weaker peaks at  $399.60$ ,  $512.31$  and  $631.98\text{ cm}^{-1}$  [6], whereas the remaining peaks are all Raman active modes of the  $\text{TiO}_2(\text{B})$  phase, particularly three strong peaks at  $122.05$ ,  $196.21$  and  $361.76\text{ cm}^{-1}$  [7]. However, the relative intensities of the anatase and  $\text{TiO}_2(\text{B})$  Raman peaks phase cannot be compared directly in order to determine phase fractions, as the relative sensitivity of the anatase-active modes is six times higher than those of the  $\text{TiO}_2(\text{B})$  phase [8][9]. Nonetheless, the Raman results do confirm that all thin film samples consist of a mixed phase of  $\text{TiO}_2(\text{B})$  plus anatase.

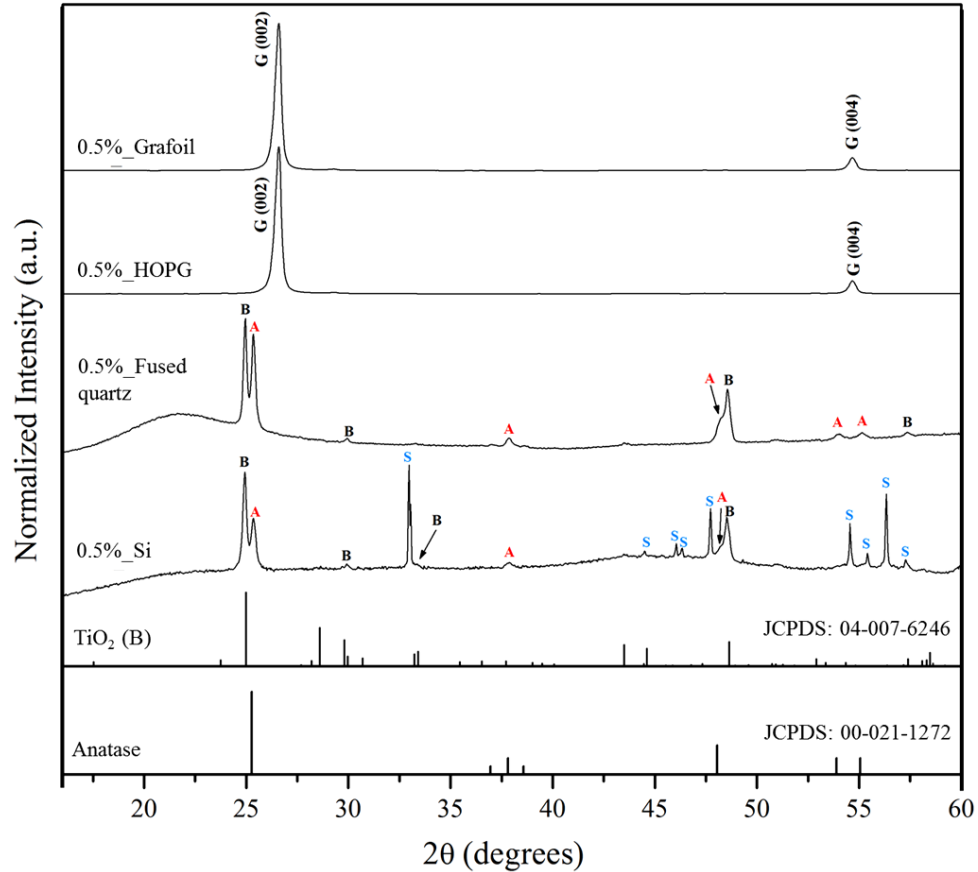


**Figure 6-1** XRD patterns of TiO<sub>2</sub> thin films deposited onto four different substrates: Si wafer, fused quartz, HOPG and Grafoil; A, B, S and G refer to peak assignments to TiO<sub>2</sub> anatase phase, TiO<sub>2</sub>(B) phase, Si substrate and graphite substrate respectively. The substrates were first prepared with a very thin layer of Na-containing compound via spraying a 0.5%<sup>W</sup>/<sub>V</sub> sodium solution onto the substrate surfaces.

### 6.2.3 Scanning Electron Microscopy

SEM plan view images of 0.5%\_Si, 0.5%\_Fused quartz, 0.5%\_HOPG and 0.5%\_Grafoil samples are shown in Figure 6-3. These all show similar particle morphologies consisting of a majority of equi-axed/spherical primary particles (possibly single crystallites) of around 20-50 nm which appear aggregated, together with a minor component of bigger particles with an irregular polygonal-like appearance. From this bimodal distribution, the average primary particle sizes in 0.5%\_Si, 0.5%\_Fused quartz, 0.5%\_HOPG and 0.5%\_Grafoil are 56.3±1.2 (S.D=19.8), 49.7±1.2 (S.D=18.6), 44.1±1.2 (S.D=15.7) and 91.7±1.2 (S.D=64.4) nm respectively. All samples show similar particle sizes except 0.5%\_Grafoil which is almost two times as large, as seen in Figure 6-3(d). SEM/EDX was also used to investigate the thin film compositions and the results are given in Table 6-1. As the electron beam interaction volume penetrates below the thin films, the exact compositions are dependent not only on the type of substrate but also the thickness of the TiO<sub>2</sub> films. However, the results confirm the presence of a titanium oxide thin film with retention of sodium in the deposited structure.

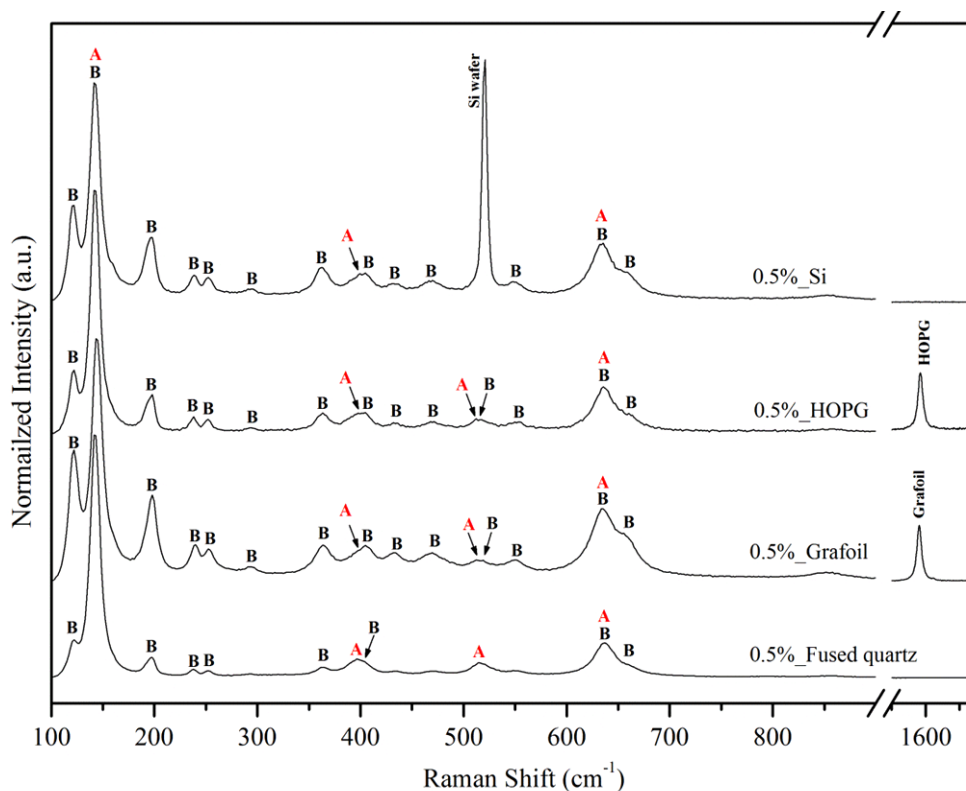


**Figure 6-2** Raman spectra of TiO<sub>2</sub> thin films deposited onto four different substrates: Si wafer, fused quartz, HOPG and Grafoil; A and B indicate peaks due to the anatase and TiO<sub>2</sub>(B) phases respectively

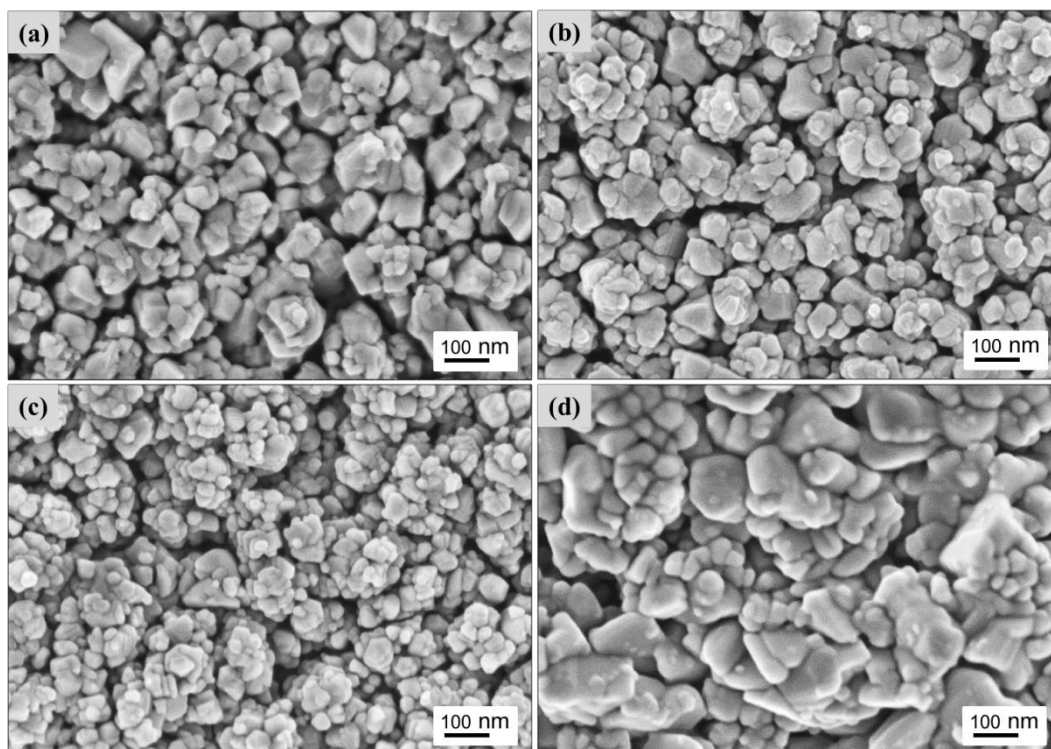


**Figure 6-3** SEM secondary electron images of TiO<sub>2</sub> particles from the top surface of thin films deposited on: (a) Si wafer (b) fused quartz (c) HOPG and (d) Grafoil substrates respectively.

In Figure 6-4, cross-sectional samples have been investigated by SEM and reveal the thickness and physical morphology of the TiO<sub>2</sub> films. The average thicknesses of the TiO<sub>2</sub> layers in 0.5%\_Si, 0.5%\_ Fused quartz and 0.5%\_HOPG are all approximately 0.5 μm as shown in Table 6-1. Interestingly, in 0.5%\_Grafoil the film is found to be significantly thicker at around 2.1 μm, which is strange as all deposition parameters (such as substrate position in furnace tube relative to the gas entry point, the quantity of TTIP precursor, the carrier gas flow rate, the reaction temperature and reaction time) were carefully controlled and remained constant. It may be that the increased surface roughness of the Grafoil may have caused the as-deposited films to become thicker [10]. The cross-sectional SEM images of 0.5%\_Si, 0.5%\_Fused quartz and 0.5%\_HOPG, all show columnar growth of TiO<sub>2</sub> nanoparticles with a minority of smaller, rounder nanoparticles predominantly present at the substrate interface. In contrast 0.5%\_Grafoil (Figure 6-4(d)) exhibits irregularly-shaped larger particles.

**Table 6-1** List of synthesised samples with results of SEM/EDX quantitative elemental analysis, XRD crystallite size and primary particle size and film thickness derived from SEM.

| Sample            | Composition in Atom% from SEM/EDX |       |       |       |       | Calculated crystallite size by Scherrer's equation (nm) |         | Measured primary particle size (nm) | Measured film thickness (μm) |
|-------------------|-----------------------------------|-------|-------|-------|-------|---|---------|-------------------------------------|------------------------------|
|                   | Na                                | Si    | Ti    | O     | C     | TiO <sub>2</sub> (B)                                    | Anatase |                                     |                              |
| 0.5%_Si           | 0.68                              | 11.19 | 22.39 | 60.41 | 5.33  | 42±5  | 30±5    | 56.3±1.2<br>(S.D=19.8)              | 0.463±0.003<br>(S.D=0.024)   |
| 0.5%_Fused quartz | 1.67                              | 31.85 | 9.73  | 48.98 | 7.77  | 40±5  | 35±5    | 49.7±1.2<br>(S.D=18.6)              | 0.650±0.003<br>(S.D=0.023)   |
| 0.5%_HOPG         | 0.95                              | 0     | 16    | 46.86 | 36.19 | N/A   | N/A     | 44.1±1.2<br>(S.D=15.8)              | 0.485±0.003<br>(S.D=0.018)   |
| 0.5%_Grafoil      | 0.29                              | 0     | 14.31 | 45.76 | 39.64 | N/A   | N/A     | 91.7±1.2<br>(S.D=64.4)              | 2.068±0.003<br>(S.D=0.209)   |

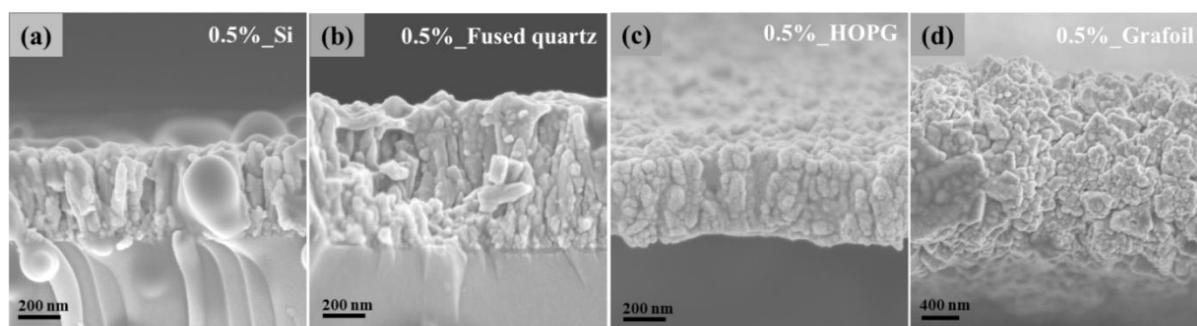


**Figure 6-4** SEM cross-sectional images of TiO<sub>2</sub> thin films deposited on: (a) Si wafer (b) fused-quartz (c) HOPG and (d) Grafoil substrates

### 6.2.4 Transmission Electron Microscopy

Figure 6-5 shows the TEM results from sample 0.5%\_Si (thin film simply scraped off onto a TEM support film) and reveals an equi-axed grain morphology with a grain-size range of 20-80 nm and an average of ca. 35 nm. The inset magnified image in Figure 6-5(a), exhibits a lattice fringe spacing of  $5.86 \pm 0.02 \text{ \AA}$  consistent with the (200) spacing of  $\text{TiO}_2(\text{B})$ . Further, the HRTEM image in figure 6(b) shows lattice fringes of spacing  $3.57 \pm 0.02 \text{ \AA}$  which can be indexed as the (110) lattice spacing of  $\text{TiO}_2(\text{B})$  whilst a Fast Fourier Transform (FFT) of the area defined by the red square in Figure 6-5(b) indexes to the  $\text{TiO}_2(\text{B})$  phase. Conversely, Figure 6-5(c) provides evidence for lattice spacings of anatase  $\text{TiO}_2$ :  $3.47 \pm 0.02 \text{ \AA}$ ,  $2.41 \pm 0.02 \text{ \AA}$  and  $2.32 \pm 0.02 \text{ \AA}$  corresponding to the (101), (103) and (004) interplanar spacings respectively. An FFT of the area defined by the red square in Figure 6-5(c) indexes to  $\text{TiO}_2$  anatase.

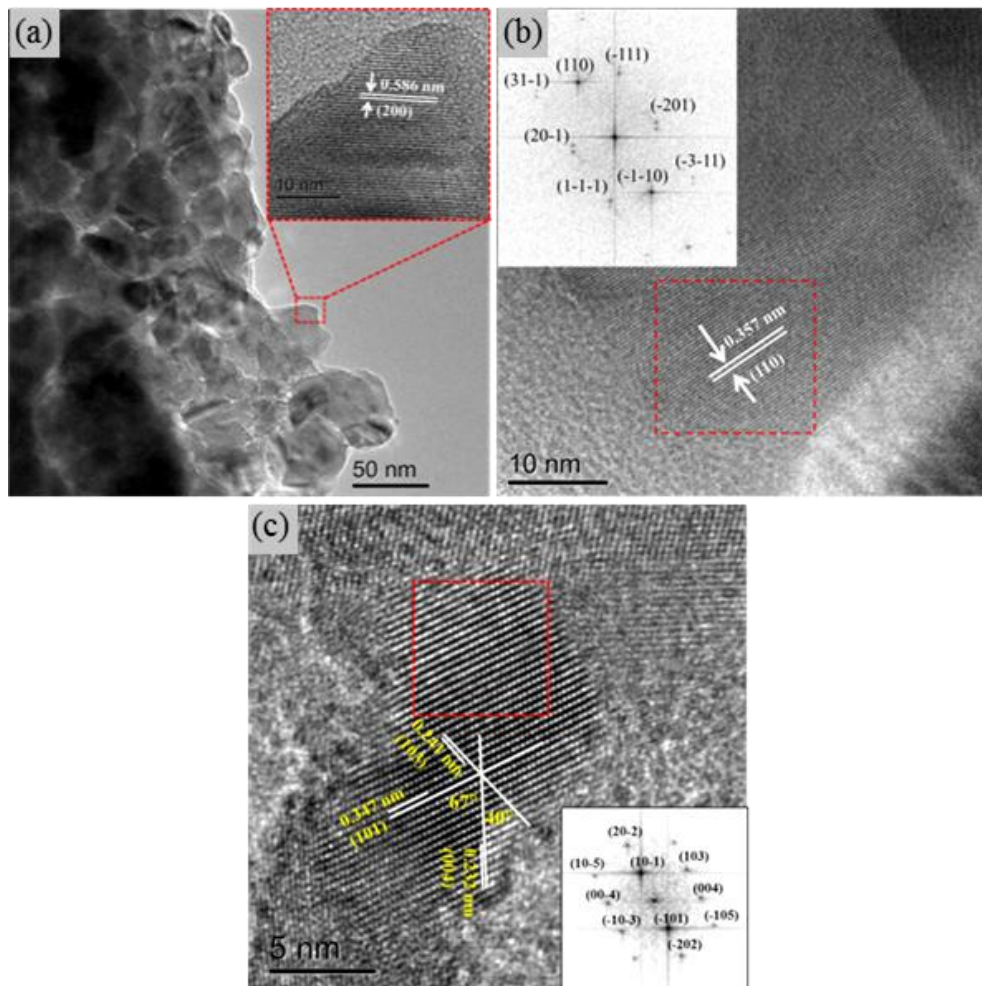


**Figure 6-5** (a) A bright field TEM image taken from 0.5%\_Si, showing an equi-axed particle morphology; (b) a HRTEM image of a  $\text{TiO}_2(\text{B})$  particle and (c) a HRTEM image of anatase particles, both with the corresponding fast Fourier transforms of the image inset.

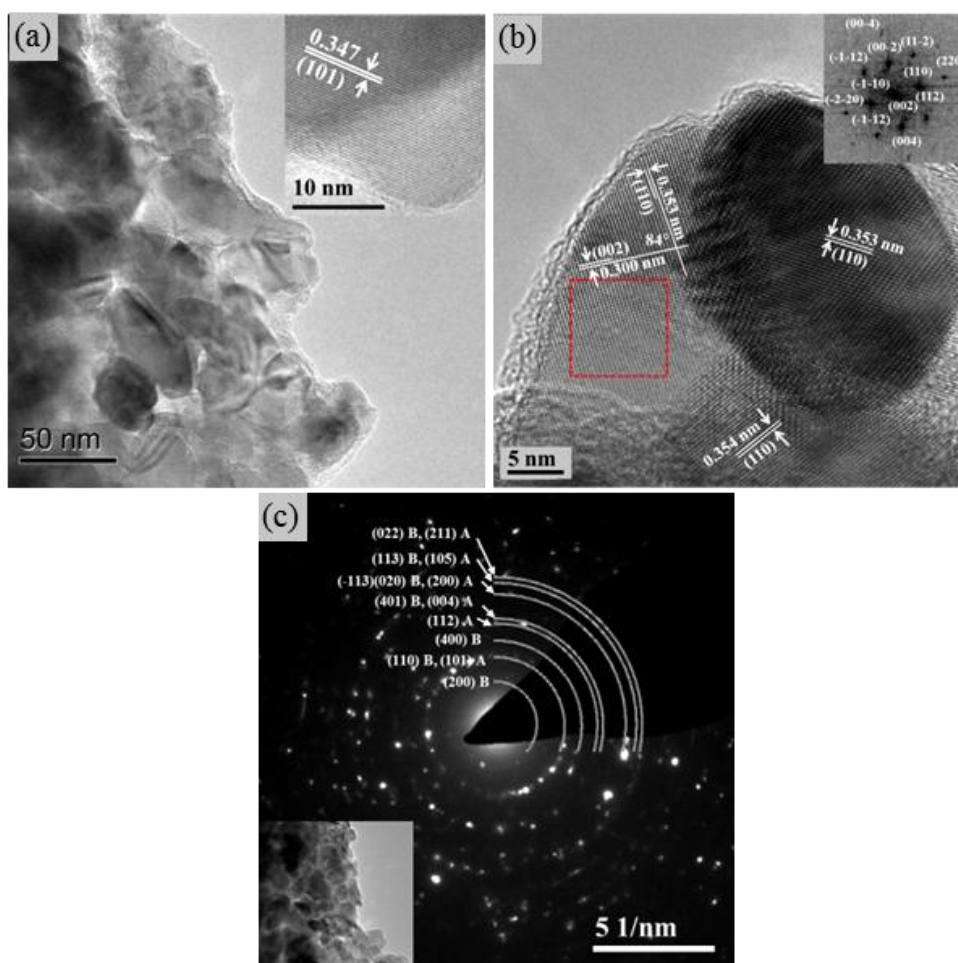


**Figure 6-6** (a) A bright field TEM image taken from 0.5%\_Fused quartz; (b) a HRTEM image of  $\text{TiO}_2(\text{B})$  with corresponding fast Fourier transform of the image inset; (c) a diffraction pattern of a group of particles shown in the image inset.

A bright-field TEM image of sample 0.5%\_Fused Quartz is shown in Figure 6-6(a) and again shows an equi-axed grain morphology with a grain size of between 20 and 80 nm. The lattice spacing of  $3.47 \pm 0.02 \text{ \AA}$  assigned as (101) of anatase is illustrated in the inset image in Figure 6-6(a). As displayed in Figure 6-6(b),  $\text{TiO}_2(\text{B})$  lattice spacings were also found to be present in other grains. Furthermore, TEM selected area diffraction from a group of grains is shown in Figure 6-6(c) and reveals ring spacings characteristic of both  $\text{TiO}_2(\text{B})$  (the (200), (110), (400), (401), (113), (020), (113) and (022) spacings) and also anatase (the (101), (112), (004), (200), (105) and (211) spacings). I observed that anatase and  $\text{TiO}_2(\text{B})$  phases possessed a similar grain size and grain morphology.

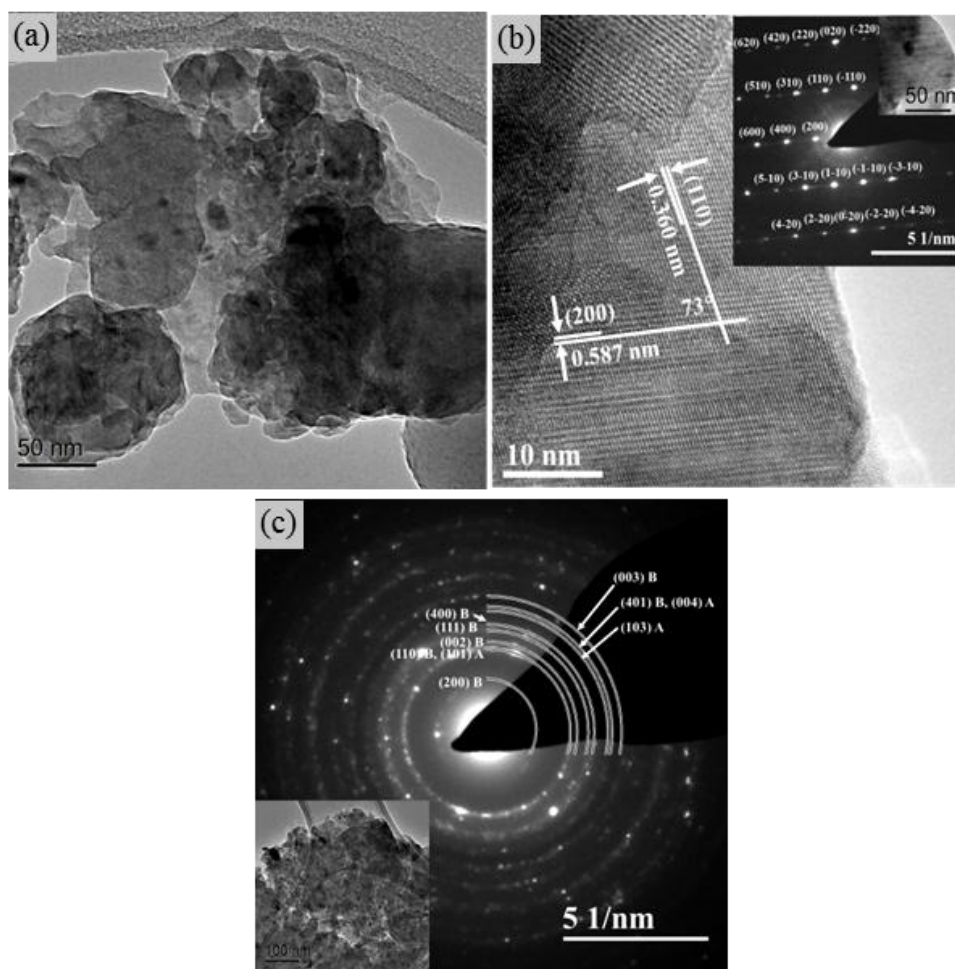


**Figure 6-7** (a) A typical TEM image taken from 0.5%\_HOPG; (b) a HRTEM image of a  $\text{TiO}_2(\text{B})$  particle with associated electron diffraction pattern; (c) diffraction pattern taken from a group of particles shown in the image inset.

A typical low-magnification TEM image of sample 0.5%\_HOPG is shown in Figure 6-7(a), suggesting a smaller grain size off between 20-60 nm than for samples 0.5%\_Si and 0.5%\_Fused quartz. A TEM image of a grain together with a selected area diffraction pattern is displayed in Figure 6-7(b), the lattice spacings of  $3.60 \pm 0.02 \text{ \AA}$  and  $5.87 \pm 0.02 \text{ \AA}$  with an interplanar angle of  $73^\circ$  are consistent with the (110) and (200) spacings of  $\text{TiO}_2(\text{B})$  whilst the diffraction pattern also indexes to  $\text{TiO}_2(\text{B})$ . In Figure 6-7(c), selected area electron diffraction from a group of grains exhibits rings corresponding to the (200), (110), (002), (111), (400), (401) and (003) lattice spacings of  $\text{TiO}_2(\text{B})$ , as well as the (101), (103) and (004) lattice spacings of the anatase phase and also reveals the coexistence of both phases in this sample

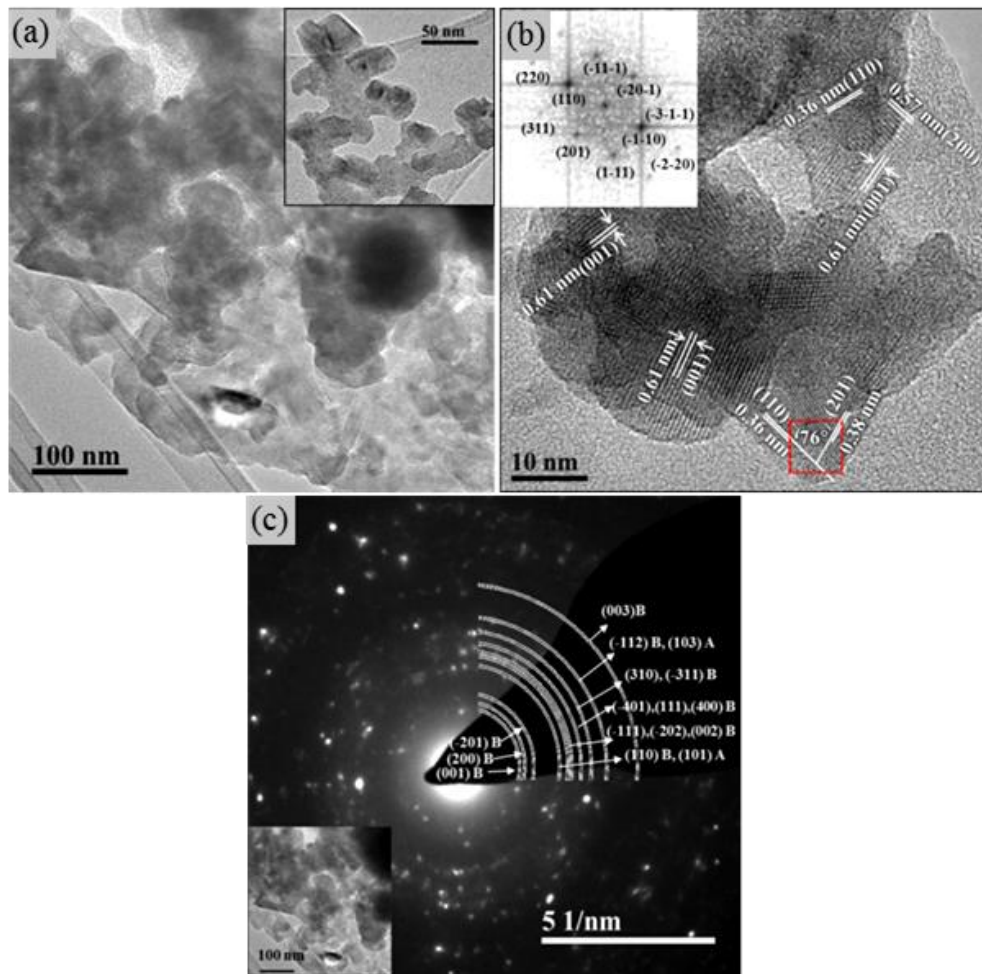


**Figure 6-8** (a) A bright field TEM image taken from 0.5%\_Grafoil; (b) a HRTEM image of a group of TiO<sub>2</sub>(B) with corresponding fast Fourier transform of the image inset; (c) a diffraction pattern of a group of particles shown in the image inset.

A range of titanium dioxide grains in the 0.5%\_Grafoil sample is presented in a typical TEM image with an inset image in Figure 6-8(a); the grains range in size between 20-100 nm which is bigger than for the other LPCVD samples and correlates with the SEM image shown in Figure 6-4(d). A high resolution TEM image of a group of titania grains with a corresponding fast Fourier transform from the area defined by the red square in Figure 6-8(b), strongly indicates the TiO<sub>2</sub>(B) phase. Finally, a selected area electron diffraction pattern from a number of grains is shown in Figure 6-8(C) and exhibits polycrystalline TiO<sub>2</sub>(B) and anatase ring spacings.

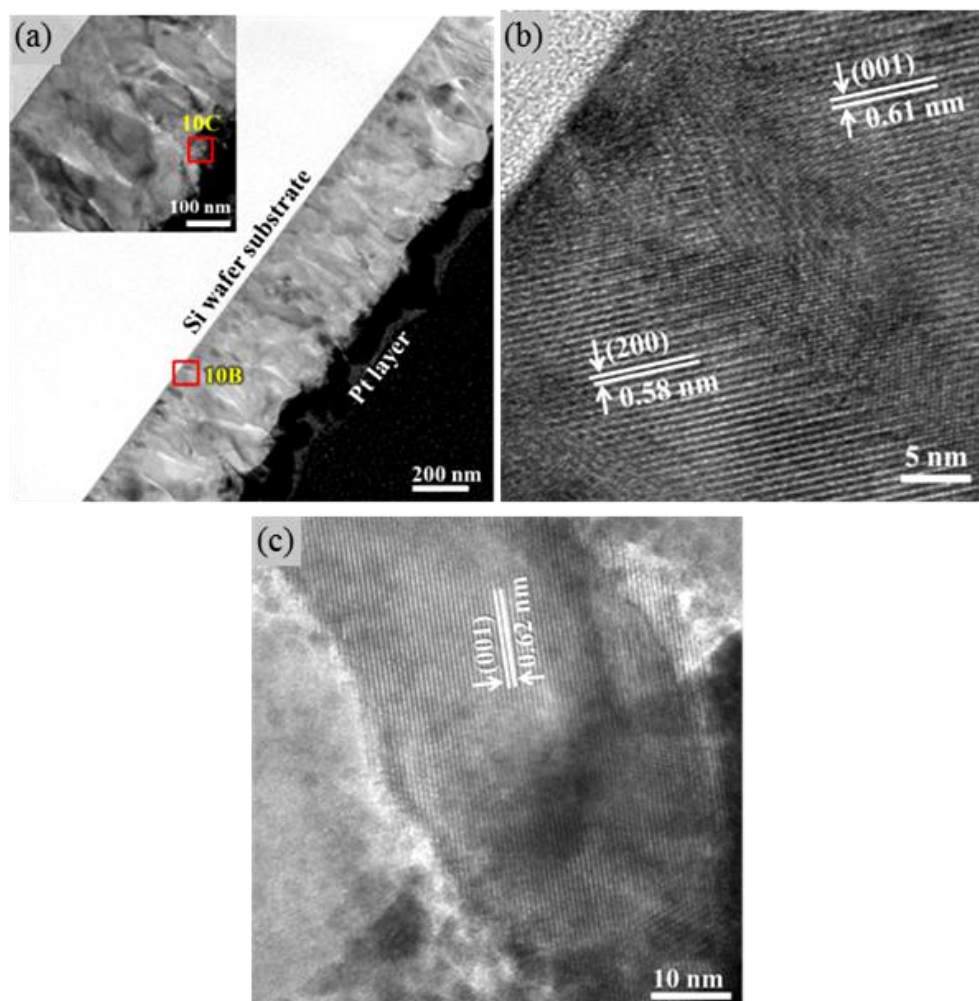


**Figure 6-9** (a) A TEM image of a FIB cross-section of 0.5%\_Si; (b) corresponding HRTEM image at the TiO<sub>2</sub>/Si wafer interface labeled as 10B in (a); (c) HRTEM image taken from the TiO<sub>2</sub>/protective Pt layer interface labeled as 10C in (a).

TEM results confirm the presence of both anatase and TiO<sub>2</sub>(B) phases in all samples, in agreement with the findings of Raman and XRD. However in order to investigate the microstructure of the film in more detail, a TEM cross-section was prepared by the Focused Ion Beam (FIB) lift out method. Bright field TEM images of a cross-sectional sample of 0.5%\_Si sample are shown in Figure 6-9(a) and reveal a columnar morphology with crystal growth perpendicular to the Si wafer substrate. Closer inspection at the interface between the substrate and the titania film reveals smaller more equi-axed grains as observed by SEM (Figure 6-4(a)). Two high resolution TEM images are presented in Figure 6-9(b) and Figure 6-9(c) which are taken from two different regions within the titania thin film: Figure 6-9(b) is an interfacial region between the Si wafer substrate and the TiO<sub>2</sub> film, whilst Figure 6-9(c) is an area of thin film near the top surface which is close to the protective Pt layer deposited in the FIB. The small grains at the interface in Figure 6-9(b), exhibit

lattice spacings of  $6.11 \pm 0.06 \text{ \AA}$  and  $5.78 \pm 0.06 \text{ \AA}$  which are assigned to the (001) and (200) planes of  $\text{TiO}_2(\text{B})$  respectively. A larger particle at the top surface (Figure 6-9(c)) shows a lattice spacing of  $6.20 \pm 0.06 \text{ \AA}$  corresponding to (001) in  $\text{TiO}_2(\text{B})$ .

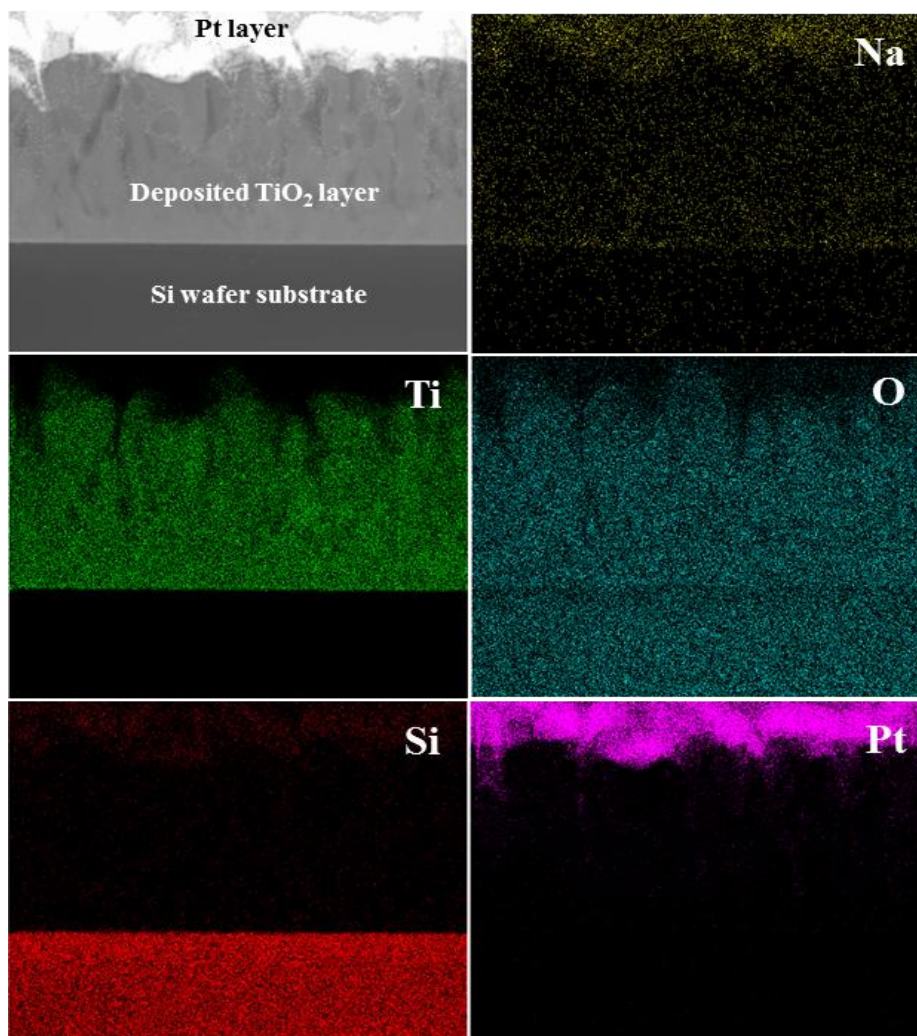


**Figure 6-10** STEM-EDX elemental maps from the FIB cross-sectional sample of 0.5%\_Si, showing the elemental distribution in the thin film and the  $\text{TiO}_2/\text{Si}$  wafer and  $\text{TiO}_2/\text{protective Pt}$  layer interfacial areas.

Thus it would appear that  $\text{TiO}_2(\text{B})$  is formed throughout the film, in contrast to the previous studies of mixed phase anatase and  $\text{TiO}_2(\text{B})$  thin films produced by LPCVD on low sodium content materials such as soda-lime glass where I observed the  $\text{TiO}_2(\text{B})$  phase only at interface with the substrate. Scanning Transmission Electron Microscopy (STEM) and EDX spectroscopy on the FIB cross-sectional 0.5%\_Si sample, was used to study the elemental distributions in the thin film. Figure 6-10 shows the element-specific maps obtained and reveal a relatively uniform distribution of Na throughout the whole  $\text{TiO}_2$  thin film. Note, due to the overlap between the Na K- and Ga  $L_{\alpha}$ - X-ray emission lines, elemental quantification in the upper portion of

the TiO<sub>2</sub> film near the protective Pt layer (strap) are unreliable due to significant Ga implantation into the Pt strap during ion beam milling.

### 6.2.5 Effect of Na content in the Substrate Pre-treatment

The % <sup>w/v</sup> of Na in the sodium ethoxide/ethanol solution used in the substrate pre-treatment was varied in order to monitor its effect on titania phase formation in the thin film. XRD patterns from thin films deposited following a range of sodium pre-treatments are shown in Figure 6-11 and reveal that for low sodium concentrations (samples: 0.05%<sub>Si</sub> and 0.10%<sub>Si</sub>) solely anatase is present. Whilst for concentrations of ≥ 0.16% <sup>w/v</sup> of Na, the pre-treatment process promoted the formation of TiO<sub>2</sub>(B) as well as the anatase phase, with an increase in the relative proportion of TiO<sub>2</sub>(B) phase with increasing sodium content up to an optimum level of 0.75% <sup>w/v</sup> Na; further increases in Na levels result in the anatase phase becoming the main component in the thin films.

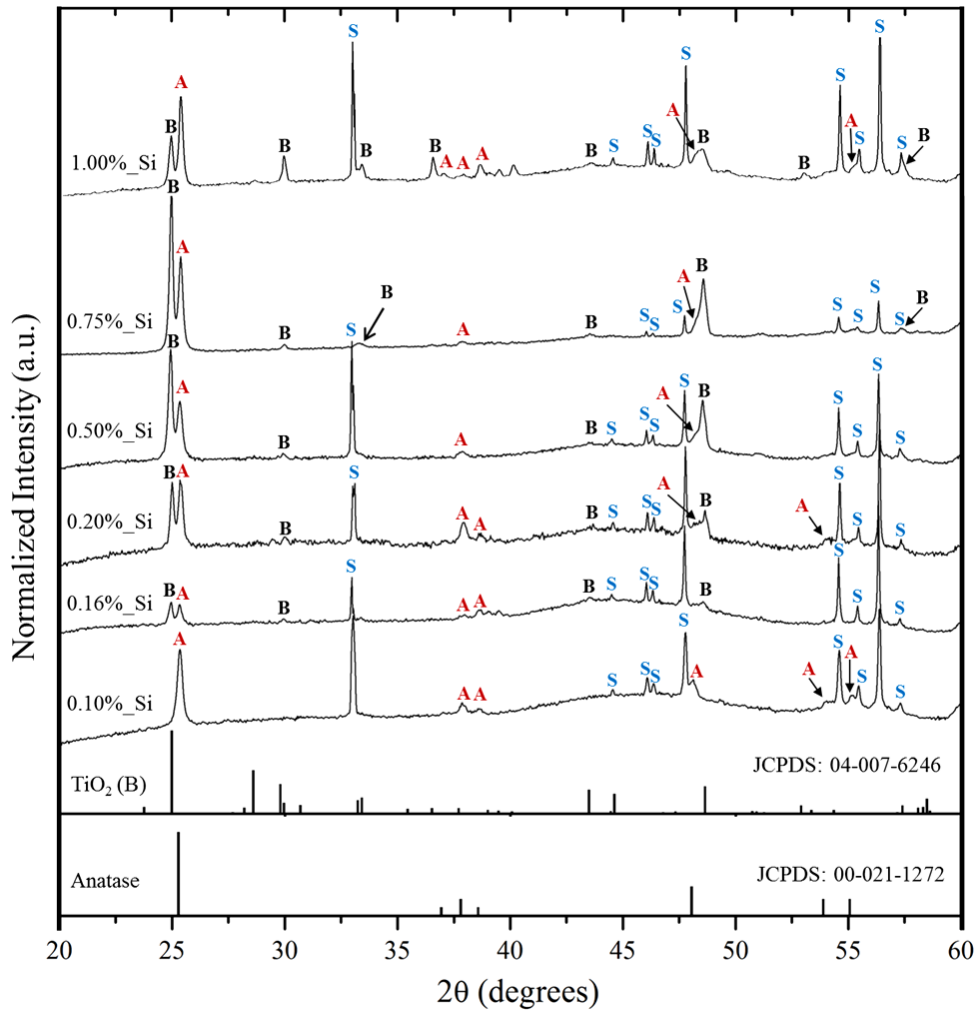


**Figure 6-11** XRD patterns of TiO<sub>2</sub> thin films deposited onto Si wafer substrates pre-coated with a very thin sodium-containing layer by spraying different concentrations of sodium ethoxide/ethanol solution; A, B and S refer to the TiO<sub>2</sub> Anatase phase, TiO<sub>2</sub>(B) phase and Si wafer substrate respectively.

This is more clearly seen in Figure 6-12 which shows XRD patterns with the sample tilted off-axis by 2 degrees with respect to a normal  $2\theta$  scan. This is to reduce the strength of the single (hkl) reflection from Si wafer substrate which would otherwise dominate the pattern, making it difficult to observe the  $\text{TiO}_2$  diffraction peaks.

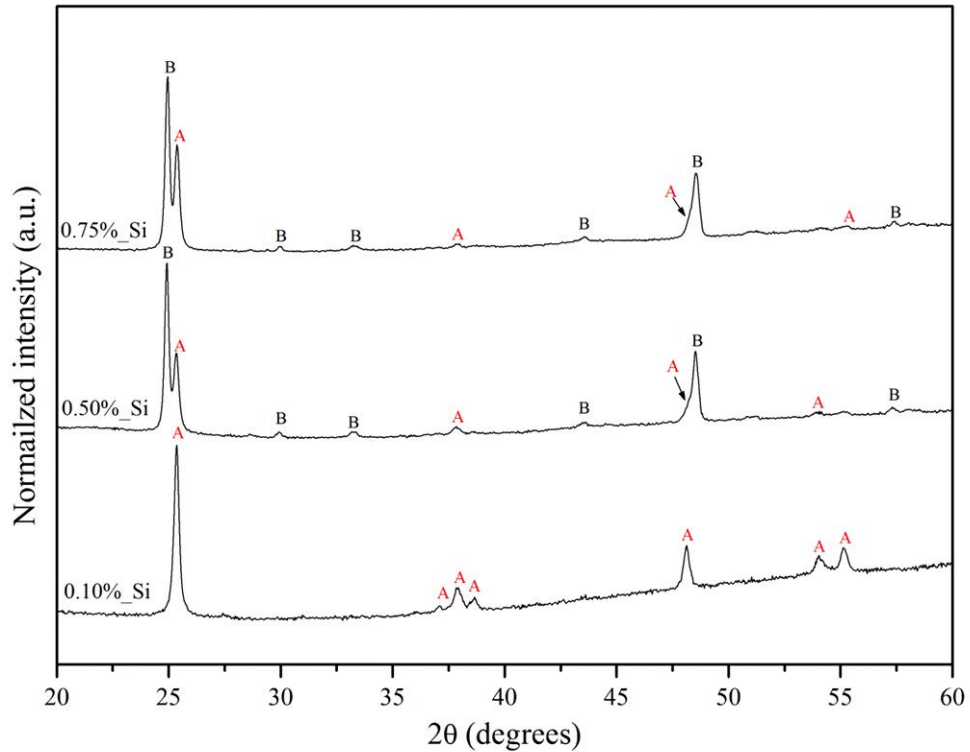


**Figure 6-12** Off axis XRD patterns of  $\text{TiO}_2$  thin film samples showing the peaks due to the  $\text{TiO}_2$  phases without interference from the silicon wafer substrate.

### 6.3 Discussion

In chapter 5, we investigated  $\text{TiO}_2(\text{B})$  phase formation in thin films deposited by LPCVD onto soda-lime glass substrates [11], where the findings suggested a mechanism involving diffusion of  $\text{Na}^+$  ions out of the substrate to form an intermediate layer at the interface which subsequently decomposed into the  $\text{TiO}_2(\text{B})$  phase. Here I have extended this work to investigate whether substrates that are sodium-free could be pre-treated with sodium so as to promote  $\text{TiO}_2(\text{B})$  formation during LPCVD. The present results demonstrate that mixed  $\text{TiO}_2(\text{B})$  and anatase phase thin films can be prepared on any general substrate using a modified LPCVD method involving pre-treatment of the substrate by a sodium spraying method using  $\text{NaOEt}$  in Ethanol.

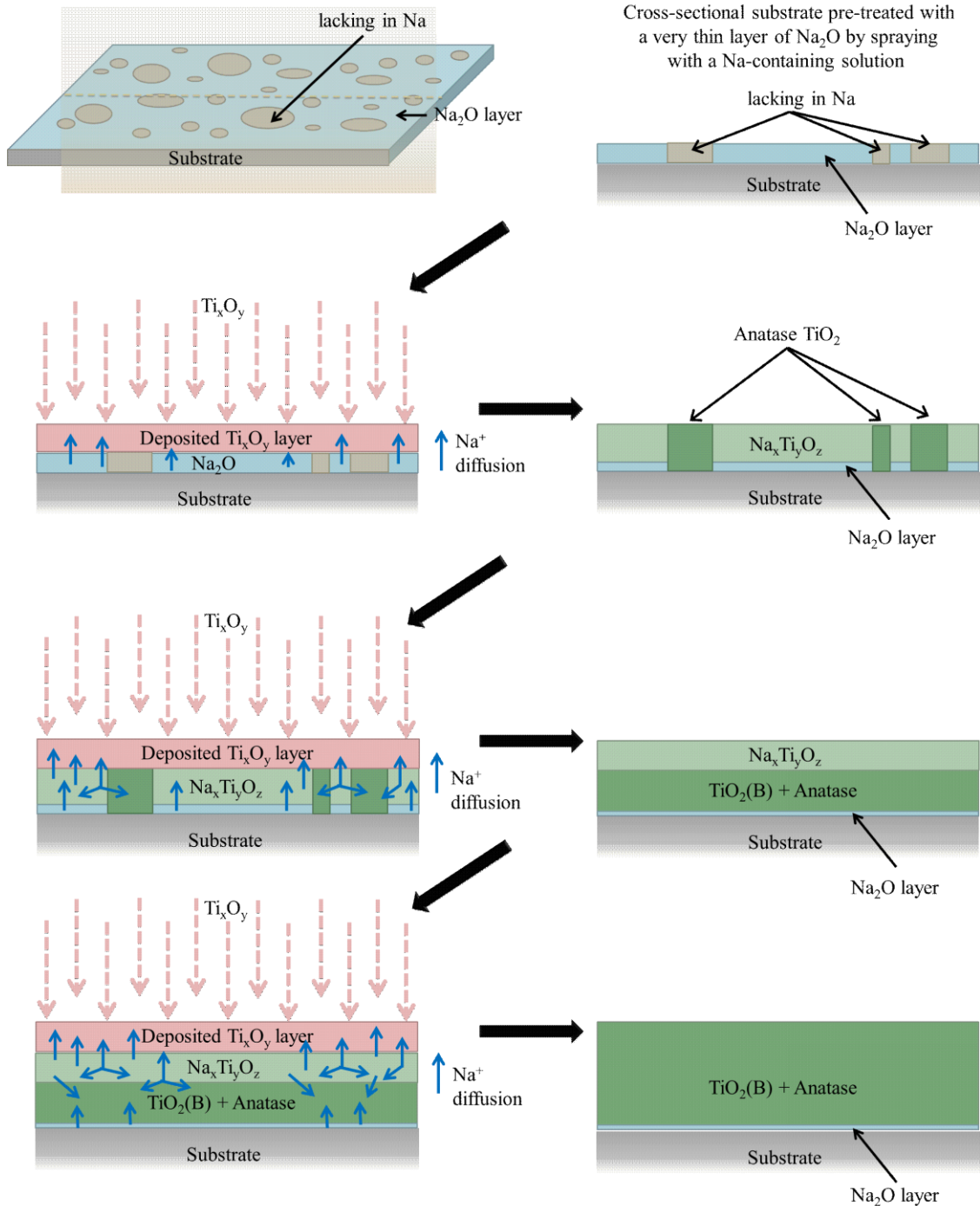
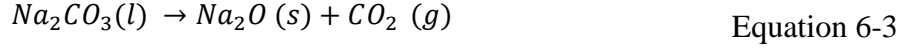
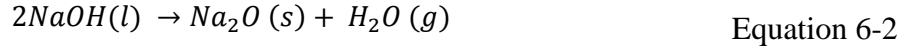
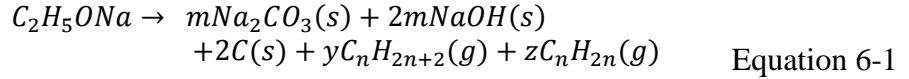


**Figure 6-13** Proposed mechanism for the synthesis of mixed phase  $\text{TiO}_2(\text{B})$  and anatase thin films by LPCVD method onto substrate pre-treated with a very thin layer of Na-containing compound

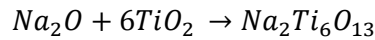
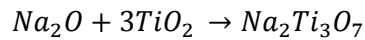
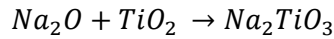
We propose a potential three-step mechanism for  $\text{TiO}_2(\text{B})$  formation as illustrated schematically in Figure 6-13:

(1) The substrate was first prepared by spraying sodium ethoxide solution onto the substrate surface. Sodium ethoxide thermally decomposes during the pre-heat treatment process at  $600^\circ\text{C}$  according to the following reaction [12]–[14]:



As in Equation 6-1, the initial decomposition step of sodium ethoxide at 1 atm in air typically occurs above 300°C and produces hydrocarbon gases, amorphous carbon and two main residues: sodium carbonate and sodium hydroxide in the mole ratio 1:2 [12]. Above 320°C NaOH melts and decomposes to form a thin layer of Na<sub>2</sub>O and steam (Equation 6-2) [14]. Above a temperature of 850°C Na<sub>2</sub>CO<sub>3</sub> can also generate Na<sub>2</sub>O [15], [16], as shown in Equation 6-3; however at low pressure this decomposition temperature may be reduced. Furthermore, decomposition reactions of metal carbonates are partially reversible reactions and the removal of gas phase of products by the vacuum system may encourage an increase in the forward reaction rate;

(2) During the LPCVD process itself, Na<sup>+</sup> ions could migrate from the Na<sub>2</sub>O layer into the nascent TiO<sub>2</sub> films formed from the decomposition of TTIP, possibly causing formation of intermediate phases of monoclinic sodium titanates with tunnel structures such as Na<sub>2</sub>TiO<sub>3</sub>, Na<sub>2</sub>Ti<sub>3</sub>O<sub>7</sub> and Na<sub>2</sub>Ti<sub>6</sub>O<sub>13</sub> and/or amorphous Na doped TiO<sub>2</sub>. According to a binary phase diagram for the Na<sub>2</sub>O-TiO<sub>2</sub> system [17], each of these intermediate sodium titanates could be formed at 600°C depending on the exact Na<sub>2</sub>O/TiO<sub>2</sub> phase ratio present, as shown in the following reactions:



Based on the current levels of Na employed in the current study I believe Na<sub>2</sub>Ti<sub>6</sub>O<sub>13</sub> is the most likely phase to be formed. This could act as a seeding material for TiO<sub>2</sub>(B) formation [18]–[20]. In sodium titanates, typically Na<sup>+</sup> ions are located in the interlayers between negatively charged sheets composed of TiO<sub>6</sub> octahedral building blocks as shown in Figure 6-14. If these Na<sup>+</sup> ions are mobile, then their migration out of the structure may effectively template a TiO<sub>2</sub> tunnel structure which may subsequently rearrange or shrink to form TiO<sub>2</sub>(B).

(3) Sodium ions in the seeding structure continuously migrate into the newly deposited layers of TiO<sub>2</sub> and promote TiO<sub>2</sub>(B) formation. In some ways this is analogous to the tip growth mechanism for carbon nanotube using (metal) catalytic chemical vapor deposition[21]. However in the absence of a significant quantity of Na, the deposited titania will form the anatase phase instead of TiO<sub>2</sub>(B).

This general hypothesis is supported by the previous findings regarding  $\text{TiO}_2(\text{B})$  formation promoted by  $\text{Na}^+$  diffusion from soda-lime glass substrates under the same synthesis conditions [11]. However, using the pre-treatment process it would appear that sodium diffuses rapidly through the film and  $\text{TiO}_2(\text{B})$  is not just confined to the interfacial region adjacent to the substrate, nor does it grow in an oriented fashion as is the case for soda lime glass substrates.

As mentioned in the introduction, mixed phase  $\text{TiO}_2(\text{B})$  and anatase thin films on anodes may offer improved Li ion battery performance. Lithium can diffuse into both the anatase and  $\text{TiO}_2(\text{B})$  frameworks in three dimensions through open channels or voids within the structures [22], [23] however  $\text{TiO}_2(\text{B})$  provides the highest %voids amongst the  $\text{TiO}_2$  polymorphs and nano- $\text{TiO}_2(\text{B})$  is able to accommodate 1  $\text{Li}^+$  per Ti which is higher than that for anatase [24]. However, for the  $\text{TiO}_2(\text{B})$  phase a significant irreversible capacity loss occurs at the initial charge-discharge cycle, whereas in anatase this effect is smaller [23], [25]. Thus, the ability to produce a thin, high surface area film with some mesoporosity and containing a combination of both polymorphs may ultimately improve overall anode performance.

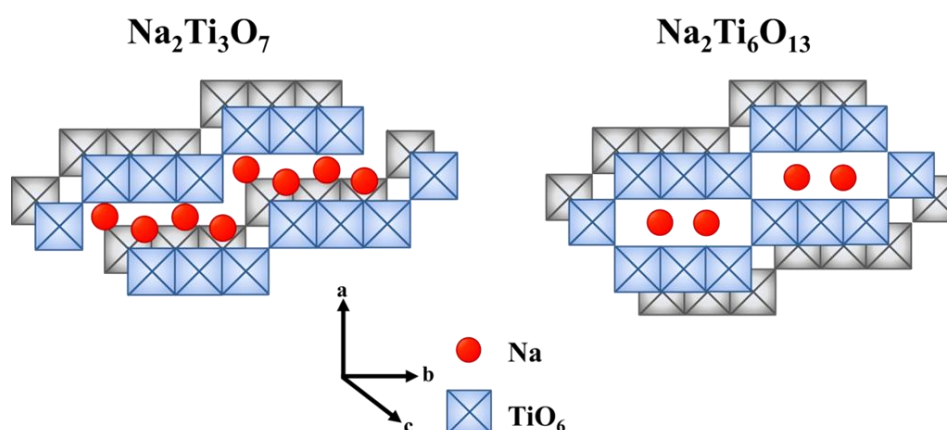


**Figure 6-14** Schematic drawing of the monoclinic sodium titanates showing the tunnel structure of  $\text{Na}_2\text{Ti}_3\text{O}_7$  and  $\text{Na}_2\text{Ti}_6\text{O}_{13}$ .

In the case of photocatalyst materials, a number of studies have reported the improved photocatalytic efficiency of mixed phase  $\text{TiO}_2(\text{B})$  and anatase over either commercial P25 (mixed phase anatase and rutile) or single phase  $\text{TiO}_2$  (anatase, rutile, brookite and  $\text{TiO}_2(\text{B})$ ). This has been investigated for several photocatalyst reactions including: methyl orange-[26], [27], sulforhodamine B-[2], [3], methylene blue-[28]–[30] and yellow XRG dry-[31] degradations; nitrate reduction [32]; acetaldehyde decomposition [33] and the water splitting reaction [34]. For the practical application of  $\text{TiO}_2$  photocatalysts, the ability to produce thin films of mixed phase  $\text{TiO}_2(\text{B})$  and

anatase on rigid substrates may be beneficial owing to their ability to be reused whilst retaining high catalyst performance.

## 6.4 Conclusions

Titania thin films consisting of a mixed phase  $\text{TiO}_2(\text{B})$  and anatase were successfully synthesized by a modified LPCVD route involving pre-treatment of the substrates by a sodium spraying method using  $\text{NaOEt}$  in Ethanol. A number of different substrates including fused quartz, Si wafer, HOPG and grafoil were deposited with around 400 nm thick mixed phase titania films using 5 mL of a TTIP precursor for 15 min at nominal temperature of  $600^\circ\text{C}$ . The optimum Na concentration of the sodium ethoxide/ethanol solution in the pre-treatment process so as to promote the highest amount of  $\text{TiO}_2(\text{B})$  phase composition in the thin films, was found to be 0.75%<sup>w/v</sup>. A mechanism for modified LPCVD preparation of  $\text{TiO}_2(\text{B})$  is proposed involving the decomposition of the thin Na-containing layer and migration of  $\text{Na}^+$  ions into the  $\text{TiO}_2$  layer to form an intermediate sodium titanate phase. Potentially this thin film fabrication process could be utilised with any desired substrate to produce anode materials and photocatalytic devices.

## 6.5 References

- [1] M. Søndergaard, Y. Shen, A. Mamakhel, M. Marinaro, M. Wohlfahrt-Mehrens, K. Wonsyld, S. Dahl, and B.B. Iversen, "TiO<sub>2</sub> nanoparticles for Li-ion battery anodes: Mitigation of growth and irreversible capacity using LiOH and NaOH," *Chem. Mater.*, vol. 27, pp. 119–126, 2015.
- [2] D. Yang, H. Liu, Z. Zheng, Y. Yuan, J. Zhao, E.R. Waclawik, X. Ke, and H. Zhu, "An efficient photocatalyst structure: TiO<sub>2</sub>(B) nanofibers with a shell of anatase nanocrystals," *J. Am. Chem. Soc.*, vol. 131, no. 49, pp. 17885–17893, 2009.
- [3] Z. Zheng, H. Liu, J. Ye, J. Zhao, E.R. Waclawik, and H. Zhu, "Structure and contribution to photocatalytic activity of the interfaces in nanofibers with mixed anatase and TiO<sub>2</sub>(B) phases," *J. Mol. Catal. A Chem.*, vol. 316, no. 1–2, pp. 75–82, 2010.
- [4] M. Fehse, F. Fischer, C. Tessier, L. Stievano, and L. Monconduit, "Tailoring of phase composition and morphology of TiO<sub>2</sub>-based electrode materials for lithium-ion batteries," *J. Power Sources*, vol. 231, pp. 23–28, 2013.
- [5] S. Reich and C. Thomsen, "Raman spectroscopy of graphite.," *Philos. Trans. A. Math. Phys. Eng. Sci.*, vol. 362, pp. 2271–2288, 2004.
- [6] T. Ohsaka, F. Izumi, and Y. Fujiki, "Raman Spectrum of Anatase, TiO<sub>2</sub>," *J. Raman Spectrosc.*, vol. 7, no. 6, pp. 321–324, 1978.

- [7] M.B. Yahia, F. Lemoigno, T. Beuvier, J.S. Filhol, M. Richard-Plouet, L. Brohan, and M.L. Doublet, "Updated references for the structural, electronic, and vibrational properties of TiO<sub>2</sub>(B) bulk using first-principles density functional theory calculations.," *J. Chem. Phys.*, vol. 130, no. 20, pp. 204501, 2009.
- [8] T. Beuvier, M. Richard-plouet, and L. Brohan, "Accurate methods for quantifying the relative ratio of anatase and TiO<sub>2</sub>(B) Nanoparticles," *J. Phys. Chem. C*, vol. 113, no. 31, pp. 13703–13706, 2009.
- [9] T. Beuvier, M. Richard-Plouet, and L. Brohan, "Ternary morphological diagram for nano(tube–ribbon–sphere) sodium titanate deduced from raman spectra analysis," *J. Phys. Chem. C*, vol. 114, no. 17, pp. 7660–7665, 2010.
- [10] V.K. Singh, "Effect of surface re-emission on the surface roughness of film growth in low pressure chemical vapor deposition," *J. Vac. Sci. Technol. A Vacuum, Surfaces, Film.*, vol. 11, no. 1993, pp. 557, 1993.
- [11] Y. Chimupala, G. Hyett, R. Simpson, R. Mitchell, R. Douthwaite, S.J. Milne, and R.D. Brydson, "Synthesis and characterization of mixed phase anatase TiO<sub>2</sub> and sodium-doped TiO<sub>2</sub>(B) thin films by low pressure chemical vapour deposition (LPCVD)," *RSC Adv.*, vol. 4, pp. 48507–48515, 2014.
- [12] K. Chandran, M. Kamruddin, P.K. Ajikumar, a. Gopalan, and V. Ganesan, "Kinetics of thermal decomposition of sodium methoxide and ethoxide," *J. Nucl. Mater.*, vol. 358, pp. 111–128, 2006.
- [13] K. Chandran, M. Kamruddin, P. K. Ajikumar, a. Gopalan, and V. Ganesan, "Thermal decomposition and kinetic analysis of sodium propoxides," *J. Nucl. Mater.*, vol. 374, pp. 158–167, 2008.
- [14] V.P. Yurkinskii, E.G. Firsova, and S.A Proskura, "Inorganic synthesis and industrial inorganic chemistry: Thermal Dissociation of Sodium Hydroxide upon Evacuation," *Russ. J. Appl. Chem.*, vol. 78, no. 3, pp. 360–362, 2005.
- [15] A.E. Newkirk and I. Aliferis, "Drying and decomposition of sodium carbonate," *Anal. Chem.*, vol. 30, pp. 982–984, 1958.
- [16] A.M. Thomas, "Thermal decomposition of sodium carbonate solutions.," *J. Chem. Eng. Data*, vol. 8, pp. 51–54, 1963.
- [17] R. Bouaziz, M. Mayer, and C.R. Hebd, "Na-O-Ti phase diagraeme," *Seances Acad. Sci. Ser. C.*, vol. 23, no. 272, pp. 1874, 1971.
- [18] Z. Guo, X. Dong, D. Zhou, Y. Du, Y. Wang, and Y. Xia, "TiO<sub>2</sub>(B) nanofiber bundles as a high performance anode for a Li-ion battery," *RSC Adv.*, vol. 3, no. 10, pp. 3352, 2013.
- [19] T.P. Feist and P.K. Davies, "The Soft chemical synthesis of TiO<sub>2</sub>(B) from layered titanates," *J. Solid State Chem.*, vol. 101, pp. 275–295, 1992.
- [20] V. Etacheri, Y. Kuo, A. Van-der-Ven, and B.M. Bartlett, "Mesoporous TiO<sub>2</sub>–B microflowers composed of (1-10) facet-exposed nanosheets for fast reversible lithium-ion storage," *J. Mater. Chem. A*, vol. 1, pp. 12028, 2013.
- [21] M. Kumar and Y. Ando, "Chemical Vapor Deposition of Carbon Nanotubes: A Review on Growth Mechanism and Mass Production, " *J. Nanosci. Nanotechnol.*, vol. 10, pp 3758, 2010

- [22] C. Jiang and J. Zhang, "Nanoengineering titania for high rate lithium storage: A review," *J. Mater. Sci. Technol.*, vol. 29, no. 2, pp. 97–122, 2013.
- [23] D. Deng, M.G. Kim, J.Y. Lee, and J. Cho, "Green energy storage materials: Nanostructured TiO<sub>2</sub> and Sn-based anodes for lithium-ion batteries," *Energy Environ. Sci.*, vol. 2, pp. 818, 2009.
- [24] A.G. Dylla, G. Henkelman, and K.J. Stevenson, "Lithium insertion in nanostructured TiO<sub>2</sub>(B) architectures," *Acc. Chem. Res.*, vol. 46, no. 5, pp. 1104–1112, 2013.
- [25] M. Wagemaker and F.M. Mulder, "Properties and promises of nanosized insertion materials for li-ion batteries," *Acc. Chem. Res.*, vol. 46, no. 5, pp. 1206–1215, 2013.
- [26] C. Huang, K. Zhu, M. Qi, Y. Zhuang, and C. Cheng, "Preparation and photocatalytic activity of bicrystal phase TiO<sub>2</sub> nanotubes containing TiO<sub>2</sub>-B and anatase," *J. Phys. Chem. Solids*, vol. 73, no. 6, pp. 757–761, 2012.
- [27] G. Xiang, T. Li, J. Zhuang, and X. Wang, "Large-scale synthesis of metastable TiO<sub>2</sub>(B) nanosheets with atomic thickness and their photocatalytic properties," *Chem. Commun.*, vol. 46, no. 36, pp. 6801–3, 2010.
- [28] V. Etacheri, J.E. Yourey, and B.M. Bartlett, "Chemically bonded TiO<sub>2</sub>-Bronze nanosheet/reduced graphene oxide hybrid for high-power lithium ion batteries," *ACS Nano*, vol. 8, no. 2, pp. 1491–1499, 2014.
- [29] C.W. Peng, M. Richard-Plouet, T.Y. Ke, C.Y. Lee, H.T. Chiu, C. Marhic, E. Puzenat, F. Lemoigno, and L. Brohan, "Chimie douce route to sodium hydroxo titanate nanowires with modulated structure and conversion to highly photoactive titanium dioxides," *Chem. Mater.*, vol. 20, no. 23, pp. 7228–7236, 2008.
- [30] H. Song, H. Jiang, T. Liu, X. Liu, and G. Meng, "Preparation and photocatalytic activity of alkali titanate nano materials A<sub>2</sub>Ti<sub>n</sub>O<sub>2n+1</sub> (A=Li, Na and K)," *Mater. Res. Bull.*, vol. 42, no. 2, pp. 334–344, 2007.
- [31] J. Zhu, J. Zhang, F. Chen, and M. Anpo, "Preparation of high photocatalytic activity TiO<sub>2</sub> with a bicrystalline phase containing anatase and TiO<sub>2</sub>(B)," *Mater. Lett.*, vol. 59, no. 27, pp. 3378–3381, 2005.
- [32] M.M. Mohamed, B.H.M. Asghar, and H.A. Muathen, "Facile synthesis of mesoporous bicrystallized TiO<sub>2</sub>(B)/anatase (rutile) phases as active photocatalysts for nitrate reduction," *Catal. Commun.*, vol. 28, pp. 58–63, 2012.
- [33] C. Wang, X. Zhang, and Y. Liu, "Coexistence of an anatase/TiO<sub>2</sub>(B) heterojunction and an exposed (001) facet in TiO<sub>2</sub> nanoribbon photocatalysts synthesized via a fluorine-free route and topotactic transformation," *Nanoscale*, vol. 6, pp. 5329, 2014.
- [34] K. Kiatkittipong, A. Iwase, J. Scott, and R. Amal, "Photocatalysis of heat treated sodium- and hydrogen-titanate nanoribbons for water splitting, H<sub>2</sub>/O<sub>2</sub> generation and oxalic acid oxidation," *Chem. Eng. Sci.*, vol. 93, pp. 341–349, 2013.

## **Chapter 7 The modified LPCVD method using an alkali metal ion pretreatment of substrate surfaces**

In the previous chapter I reported a new method involving pre-treatment of substrates with  $\text{Na}^+$  ions from external sources prior to LPCVD deposition in order to promote  $\text{TiO}_2(\text{B})$  formation. The successful synthesis of  $\text{TiO}_2(\text{B})$  phase onto Si wafer, fused quartz, HOPG and grafoil substrates was proposed as a result of  $\text{Na}^+$  ion diffusion from the pre-treated surface substrate. In this chapter, the main objective is to study the effect of different type of alkali metal ions ( $\text{Li}^+$ ,  $\text{Na}^+$  and  $\text{K}^+$ ) in the pre-treatment process on synthesised  $\text{TiO}_2$  thin films by modified LPCVD method.

### **7.1 Experiment procedure**

#### **7.1.1 Pre-treatment of the Si wafer substrate**

The pre-treatment process involved thin film deposition of an alkali metal hydroxide solution onto a Si wafer substrates. Three different alkali metal hydroxides (LiOH, NaOH and KOH) were used. These were dissolved in 20 mL of Di water, followed by stirring and sonication of 15 min each. The concentrations of each alkali metal hydroxide solution were varied in the range of 0.1-5.0 %weight of alkali metal per volume of Di water. The individual details of the alkaline hydroxide solutions prepared are listed in the Table 7-1.

#### **7.1.2 Deposition of $\text{TiO}_2$ thin films on pre-treatment substrates by LPCVD method**

The pretreated substrate was placed at the middle of the tube furnace inside the quartz tube. The LPCVD method was carried out using the same preparation procedure as described in chapter 3. The LPCVD synthesis conditions were the same as chapter 6, in which TTIP was used as a Ti precursor with  $\text{N}_2$  carrier gas,  $600^\circ\text{C}$  reaction temperature, 15 minutes reaction time and 25 mbar pressure.

#### **7.1.3 Materials characterization**

All of the synthesised samples were characterized by the off-set XRD method. SEM and EDX were employed to study the physical morphology and chemistry of the samples. Specimen preparation for all techniques was the same as described in chapter 3.

**Table 7-1** List of synthesized samples with the details of alkaline hydroxide concentration used in pre-treatment of substrates by spraying

| Alkaline hydroxide | % <sup>W</sup> / <sub>V</sub> of weight of alkali metal ions per volume of solution | moles of alkali metal ions | Sample name |
|--------------------|---|----------------------------|-------------|
| LiOH               | ~0.10   | $1.44 \times 10^{-2}$      | 0.1%_Li     |
|                    | ~0.30   | $4.32 \times 10^{-2}$      | 0.3%_Li     |
|                    | ~1.00   | $1.44 \times 10^{-1}$      | 1.0%_Li     |
|                    | ~2.50   | $3.60 \times 10^{-1}$      | 2.0%_Li     |
| NaOH               | ~1.00   | $4.32 \times 10^{-2}$      | 1.0%_Na     |
|                    | ~2.00   | $8.64 \times 10^{-2}$      | 2.0%_Na     |
|                    | ~5.00   | $2.16 \times 10^{-1}$      | 5.0%_Na     |
|                    | ~10.0   | $4.32 \times 10^{-1}$      | 10%_Na      |
| KOH                | ~0.50   | $1.28 \times 10^{-2}$      | 0.5%_K      |
|                    | ~1.00   | $2.56 \times 10^{-2}$      | 1.0%_K      |
|                    | ~1.69   | $4.32 \times 10^{-2}$      | 1.69%_K     |
|                    | ~2.50   | $6.39 \times 10^{-2}$      | 2.5%_K      |

## 7.2 Results

### 7.2.1 Effect of type of alkali metal ion on titania or titanate thin films composition prepared by LPCVD method

Samples with the same mole fraction of alkali metal ions (0.3%\_Li, 1.0%\_Na, 1.69%\_K), were examined by XRD as shown in Figure 7-1. The XRD results show that different types of alkali-metal ions (Li<sup>+</sup>, Na<sup>+</sup>, and K<sup>+</sup>) promote differences in phase composition in the thin film samples. Without a pre-treatment process with alkali metal hydroxide, only the anatase phase was indicated in the XRD pattern (anatase TiO<sub>2</sub> is the typical product synthesised by CVD preparation at 600°C), whereas other phases of titania or titanate compounds occurred in addition to anatase when the alkaline pre-treatment processes were applied. The existence of alkali metals in the LPCVD system, promoted the formation of the following extra phases in addition to anatase TiO<sub>2</sub>: Brookite, Rutile and Li<sub>2</sub>TiO<sub>3</sub> in case of Li<sup>+</sup>; TiO<sub>2</sub>(B) in case of Na<sup>+</sup>; K<sub>2</sub>Ti<sub>6</sub>O<sub>13</sub> and TiO<sub>2</sub>(B) in case of K<sup>+</sup>. The phases of LPCVD products in every synthesis condition are summarised in Table 7.2.

Focusing only on  $\text{TiO}_2(\text{B})$  phase formation through the LPCVD process, it was found that  $\text{Na}^+$  is the most useful alkali metal for participating in  $\text{TiO}_2(\text{B})$  phase formation. The  $\text{TiO}_2(\text{B})$  peak pattern was obviously seen in the XRD pattern of 1.0%\_Na. This result was supported by similar previous results in chapter 6. A mechanism for  $\text{TiO}_2(\text{B})$  phase formation should correspond with the previously proposed mechanism in chapter 6, owing to the same synthesis conditions and preparation process of both experiments except that NaOH was used instead of NaOEt. Not only  $\text{Na}^+$  ions promoted  $\text{TiO}_2(\text{B})$  phase formation,  $\text{K}^+$  ions also produced a minority peak pattern of  $\text{TiO}_2(\text{B})$  at  $2\theta=14.14, 28.63, 43.54^\circ$  as shown in 1.69%\_K.

To confirm the XRD interpretation for the 1.69%\_K sample, especially the presence of  $\text{TiO}_2(\text{B})$ , Raman spectroscopy was employed to investigate phase composition as shown in Figure 7-2. The Raman spectra show the characteristic peaks of  $\text{TiO}_2(\text{B})$  which were indexed at 118.4, 238.2, 250.4, 360.7, 432.1 and 552.8  $\text{cm}^{-1}$ , including four strong overlapping peaks of both  $\text{TiO}_2(\text{B})$  and anatase at Raman shifts of 143.15, 197.81, 396.01, 638.54  $\text{cm}^{-1}$ . This Raman result guarantees the coexistence of  $\text{TiO}_2(\text{B})$  phase and anatase in the thin film samples. However, it seems that  $\text{K}^+$  ions have a limitation in promoting the  $\text{TiO}_2(\text{B})$  phase and prefer to form  $\text{K}_2\text{Ti}_6\text{O}_{13}$  instead as seen from the relative intensity of the peaks. Conversely, the XRD pattern of thin film samples prepared using  $\text{Li}^+$  ion pre-treatment (0.3%\_Li) does not show the  $\text{TiO}_2(\text{B})$  phase and provides three more titania/titanate phases of brookite, rutile and  $\text{Li}_2\text{TiO}_3$  plus anatase  $\text{TiO}_2$ . Some of the XRD patterns show a group of small peaks of Si/ $\text{SiO}_2$  due to interfering signals from the Si wafer substrate.

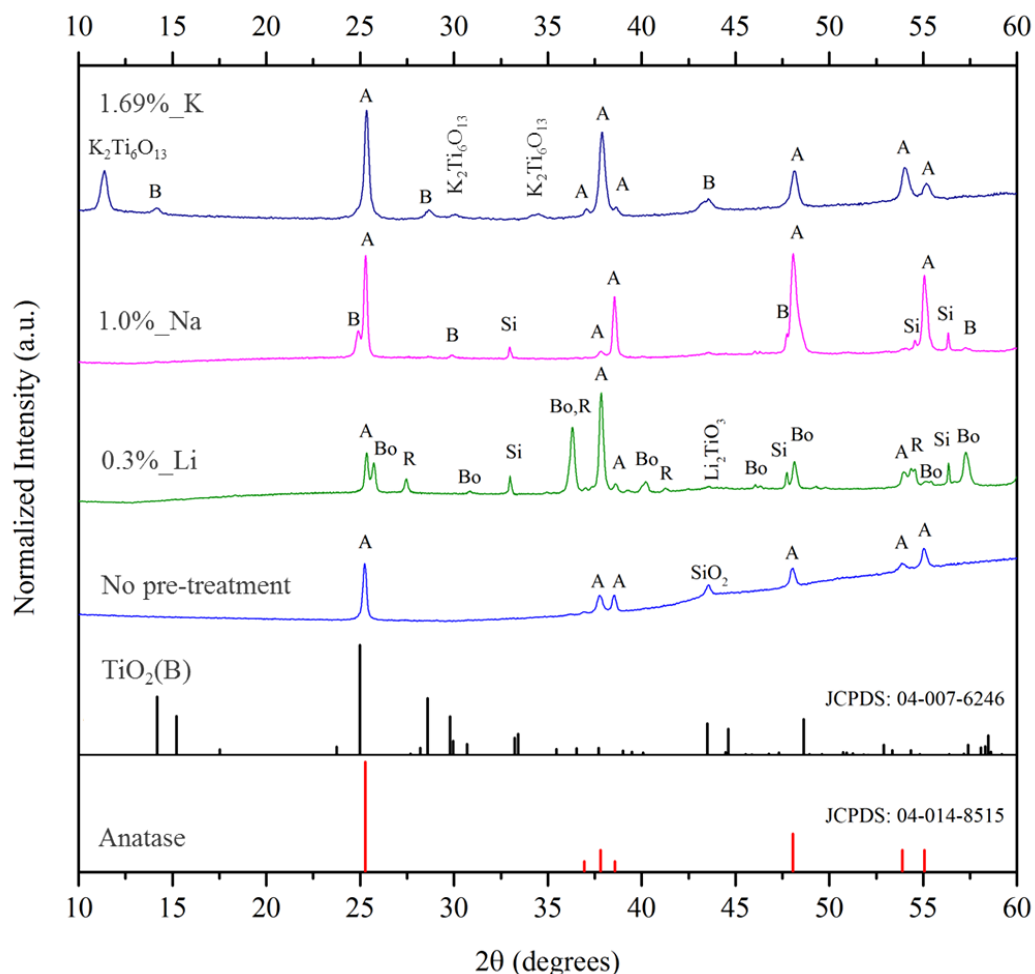


**Figure 7-1** XRD patterns of thin film samples deposited by LPCVD on the Si wafer substrates which were pre-treated by spraying LiOH, NaOH and KOH solution in the same mole amount of alkali metal ions ( $4.32 \times 10^{-2}$  mole).

To confirm the XRD interpretation for the 1.69%\_K sample, especially the presence of TiO<sub>2</sub>(B), Raman spectroscopy was employed to investigate phase composition as shown in Figure 7-2. The Raman spectra show the characteristic peaks of TiO<sub>2</sub>(B) which were indexed at 118.4, 238.2, 250.4, 360.7, 432.1 and 552.8  $cm^{-1}$ , including four strong overlapping peaks of both TiO<sub>2</sub>(B) and anatase at Raman shifts of 143.15, 197.81, 396.01, 638.54  $cm^{-1}$ . This Raman result guarantees the coexistence of TiO<sub>2</sub>(B) phase and anatase in the thin film samples. However, it seems that K<sup>+</sup> ions have a limitation in promoting the TiO<sub>2</sub>(B) phase and prefer to form K<sub>2</sub>Ti<sub>6</sub>O<sub>13</sub> instead as seen from the relative intensity of the peaks. Conversely, the XRD pattern of thin film samples prepared using Li<sup>+</sup> ion pre-treatment (0.3%\_Li) does not show the TiO<sub>2</sub>(B) phase and provides three more titania/titanate phases of brookite, rutile and Li<sub>2</sub>TiO<sub>3</sub> plus anatase TiO<sub>2</sub>. Some of the XRD patterns show a group of small peaks of Si/SiO<sub>2</sub> due to interfering signals from the Si wafer substrate.

**Table 7-2** The conclusions of titania/titanate phases of thin film products synthesized by modified LPCVD with pre-treatment of Si wafer substrates by spraying three different alkaline hydroxide solution in varied concentration.

| Alkali metal ion source | % <sup>W</sup> / <sub>V</sub> of alkali ion in Di water | Phases composition of thin film sample   |
|-------------------------|---|--|
| LiOH                    | 0.1   | <b>Anatase*</b> , Rutile, Brookite, Li <sub>2</sub> TiO <sub>3</sub>                   |
|                         | 0.3   | <b>Anatase*</b> , Rutile, Brookite, Li <sub>2</sub> TiO <sub>3</sub>                   |
|                         | 1.0   | <b>Anatase*</b> , Rutile, Brookite, Li <sub>2</sub> TiO <sub>3</sub>                   |
|                         | 2.5   | <b>Anatase*</b> , Rutile, Brookite, Li <sub>2</sub> TiO <sub>3</sub>                   |
| NaOH                    | 1.0   | <b>Anatase*</b> , TiO <sub>2</sub> (B)   |
|                         | 2.0   | <b>Anatase*</b> , TiO <sub>2</sub> (B)   |
|                         | 5.0   | <b>Anatase*</b> , TiO <sub>2</sub> (B)   |
| KOH                     | 0.5   | <b>Anatase*</b> , TiO <sub>2</sub> (B)   |
|                         | 1.0   | <b>Anatase*</b> , TiO <sub>2</sub> (B), K <sub>2</sub> Ti <sub>6</sub> O <sub>13</sub> |
|                         | 1.69  | <b>Anatase*</b> , TiO <sub>2</sub> (B), K <sub>2</sub> Ti <sub>6</sub> O <sub>13</sub> |
|                         | 2.5   | <b>K<sub>2</sub>Ti<sub>6</sub>O<sub>13</sub>*</b> , Anatase, TiO <sub>2</sub> (B)      |

\* the majority phase

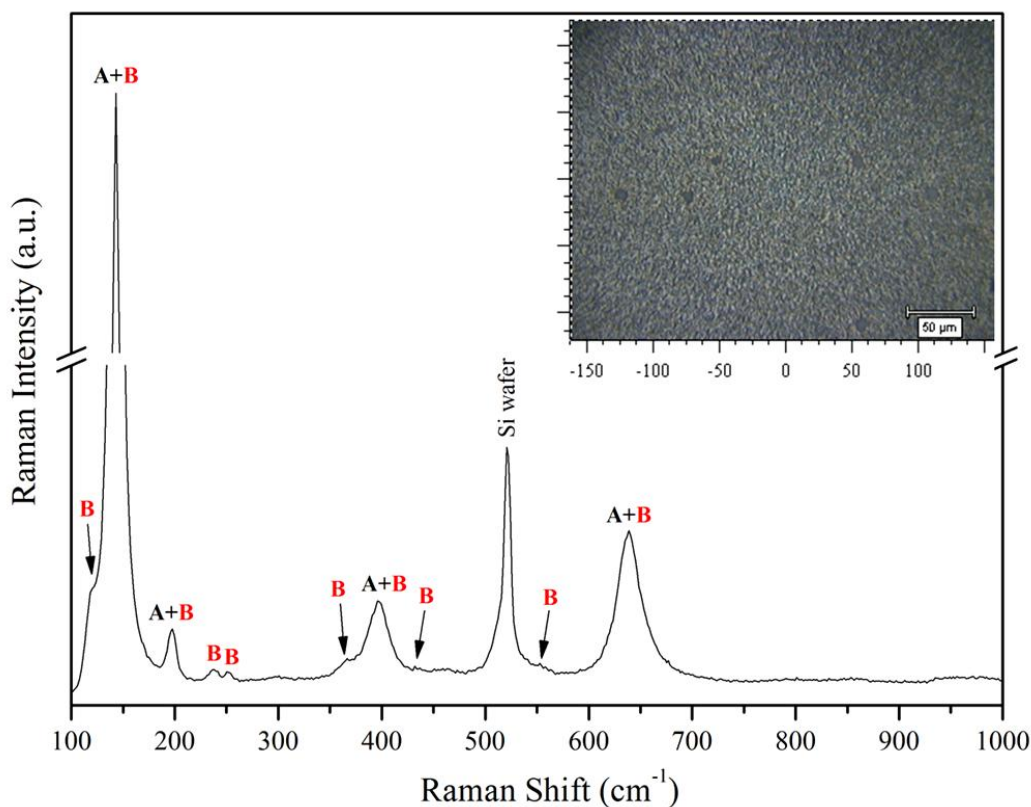


**Figure 7-2** Raman spectrum of thin film sample deposited on a pre-treatment Si wafer substrate by spraying 1.69% W/V of KOH solution. Inset is a light microscope image of thin film in plan view.

### 7.2.2 Influence of alkali metal hydroxide concentration used in pre-treatment process on phase formation

The titania/titanate phases of thin film samples synthesized by the modified LPCVD with pre-treatment by spraying alkali metal hydroxide solution onto the Si wafer substrate are briefly summarized in Table 7.2. The details of phase formation in the different systems are described below.

#### 7.2.2.1 Pre-treatment with LiOH solution

Figure 7-3 illustrates the XRD patterns of the thin films samples fabricated by LPCVD method with different concentrations of LiOH in the pre-treatment process. The concentration of LiOH was varied in the range of 0.1-2.5%<sup>w/v</sup> as explained in Table 7-1.

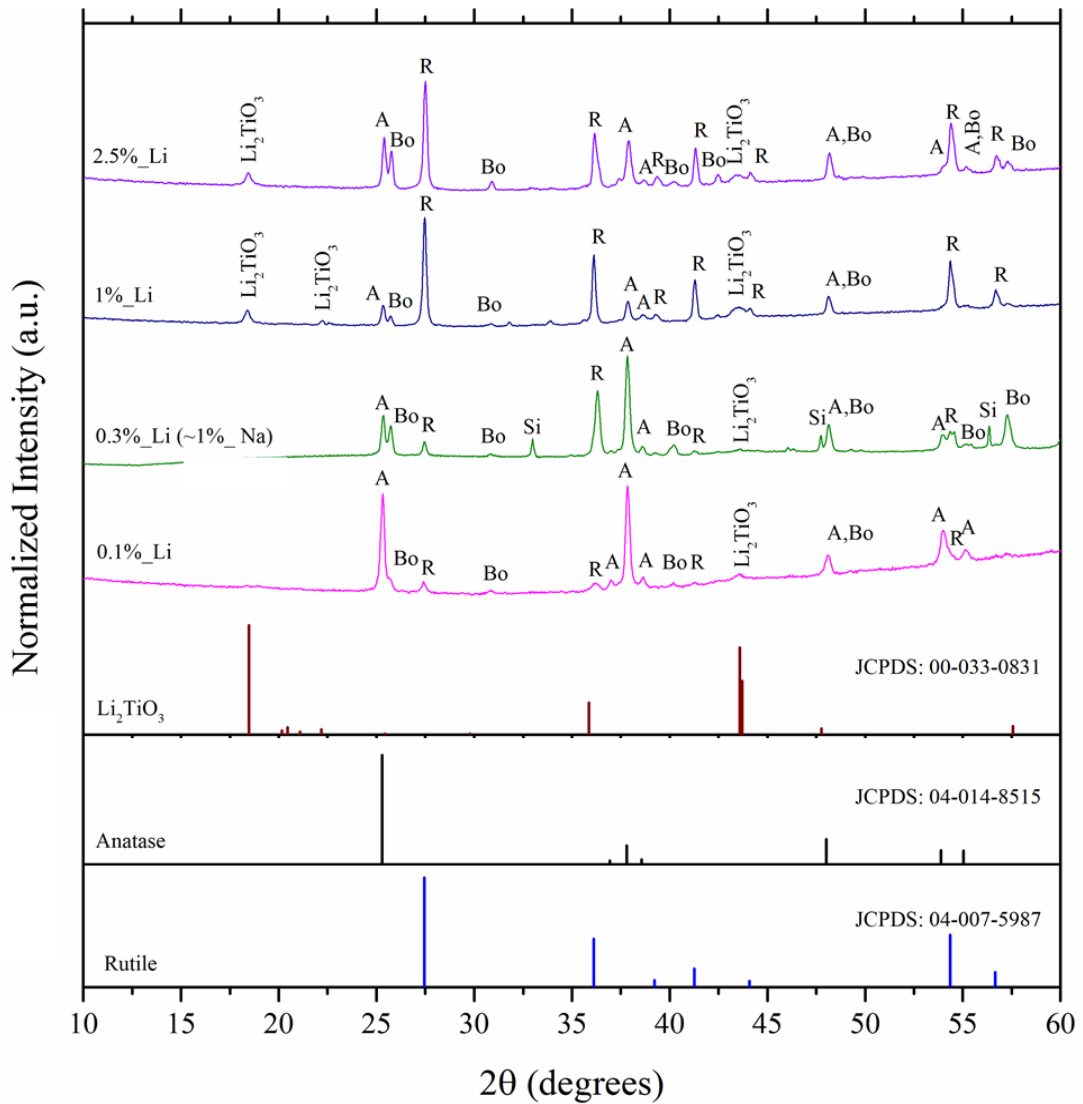


**Figure 7-3** XRD patterns of titania/titanate thin film samples deposited onto a Si wafer substrate which was pre-treated by spraying LiOH solution in four different concentrations of 0.1, 0.3, 1.0, and 2.5%<sup>w/v</sup>.

The results showed that whilst the anatase phase is a typical product from this LPCVD condition at 600°C, all of the patterns indicated mixed titania and titanate phases, consisting of anatase TiO<sub>2</sub>, rutile TiO<sub>2</sub>, brookite TiO<sub>2</sub> and lithium titanate (Li<sub>2</sub>TiO<sub>3</sub>) in varying proportions. The anatase phase showed a preferred orientation in the [001] direction as seen by a very strong peak at 2θ=37.8° the (004) lattice spacing. Unexpectedly, no evidence for TiO<sub>2</sub>(B) can be seen in any of the XRD patterns even at high or low concentrations of Li<sup>+</sup>, indicating that TiO<sub>2</sub>(B) cannot be prepared by the LPCVD method with Li<sup>+</sup> pre-treatment. Interestingly, the extra titania phases of brookite and rutile can be produced in this system which is untypical at 600°C for CVD preparation system. The relative proportion of the brookite phase remains almost the same in every level of Li<sup>+</sup> concentration. A higher concentration of Li<sup>+</sup> encourages an increase in the relative proportion of rutile and Li<sub>2</sub>TiO<sub>3</sub> in the thin films. The majority phase is changed from anatase at low Li<sup>+</sup> concentration to rutile at concentrations higher than 0.3% w/v. Calculated crystallite sizes of anatase, rutile and Li<sub>2</sub>TiO<sub>3</sub> derived using Scherrer's equation are all about 50 nm (the individual details of each samples are summarised in Table 7-3).

#### **7.2.2.2 Pre-treatment with NaOH solution**

For the case of Si wafer substrate pre-treatment by NaOH solution at three different Na<sup>+</sup> concentrations of 1.0, 2.0 and 5.0% w/v, the XRD diffractograms are shown in Figure 7-4. Both TiO<sub>2</sub>(B) and a majority phase of anatase are present in all samples. An extra monoclinic phase of Na<sub>2</sub>Ti<sub>6</sub>O<sub>13</sub> (JCPDS: 04-008-9451) occurs only at the high concentration of Na<sup>+</sup> of 5.0% w/v. The majority phase in every sample was anatase with a preferred orientation in the [100] direction as shown by a very strong peak at 2θ=48.0°. The relative proportion of TiO<sub>2</sub>(B) compared to the anatase phase increased with increasing Na<sup>+</sup> concentration; suggesting that TiO<sub>2</sub>(B) will become a majority phase when the Na<sup>+</sup> concentration is higher than 5.0% w/v. TiO<sub>2</sub>(B) phase formation arising from the effect of Na<sup>+</sup> ions in or on the LPCVD substrate is similar to the previous results in chapter 5 and chapter 6. The crystallite sizes derived from XRD line broadening in Figure 7-4 were estimated to be in the range 49-60 nm for both anatase and TiO<sub>2</sub>(B) as presented in Table 7-4.

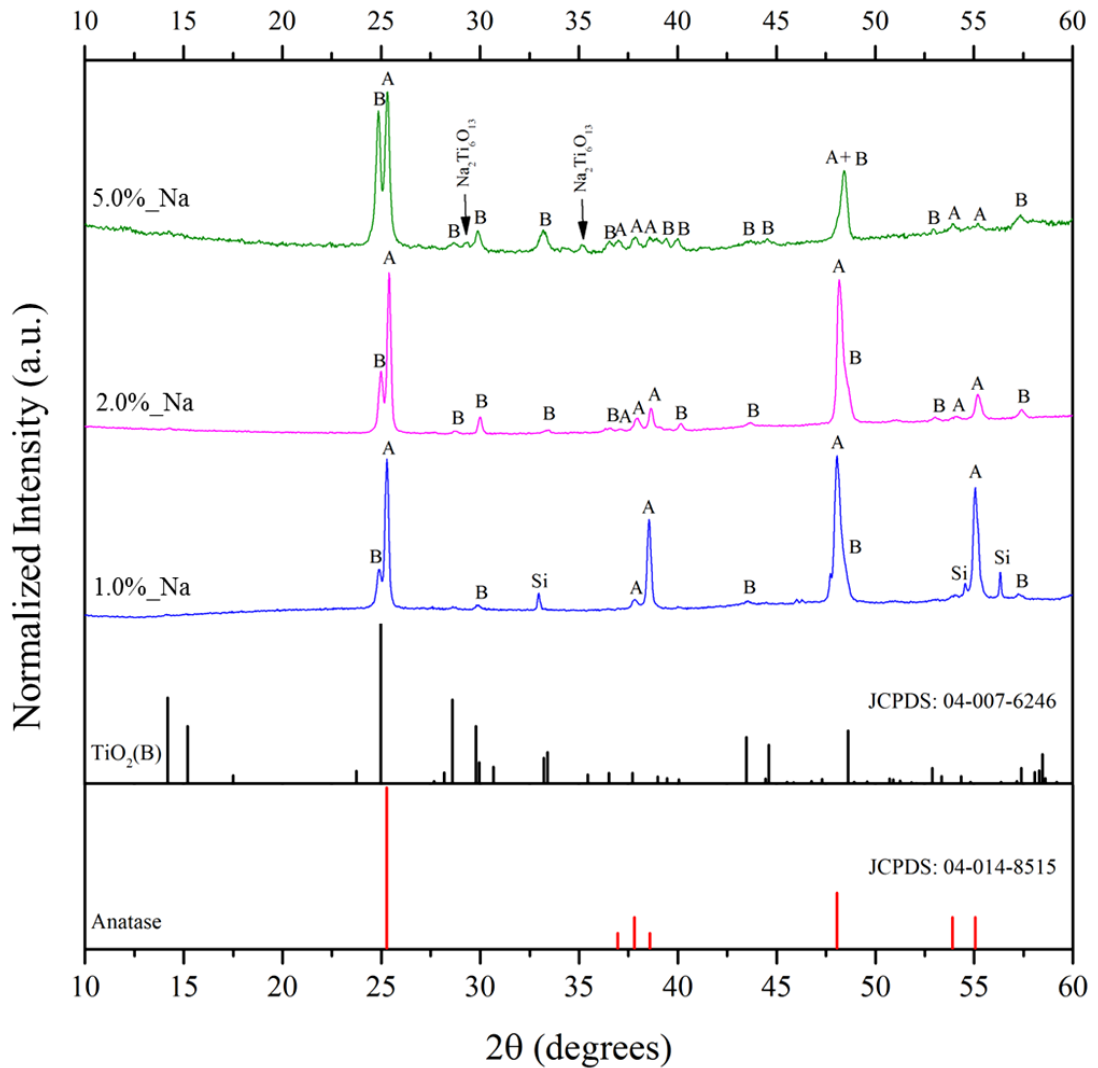


**Figure 7-4** XRD patterns of TiO<sub>2</sub> thin film samples deposited onto a Si wafer substrate which was pre-treated by spraying NaOH solution in three different concentrations of 1.0, 2.0, and 5.0% w/v.

### 7.2.2.3 Pre-treatment with KOH solution

Pre-treatment of Si wafer substrates by spraying with four different concentrations of KOH solutions (of 0.5, 1.0, 1.69, and 2.5% w/v) was studied. The XRD patterns of the films are shown in Figure 7-5. XRD of the 1.0%\_K, 1.69%\_K and 2.5%\_K samples do not show obvious peaks due to TiO<sub>2</sub>(B) however, an optimum condition to promote TiO<sub>2</sub>(B) phase formation appears to lie in the range between 1.0% w/v and 2.5% w/v. This trend is totally different from the results of NaOH in which the relative proportion of the TiO<sub>2</sub>(B) phase in the thin films increased with increasing alkali metal ion concentration. Unsurprisingly anatase appears for every synthesis condition and is the main component of the films. In addition, an unusual monoclinic phase of K<sub>2</sub>Ti<sub>6</sub>O<sub>13</sub> appears in every sample; it becomes the majority phase in the thin films when the concentration of KOH is 2.5% w/v. It can be noticed that the formation of a

monoclinic alkaline titanate is observed for all types of alkali metal ion (Li, Na and K) used in pre-treatment processes, nevertheless, there are significant differences in the relative proportion in each alkali-metal ion systems even though the number of moles of alkali metal ion are controlled. The crystallite sizes for anatase,  $K_2Ti_6O_{13}$  and  $TiO_2(B)$  phases, derived from XRD line broadening and Scherrer's Equation were all estimated to be in the range of 12-80 nm (Table 7-5)

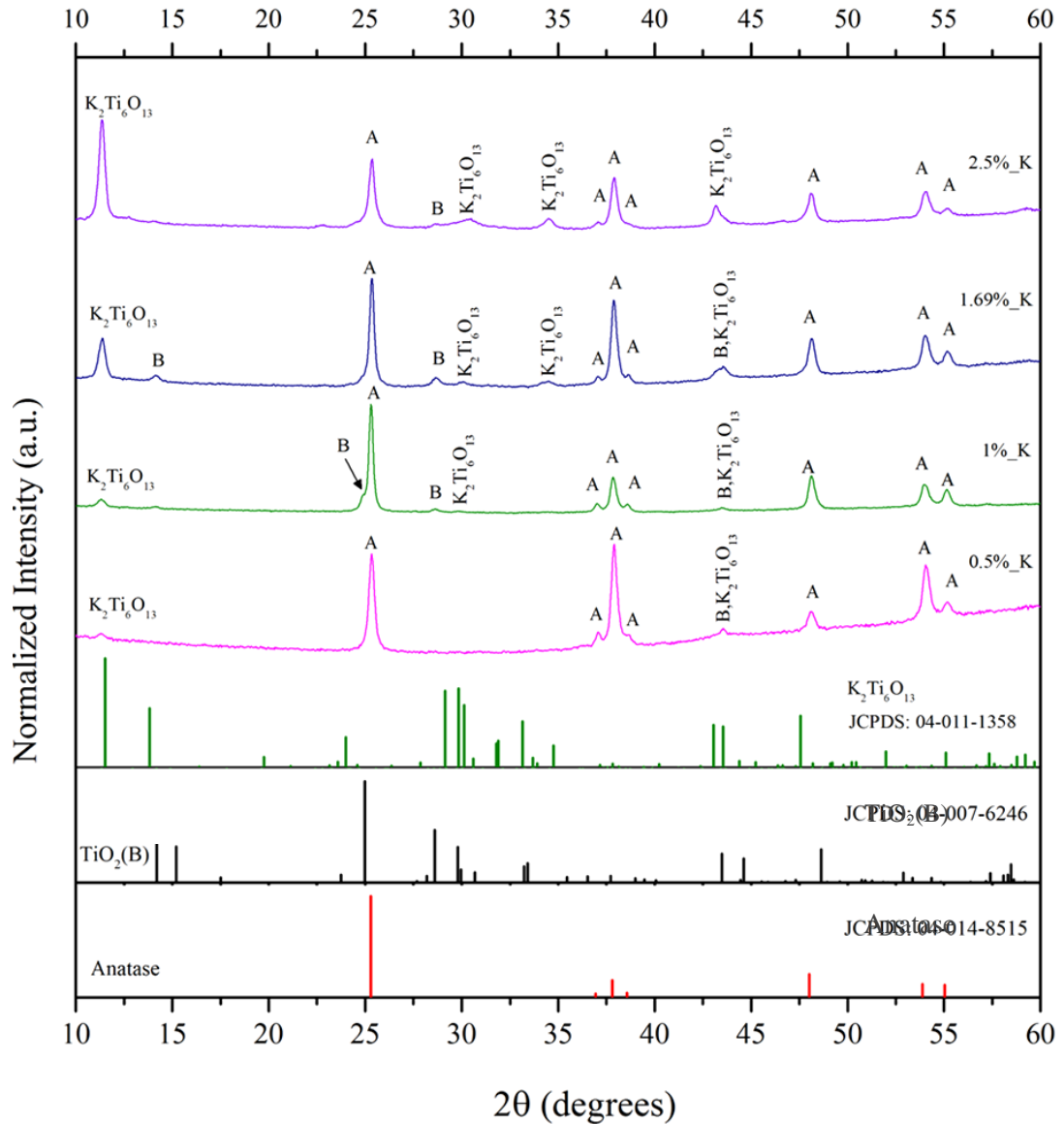


**Figure 7-5** XRD patterns of titania/titanate thin film samples deposited on a Si wafer substrate which was pre-treated by spraying KOH solution in four different concentrations of 0.5, 1.0, 1.69, and 2.5% w/v.

### 7.2.3 Influence of the different type of alkali metal ion on the physical appearance of the films

SEM secondary electron images were used to study the physical morphology of the thin film samples. SEM plan-view and SEM cross-sectional images of the thin film samples are shown in Figure 7-6. Thin film samples with the same molar concentration of alkali metals ions were investigated.

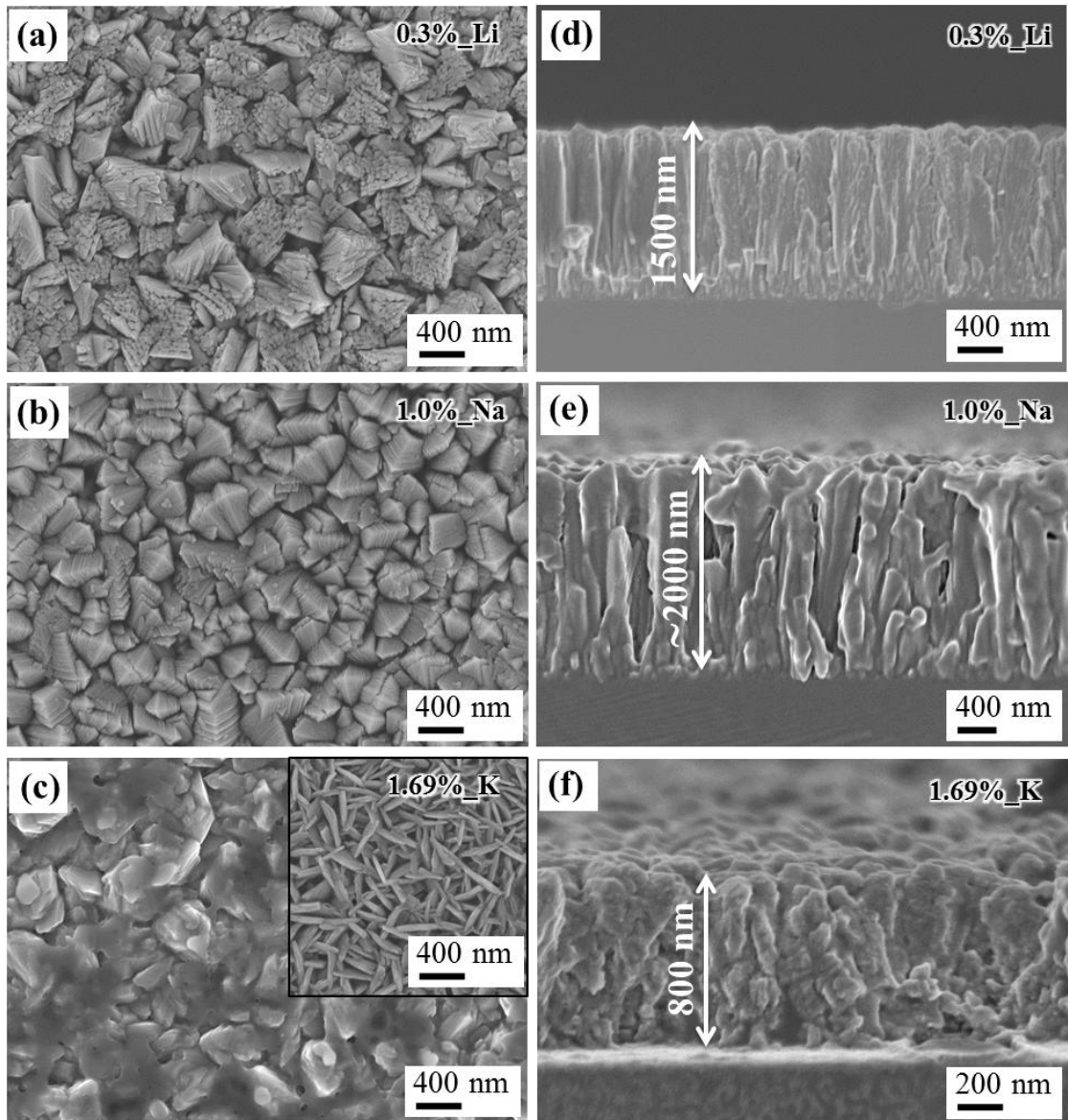


**Figure 7-6** SEM plan-view images of titania/titanate thin film samples deposited by LPCVD onto a pre-treated Si wafer substrate by spraying: (a) 0.3%<sup>w/v</sup> of LiOH; (b) 0.1%<sup>w/v</sup> of NaOH; (c) 1.69%<sup>w/v</sup> of KOH and SEM cross-sectional images of the thin films deposited on pre-treated Si wafer substrates: (d) 0.3%<sup>w/v</sup> of LiOH; (e) 0.1%<sup>w/v</sup> of NaOH; (f) 1.69%<sup>w/v</sup> of KOH

SEM plan view images of 0.3%\_Li, 1.0%\_Na and 1.69%\_K are shown in Figure 7-6 (a), (b) and (c) respectively. All show dense films consisting of polygonal-shaped grains except for 1.69%\_K which shows a few areas (see inset) composed of discrete needle particles with a needle width and length of around 50 and 200 nm. The average aggregated particle sizes derived from SEM images of the particles from the top surface of the films in 0.3%\_Li, 1.0%\_Na and 1.69%\_K are  $521 \pm 10.0$  (S.D.=148),  $368 \pm 2.0$  (S.D.=98) and  $230 \pm 2.0$  (S.D.=68) respectively.

The film thicknesses and physical morphologies have been investigated in SEM cross-sectional images illustrated in Figure 7-6(d), (e) and (f) of 0.3%\_Li, 1.0%\_Na and 1.69%\_K samples respectively. Basically, the film thickness remains constant when the LPCVD conditions are the same. However, these film thicknesses are quite variable and thicker than previous results in chapters 5 and 6 with approximate thicknesses of 1500, 2000 and 800 nm in 0.3%\_Li, 1.0%\_Na and 1.69%\_K samples respectively. All SEM cross-sectional images show a uniformed columnar structure, most obvious in 0.3%\_Li and 1.0%\_Na. The average aggregated particle sizes and film thicknesses for the other concentrations of  $\text{Li}^+$ ,  $\text{Na}^+$  and  $\text{K}^+$  samples are summarized in Table 7-3, Table 7-4 and Table 7-5.

The elemental analysis of all thin film samples were determined by SEM/EDX and the individual results relevant to the different types of alkali metal ions in pre-treatment process are given in Table 7-3, Table 7-4 and Table 7-5. It can be clearly seen that the EDX results confirm the existence of titanium oxide with a retention of Na and K in the individual samples corresponding to the alkali metal hydroxide solution used in the pre-treatment process. The atomic percentages of Na and K increase with an increase in nominal alkali metal hydroxide concentration. This means that the alkali metal ions in the titania/titanate thin films depend directly on the concentration of the alkali metal solution applied. However, the relative atomic composition of Ti, O and alkali metals may be affected by the electron beam interaction with the Si wafer substrate or by an inhomogeneous region of spraying by the alkali metal hydroxide. In the case of  $\text{Li}^+$  pre-treatment, EDX cannot detect a signal of Li element due to the limitation of the characterization technique for such light elements (if produced,  $\text{Li K}\alpha$  X-rays are absorbed in detector window).

**Table 7-3** List of synthesised samples following LiOH pre-treatment with results of SEM/EDX quantitative elemental analysis, XRD crystallite size and measured aggregate particle size and film thickness derived from SEM images. Note Li not detectable by EDX.

| Sample name | Calculated crystallized size by Scherrer's equation (nm)<br>*From X'Pert High Score Plus |            |                                  | Measured aggregated particle size (nm)                         | Measured film thickness (nm) | Atomic percent composition from SEM/EDX |      |      |      |      |
|-------------|--|------------|----------------------------------|--|------------------------------|---|------|------|------|------|
|             | Anatase  | Rutile     | Li <sub>2</sub> TiO <sub>3</sub> |  |                              | Li                                      | Ti   | O    | Si   | C    |
| 0.1%_Li     | 43<br>±5.0   | 50<br>±5.0 | 12<br>±5.0                       | 136±2.0<br>(S.D.= 5.4)   | 371±5.0<br>(S.D.=14.8)       | N/A                                     | 13.5 | 46.2 | 27.5 | 12.8 |
| 0.3%_Li     | 51<br>±5.0   | 81<br>±5.0 | -                                | 521±10.0<br>(S.D.=148.1)*<br>primary<br>59±2.0<br>(S.D.= 19.6) | 1623±5.0<br>(S.D.=41.9)      | N/A                                     | 32.2 | 62.5 | 0.1  | 5.2  |
| 1.0%_Li     | 43<br>±5.0   | 50<br>±5.0 | 49<br>±5.0                       | 176±2.0<br>(S.D.=80.1)   | 996±5.0<br>(S.D.=55.4)       | N/A                                     | 19.2 | 64.5 | 8.9  | 7.3  |
| 2.5%_Li     | 51<br>±5.0   | 50<br>±5.0 | 49<br>±5.0                       | 132±2.0<br>(S.D.=43.2)   | 680±5.0<br>(S.D.=47.2)       | N/A                                     | 17.2 | 56.3 | 17.1 | 9.4  |

**Table 7-4** List of synthesised samples following NaOH pre-treatment with results of SEM/EDX quantitative elemental analysis, XRD crystallite size and measured aggregate particle size and film thickness derived from SEM images.

| Sample name | Calculated crystallized size from Scherrer's equation (nm) *From X'Pert High Score Plus |                                 | Measured primary particle size (nm) | Measured film thickness (nm) | Atomic percent composition from SEM/EDX |      |      |      |     |
|-------------|---|---------------------------------|-------------------------------------|------------------------------|---|------|------|------|-----|
|             | TiO <sub>2</sub> (B)  | Anatase                         |                                     |                              | Na                                      | Ti   | O    | Si   | C   |
| 1%_Na       | 62±5.0  | 50±5.0                          | 368±2.0<br>(S.D.=97.6)              | 2436±5.0<br>(S.D.=119.8)     | 0.6                                     | 31.6 | 64.4 | 0.1  | 3.4 |
| 2%_Na       | 50±5.0  | 62±5.0<br>(Peak48,<br>38.9±5.0) | 191±2.0<br>(S.D.=61.7)              | 1175±5.0<br>(S.D.=44.4)      | 1.5                                     | 30.7 | 65.2 | 0.5  | 2.2 |
| 5%_Na       | 50±5.0<br>(Peak30,<br>62.1)   | 50±5.0                          | 132±2.0<br>(S.D.=53.8)              | 959±5.0<br>(S.D.=50.6)       | 2.5                                     | 33.4 | 53.7 | 10.3 | -   |

**Table 7-5** List of synthesised samples following KOH pre-treatment with results of SEM/EDX quantitative elemental analysis, XRD crystallite size and measured aggregate particle size and film thickness derived from SEM images.

| Sample name | Calculated crystallized size from Scherrer's equation (nm)<br>*From X'Pert High Score Plus |            |  | Measured primary particle size (nm) | Measured film thickness (nm) | Atomic percent composition from SEM/EDX |      |      |      |     |
|-------------|--|------------|--|-------------------------------------|------------------------------|---|------|------|------|-----|
|             | TiO <sub>2</sub> (B)   | Anatase    | K <sub>2</sub> Ti <sub>6</sub> O <sub>13</sub> |                                     |                              | K                                       | Ti   | O    | Si   | C   |
| 0.5%_K      | -  | 37<br>±5.0 | 12<br>±5.0                                     | 79±2.0<br>(S.D.= 27.3)              | 637±5.0<br>(S.D.=28.6)       | 0.2                                     | 15.2 | 48.7 | 26.9 | 9.1 |
| 1.0%_K      | 81<br>±5.0   | 50<br>±5.0 | 36<br>±5.0                                     | 67±2.0<br>(S.D.=30.7)               | 752±5.0<br>(S.D.=132.7)      | 0.4                                     | 20.7 | 54.3 | 24.7 | -   |
| 1.69%_K     | 36<br>±5.0   | 42<br>±5.0 | 26<br>±5.0                                     | 229±2.0<br>(S.D.=67.8)              | 846±5.0<br>(S.D.=24.5)       | 1.4                                     | 17.6 | 69.6 | 5.3  | 6.2 |
| 2.5%_K      | 38<br>±5.0   | 42<br>±5.0 | 32<br>±5.0                                     | 150±2.0<br>(S.D.=109.8)             | 764±5.0<br>(S.D.=76.9)       | 1.7                                     | 17.8 | 62.0 | 9.0  | 9.5 |

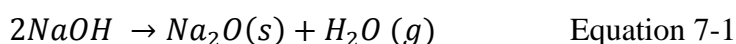
### 7.3 Discussion

In chapter 6, mixed phase  $\text{TiO}_2(\text{B})$  and anatase thin films on different substrates were successfully prepared *via* the modified LPCVD route. A mechanism of  $\text{TiO}_2(\text{B})$  formation was proposed involving the decomposition of a pre-deposited sodium-containing solution ( $\text{NaOEt}$ ) and the diffusion of  $\text{Na}^+$  ions into the deposited  $\text{TiO}_2$  layer. The diffusion of  $\text{Na}^+$  ions through the titania/titanate structure is the key concept to form  $\text{TiO}_2(\text{B})$ . In this section of the research, the work has been extended by investigating the effect of different alkali metal ions on titania/titanate phase formation using a modified LPCVD method.  $\text{Li}^+$ ,  $\text{Na}^+$  and  $\text{K}^+$  ions from  $\text{LiOH}$ ,  $\text{NaOH}$  and  $\text{KOH}$  solution were used as pre-treatments prior to formation of thin film products. The summary of results of phase formation can be hierarchically illustrated as schematically shown in Figure 7-7.

From the evidence provided by XRD and SEM/EDX and the previously proposed mechanism in chapters 5 and 6, I can separate the phase formation mechanism during the LPCVD process into 2 main pathways: (1) the general LPCVD process without the presence of alkali metal ions and (2) a pathway involving the presence of alkali metal ions ( $\text{Li}^+$ ,  $\text{Na}^+$  and  $\text{K}^+$ ). Both are briefly described in Figure 7-7. For pathway (1), the phase of titania films prepared by LPCVD on any substrate in the absence of alkali metal ions is typically anatase. This result is supported by the literature [1]–[4] and my research in chapters 5 and 6 [5] that suggests only the anatase phase can be prepared when the substrates were fused quartz and Si-wafer whereas the alkali-metal ions ( $\text{Na}^+$ )-containing substrates produced the  $\text{TiO}_2(\text{B})$  phase instead. This also can be applied to describe the formation of anatase phase in my samples when the thin films exhibit an absence or depletion of alkali metal ions. On the other hand, the presence of alkali metal ions can promote additional phase formation *via* the phase transformation from an alkali metal titanate intermediate phase formed during the migration of alkali metal ions (pathway (2)). Pathway (2) is specific to each alkali metal ion system.

### 7.3.1 The influence of Na<sup>+</sup> ions on titania/titanate phase formation during LPCVD method

The pre-treated substrate produced by the NaOH spraying method, was first pre-heated at 600°C under vacuum. During this process, NaOH thermally decomposes, according to the following reaction.



Above 320°C, which is lower than the temperature for pre-heating the substrate, NaOH can easily decompose to form a thin layer Na<sub>2</sub>O covering the substrate and also gas phase water as presented in Equation 7-1 [6]–[8]. Gaseous water is quickly removed from the system by the vacuum environment, encouraging the rate of NaOH decomposition.

During TiO<sub>2</sub> deposition onto the surface substrate (TiO<sub>2</sub> formed from TTIP decomposition in LPCVD system), Na<sup>+</sup> ions could migrate from the layer of Na<sub>2</sub>O into the nascent TiO<sub>2</sub> structure and form an intermediate phase of a layered monoclinic alkali metal titanate (Na<sub>x</sub>Ti<sub>y</sub>O<sub>z</sub>) [5]. The Na<sup>+</sup> ions possibly work as a templating agent for the construction and growth of the monoclinic alkali metal titanate layered structure. The Na<sub>x</sub>Ti<sub>y</sub>O<sub>z</sub> phase is supposedly a meta-stable phase which can easily reconstruct itself or completely eliminate Na<sup>+</sup> to form a more stable phase of Na<sub>2</sub>Ti<sub>n</sub>O<sub>2n+1</sub> and TiO<sub>2</sub>(B) respectively which have a homologous structure. Na<sub>2</sub>Ti<sub>n</sub>O<sub>2n+1</sub> has been normally reported as a final product of many synthesis methods when titania and alkali metal ion are used as the precursors [9]–[12]. There are many stable forms of the Na<sub>2</sub>Ti<sub>n</sub>O<sub>2n+1</sub> such as Na<sub>2</sub>Ti<sub>3</sub>O<sub>7</sub>, Na<sub>2</sub>Ti<sub>4</sub>O<sub>9</sub>, Na<sub>2</sub>Ti<sub>6</sub>O<sub>13</sub> and Na<sub>2</sub>Ti<sub>8</sub>O<sub>17</sub>, however the most commonly found structure is Na<sub>2</sub>Ti<sub>6</sub>O<sub>13</sub> which corresponds with evidence from XRD of the 5.0%\_Na sample and from the hydrothermal synthesis sample in chapter 4.

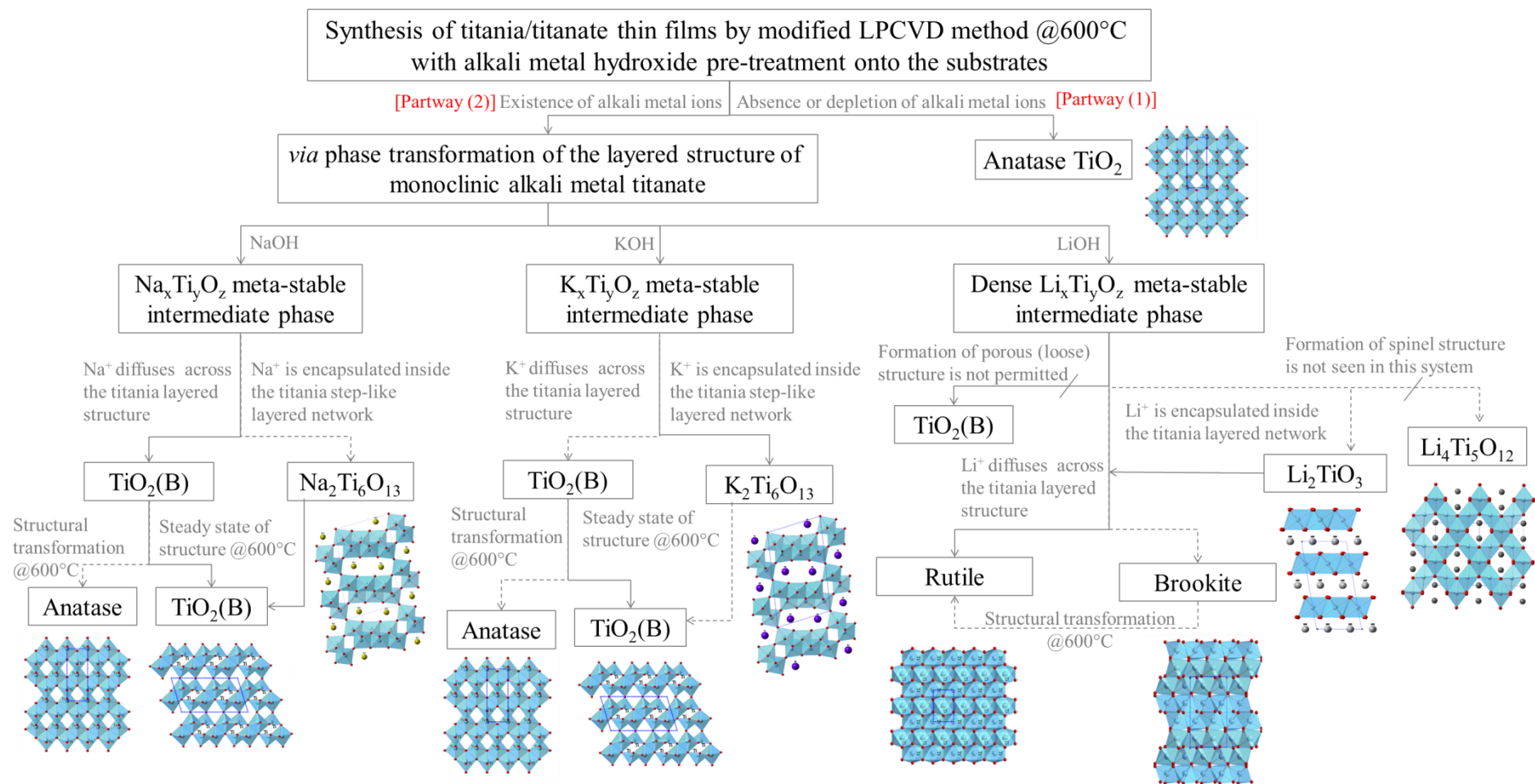


**Figure 7-7** Schematic diagram summarizing the hierarchical phase formation of titania/titanate thin films fabricated by modified LPCVD process using alkali metal ions (Li<sup>+</sup>, Na<sup>+</sup>, K<sup>+</sup>) pre-treatment of the substrate surface.

As well as the experimental evidence, theoretical data from the Na<sub>2</sub>O-Ti<sub>2</sub>O binary phase diagram (Figure 7-8) also suggests a preferred formation of Na<sub>2</sub>Ti<sub>6</sub>O<sub>13</sub> and TiO<sub>2</sub> at high temperatures and when the mole fraction of Ti<sub>2</sub>O/Na<sub>2</sub>O is higher than 0.75. According to the EDX results of 5.0%\_Na sample, this suggests that the atomic ratio of Ti/Na is around 0.93 (33.4/(33.4+2.5)); at Ti<sub>2</sub>O/Na<sub>2</sub>O=0.9 the phase separates into TiO<sub>2</sub> and Na<sub>2</sub>Ti<sub>6</sub>O<sub>13</sub>. However, as found in chapter 5 and 6, the thin film sample prepared by LPCVD is not a homogeneous phase composition and therefore, the atomic ratio from EDX cannot directly refer to an initial atomic ratio during the phase formation reaction.

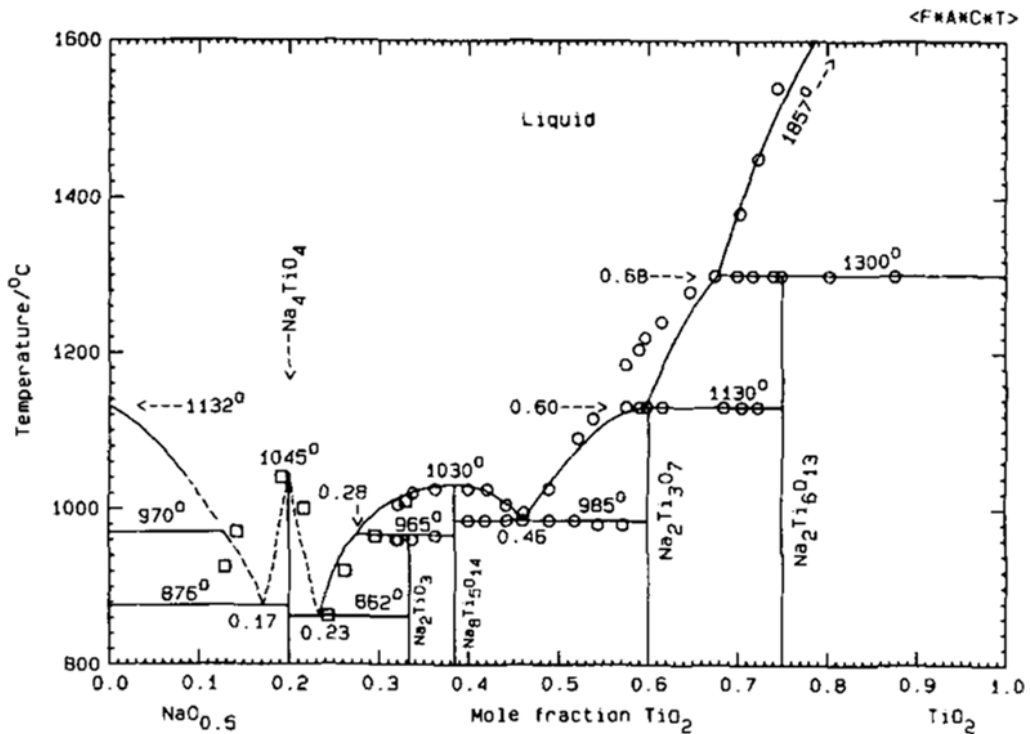


**Figure 7-8** The phase diagram of the Na<sub>2</sub>O-TiO<sub>2</sub> system [13]

Thus in a homogeneous system of the Na<sub>2</sub>O and Ti<sub>2</sub>O, the formation reaction of Na<sub>2</sub>Ti<sub>6</sub>O<sub>13</sub> formation is given by Equation 7-2.



According to thermodynamic databases [13], [14], the calculated Gibbs free energy of the above reaction ( $\Delta G$ ) is -2416.13 kJ/mol, indicating the formation reaction of Na<sub>2</sub>Ti<sub>6</sub>O<sub>13</sub> is a spontaneous reaction.

Small cations such as Li<sup>+</sup>, Na<sup>+</sup> and K<sup>+</sup> ions play an important role in a function of cationic counterpart in order to balance an anionic surface of Ti<sub>x</sub>O<sub>y</sub> layered structure, for this reason the cations are considered to be mobile species in the alkali metal titanate layered structure. The Na<sup>+</sup> ions in the sodium titanate layered structures (both

of  $\text{Na}_x\text{Ti}_y\text{O}_z$  and  $\text{Na}_2\text{Ti}_6\text{O}_{13}$ ) can migrate out of the interlayer spacing *via* ion diffusion during heat treatment at 600°C.

The structure of  $\text{TiO}_2(\text{B})$  exhibits channels or voids sizes of around 2.5-3.2 Å which is very close to the interlayer spacing of the intermediate sodium titanate structure (~3.2 Å). This might support an assumption that after the  $\text{Na}^+$  is removed out of the interlayers, the layered structures may subsequently rearrange to form the more stable structure of  $\text{TiO}_2(\text{B})$  as shown in Figure 7-9.

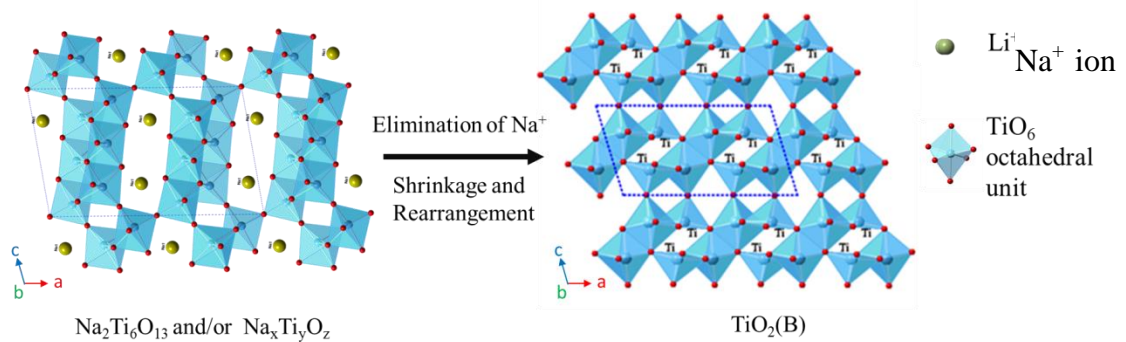


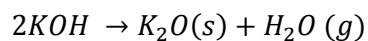
**Figure 7-9** Schematic diagram representation of a phase transformation from an intermediate phase ( $\text{Na}_2\text{Ti}_6\text{O}_{13}$  and/or  $\text{Na}_x\text{Ti}_y\text{O}_z$ ) with the step-like layered structure to a porous structure of  $\text{TiO}_2(\text{B})$  phase.

$\text{Na}^+$  ions from the lower thin film layers can continuously migrate into freshly deposited  $\text{TiO}_2$  (upper layer), forming a new layered sodium titanate phase [5]. This seems to be a cycle of  $\text{TiO}_2(\text{B})$  phase formation layer by layer via transformation of the sodium titanate layered structure. However, in the absence of  $\text{Na}^+$  ions or in a region where  $\text{Na}^+$  ions are depleted, the anatase phase will be formed instead of  $\text{TiO}_2(\text{B})$ .

Generally,  $\text{TiO}_2(\text{B})$  is considered to be a meta-stable phase which easily structurally transforms to the anatase phase at temperatures higher than 600°C [15], [16].

### 7.3.2 The influence of $\text{K}^+$ ions on titania/titanate phase formation during LPCVD

During the pre-treatment process at 600°C, KOH can thermally decompose, providing a thin layer of  $\text{K}_2\text{O}$  as shown in the following reaction [17].



Equation 7-3

The mechanism of the titania/titanate phase formation under the influence of  $K^+$  ions is presumed to be analogous to the effect of  $Na^+$  ions due to the similar chemical and physical properties of both cations including the evidence from XRD and SEM/EDX results. This potential mechanism is schematically illustrated in Figure 7-7.

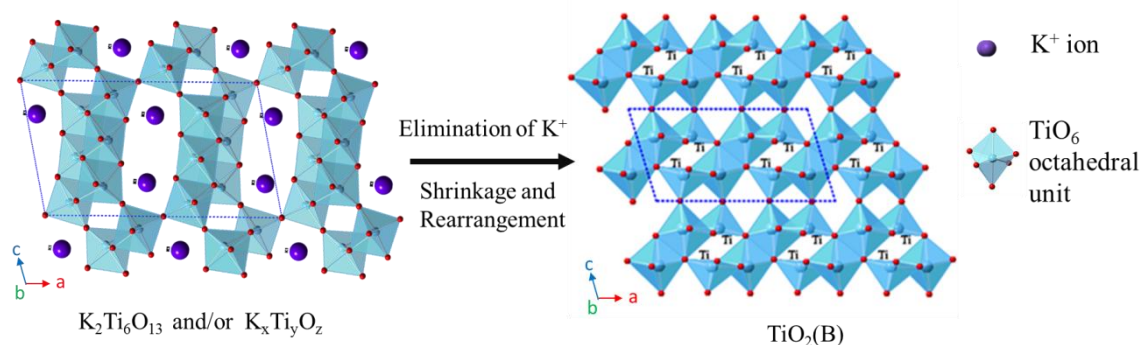


**Figure 7-10** Schematic diagram of the phase transformation from an intermediate phase ( $K_2Ti_6O_{13}$  and/or  $K_xTi_yO_z$ ) with the step-like layered structure to a porous structure of  $TiO_2(B)$  phase.

In a region absent of  $K^+$  ions, the LPCVD deposition method with a TTIP precursor at  $600^\circ C$  generally promotes only the formation of anatase  $TiO_2$  whereas in the region containing  $K^+$  ions, the diffusion of  $K^+$  from the  $K_2O$  layer into a nascent deposited  $TiO_2$  encourages the formation of a step-like layered structure of the potassium titanate intermediate phase ( $K_xTi_yO_z$ ) during  $TiO_2$  thin film deposition. The meta-stable phase of  $K_xTi_yO_z$  can rapidly reconstruct to form a more stable phase with a similar step-like layered structure to  $K_2Ti_6O_{13}$ . In some case, the  $K^+$  ions inside the layered structure (both of  $K_xTi_yO_z$  and  $K_2Ti_6O_{13}$ ) can be removed, leaving vacancies between the interlayered spacing. This structure is unstable which rearranges itself to form  $TiO_2(B)$  structure as schematically shown in Figure 7-10.

However, the results from XRD obviously show the presence of two main phases in the thin films: anatase and  $K_2Ti_6O_{13}$ . Surprisingly, the  $TiO_2(B)$  phase is a minority component and the most intense peaks are from  $K_2Ti_6O_{13}$ . Interestingly, this is an inversion of the results from the thin films synthesized by pre-treatment with  $Na^+$  ions in which  $TiO_2(B)$  is the majority component and  $Na_2Ti_6O_{13}$  is in the minority. This implies that the structural stability of  $K_2Ti_6O_{13}$  is higher than that of  $Na_2Ti_6O_{13}$  and  $TiO_2(B)$  even though  $\Delta G$  formation for  $K_2Ti_6O_{13}$  is less negative than for  $Na_2Ti_6O_{13}$ . The relative ratio of the  $K^+$  ionic radius to the layer spacing of  $K_2Ti_6O_{13}$  structure is around 0.37 which is significantly bigger than for the  $Na^+/Na_2Ti_6O_{13}$  system (0.31), making it harder and slower for the migration of  $K^+$  out of the layered structure to form  $TiO_2(B)$ . These may cause a preferred formation of  $K_2Ti_6O_{13}$  rather than  $TiO_2(B)$ . Increased amounts of  $K^+$  ions should promote the phase component of

$K_2Ti_6O_{13}$  in the thin film and indeed it was found that the relative proportion of the  $K_2Ti_6O_{13}$  phase in the thin-film products increased with increasing alkali metal ion ( $K^+$ ) concentration as seen in XRD patterns of Figure 7-5.

Considering the binary phase diagram of a  $K_2O$ - $Ti_2O$  system as shown in Figure 7-11 when the  $TiO_2/K_2O$  mole ratio is close to 1.0 (0.75-1.0) at  $600^\circ C$  (the Ti/K atomic ratios from EDX results is in range of 0.91-0.99), the phase separates into  $K_2Ti_6O_{13}$  and  $TiO_2$  in agreement with the XRD results.

The thermodynamic data of a  $K_2Ti_6O_{13}$  phase formation reaction has been considered through an equation below.



The calculated Gibbs free energy ( $\Delta G$ ) of the above reaction is around  $-2256.41 \text{ kJ.mol}^{-1}$ . This suggests that a spontaneous reaction of  $K_2Ti_6O_{13}$  can occur during the LPCVD process [13], [14].

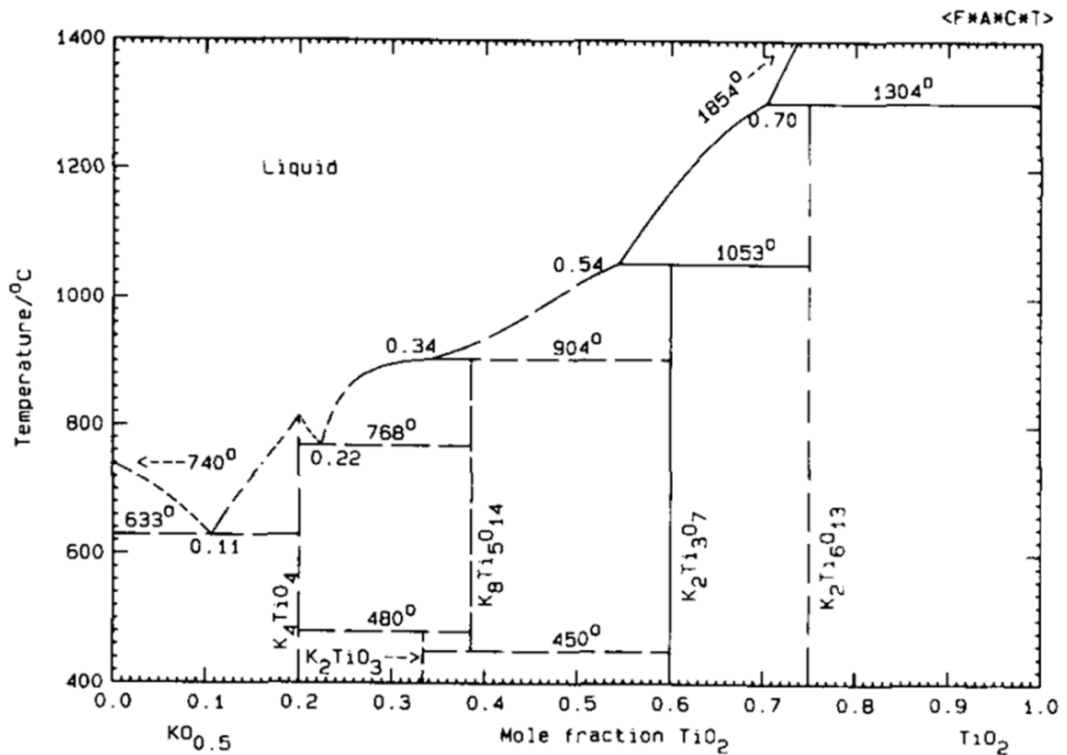


**Figure 7-11** The phase diagram of the  $K_2O$ - $TiO_2$  system [13]

### 7.3.3 The influence of Li<sup>+</sup> on titania/titanate phase formation during LPCVD method

In case of Li<sup>+</sup> ions applied during pre-treatment of the substrate before the LPCVD synthesis process, the XRD results are significantly different from the results with Na<sup>+</sup> and K<sup>+</sup> ions. The final phases in the thin films are anatase, rutile, brookite and Li<sub>2</sub>TiO<sub>3</sub>. The XRD pattern shows an obvious increase in the amount of the rutile phase together with a decrease in the anatase phase in the thin film as the concentration of Li<sup>+</sup> ions was increased; whereas the percentage phase composition of brookite and Li<sub>2</sub>TiO<sub>3</sub> are relatively constant in every condition. The influence of Li<sup>+</sup> will be described using a similar concept to that used for Na<sup>+</sup> and K<sup>+</sup>.

During the pre-heat treatment process, the deposited LiOH on the Si wafer substrate surface can decompose as shown in Equation 7-5 [18], generating a thin layer of Li<sub>2</sub>O coated on the surface substrate before the start of the LPCVD reaction.



In an area of insufficient Li<sup>+</sup>, the LPCVD deposition method at 600°C promotes the phase formation of anatase as seen in results for typical CVD methods at 600°C in the literature. Whereas in the area containing Li<sup>+</sup>, Li<sup>+</sup> ion migration from the Li<sub>2</sub>O layer, into the structure of the nascent TiO<sub>2</sub> thin film, forms an intermediate phase of a layered sheet Li<sub>x</sub>Ti<sub>y</sub>O<sub>z</sub> structure with a monoclinic crystal structure (note this is not the same as the step-like layered structure of Na<sub>x</sub>Ti<sub>y</sub>O<sub>z</sub> and K<sub>x</sub>Ti<sub>y</sub>O<sub>z</sub>).

From the previous proposed assumptions in the LPCVD system in the presence of K<sup>+</sup> and Na<sup>+</sup>, it was suggested that the ionic radius and the ionic diffusion of alkali metal ions in the layered titanate structure directly controls the phase formation at 600°C during the LPCVD process. These assumptions can be applied to the Li<sup>+</sup> system as well. The small size of Li<sup>+</sup> ions suggests a difference in crystal structure formation *via* cation templating leading to the construction of a plane layered structure such as Li<sub>x</sub>Ti<sub>y</sub>O<sub>z</sub> and Li<sub>2</sub>TiO<sub>3</sub>, instead of the layered step-like structure seen for Na and K derivatives. This is supported by literature [19], [20] in that the formation of monoclinic Li<sub>2</sub>TiO<sub>3</sub> usually occurs in the hydrothermal synthesis method with TiO<sub>2</sub> precursors in a LiOH solution.

Focusing on the crystal structure of the plane layered framework such as Li<sub>2</sub>TiO<sub>3</sub>, If the Li<sup>+</sup> ions located in the interlayers are removed out of the structure, each of the titania planes (Ti<sub>n</sub>O<sub>2n+1</sub>) may rearrange together to form a high-density structural form of TiO<sub>2</sub> such as brookite and rutile as shown in Figure 7-12. Owing to a meta-stable

nature of brookite at 600°C. It may subsequently structurally transform to the more stable phase of rutile [21].

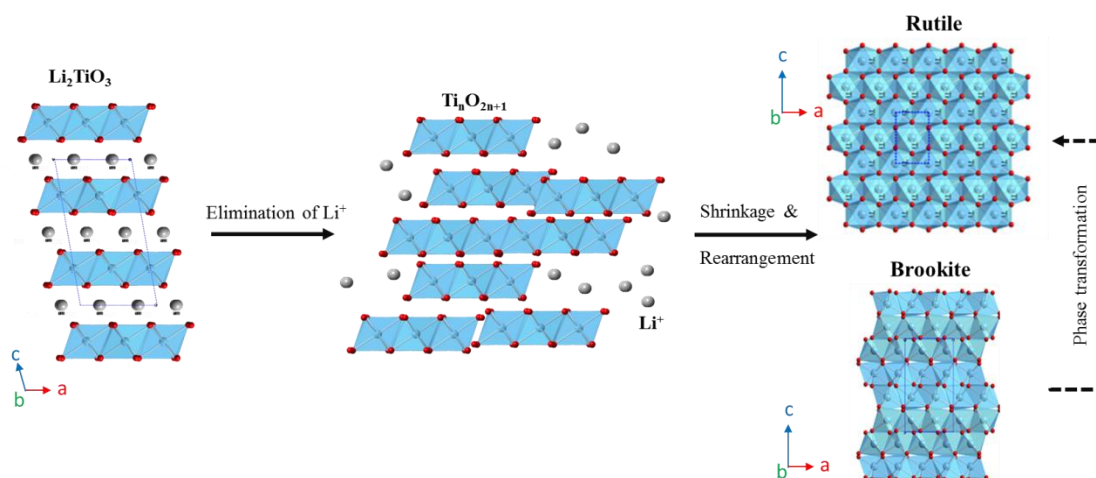


**Figure 7-12** Proposed steps of structural transformation during the process of an elimination of  $\text{Li}^+$  at 600°C

It appears to be difficult to form the  $\text{TiO}_2(\text{B})$  phase through  $\text{Li}^+$  ion templating,  $\text{Li}^+$  elimination and structural transformation as there is an absence of  $\text{TiO}_2(\text{B})$  peaks in XRD. The possible reasons for this may be:

(1) the lithium titanate intermediate structure is not a step-like layered framework like the sodium and potassium titanate phases which allow themselves to rearrange to form the porous structure of  $\text{TiO}_2(\text{B})$ . Instead the lithium titanate intermediate phase forms a sheet-like structure which is easily rearranged after elimination of  $\text{Li}^+$  ions to form the more close packed structures such as rutile and brookite;

(2) The relative ratio of the  $\text{Li}^+$  ionic radius to the layer spacing of  $\text{Li}_2\text{TiO}_3$  structure is 0.29 which is the smallest in the group of layered structures ( $\text{Na}_2\text{Ti}_6\text{O}_{13}$  &  $\text{K}_2\text{Ti}_6\text{O}_{13}$ ), causing easy migration of  $\text{Li}^+$  out of the plane layered structure to form a dense structure of rutile and brookite. The  $\text{Li}^+$  diffuse rapidly as compared to the other alkali metal ions ( $\text{Na}^+$  and  $\text{K}^+$ ) for example, the diffusion coefficients of the respective ions are  $D_{\text{Li}^+} = 2.29 \times 10^5 \text{ cm}^2/\text{s}$ ,  $D_{\text{Na}^+} = 2.08 \times 10^5 \text{ cm}^2/\text{s}$  and  $D_{\text{K}^+} = 1.69 \times 10^5 \text{ cm}^2/\text{s}$  at 327°C in  $\text{LiNO}_3$  as a matrix [22]. The faster migration of  $\text{Li}^+$  ions could cause a more rapid shrinkage producing more close-packed structures of  $\text{TiO}_2$ .

Figure 7-14 shows the binary phase diagram of the  $\text{Li}_2\text{O}-\text{Ti}_2\text{O}$  system [23]. According to LPCVD synthesis conditions when the  $\text{TiO}_2/\text{Li}_2\text{O}$  mole fraction is close to 1.0 at 600°C, the phase diagram suggests the phase formation of  $\text{Li}_4\text{Ti}_5\text{O}_{12}$ . However,  $\text{Li}_4\text{Ti}_5\text{O}_{12}$  exhibits a cubic spinel structure [24] which is dissimilar to the results from the  $\text{Na}_2\text{O}/\text{TiO}_2$  and  $\text{K}_2\text{O}/\text{TiO}_2$  phase diagrams which generally promote the formation of monoclinic sodium and potassium titanate intermediate phases. An

infinite-net structure of  $\text{Li}_4\text{Ti}_5\text{O}_{12}$  is constructed by self-assembly of  $\text{TiO}_6$  octahedral-building blocks with the isolated  $\text{Li}^+$  ions located as shown in Figure 7-13. However, as has been found in case of  $\text{K}^+$  and  $\text{Na}^+$  ions that the effect of cation templating on titanate phase formation in LPCVD systems typically promotes the monoclinic layered structure. Here XRD results suggest the formation of monoclinic layered structure of  $\text{Li}_2\text{TiO}_3$  over the cubic spinel structure of  $\text{Li}_4\text{Ti}_5\text{O}_{12}$ . This implies that the effect of cation template is more influential on the structural formation than the composition in the LPCVD system.

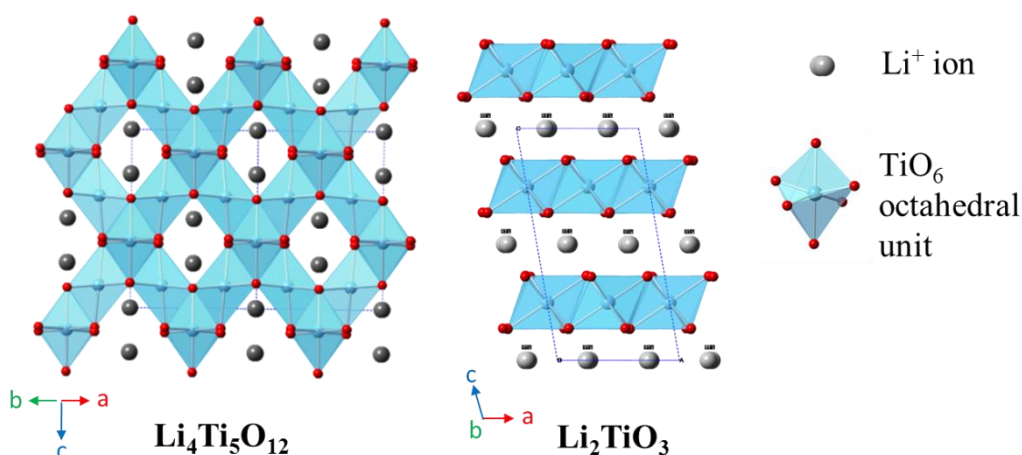


**Figure 7-13** Schematic diagram of a cubic crystal structure of  $\text{Li}_4\text{Ti}_5\text{O}_{12}$  and a monoclinic crystal structure of  $\text{Li}_2\text{TiO}_3$  showing a net-like framework and a plane layered structure respectively.

The Gibbs free energy ( $\Delta G$ ) of the  $\text{Li}_2\text{TiO}_3$  phase formation reaction calculated from the equation below is  $-261.62 \text{ kJ}\cdot\text{mol}^{-1}$ [14]. This suggests the spontaneous formation of  $\text{Li}_2\text{TiO}_3$  during the LPCVD process at  $600^\circ\text{C}$ .



As mentioned before, the aim of this chapter is to study the effects of the migration of different types of alkali metal ions on the phase formation during the LPCVD process with TTIP as a precursor. It was found that the phase formation in the thin films directly depended on the types of alkali metal ions used in the pre-treatment process of the Si wafer substrate. The different types of alkali metal ions produced different phase components. Only the substrate pre-treated with  $\text{Na}^+$  ions promoted the formation of  $\text{TiO}_2(\text{B})$  in the thin film in significant amounts. However,  $\text{K}^+$  and  $\text{Li}^+$  also produced interesting results, for example, forming extra phases in the thin film such as  $\text{K}_2\text{Ti}_6\text{O}_{13}$ ,  $\text{Li}_2\text{TiO}_3$ , brookite and rutile in different relative proportions depending on the concentration of alkali metal ions used in pre-treatment process. This may suggest the ability to control phase formation in thin films at the nanoscale. Moreover, the

modified LPCVD method with pre-treatment of alkali metal ions may offer a potential alternative route for a desired thin film preparation in a one-step synthesis.

Last but not least, the modified LPCVD method would be interesting for further study of the effect of other metal ions on titania/titanate phase formation in LPCVD such as the alkaline earth group.

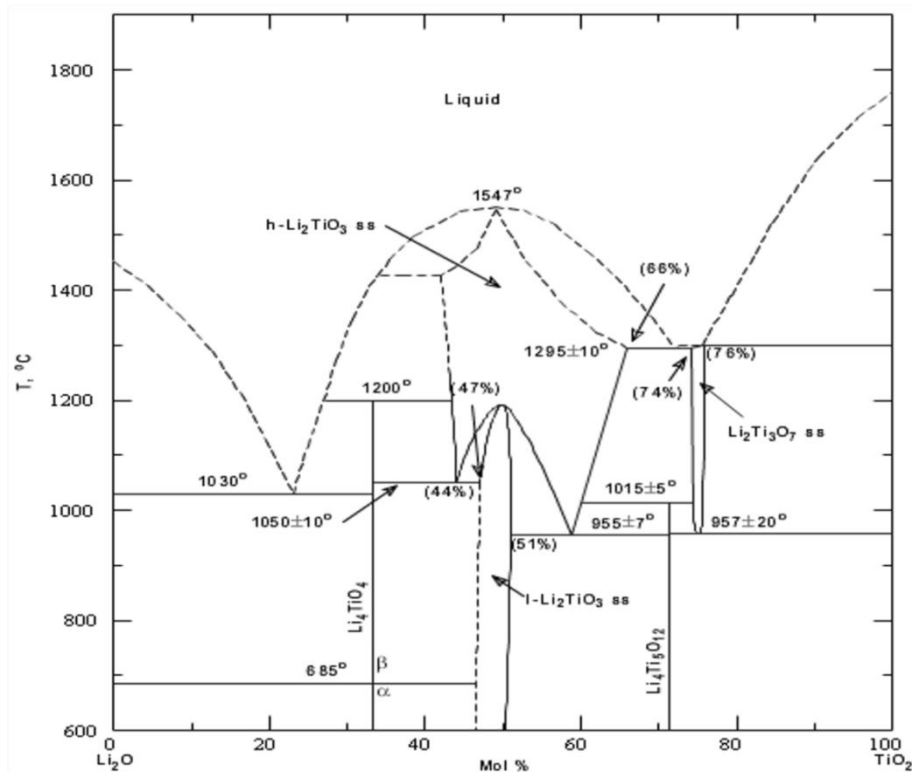


Figure 7-14 The binary phase diagram of the  $\text{Li}_2\text{O}$ - $\text{TiO}_2$  system.

## 7.4 Conclusions

Titania/titanate thin films were successfully prepared by a modified LPCVD method involving an alkali metal hydroxide solution sprayed onto a Si wafer substrate. A number of different types of alkali metal ions including  $\text{Li}^+$ ,  $\text{Na}^+$  and  $\text{K}^+$  from  $\text{LiOH}$ ,  $\text{NaOH}$  and  $\text{KOH}$  solutions in various concentrations have been investigated in terms of titania/titanate phase formation. TTIP and  $\text{N}_2$  gas were used as a titanium precursor and a carrier gas respectively in the LPCVD synthesis method operating at  $600^\circ\text{C}$  for 15 minutes.

Without the alkali metal hydroxide pre-treatment process, only the anatase phase was produced. Whereas other phases of titania/titanate in thin film samples such as  $\text{TiO}_2(\text{B})$ ,  $\text{K}_2\text{Ti}_6\text{O}_{13}$ ,  $\text{Na}_2\text{Ti}_6\text{O}_{13}$ ,  $\text{Li}_2\text{Ti}_3\text{O}_7$ , brookite and rutile, occurred when alkali metal ions were applied prior to the LPCVD process. All synthesised thin film samples were

investigated and a possible phase transformation mechanism proposed for the LPCVD process. All the proposed mechanisms involved formation of an intermediate phase of an alkali metal titanate, a structural transformation of the this intermediate phase, elimination of alkali metal ions out of the intermediate structure and finally a structural rearrangement process. The influence of  $\text{Na}^+$  and  $\text{K}^+$  can promote the formation of the  $\text{TiO}_2(\text{B})$  phase via the phase transformation of  $\text{Na}^+/\text{K}^+$ -free step-like layered structures. Only  $\text{Li}^+$  ions suggested a possible mechanism via transformation of a sheet-like  $\text{Li}_2\text{TiO}_3$  structure instead of the step-like frameworks owing to the small ionic radius and the fast diffusion coefficient. This leads to the presence of  $\text{Li}^+$  ions promoting formation of the dense phases of brookite and rutile instead of  $\text{TiO}_2(\text{B})$  during the structural transformation.

## 7.5 References

- [1] T. Yazawa, F. Machida, N. Kubo, and T. Jin, "Photocatalytic activity of transparent porous glass supported  $\text{TiO}_2$ ," *Ceram. Int.*, vol. 35, no. 8, pp. 3321–3325, 2009.
- [2] Z. ding, X. Hu, P.L. Yue, G.Q. Lu, and P.F. Greenfield, "Synthesis of anatase  $\text{TiO}_2$  supported on porous solids by chemical vapor deposition," *Catal. today*, vol. 68, pp. 173–182, 2001.
- [3] Z. Ding, X. Hu, G.Q. Lu, P.L. Yue, and P.F. Greenfield, "Novel silica gel supported  $\text{TiO}_2$  photocatalyst synthesized by CVD method," *Langmuir*, vol. 16, pp. 6216–6222, 2000.
- [4] W. Li, S.I. Shaa, C.P. Huang, O. jung, and C. Ni, "Metallorganic chemical vapor deposition and characterization of  $\text{TiO}$  nanoparticles," *Mater. Sci. Eng. B*, vol. 96, pp. 247–253, 2002.
- [5] Y. Chimupala, G. Hyett, R. Simpson, R. Mitchell, R. Douthwaite, S.J. Milne, and R.D. Brydson, "Synthesis and characterization of mixed phase anatase  $\text{TiO}_2$  and sodium-doped  $\text{TiO}_2(\text{B})$  thin films by low pressure chemical vapour deposition (LPCVD)," *RSC Adv.*, vol. 4, pp. 48507–48515, 2014.
- [6] K. Chandran, M. Kamruddin, P.K. Ajikumar, A. Gopalan, and V. Ganesan, "Kinetics of thermal decomposition of sodium methoxide and ethoxide," *J. Nucl. Mater.*, vol. 358, pp. 111–128, 2006.
- [7] K. Chandran, M. Kamruddin, P.K. Ajikumar, A. Gopalan, and V. Ganesan, "Thermal decomposition and kinetic analysis of sodium propoxides," *J. Nucl. Mater.*, vol. 374, pp. 158–167, 2008.
- [8] V.P. Yurkinskii, E.G. Firsova, and S.A. Proskura, "Inorganic synthesis and industrial inorganic chemistry: Thermal dissociation of sodium hydroxide upon evacuation," *Russ. J. Appl. Chem.*, vol. 78, no. 3, pp. 360–362, 2005.
- [9] N. Liu, X. Chen, J. Zhang, and J.W. Schwank, "A review on  $\text{TiO}_2$ -based nanotubes synthesized via hydrothermal method: Formation mechanism, structure modification, and photocatalytic applications," *Catal. Today*, vol. 225, pp. 34–51, 2014.

- [10] J. Akimoto, K. Kataoka, N. Kojima, S. Hayashi, Y. Gotoh, T. Sotokawa, and Y. Kumashiro, "A novel soft-chemical synthetic route using  $\text{Na}_2\text{Ti}_6\text{O}_{13}$  as a starting compound and electrochemical properties of  $\text{H}_2\text{Ti}_{12}\text{O}_{25}$ ," *J. Power Sources*, vol. 244, pp. 679–683, 2013.
- [11] Y. Suzuki and S. Yoshikawa, "Synthesis and Thermal analyses of  $\text{TiO}_2$ -derived nanotubes prepared by the hydrothermal method," *J. Mater. Res.*, vol. 19, no. 4., pp. 982–985, 2004.
- [12] V. Etacheri, Y. Kuo, A. Van-der-Ven, and B.M. Bartlett, "Mesoporous  $\text{TiO}_2$ -B microflowers composed of (1-10) facet-exposed nanosheets for fast reversible lithium-ion storage," *J. Mater. Chem. A*, vol. 1, pp. 12028, 2013.
- [13] G. Eriksson, P. Wu, and A.D. Pelton, "Critical evaluation and optimization of the thermodynamic properties and phase diagrams of the  $\text{MnO-TiO}_2$ ,  $\text{MgO-TiO}_2$ ,  $\text{FeO-TiO}_2$ ,  $\text{Ti}_2\text{O}_3\text{-TiO}_2$ ,  $\text{Na}_2\text{O-TiO}_2$ , and  $\text{K}_2\text{O-TiO}_2$  systems," *Metall. Trans. B*, vol. 17, no. October, pp. 189–205, 1993.
- [14] M.W. Chase, "NIST-JANAF Thermochemical Tables, 4th Ed.," *J. Phys. Chem. Ref. Data.*, Part I&II, 1998.
- [15] L. Brohan, A. Verbaere, M. Tournoux, and G. Demazeau, "La tranformation  $\text{TiO}_2(\text{B}) \rightarrow \text{anatase}$ ," *Mater. Res. Bull.*, vol. 17, pp. 355–361, 1982.
- [16] J.F. Banfield, D.F. Veblen, and D.J. Smith, "The identification of naturally occurring  $\text{TiO}_2(\text{B})$  by structure determination using high-resolution electron microscopy, image simulation, and refinement," *Am. Mineral.*, vol. 76, pp. 343–353, 1991.
- [17] A.N. Panova, R.K. Mustafina, and T.A. Charkina, "Nature of thermal decomposition of  $\text{NaOH}$  and  $\text{KOH}$  in a melt of alkali metal halide salts," *Transl. from Zhurnal Prikl. Spektrosk.*, vol. 24, no. 6, pp. 1105–1106, 1976.
- [18] H. Kudo, "The rates of thermal decomposition of  $\text{LiOH}(\text{s})$ ,  $\text{LiOD}(\text{s})$  and  $\text{LiOT}(\text{s})$ ," *J. Nucl. Mater.*, vol. 87, pp. 185–188, 1979.
- [19] C.L. Yu, K. Yanagisawa, S. Kamiya, T. Kozawa, and T. Ueda, "Monoclinic  $\text{Li}_2\text{TiO}_3$  nano-particles via hydrothermal reaction: Processing and structure," *Ceram. Int.*, vol. 40, no. 1, pp. 1901–1908, 2014.
- [20] M. Tomiha, N. Masaki, S. Uchida, and T. Sato, "Hydrothermal synthesis of alkali titanates from nano size titania powder," *J. Mater. Sci.*, vol. 37, pp. 2341–2344, 2002.
- [21] J. Huberty and H. Xu, "Kinetics study on phase transformation from titania polymorph brookite to rutile," *J. Solid State Chem.*, vol. 181, pp. 508–514, 2008.
- [22] G.J. Janz and N.P. Bansal, "Molten salts data: diffusion coefficients in single and multi-component salt systems," *J phys.chem.ref.data*, vol. 11. pp. 505, 1982.
- [23] G. Izquierdo and A.R. West, "Phase equilibria in the system  $\text{Li}_2\text{O-TiO}_2$ ," *Mater. Res. Bull.*, vol. 15, no. c, pp. 1655–1660, 1980.
- [24] K. Kataoka, Y. Takahashi, N. Kijima, J. Akimoto, and K.I. Ohshima, "Single crystal growth and structure refinement of  $\text{Li}_4\text{Ti}_5\text{O}_{12}$ ," *J. Phys. Chem. Solids*, vol. 69, pp. 1454–1456, 2008.

## Chapter 8 Conclusions and Future work

This thesis has successfully synthesised  $\text{TiO}_2(\text{B})$  by both a hydrothermal route and a LPCVD process. Characterisation using powder-XRD, Raman spectroscopy, TEM, SEM, and UV-Vis spectroscopy were employed to investigate the samples. Finally, mechanisms for the phase formation through both the LPCVD process and the hydrothermal route were proposed. The research content may be briefly described as follows:

Firstly, in order to investigate  $\text{TiO}_2(\text{B})$  phase formation mechanism through the structural transformation of an alkali titanate intermediate phase, the hydrothermal synthesis method was employed to synthesise  $\text{TiO}_2(\text{B})$  nanoparticles including a study of the phase formation mechanism;

Secondly, this research has achieved, for the first time, the synthesis of mixed phase  $\text{TiO}_2(\text{B})$  and anatase thin films on a soda lime glass substrate by an LPCVD synthesis method. A possible thin-film formation mechanism during the LPCVD process has been proposed;

Thirdly, a pre-treatment method involving spraying an  $\text{Na}^+$ -containing solution such as NaOEt or NaOH onto a number of different substrates was applied in conjunction with the LPCVD method in order to promote the formation of  $\text{TiO}_2(\text{B})$  phase in the thin film products formed on any substrate;

Finally, the effects of different alkali metal ions ( $\text{Li}^+$ ,  $\text{Na}^+$  and  $\text{K}^+$ ) during the pre-treatment step were investigated in relation to the phase formation in the titania/titanate thin films produced during the LPCVD process. Phase formation mechanisms based on the effects of alkali metal migration into the deposited titania thin films were proposed.

### 8.1 Research Summary

**Chapter 4**  $\text{TiO}_2(\text{B})$  1-D structures were successfully synthesized by a hydrothermal method using concentrated NaOH solution at  $180^\circ\text{C}$  for 2 days with subsequent ion-exchange and calcination. P25, rutile, anatase and also TTIP were used as Ti precursors in the alkali hydrothermal system.  $\text{Na}_2\text{Ti}_6\text{O}_{13}$  is the primary intermediate product after the hydrothermal treatment. It was ion-exchanged by immersing in 0.1M  $\text{HNO}_3$  solution for 1 day to form the intermediate phase of  $\text{H}_2\text{Ti}_3\text{O}_7$ . The dry samples of  $\text{H}_2\text{Ti}_3\text{O}_7$  were subsequently calcined at  $400^\circ\text{C}$  for 5 hr to produce the final products. Tracking of the phase transformations via an investigation of the products at each of

the steps was undertaken using powder-XRD and used to propose an integrated phase formation mechanism which is consistent with the literature. The phase transformation mechanism via a sodium titanate phase transformation is of interest in relation to  $\text{TiO}_2(\text{B})$  fabricated by the other methods when  $\text{Na}^+$  ions are present in the system.

**Chapter 5**  $\text{TiO}_2$  thin films were synthesized using a Low Pressure Chemical Vapour Deposition (LPCVD) process onto glass substrates. Titanium isopropoxide (TTIP) and  $\text{N}_2$  gas were used as the precursor and carrier gas respectively. The effects of reaction temperature, carrier gas flow rate and substrate position in the furnace were studied. SEM, TEM, powder XRD and UV-Vis and Raman spectroscopy were employed to characterize the phase and morphology of the synthesized materials. The results showed that a dual phase (sodium-doped  $\text{TiO}_2(\text{B})$  and anatase) nanocrystalline thin film was successfully prepared by LPCVD with needle- and polygonal plate-shape crystallites respectively. At the interface with the substrate, the thin film deposit exhibited a preferred orientation of  $\text{TiO}_2(\text{B})$  needles in the [001] direction of average crystallite size 50-80 nm in length and 5-10 nm in width, whilst the crystallite size of anatase polygonal-plates was around 200 nm. The optimal LPCVD condition for preparing this mixed phase of  $\text{TiO}_2$  was  $550^\circ\text{C}$  (actual temperature) with a 1 mL/s  $\text{N}_2$  flow rate. A possible mechanism for the mixed-phase formation by LPCVD on the glass substrates was described as well as the implications for the production of self-cleaning structures. The finding in this chapter suggested a possible general fabrication route via provision of a suitable sodium source.

**Chapter 6** Titania thin films consisting of a mixed phase of  $\text{TiO}_2(\text{B})$  and anatase were synthesized by Low Pressure Chemical Vapour Deposition (LPCVD) onto a number of different substrates including silicon wafer, fused quartz, highly ordered pyrolytic graphite (HOPG) and pressed graphite flake (grafoil). General LPCVD conditions were titanium isopropoxide (TTIP) and  $\text{N}_2$  gas as the precursor and carrier gas respectively,  $600^\circ\text{C}$  nominal reaction temperature, and 15 min reaction time. XRD, Raman spectroscopy, scanning and transmission electron microscopy were used to characterise the thin films which exhibited a columnar morphology together with smaller equi-axed particles. Pre-treatment of substrates by spraying with a NaOEt solution was found to encourage the crystallization of  $\text{TiO}_2(\text{B})$  during the LPCVD process. Increasing the concentration of Na in the pre-treatment process resulted in a higher proportion of  $\text{TiO}_2(\text{B})$  in the thin films up to an optimum condition of 0.75%  $\text{W}/\text{V}$  of Na. Na diffusion from the substrate surface into the adjacent  $\text{TiO}_2$  is the proposed mechanism for promoting  $\text{TiO}_2(\text{B})$  formation as opposed to the anatase phase.

**Chapter 7** Nano-particulate titania/titanate thin films were deposited onto a Si-wafer substrate via modified LPCVD method at 600°C. Substrates were pre-treated by spraying with a hydroxide solution containing alkali metal ions such as  $\text{Li}^+$ ,  $\text{Na}^+$  and  $\text{K}^+$  and used with the general LPCVD method. The same LPCVD synthesis conditions as chapter 6 were operated during the titania deposition. In a region containing an absence of alkali metal ions, this promotes solely the anatase phase in all thin film samples similar to the results in chapter 5 and 6, whereas, the presence of different types of alkali metal ions on the substrate surface promotes a different titania/titanate phase composition in the thin films. The effect of different alkali metal ions was found to complicate the phase formation: It was found that only  $\text{Na}^+$  ions can encourage the phase formation of  $\text{TiO}_2(\text{B})$  and  $\text{K}^+$  ions provide only a very small minority of the  $\text{TiO}_2(\text{B})$  phase in the thin films, whereas  $\text{Li}^+$  ions cannot produce the  $\text{TiO}_2(\text{B})$  phase. Interestingly, layered alkali metal titanates with a monoclinic crystal structure of  $\text{Na}_2\text{Ti}_6\text{O}_{13}$ ,  $\text{Li}_2\text{TiO}_3$ , and  $\text{K}_2\text{Ti}_6\text{O}_{13}$  were all detected in the thin film samples which were substrate pre-treated with  $\text{NaOH}$ ,  $\text{LiOH}$ , and  $\text{KOH}$  solution, respectively. The presence of  $\text{Li}^+$  ions also encouraged an unusual phase formation of rutile and brookite. Phase formation mechanisms based on the migration effect of alkali metal ions from the pre-treatment layer into the deposited nascent titania and formation of intermediate titanate phases, have been proposed.

## 8.2 Main Findings from the Research

- This research demonstrates for the first time the synthesis of mixed phase  $\text{TiO}_2(\text{B})$  and anatase on soda-lime glass substrates by LPCVD and suggests a potential mechanism for  $\text{TiO}_2(\text{B})$  formation during the LPCVD process.
- A new synthetic strategy based on a modified LPCVD method has been used to synthesise mixed phase  $\text{TiO}_2(\text{B})$  and anatase thin films on any general substrate. This novel synthesis method involves a substrate pre-treatment process using a sodium-containing solution followed by LPCVD. This is the first time that the highly interesting  $\text{TiO}_2(\text{B})$  phase (mixed with anatase) has been prepared by CVD on substrates other than soda-lime glass. Accordingly, this modified LPCVD method is considered to be a universal synthesis method for mixed phase  $\text{TiO}_2(\text{B})$  and anatase thin films on any desired substrate.
- This thesis demonstrates, for the first time, the effect of different alkali metal ions ( $\text{Li}^+$ ,  $\text{Na}^+$  and  $\text{K}^+$ ) on the phase formation in the titania/titanate thin films during the LPCVD process. A phase formation mechanism based on the effects of alkali metal migration into the deposited titania thin films and formation of an alkali metal titanate intermediate phase is proposed.

- This research demonstrates a full characterization of the thin film morphology, structure and chemistry leading to propose a potential mechanism for TiO<sub>2</sub>(B) formation during the modified LPCVD process. This may suggest other possible fabrication processes using a similar strategy via provision of the other metal cations.
- This work is topical as there are many proposed benefits of mixed phase nanoparticulate TiO<sub>2</sub>(B)/anatase thin films on rigid substrates, including their use as anode materials in Lithium ion battery anodes and also as photocatalytic materials.

### 8.3 Future Work

- **Thin film Preparation**
  - Study the use of the other monovalent cations (the chemical and physical properties of which are supposedly close to alkali metal cations) such as Cs<sup>+</sup>, NH<sub>4</sub><sup>+</sup> and Ag<sup>+</sup> on titania/titanate phase formation under the LPCVD synthesis process;
  - Investigate the use of the divalent and trivalent cations such as alkaline earth metal cations (Mg<sup>2+</sup>, Ca<sup>2+</sup>), Al<sup>3+</sup> and transition metal cations (Cu<sup>2+</sup>, Fe<sup>2+</sup>, Zr<sup>2+</sup>) on the phase formation of titania/titanate thin film samples during the LPCVD synthesis process;
  - The LPCVD synthesis conditions could be changed, for example: 1.) by changing the Ti source from TTIP to TiCl<sub>4</sub>, using a dilution of TTIP in isopropanol solution instead of the commercial TTIP and using a mixed carrier gas e.g. O<sub>2</sub> and N<sub>2</sub> instead of pure N<sub>2</sub> gas to study the effect on phase formation in the thin films; 2.) by using a reaction temperature lower or higher than 600°C in order to study the effect of temperature on ion migration; 3.) by using a longer reaction time than 15 min to study the influence of a diffusion time and diffusion distance of alkali metal ions on the phase formation and the phase distribution in the thin films;
  - Study hydrothermal synthesis using other metal hydroxide solutions and investigate the phase formation mechanism and compare with the results from the LPCVD synthesis process when the substrate is pre-treated with those metal ions;
  - Other oxide matrices such as Zr<sub>x</sub>O<sub>y</sub>, Zn<sub>x</sub>O<sub>y</sub>, Nb<sub>x</sub>O<sub>y</sub>, Ta<sub>x</sub>O<sub>y</sub>, W<sub>x</sub>O<sub>y</sub> could be studied instead of Ti<sub>x</sub>O<sub>y</sub> using the modified LPCVD process with a pre-treated substrate.

- **Characterisation**

- To identify more clearly phase formation in the thin films and the phase transformation mechanism during the LPCVD process, all thin film samples in chapter 7 should be prepared as a FIB cross-sectional sample for TEM investigation both for STEM/EDX elemental mapping and HRTEM imaging, to see the relative distribution of elemental composition and to examine the phase location in the thin films relative to the position from the pre-treated substrate. Chemical analysis using depth profiling XPS (determination of elemental composition of the thin films as a function of depth by ion beam etching) should be carried out to confirm the chemical analysis results from EDX. Moreover, typical TEM samples prepared by simply scraping the thin film samples from the substrate should also be investigated to obtain more supporting data.

- **Applications**

- As such this research could be of interest to a broad group focused on materials for energy storage and sustainability including those interested in the application of such materials in photocatalysts, including self-cleaning glass, and also as modified anodes in lithium ion batteries. Therefore, some functional characterization such as photocatalytic dye degradation or photocatalytic water-splitting reactions should be undertaken and compared to the results obtained using same mass of a standard titania powder (such as P25). In addition, if the thin films were deposited onto a conductive electrode, the electrochemical properties should be tested to provide the charge/discharge capacity and also the number of charge/discharge cycles; in addition simple photocurrents could be measured.

## Appendix I

### STANDARD OPERATING PROCEDURE

| MAIN                  |  |
|-----------------------|--|
| SOP REFERENCE NUMBER: | LUESP00001-2                                 |
| EQUIPMENT             | Low Pressure Chemical Deposition Rig (LPCVD) |
| LOCATION:             | SPEME B.40                                   |

| ORIGINATOR DETAILS |                                  |                     |             |
|--------------------|----------------------------------|---------------------|-------------|
| NAME:              | Yothin Chimupala / Rob Simpson   | SCHOOL / INSTITUTE: | SPEME / IMR |
| E-MAIL:            | pmyc@leeds.ac.uk                 | TEL:                | 3432366     |
| SUPERVISOR:        | Prof. R. Brydson                 | SCHOOL / INSTITUTE: | SPEME / IMR |
| E-MAIL:            | r.m.drummond-brydson@leeds.ac.uk | TEL:                | 3432369     |

| COPIES   |  |
|--|--|
| ORIGINAL:  | Retained by the Originator/supervisor/PI/Manager electronically.                     |
| COPY AND ANY APPENDICES OR CROSS-REFERENCED DOCUMENTS: | Retained by the Originator/supervisor/PI/Manager electronically/ and with equipment. |

| DOCUMENT AND ENVIRONMENT PREREQUISITES   |            |
|--|------------|
| LOCATION:  | SPEME B.40 |
| (LIST DOCUMENT AND ENVIRONMENT PRE-REQUISITES ETC...ATTACH REFERENCES AS REQUIRED)   |            |
| <p>1. Pre experiment document and environment prerequisites:</p> <ul style="list-style-type: none"> <li>1.1. Signed and laboratory induction.</li> <li>1.2. Access to laboratory.</li> <li>1.3. Signed risk assessment completed on RIVO Safeguard.</li> <li>1.4. Signed COSHH documentation attached to risk assessment in RIVO Safeguard.</li> <li>1.5. Ensure mains cold water supply is running cold.</li> <li>1.6. Ensure crushed ice supply is available.</li> </ul> |            |

| HEALTH AND SAFETY PREREQUISITES  |  |
|--|--|
| (LIST HEALTH AND SAFETY PRE-REQUISITES ETC...ATTACH REFERENCES AS REQUIRED)  |  |
| <p>1. Pre experiment Health and Safety prerequisites:</p> <ul style="list-style-type: none"> <li>1.1. Ensure laboratory Local Exhaust Ventilation (LEV) is operating correctly.</li> <li>1.2. Ensure equipment fume cupboard is operating correctly.</li> <li>1.3. Ensure all electrical equipment is within PAT test.</li> <li>1.4. Ensure all PPE is available and in serviceable condition.</li> <li>1.5. Ensure correct use of PPE including Lab coat, Disposable nitrile gloves, Safety glasses / goggles.</li> </ul> |  |

|                       |  |
|-----------------------|--|
| EQUIPMENT:            | Low Pressure Chemical Deposition Rig (LPCVD) |
| SOP REFERENCE NUMBER: | LUESP00001-2                                 |

| STANDARD OPERATING PROCEDURE  |   |
|---|---|
| (LIST STANDARD, SAFE START-UP, USE AND SHUTDOWN PROCEDURE, ATTACH REFERENCES AS REQUIRED) |   |
| 1.  | Pre experiment equipment checks: (Reference Fig.1)  |
| 1.1.  | Ensure all pipe work is clean and correctly fitted.   |
| 1.2.  | Pre-test system for overpressure pressure relief at $\leq 0.5$ bar: <ul style="list-style-type: none"> <li>1.2.1. Ensure dreschel bottle side opening is pointing away from the normal operator position. This way in the unlikely scenario that the clamped plug is ejected from the bottle by pressure in the system, the plug's trajectory should not incur any undue safety implications.</li> <li>1.2.2. Close valves V1, V3, and V4.</li> <li>1.2.3. Open Rotameter slightly.</li> <li>1.2.4. Close fume cupboard.</li> <li>1.2.5. Ensure regulator and in-line gas valves are closed.</li> <li>1.2.6. Open Nitrogen gas cylinder valve slowly.</li> <li>1.2.7. Set Nitrogen regulator to 0.5 bar.</li> <li>1.2.8. Open Nitrogen gas in-line valve. Nitrogen should enter the system and not exceed 0.5 bar pressure.</li> <li>1.2.9. Close Nitrogen gas cylinder valve.</li> <li>1.2.10. Slightly increase the Nitrogen pressure by slowly opening the Nitrogen regulator towards but not exceeding 0.75 bar. Valve V2 should open to relieve any excess system pressure over 0.5 bar. The system should then stabilise at approximately 0.5 bar with no leakage. (If this is not the case, Valve V2 must be checked and set for correct operation).</li> <li>1.2.11. Open valve V3 to vent system pressure.</li> <li>1.2.12. Wait for Nitrogen gas regulator outlet pressure gauge to reach 0.</li> <li>1.2.13. Close Nitrogen gas in-line valve.</li> <li>1.2.14. Close valve V3.</li> </ul> |
| 1.1.  | Ensure vacuum pump oil is clear. (If oil is cloudy, it is most likely contaminated or has water in it, run pump with system isolated and pump gas ballast valve open until oil is clear, once satisfied oil is clear shut gas ballast valve and stop pump).   |
| 1.2.  | Ensure chemical inlet trap is not over contaminated. (See manufacturer's documentation).  |
| 1.3.  | Ensure level of silicon oil in the heated oil bath is at the correct level.   |
| 1.4.  | Ensure the dreschel bottle is correctly located, centrally into the silicon oil ensuring a gap of approximately 10mm from the bottom of the bottle to the floor of the oil bath and that side opening is pointing away from the normal operator position and securely plugged using stopper clamp.  |
| 1.5.  | Ensure there is sufficient compressed gas supply for the experiment.  |
| 1.6.  | Ensure Experiment in Progress document is correctly completed and displayed in a prominent position near the experiment.  |
| 2.  | Experimental procedure: (Reference Fig.1)   |
| 2.1.  | Load substrate into glass furnace tube ensuring the substrate is horizontally level and located in the centre of the furnace hot zone.  |
| 2.2.  | Connect glassware ensuring correct connection.  |
| 2.3.  | Turn on mains cold water supply to the condenser and run water at suitable rate.  |
| 2.4.  | Pack the flask around the cold trap with ice.   |
| 2.5.  | Check system for vacuum: <ul style="list-style-type: none"> <li>2.5.1. Switch on pirani gauge (ensure atmospheric pressure is displayed).</li> <li>2.5.2. Close Rotameter, valves V1, V3.</li> <li>2.5.3. Open valve V4.</li> <li>2.5.4. Close fume cupboard.</li> </ul>  |

- 2.5.5. Switch on vacuum pump.
  - 2.5.6. Open valve V5 slowly whilst observing pirani and capsule gauges.
  - 2.5.7. Ensure the system can sustain vacuum at  $\leq 50$  mbar.
  - 2.5.8. Close valve V5.
  - 2.5.9. Release vacuum from system by opening valves V1 and V3.
  - 2.5.10. Close valve V4.
  - 2.5.11. Leave vacuum pump running.
  - 2.6. Switch on Hot plate and set to approximately  $80^{\circ}\text{C}$ .(adjust to suit) Insert thermometer into silicon oil if needed.
  - 2.7. Pre-set gas flow:
    - 2.7.1. Close valve V1 (leave V3 open).
    - 2.7.2. Ensure regulator and in-line gas valves are closed.
    - 2.7.3. Open Nitrogen gas cylinder valve slowly.
    - 2.7.4. Set Nitrogen regulator to 0.5 bar.
    - 2.7.5. Open Nitrogen gas in-line valve.
    - 2.7.6. Open rotameter and set nitrogen flow to 1L/min. (or adjust to suit).
    - 2.7.7. Close Nitrogen gas cylinder valve.
    - 2.7.8. Wait for Nitrogen gas regulator outlet pressure gauge to reach 0.
    - 2.7.9. Close Nitrogen gas in-line valve.
    - 2.7.10. Close valve V3.
  - 2.8. Open valve V5.
  - 2.9. Switch on tube furnace and set to desired temperature.
  - 2.10. Ensure correct vacuum pressure, furnace temperature and oil bath temperature have been attained.
  - 2.11. Remove clamped plug from side opening of dreschel bottle.
  - 2.12. Carefully load premeasured amount of precursor into dreschel bottle through the newly opened opening using a suitable pipette. Be sure not to expose ground glass sealing area to precursor.
  - 2.13. Re-plug dreschel bottle opening with plug and ensure it is securely plugged using stopper clamp.
  - 2.14. Slowly open valve V4.
  - 2.15. Close fume cupboard.
  - 2.16. Open Nitrogen gas bottle valve and set the regulator to 0.5 bar.
  - 2.17. Slowly open Nitrogen gas in-line valve.
  - 2.18. Precursor should start to boil inside dreschel bottle and vapours should be seen entering to glass furnace tube.(the deposition inside the tube furnace should now be starting).
  - 2.19. Monitor whole system until all precursor is used. Any un-deposited precursor should be trapped in the condenser and the cold trap and should not enter the downstream pipe-work.
  - 2.20. When satisfied that all the precursor has been used, shut down the system.
3. System shut down (normal): (Reference Fig.1)
- 3.1. Close Nitrogen gas cylinder valve.
  - 3.2. Open the fume cupboard.
  - 3.3. Close valve V4 and immediately open valves V1 and V3.
  - 3.4. Set furnace to  $0^{\circ}\text{C}$ . (do not switch off furnace as temperature indication is required to enable safe removal of sample).
  - 3.5. Switch off hot plate.
  - 3.6. Wait for inert gas regulator outlet pressure gauge to reach 0.
  - 3.7. Close inert gas regulator.
  - 3.8. Close inert gas in-line valve.
  - 3.9. Close rotameter.
  - 3.10. Close valve V5.
  - 3.11. Switch off vacuum pump.
  - 3.12. Switch off pirani gauge.
  - 3.13. Wait until furnace has reached safe temperature ( $<50^{\circ}\text{C}$ ). This may take several hours.
  - 3.14. Turn off mains cold water supply.

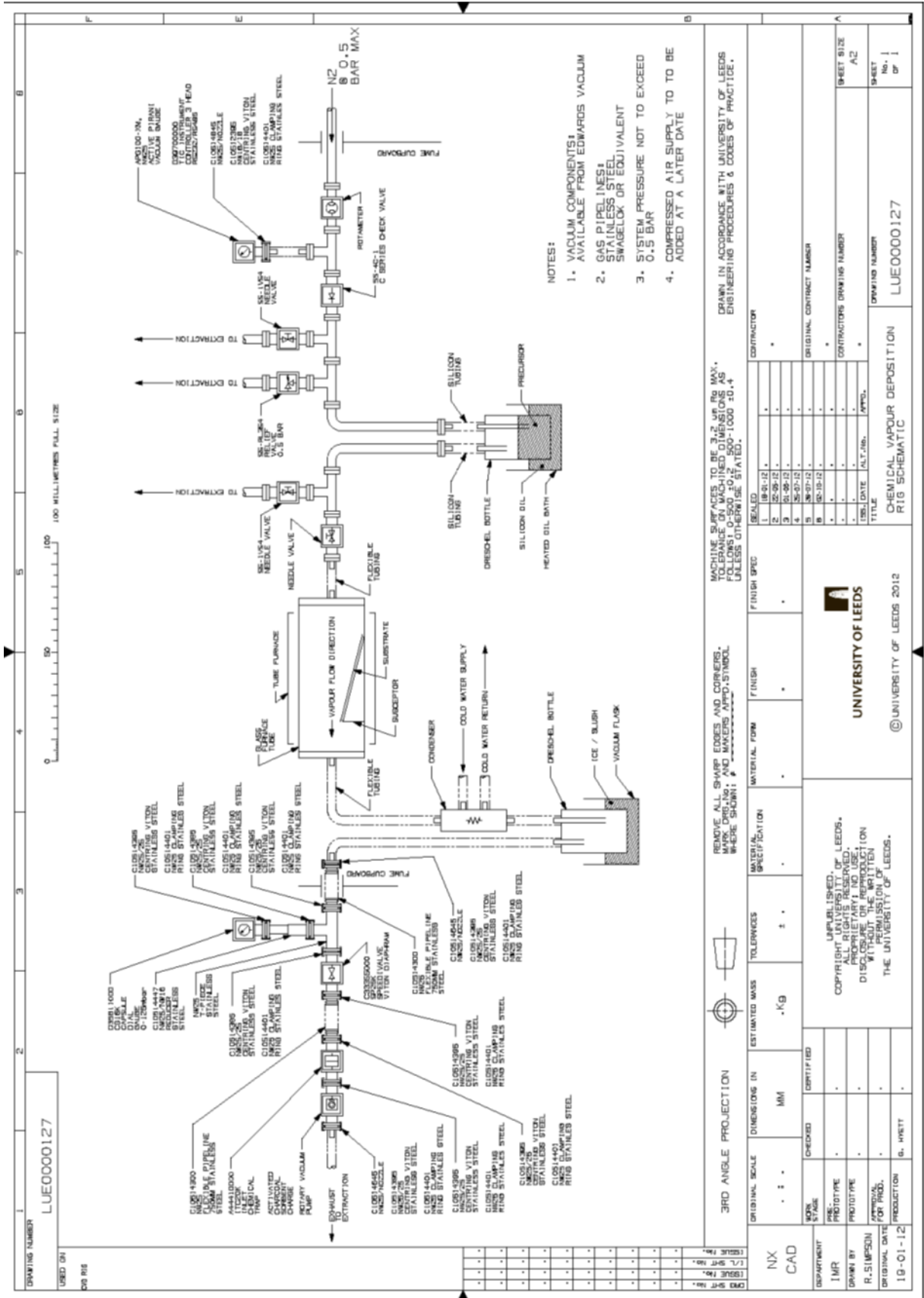
- 3.15. Switch off furnace.
- 3.16. Disconnect furnace tube and remove sample.

4. System shutdown (emergency): (Reference Fig.1)

- 4.1. Do not open fume cupboard.
- 4.2. Close inert gas cylinder valve.
- 4.3. Switch off furnace.
- 4.4. Switch off hot plate.
- 4.5. Do not leave system if not in safe condition.
- 4.6. Wait for system to cool to a safe temperature.
- 4.7. If internal system pressure exceeds 0.5 bar, valve V2 will open to relieve excess pressure to protect rest of system.

5. System cleaning:

- 5.1. Obtain receptacles for waste collection.
- 5.2. Disassemble all contaminated glassware.
- 5.3. Clean contaminated glassware using either mechanical or chemical methods.
- 5.4. If chemical methods are used, separate risk and COSHH assessments will need to be completed and signed in RIVO Safeguard.
- 5.5. Inspect all pipe work and mechanically clean if necessary.
- 5.6. Inspect Inlet chemical trap sorbent for contamination levels. If necessary clean trap and replace sorbent charge following chemical inlet trap manufacturer's documentation.
- 5.7. Ensuring all components are fully dry, re-assemble the system.
- 5.8. Dispose of any waste according to the faculty's chemical waste disposal procedures.



LUE0000127 LOW PRESSURE CHEMICAL VAPOUR DEPOSITION RIG SCHEMATIC.

## Appendix II

### SUPPORTING INFORMATION

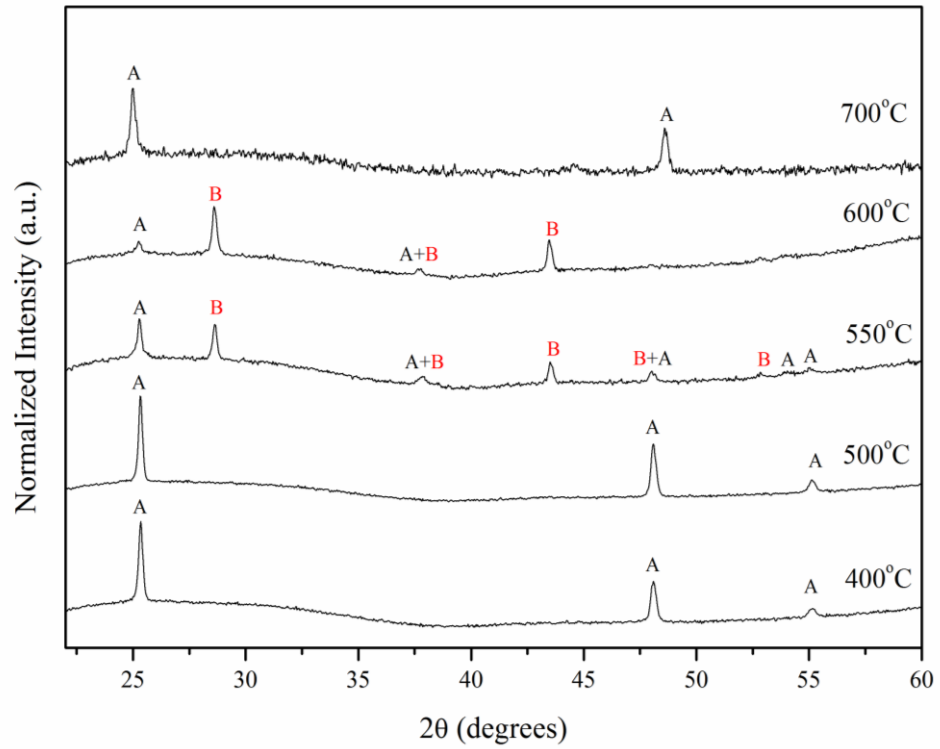


**Figure I** Out of plane XRD patterns of TiO<sub>2</sub> Thin film deposited onto soda-line glass substrates prepared by LPCVD at 400°C, 500°C, 550°C, 600°C and 700°C: A and B refer to the assignment of the anatase TiO<sub>2</sub> and TiO<sub>2</sub>(B) respectively.